FACULTY OF SCIENCES

Hunting for nuclear short-range correlations: the connection to electroinduced two-nucleon knockout reactions

– Camille Colle –

Supervisor: prof. dr. J. Ryckebusch
Dissertation submitted in fulfillment of the requirements for the degree of Doctor (Ph.D.) in Science: Physics

Department of Physics and Astronomy
Faculty of Sciences
Ghent University
Academic year 2016-2017

GHENT UNIVERSITY

Contents

CHAPTER 1

Introduction

1.1 Introduction

The nucleus is a complex many-body quantum-mechanical system. Up to the present day it remains a very challenging problem to determine the corresponding wave functions and obtain reliable observables.

The direct approach of calculating the non-relativistic many-body wave function starting from the nucleon-nucleon interaction is a computationally very hard and high-dimensional problem. Due to this complexity this approach is only feasible for light nuclei up to $A = 12$ [1–4]. When larger nuclei are considered the complex many-body problem has to be approximated. The correlated basis function theory [5, 6] and cluster expansion techniques [7–9] are examples of models that approximate the many-body problem. For infinite nuclear matter ($A \to \infty$) it is possible the solve the many-body problem with realistic nucleon-nucleon potentials [10].

A very successful model, reproducing many nuclear properties, is the independent-particle model (IPM) [11, 12]. The independent-particle model treats the nucleons in the nucleus as independent particles moving in an averaged nuclear potential. This mean-field potential encodes the average effect of the individual nucleon-nucleon interactions. The IPM essentially reduces the A-body problem to a sum of A single-body problems. This cuts down the curse of dimensionality in the many-body wave function tremendously. Despite its simplicity the IPM manages to capture a lot of the nuclear properties such as the exceptional stability of nuclei with certain combinations of protons and neutrons, nucleon binding energies and the spin and parity of the ground state of stable and unstable nuclei.

In order to get a feeling about the structure of nuclei, the nuclear packing fraction (NPF) can be considered. The nuclear packing fraction is defined as the fractional volume occupied by the nucleons with regard to the total nucleus. The NPF can be estimated by considering the

nucleons and nucleus as solid spheres. The nucleon is a diffuse system with a hard repulsive core with radius ≈ 0.5 fm. The proton-mean-squared charge radius, as extracted from electron-proton scattering data [13] is approximately 0.9 fm. With the radius of a nucleus given by the empirical formula $1.2A^{\frac{1}{3}}$ fm, the NPF is in the range $[0.07, 0.42]$. Comparing the NPF to the maximum packing fraction of solid spheres of ≈ 0.74 it can be concluded that the nucleus can be interpreted as a dense quantum liquid. Given this observation it is rather surprising that the IPM accurately describes many nuclear properties.

As the IPM treats the nucleons as moving independently from each other in a mean-field potential, it fails to capture features generated by nucleon-nucleon correlations. As such the IPM cannot reproduce nuclear properties that are sensitive to the fluctuations about the mean-field predictions. In order to build more realistic models the nucleon-nucleon correlations have to be included. When correlations are introduced, however, the many-body nature of the nucleus quickly resurfaces, increasing the dimensionality beyond numerical feasibility. The nuclear correlations are generally classified into two categories: the long-range correlations (LRC) and the short-range correlations (SRC). The aim of this dissertation is to investigate short-range nuclear correlations. Starting from the IPM the short-range nucleon-nucleon correlations are introduced in a tractable way, keeping the complexity under control. Thereby the model includes the correlations which are expected to drive nuclear features under study. Imposing such a restriction is non-trivial and requires a thorough understanding of the dynamics of nucleon-nucleon correlations. The LRC are connected with the long-range attractive part of the nucleon-nucleon interaction. They can be incorporated in an independent-particle model by explicitly coupling the single-particle degrees-of-freedom to collective nuclear states, such as giant resonances and surface modes. The effect of LRC is confined to nucleon momenta approximately smaller than the Fermi momentum. The bulk of the SRC, on the other hand, is associated with the short-range repulsive core and the tensor component of the nucleon-nucleon interaction. The SRC generate strong-fluctuations from the mean-field picture whereby the individual nucleons receive large momenta compared to the Fermi momentum. All IPM single-particle orbitals are depleted by SRC and higher energy levels are populated. This reduces the occupation probability, or spectroscopic strength, of the IPM single-particle orbitals [14]. Recent reviews of nuclear SRC can be found in Refs. [15–18].

Because of the separation between SRC and LRC in momentum space, the SRC can be readily isolated by limiting ourselves to the appropriate momentum range. The effect of SRC can be introduced in a systematic way using the low-order correlation operator approximation (LCA), outlined in chapter 2. Thereby the expectation value of a general operator is calculated by transforming the operator to an effective operator, which incorporates the effect of SRC. The LCA introduces nuclear correlations while keeping the numerical complexity under control. It allows the study of SRC across the whole nuclear mass range. In [19] it is shown that the LCA yields similar results when compared to advanced quantum Monte-Carlo results [20], which are limited to $A \leq 12$.

The effect of SRC on the nuclear momentum distribution (NMD) is studied in chapter 2. The NMD is connected to the probability of finding a nucleon (nucleons) with a certain momentum inside a nucleus. As the LRC and SRC dominate in different momentum regions, the effect of SRC can be readily isolated by limiting ourselves to the study of the NMD in the appropriate momentum range. The one-body momentum distribution $n(\vec{k})$ corresponds

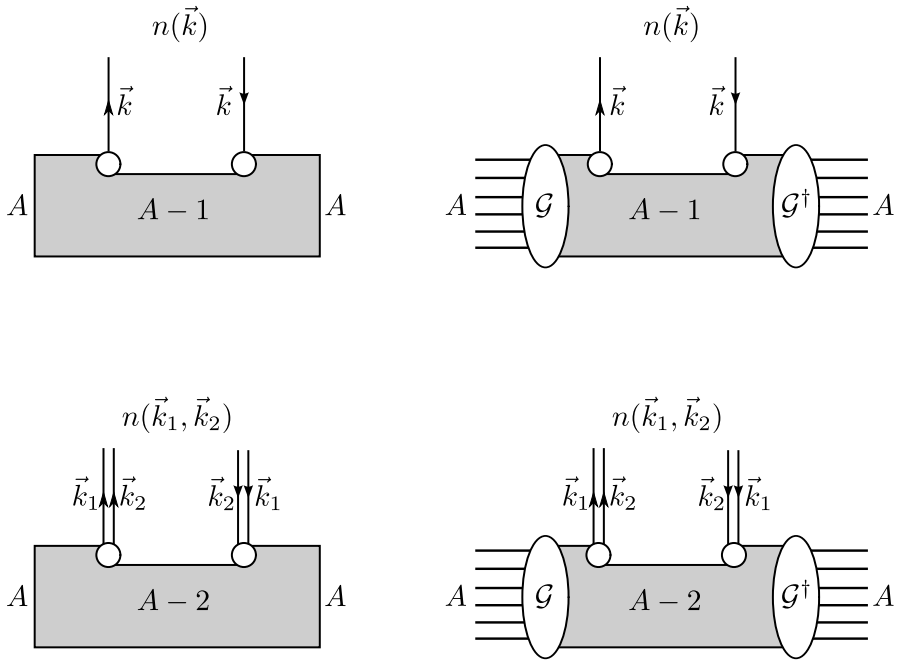

Figure 1.1 – Diagrams depicting the one-body momentum distribution $n(\vec{k})$ (top) and the two-body momentum distribution $n(\vec{k}_1, \vec{k}_2)$ (bottom). The momentum distributions can be interpreted as the probability of removing and adding a nucleon (nucleons) with momentum $\vec{k}$ (momenta $\vec{k}_1, \vec{k}_2$). The correlated nuclear systems $A, A-1$ and $A-2$ are represented by the gray band. Throughout this work the correlated wave functions are constructed by introducing a correlation operator $\mathcal{G}$ acting on the IPM nucleons, represented with the individual lines.

with the probability of finding a single nucleon with a certain momentum in the interval $[\vec{k}, \vec{k} + \mathrm{d}\vec{k}]$. The two-body momentum distribution $n(\vec{k}_1, \vec{k}_2)$ denotes the joint probability of simultaneously finding two nucleons with momenta $[\vec{k}_1, \vec{k}_1 + \mathrm{d}\vec{k}_1]$ and $[\vec{k}_2, \vec{k}_2 + \mathrm{d}\vec{k}_2]$. In the IPM, the two-body momentum distribution is given by the product of single-body momentum distributions, $n(\vec{k}_1, \vec{k}_2) = n(\vec{k}_1)n(\vec{k}_2)$. A diagram depicting the nuclear one and two-body momentum distribution is shown in Fig. 1.1. The correlated momentum distributions are calculated by correlating the IPM wave function by means of a correlation operator $\mathcal{G}$.

The SRC or NMD are not directly observable and have to be probed in nuclear scattering reactions. In this dissertation we seek to extract information about nuclear SRC from the analysis of measurements of exclusive electroinduced two-nucleon knockout reactions. Thereby nucleons are knocked out of the nucleus by a hard electromagnetic interaction and the energy and momentum of both outgoing nucleons is determined. These reactions are ideal for the study of SRC. In chapter 3 the connection of SRC physics and two-nucleon knockout reactions is discussed. The diagrams depicting one and two-nucleon knockout reactions are depicted in Fig. 1.2. In scattering reactions the NMD are not probed directly. In the NMD description of Fig. 1.1 there is no time flow and hence no exchanged energy. The only relevant quantity is the three-momentum of the nucleon(s). In scattering

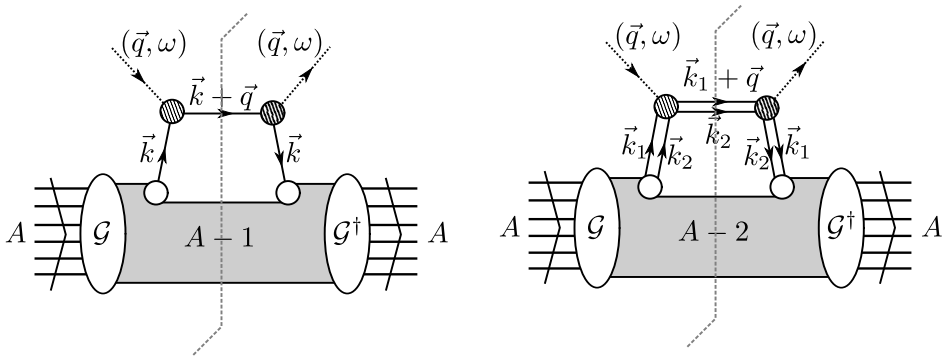

Figure 1.2 – The electroinduced one (two) nucleon-knockout reactions is depicted. A probe exchanges a virtual photon with energy ω and three-momentum $\vec{q}$ with the struck nucleon. The hatched circles denote the photon (two-)nucleon coupling. The correlated nucleus is constructed with the correlation operator $\mathcal{G}$ acting on the IPM nucleons.

reactions, where time flows and energy is exchanged, the corresponding quantity is called the spectral function. The spectral function is connected to the probability of finding a nucleon (nucleons) with a certain momentum and energy in the nucleus. It can be shown that in single-nucleon knockout reactions the one-body spectral function can be connected to the one-nucleon knockout cross section [21]. For the two-body spectral function and the two-nucleon knockout cross section such a connection is not evident, if not impossible.

A central issue of this dissertation is how information about the energy and momentum of the initial SRC nucleon pair can be recovered in the two-nucleon knockout reaction. It is shown that under appropriate kinematical constraints, the exclusive two-nucleon knockout cross section can be connected to the probability of finding a SRC pair with a certain center-of-mass (c.m.) momentum. Thereby the information about the relative momentum is inherently tied to the details of the photon two-nucleon interaction. It is not possible to make a direct connection between the cross section and the relative-momentum probability distribution of the SRC pair.

Final state interactions (FSI) have a large impact on measured cross sections for nuclear knockout reactions. The FSI are the interactions of the knocked out nucleon(s) with the recoiling nucleus. FSI cause a significant attenuation of the nuclear knockout cross section. In order to extract SRC properties from measured cross sections, the data has to be corrected for FSI. The modelling of the processes contained in the FSI poses a difficult problem. The FSI can be kept under control by considering reactions whereby the recoiling nucleus is left with little or no excitation energy.

The attenuation of the cross section can be connected to the nuclear transparency. The nuclear transparency is a measure of the attenuation strength of the FSI. For very soft FSI the recoiling nucleus is very transparent for the ejected nucleon(s) and the nuclear transparency will be high. Strong FSI will make the recoiling nucleus appear very opaque to the outgoing nucleon(s) and lead to a very low nuclear transparency. In Fig. 1.3 the electroinduced two-nucleon knockout reaction is depicted. Details about the description of the FSI and the electrodinduced two-nucleon knockout cross section can be found in chapter 3 and appendices A, B.

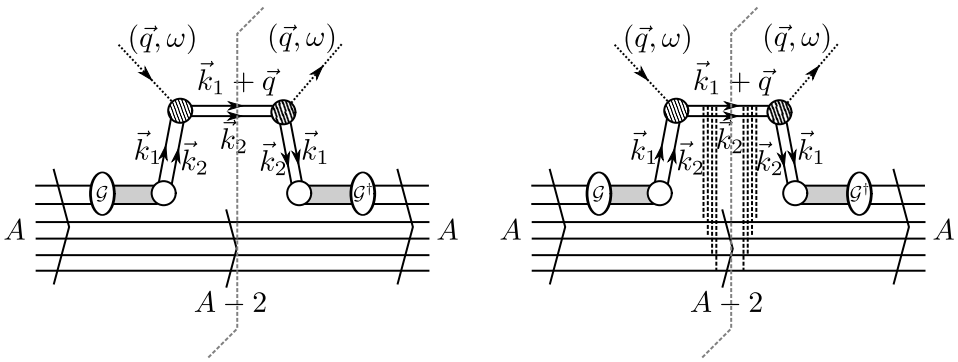

Figure 1.3 – A schematic representation of the SRC driven two-nucleon knockout reaction. In the reaction model of this dissertation only the initial pair, which is knocked out of the nucleus, is correlated. The $A-2$ nucleons are described by IPM nucleons. The dashed lines in the diagram on the left denote the final-state interactions (FSI) of the knocked out nucleon-pair with the $A-2$ nucleons in the recoiling nucleus.

1.2 Outline

The goal of this dissertation is to forge a bridge between the SRC physics and the measured observables for electroinduced two-nucleon knockout reactions. The major research topics can be summarized as follows:

- The characterization of SRC, uncovering:
  - The structure and isospin composition of SRC nucleon pairs; the identification of the dominant relative quantum numbers of SRC pairs sheds light on the internal structure of SRC pairs. The isospin composition of SRC pairs is sensitive to the tensor component of the nucleon-nucleon force and induces a heavy proton-neutron SRC pair dominance over proton-proton and neutron-neutron SRC pairs [22]. This has a large influence on the dynamics or SRC pairs in asymmetric nuclei with an unequal number of protons and neutrons. This topic is of more general interest as it is closely related to the universal properties of imbalanced two-component Fermi systems [23].
  - SRC dynamical features such as the c.m. momentum and opening-angle distribution. The SRC pair c.m. momentum distribution is the probability of finding a SRC nucleon pair with a certain c.m. momentum in the nucleus. Under the appropriate constraints it can be tied directly to the two-nucleon knockout cross section. It offers a clear connection between a measurable quantity and the SRC dynamics in the nuclear ground state. SRC pairs have a small c.m. and large relative momentum compared to the Fermi momentum in a nucleus. This implies that the individual nucleons are roughly moving back-to-back, with anti-parallel momenta. This feature can be probed in opening-angle distributions accessible in exclusive two-nucleon knockout scattering experiments.
- The study of the electroinduced exclusive two-nucleon knockout reaction, thereby establishing:

  - The mass dependence of the two-nucleon knockout scattering reaction across the whole nuclear mass range. By means of studies of cross-section ratios between targets of different mass, the mass dependence can be calculated independently from the details of the photon 2-nucleon coupling leading to robust results. From the mass dependence of the cross section it is possible to infer information about the SRC. In particular the mass dependence of the amount of SRC pairs in the nucleus can be derived.
  - The influence of FSI in the scattering reaction. The FSI have a large impact on the cross section and its mass dependence. An accurate description of FSI is essential. Without FSI corrections the SRC properties inferred from the mass dependence of the cross section would be heavily distorted.
  - The mass dependence of the nuclear transparency. The FSI attenuation effects are encoded in the nuclear transparency. With its mass dependence, the impact of FSI on the cross section can be quickly estimated across the nuclear mass range.

An outline of the structure of this dissertation is schematically represented in Fig. 1.4.

- Chapter 2 discusses the nuclear momentum distributions and how these can be accurately calculated within the low-order correlation operator approximation (LCA). The LCA corrects IPM wave functions for correlations by the means of a correlation operator acting on a many-body Slater determinant, representing the IPM wave function.
- Chapter 3 focusses on the electroinduced exclusive two-nucleon knockout cross section. This reaction is used to probe and characterize the short-range dynamics in a nucleus. The published results obtained for the reaction are also presented in this chapter. In addition to the published articles, supplementary material is presented in Secs. 3.2 and 3.3 complementing the corresponding article. Sec. 3.4 researches the possibility of reconstructing initial SRC properties from the measured two-nucleon knockout cross section.
- Chapter 4 provides a brief summary of the work presented in this dissertation accompanied by an outlook on future research and possible extensions of the developed framework for extracting the SRC information from the measured observables in two-nucleon knockout reactions.
- Appendix A gives a short introduction to the eikonal approximation, followed by its application in the Relativistic Multiple Scattering Glauber Approximation (RMSGA). The RMSGA is used to describe the FSI in our reaction model. The accuracy of different approximations within the RMSGA is investigated in a test model considering nucleon-nucleus scattering.

  Appendix B gives a detailed derivation of the factorized expression for the exclusive two-nucleon knockout cross section. The validity of the approximations that are necessary for the factorization of the cross section are examined.

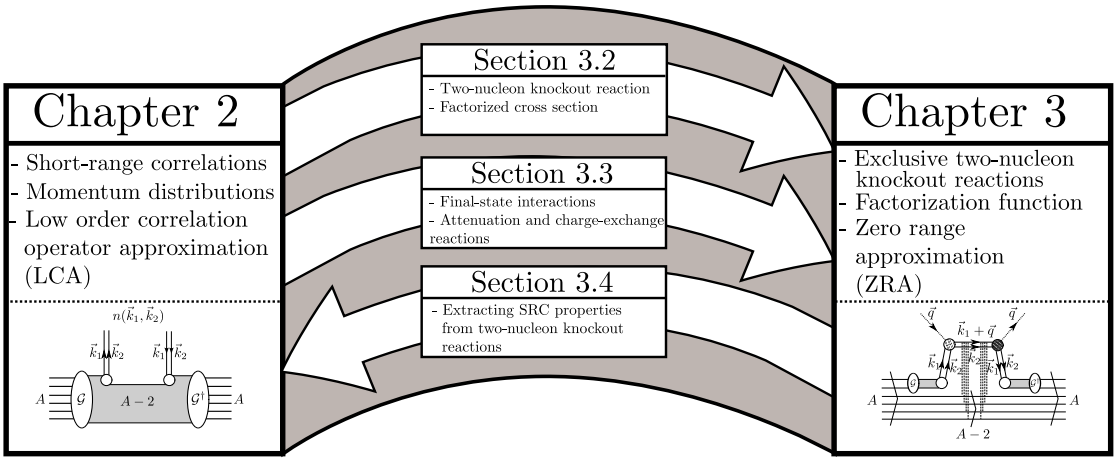

Figure 1.4 – Flowchart of the structure of this dissertation. In chapter 2 the nuclear momentum distributions are discussed. They contain all the information about the nuclear ground-state dynamics. Momentum distributions are sensitive to the effects of short-range correlations (SRC), making them very relevant to the study of SRC. The SRC are implemented using the LCA framework. Nuclear momentum distributions cannot be measured directly and have to be accessed in scattering experiments. The exclusive two-nucleon knockout scattering reaction is outlined in chapter 3. Thereby the SRC are implemented using the zero-range approximation (ZRA), which serves as a proxy for the more advanced correlation description of the LCA outlined in chapter 2. In Sec. 3.2 we focus on the theoretical derivation of the two-nucleon knockout cross section. This is followed by the discussion of the influence of final-state interactions (FSI) on the cross section in Sec. 3.3. Finally the issue of how initial SRC properties can be inferred from experimental two-nucleon knockout cross sections is investigated in Sec. 3.4.

1.3 References

[1] R. Schiavilla, R. B. Wiringa, S. C. Pieper, and J. Carlson, Phys. Rev. Lett. **98**, 132501 (2007).
[2] R. B. Wiringa, R. Schiavilla, S. C. Pieper, and J. Carlson, Phys. Rev. C **78**, 021001 (2008).
[3] H. Feldmeier, W. Horiuchi, T. Neff, and Y. Suzuki, Phys. Rev. C **84**, 054003 (2011).
[4] T. Neff, H. Feldmeier, and W. Horiuchi, Phys. Rev. C **92**, 024003 (2015).
[5] F. Arias de Saavedra, C. Bisconti, G. Co', and A. Fabrocini, Phys.Rept. **450**, 1 (2007).
[6] C. Bisconti, F. A. d. Saavedra, and G. Co', Phys. Rev. C **75**, 054302 (2007).
[7] M. Alvioli, C. Ciofi degli Atti, and H. Morita, Phys. Rev. Lett. **100**, 162503 (2008).
[8] M. Alvioli, C. Ciofi degli Atti, L. P. Kaptari, et al., Phys. Rev. C **85**, 021001 (2012).
[9] M. Alvioli, C. Ciofi degli Atti, L. P. Kaptari, et al., Phys. Rev. C **87**, 034603 (2013).
[10] A. Rios, A. Polls, and W. H. Dickhoff, Phys. Rev. C **89**, 044303 (2014).
[11] M. G. Mayer, Phys. Rev. **74**, 235 (1948).
[12] O. Haxel, J. H. D. Jensen, and H. E. Suess, Phys. Rev. **75**, 1766 (1949).

[13] P. G. Blunden and I. Sick, Phys. Rev. C **72**, 057601 (2005).
[14] L. Lapikás, Nucl. Phys. A **553**, 297 (1993).
[15] L. Frankfurt, M. Sargsian, and M. Strikman, Int. J. Mod. Phys. A **23**, 2991 (2008).
[16] J. Arrington, D. Higinbotham, G. Rosner, and M. Sargsian, Prog. Part. Nucl. Phys. **67**, 898 (2012).
[17] O. Hen, G. A. Miller, E. Piasetzky, and L. B. Weinstein, ArXiv e-prints, 1611.09748 (2016).
[18] M. Alvioli, C. Ciofi degli Atti, and H. Morita, Phys. Rev. C **94**, 044309 (2016).
[19] J. Ryckebusch, W. Cosyn, and M. Vanhalst, J. Phys. G **42**, 055104 (2015).
[20] R. B. Wiringa, R. Schiavilla, S. C. Pieper, and J. Carlson, Phys. Rev. C **89**, 024305 (2014).
[21] J. Caballero, T. Donnelly, E. Moya de Guerra, and J. Udias, Nucl.Phys. A **632**, 323 (1998).
[22] R. Subedi, R Shneor, P. Monaghan, et al., Science **320**, 1476 (2008).
[23] O. Hen, M. Sargsian, L. B. Weinstein, et al., Science **346**, 614 (2014).

CHAPTER 2

Short-range correlations and nuclear momentum distributions

2.1 Momentum distributions

The short-range correlations (SRC) generate nucleons with high-momentum compared to the Fermi momentum. Compared to the IPM, the SRC increase the probability of finding a nucleon with a momentum above the Fermi momentum by several orders of magnitude. This makes the nuclear momentum distribution a very relevant quantity in the study of SRC dynamics. The presence of significant strength in the momentum distribution above the Fermi momentum is one of the hallmarks of SRC.

For a given system the momentum distribution is connected with the probability of finding a particle with a certain momentum p. In nuclear systems, the momentum distribution contains all the information about the momentum decomposition of the nuclear ground state. Nuclear momentum distributions are an essential ingredient in the description of nuclear scattering reactions. When appropriate kinematic constraints are imposed in those scattering reactions, specific components of the nuclear momentum distribution can be probed. This can allow us to isolate and study particular dynamical features affecting the nuclear momentum distribution.

In this chapter the momentum distribution of a few prototypical systems is highlighted first. Qualitative features of the momentum distributions for these cases are discussed. This provides a context to interpret the nuclear momentum distributions calculated in more advanced models, as for example, presented later on in this chapter.

Throughout this introductory chapter the momentum distributions are investigated in systems where a particle is placed in a potential $V(\vec{r})$. The results of these simple models can be related to SRC dynamics in the following way. Given that the SRC are a local effect, it is expected that the correlations induced by two-body interactions will dominate the dynamics, while higher-order contributions are of less importance. The Schrödinger equation

for a two-body problem with the potential depending only on the relative coordinate, can be separated into center-of-mass (c.m.) and relative coordinates,

$$\hat{H} = \frac{\hat{\vec{p}}_1^{\,2}}{2m_1} + \frac{\hat{\vec{p}}_2^{\,2}}{2m_2} + V(\vec{r}_1 - \vec{r}_2) = \frac{\hat{\vec{P}}_{12}^{\,2}}{2M} + \frac{\hat{\vec{k}}_{12}^{\,2}}{2m} + V(\vec{r}_{12})$$

with $M = m_1 + m_2$, $m = \frac{m_1 m_2}{m_1+m_2}$, $\hat{\vec{P}}_{12} = \hat{\vec{p}}_1 + \hat{\vec{p}}_2$ and $\hat{\vec{k}}_{12} = \frac{m_2}{M}\hat{\vec{p}}_1 - \frac{m_1}{M}\hat{\vec{p}}_2$. The problem in the relative coordinate is then equivalent to solving the Schrödinger equation for a single particle with mass m moving in a potential $V(\vec{r})$, where $\vec{r}$ is the relative coordinate. This implies that, in the context of SRC and nucleon pairs, the momentum distributions presented in this chapter should be related to the relative-momentum distribution of nucleon pairs. The range of SRC is much smaller than the typical size of the nucleus, therefore the dynamical features generated by the SRC are predominantly independent of the size of the nucleus. In nuclei, the c.m. motion will be largely dictated by the global nuclear potential, mostly unaffected by the dynamics introduced by the explicit inclusion of two-body nucleon-nucleon interactions. It is therefore expected that the c.m.-momentum distribution mainly depends on the nucleus (A), while remaining insensitive to the SRC dynamics.

As a first approach in the study of high-momentum components in momentum distributions, the Schrödinger equation in three dimensions is examined, in particular the behaviour in the large-momentum limit.

$$\begin{aligned} \left[-\frac{\hbar^2}{2m}\nabla^2 + V(\vec{r})\right]\psi(\vec{r}) &= E\psi(\vec{r})\,, \\ \left[\nabla^2 + k^2\right]\psi(\vec{r}) &= U(\vec{r})\psi(\vec{r}) \end{aligned} \tag{2.1}$$

with $\frac{2mE}{\hbar^2} = k^2$ and $U(\vec{r}) = \frac{2m}{\hbar^2}V(\vec{r})$. Defining $\phi(\vec{p}) = \frac{1}{(2\pi)^{3/2}}\int \mathrm{d}\vec{r}\psi(\vec{r})e^{i\vec{p}\cdot\vec{r}}$, it follows from Eq. (2.1) that

$$\phi(\vec{p}) = \frac{1}{k^2 - p^2}\int \mathrm{d}\vec{r}\,U(\vec{r})\psi(\vec{r})e^{-i\vec{p}\cdot\vec{r}}\,. \tag{2.2}$$

In the extreme limit of short-range interactions, the potential $U(\vec{r})$ can be replaced with a delta-potential $U(\vec{r}) = U_0\delta(\vec{r})$,

$$\phi(\vec{p}) = \frac{U_0\psi(\vec{0})}{k^2 - p^2}\,.$$

The momentum distribution, given by $|\phi(\vec{p})|^2$, is then proportional to p^{-4} in the high-momentum limit. In Ref. [1] it is shown that the nuclear momentum distribution is proportional to $[p^{-2}v(p)]^2$, where $v(p)$ is the Fourier transform of the nucleon-nucleon potential. This is proportional to p^{-4} if $v(p)$ is momentum independent. In the context of SRC, it is possible to show that the tensor force induces a p^{-4} fall-off in the nuclear momentum distribution [2].

2.2 Momentum distributions in an infinite square well

The momentum distribution of the infinite square well in one, two and three dimensions is examined here. It is shown that the shape of the momentum distribution is very similar in

the different numbers of dimensions and that the asymptotic behaviour for large momenta is proportional to p^{-4}.

One-dimensional square well

The infinite square well is a well known quantum-mechanical problem. We study the momentum distribution of this system. The wave functions in coordinate space for a infinite square well in the region $[0, L]$ are given by

$$\psi_n(x) = \begin{cases} \sqrt{\frac{2}{L}} \sin(k_n x) & x \in [0, L] \\ 0 & x \notin [0, L] \end{cases} , \tag{2.3}$$

with $k_n = \frac{n\pi}{L}$, $n \in \mathbb{N}$ and $E_n = \frac{\hbar^2 k_n^2}{2m}$. As the Hamiltonian is time independent the eigenstates have definite energy E_n. Because the system is not translationally invariant the solutions (Eq. (2.3)) are not eigenstates of the momentum operator, and do not have a well defined momentum. The corresponding wave function in the momentum space $\phi_n(p)$ is given by

$$\phi_n(p) = \frac{1}{\sqrt{2\pi}} \int_{-\infty}^{+\infty} \mathrm{d}x\, e^{-ipx} \psi_n(x) = \sqrt{\pi L} n \frac{[1 - (-1)^n e^{-ipL}]}{\pi^2 n^2 - p^2 L^2} . \tag{2.4}$$

Note that p is defined in units of $\hbar$ making the dimension of p fm^{-1}. The corresponding momentum probability distribution reads

$$P_n(p) = |\phi_n(p)|^2 = 2\pi L n^2 \frac{(1 - (-1)^n \cos(pL))}{(\pi^2 n^2 - p^2 L^2)^2} . \tag{2.5}$$

$P_n(p)$ is depicted in Figure 2.2. The energy can be calculated from the momentum probability distribution,

$$\langle p^2 \rangle_n = \int \mathrm{d}p\, p^2 P_n(p) = \frac{2m}{\hbar^2} E_n = k_n^2 . \tag{2.6}$$

From Eq. (2.5) it is clear that the asymptotic behaviour of the probability distribution is proportional to p^{-4} for large values of p.

Two-dimensional square well

The coordinate-space wave functions for a two-dimensional infinite square well are given by

$$\psi_{nm}(\vec{r}) = \begin{cases} N_{nm} J_m(k_{m,n} r) \frac{e^{im\theta}}{\sqrt{2\pi}} & r \in [0, L] \\ 0 & r > L \end{cases} , \tag{2.7}$$

with $n, m \in \mathbb{N}$. Here, N_{nm} is a normalisation factor given by $\frac{\sqrt{2}}{L J_{m+1}(k_{m,n} L)}$. Furthermore, J_m are the Bessel functions of the first kind. The n'th root of the m'th order Bessel function J_m is given by $k_{m,n} L$, $J_m(k_{m,n} L) = 0$. As there is no closed form for the roots of the Bessel

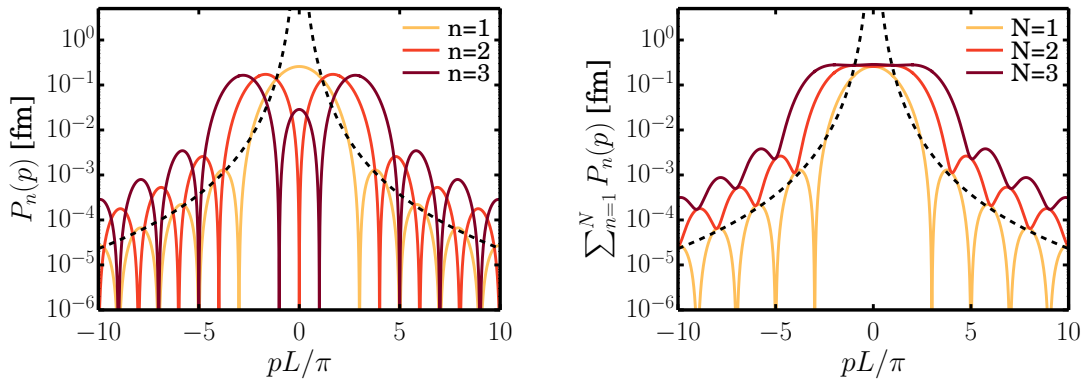

Figure 2.1 – The momentum probability distribution for a one-dimensional infinite square well with width L. The dashed line shows a power-law distribution $\propto p^{-4}$.

functions the allowed values for $k_{m,n}$ have to be calculated numerically. The solutions in momentum space (with p in units $\hbar$) are given by

$$\phi_{nm}(\vec{p}) = \sqrt{2}L^2 k_{m,n} \frac{J_{m-1}(k_{m,n}L)}{J_{m+1}(k_{m,n}L)} \frac{J_m(pL)}{(p^2L^2 - k_n^2L^2)} (-i)^m \frac{e^{im\theta_p}}{\sqrt{2\pi}} \,. \tag{2.8}$$

The corresponding momentum distribution reads

$$P_{nm}(p) = p \int \mathrm{d}\theta_p |\phi_{n,m}(\vec{p})|^2 = 2L^4 k_{m,n}^2 \left(\frac{J_{m-1}(k_{m,n}L)}{J_{m+1}(k_{m,n}L)} \right)^2 \frac{pJ_m^2(pL)}{(p^2L^2 - k_n^2L^2)^2} \,. \tag{2.9}$$

Given that the asymptotic behaviour of the Bessel function $J_m(x)$ for large x is proportional to $1/\sqrt{x}$ it can be inferred the asymptotic behaviour of $P_{nm}(p)$ of Eq. (2.9) is proportional to p^{-4} for large values of p.

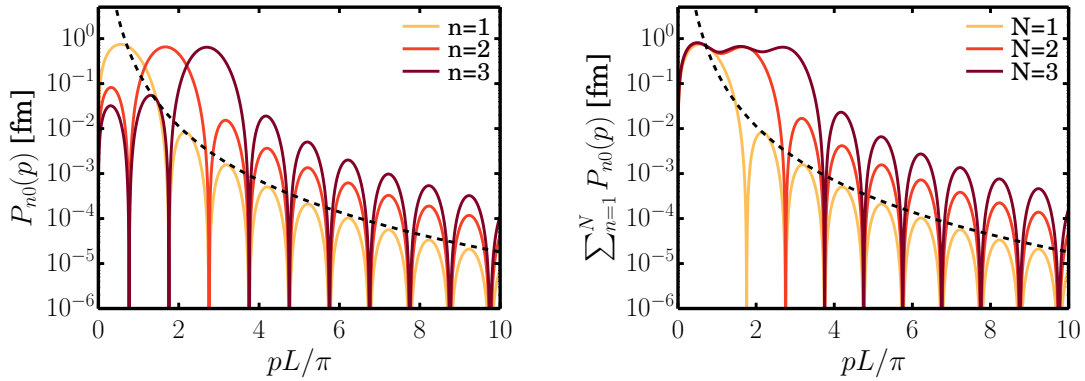

Figure 2.2 – The momentum probability distribution $P_{nm}(p)$ of Eq. (2.9), with $m = 0$ for a two-dimensional infinite square well with width L. The dashed line shows a power-law distribution $\propto p^{-4}$.

Three-dimensional square well

For an infinite three-dimensional square well the solutions in coordinate space are given by

$$\psi_{nlm}(\vec{r}) = \begin{cases} N_{nl} j_l(k_{l,n} r) Y_{lm}(\Omega_r) & r \in [0, L] \\ 0 & r > L \end{cases} . \tag{2.10}$$

Here, N_{nl} is a normalisation factor equal to $\frac{\sqrt{2}}{L^{3/2} j_{l+1}(k_{l,n} L)}$. Further, j_l are the spherical Bessel functions of the first kind. The values of $k_{l,n}$, $n \in \mathbb{N}$ are fixed through the requirement $j_l(k_{n,l} L) = 0$, they have to be determined numerically as there is no closed form for the roots of the spherical Bessel functions j_l. The solutions in momentum space (with p in units of $\hbar$) are given by

$$\phi_{nlm}(\vec{p}) = \frac{2 k_{l,n} L^{\frac{5}{2}}}{\sqrt{\pi}} \frac{j_{l-1}(k_{l,n} L)}{j_{l+1}(k_{l,n} L)} \frac{j_l(pL)}{(p^2 L^2 - k_n^2 L^2)} (-i)^l Y_{lm}(\Omega_p) , \tag{2.11}$$

with the corresponding momentum probability distribution $P_{nlm}(p)$,

$$P_{nlm}(p) = p^2 \int \mathrm{d}^2\Omega_p |\phi_{nlm}(\vec{p})|^2 = \frac{4 k_{l,n}^2 L^5}{\pi} \left(\frac{j_{l-1}(k_{l,n} L)}{j_{l+1}(k_{l,n} L)} \right)^2 \frac{p^2 j_l^2(pL)}{(p^2 L^2 - k_n^2 L^2)^2} . \tag{2.12}$$

Given that the dominant asymptotic behaviour of the spherical Bessel functions $j_l(x)$ for large x is proportional to $1/x$, the momentum distribution of Eq. (2.12) is proportional to p^{-4} for large p.

In the specific case $l = 0, m = 0$, the roots are given by $k_n = n\pi$ and the momentum distribution reads

$$P_{n00}(p) = 4\pi L^3 n^2 \frac{p^2 j_0^2(Lp)}{(\pi^2 n^2 - L^2 p^2)^2} = 4\pi L n^2 \frac{\sin^2(Lp)}{(p^2 L^2 - n^2 \pi^2)^2} . \tag{2.13}$$

The momentum distribution of Eq. (2.13) is displayed in Figure 2.3.

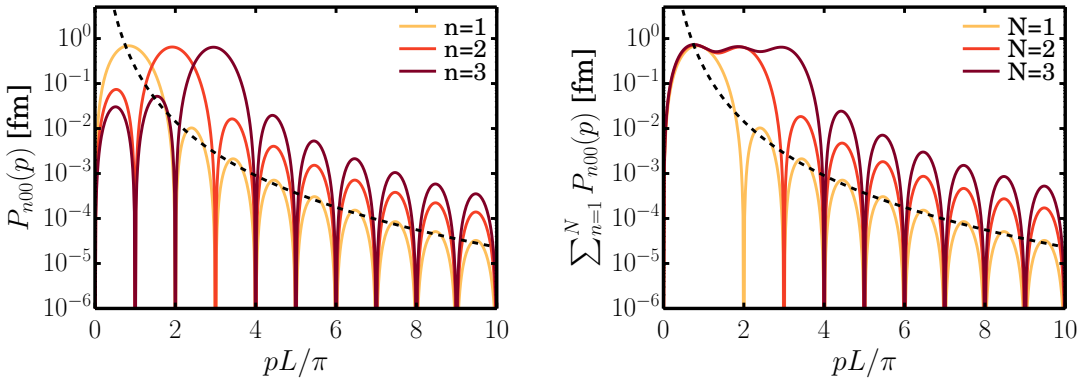

Figure 2.3 – The momentum probability distribution $P_{nlm}(p)$ of Eq. (2.13) with $l = 0, m = 0$, for a three-dimensional infinite square well with width L. The dashed line shows a power-law distribution $\propto p^{-4}$.

2.3 On the origin of high-momentum components in momentum distributions

It is often posed that a hard-core repulsive potential induces high-momentum components in the momentum distribution. We will investigate this in more detail using a simple approach. The Schrödinger equation is solved for a spherically symmetric potential $V(r)$. The ground-state wave function is investigated in coordinate space, $\psi_0(\vec{r}) = R_{n=0,l=0}(r)Y_{l=0,m=0}(\Omega_r)$, and momentum space, $\phi_0(\vec{p}) = 1/(2\pi)^{3/2} \int \mathrm{d}^3\vec{r}\, e^{-i\vec{p}\cdot\vec{r}}\psi_0(\vec{r}) = \Phi_{n=0,l=0}(p)Y_{l=0,m=0}(\Omega_p)$. The radial Schrödinger equation adopts the form,

$$\left[-\frac{\hbar^2}{2mr^2}\frac{\mathrm{d}}{\mathrm{d}r}\left(r^2\frac{\mathrm{d}}{\mathrm{d}r}\right) + \frac{\hbar^2\hat{L}^2}{2mr^2} + V(r)\right] R(r)Y_{00}(\Omega_r) = ER(r)Y_{00}(\Omega_r)$$

$$\left[-\frac{\hbar^2}{2mr^2}\frac{\mathrm{d}}{\mathrm{d}r}\left(r^2\frac{\mathrm{d}}{\mathrm{d}r}\right) + V(r)\right] R(r) = E_0R(r)\,.$$

Defining $u(r) = rR(r)$ results in,

$$\left[-\frac{\hbar^2}{2mr^2}\frac{\mathrm{d}}{\mathrm{d}r^2} + V(r)\right] u(r) = E_0u(r)\,. \tag{2.14}$$

Bound states are investigated by introducing a harmonic-oscillator potential $\frac{1}{2}m\omega^2r^2$. A repulsive-core term $V_{\mathrm{core}}(r)$ is added to the harmonic-oscillator potential,

$$V(r) = \frac{1}{2}m\omega^2r^2 + V_{\mathrm{core}}(r)\,.$$

Inserting this potential into Eq. (2.14) results in,

$$\left[-\frac{\hbar^2}{2m}\frac{\mathrm{d}}{\mathrm{d}r^2} + \frac{1}{2}m\omega^2r^2 + V_{\mathrm{core}}(r)\right] u(r) = E_0u(r)\,. \tag{2.15}$$

Dividing this equation by $\hbar\omega$ and expressing r in units of $\sqrt{\frac{\hbar}{m\omega}}$ and the energy in units of $\hbar\omega$, this equation becomes,

$$\left[-\frac{1}{2}\frac{\mathrm{d}}{\mathrm{d}r^2} + \frac{1}{2}r^2 + V_{\mathrm{core}}(r)\right] u(r) = E_0u(r)\,. \tag{2.16}$$

Note that this particular choice of units makes $r, u(r), R(r), V(r)$, and E_0 dimensionless. In units $\hbar$ the dimension of p is the inverse of the dimension of r, which is dimensionless is this case.

The repulsive-core potential is modelled using a spherical rectangular potential, $V_{\mathrm{core}}(r)$ of Eq. (2.16) reads,

$$V_{\mathrm{core}}(r) = \begin{cases} V_0 & \text{if } r < 1 \\ 0 & \text{if } r \geq 1 \end{cases}\,, \tag{2.17}$$

r is expressed in units of $\sqrt{\frac{\hbar}{m\omega}}$ and V_0 in units of $\hbar\omega$ making these variables dimensionless. The ground-state wave function in coordinate and momentum space for varying "height"

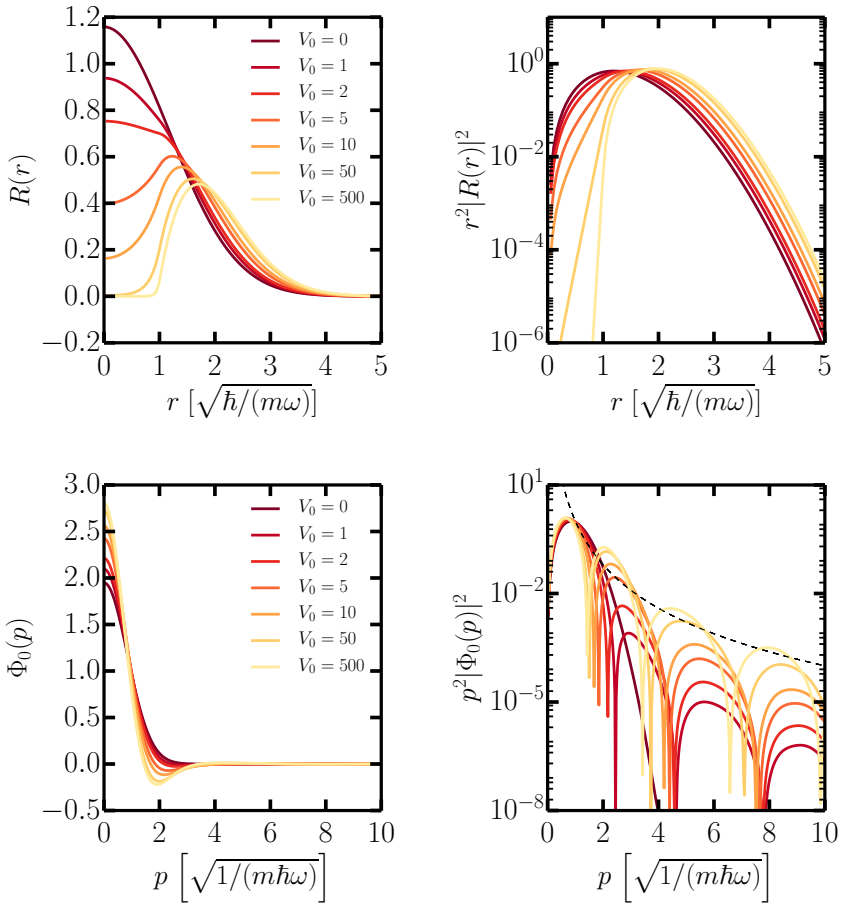

Figure 2.4 – The ground-state radial wave function and its corresponding probability distribution in $r-$space (upper row) and $p-$space (bottom row), for a rectangular repulsive-core potential with varying strength V_0 (Eq. (2.17)). Both r and p and the corresponding radial wave functions $R(r), \Phi(p)$ are dimensionless through the specific choice of units. The dashed line shows a curve $\propto p^{-4}$. The curve labelled $V_0 = 0$ corresponds to the ground-state wave function of the harmonic oscillator, which is a Gaussian in both r and p space.

V_0 is depicted in Figure (2.4). It is clear that as the height of the potential rises the high-momentum components in the wave function increase. High-momentum tails are essentially generated by short-range structure in the r-space wave function. Strong repulsive potentials can induce this the short-range structure, but this feature is certainly not limited to this type of potentials.

2.4 Nuclear momentum distributions

Nuclear momentum distributions encode the probability density of finding a nucleon with a certain momentum in a given nucleus. The strong short-range repulsion and the attractive tensor part of the nucleon-nucleon force induce short-range correlations (SRC) in the wave functions for atomic nuclei. One of the hallmarks of SRC is the presence of high-momentum tails in the one-body momentum distributions. The short-range structure of the wave function, partly generated by the hard repulsive core, induces high-momentum components.

A lot of effort has been put into calculating single-nucleon momentum distributions. For small nuclei up to $A = 12$ ab-initio methods with variational wave functions can be used [3–7]. For higher mass numbers approximation schemes such as cluster expansions [7–9] and correlated basis function theory [10, 11] can be used to compute the momentum distributions. In this chapter we give a short overview of an approximate method of including SRC contributions to the momentum distributions for stable nuclei over the entire mass range [12]. In this framework the SRC are included through correlation operators acting on a Slater determinant A-body wave function. The correlation operators generate up to A-body contributions when calculating any expectation value of the nucleus. It is necessary to truncate the many-body contributions to keep the numerical computations feasible. A low-order correlation operator approximation, dubbed LCA [12], is proposed in Sec. 2.4.1.

2.4.1 Short-range correlations

A time-honoured method of constructing a normalized correlated many-body wave function $|\Psi\rangle$ constitutes of applying a correlation operator $\widehat{\mathcal{G}}$ to the independent-particle model (IPM) Slater determinant $|\Phi\rangle$ [13] :

$$\begin{aligned} |\Phi\rangle &= |\alpha_1\alpha_2\ldots\alpha_A\rangle\,, \\ |\Psi\rangle &= \frac{1}{\sqrt{\langle\Phi|\widehat{\mathcal{G}}^\dagger\widehat{\mathcal{G}}|\Phi\rangle}}\widehat{\mathcal{G}}\,|\Phi\rangle\ . \end{aligned} \tag{2.18}$$

The single-particle states are denotes with α_i. The correlation operator $\widehat{G}$ is written as a symmetrized product of two-body operators,

$$\widehat{\mathcal{G}} = \widehat{\mathcal{S}}\left(\prod_{i<j}^{A}\hat{f}_{ij}\right)\,, \tag{2.19}$$

with $\hat{f}_{ij} = \hat{f}_{ji}$. Furthermore, $\widehat{\mathcal{S}}$ is the symmetrization operator that guarantees that $\widehat{\mathcal{G}}\,|\Phi\rangle$ is antisymmetric. In order to isolate the effect of the correlations $\widehat{\mathcal{G}}$ can be conveniently rewritten as,

$$\widehat{\mathcal{G}} = \widehat{\mathcal{S}}\left(\prod_{i<j}^{A}\left[1+\hat{l}_{ij}\right]\right)\,. \tag{2.20}$$

For vanishing correlations we have $\hat{l}_{ij} = 0$.

In the calculation of the expectation value of an arbitrary operator $\widehat{\Omega}$, the complexity introduced by the correlations can be shifted from the wave functions to the operator. This procedure amounts to defining an effective operator $\widehat{\Omega}^{\text{eff}} = \widehat{\mathcal{G}}^\dagger\widehat{\Omega}\,\widehat{\mathcal{G}}$, and evaluating its expectation value between uncorrelated (IPM) wave functions,

$$\langle\Psi|\widehat{\Omega}|\Psi\rangle = \frac{\langle\Phi|\widehat{\mathcal{G}}^\dagger\widehat{\Omega}\mathcal{G}|\Phi\rangle}{\langle\Phi|\widehat{\mathcal{G}}^\dagger\mathcal{G}|\Phi\rangle} = \frac{\langle\Phi|\widehat{\Omega}^{\text{eff}}|\Phi\rangle}{\langle\Phi|\widehat{\mathcal{G}}^\dagger\mathcal{G}|\Phi\rangle}\,, \tag{2.21}$$

$$\widehat{\Omega}^{\text{eff}} = \widehat{\mathcal{G}}^{\dagger}\widehat{\Omega}\,\widehat{\mathcal{G}} = \left(\prod_{i<j}^{A}\left[1+\hat{l}_{ij}\right]\right)^{\dagger}\widehat{\mathcal{S}}^{\dagger}\Omega\,\widehat{\mathcal{S}}\left(\prod_{p<q}^{A}\left[1+\hat{l}_{pq}\right]\right) . \tag{2.22}$$

The product of the two-body operators $\hat{l}$ can be expanded in a series in the order of the correlation operators $\hat{l}$,

$$\prod_{i<j}^{A}\left[1+\hat{l}_{ij}\right] = 1+\sum_{i<j}^{A}\hat{l}_{ij}+\sum_{\substack{i<j\,,\,m<n\\(i,j)<(m,n)}}^{A}\hat{l}_{ij}\hat{l}_{mn}+\sum_{\substack{i<j\,,\,m<n\,,\,p<q\\(i,j)<(m,n)<(p,q)}}^{A}\hat{l}_{ij}\hat{l}_{mn}\hat{l}_{pq}+O(\hat{l}^4)\,. \tag{2.23}$$

The relation $(i,j)<(k,l)$ is defined as $(i,j)<(k,l)\Leftrightarrow i<k\vee(i=k\wedge j<l)$. The effective operator $\widehat{\Omega}^{\text{eff}}$ can then be written as,

$$\begin{aligned}\widehat{\Omega}^{\text{eff}} &= \widehat{\mathcal{G}}^{\dagger}\widehat{\Omega}\,\widehat{\mathcal{G}}\\ &= \Big(1+\sum_{i<j}^{A}\hat{l}_{ij}+\sum_{\substack{i<j\,,\,m<n\\(i,j)<(m,n)}}^{A}\hat{l}_{ij}\hat{l}_{mn}+\sum_{\substack{i<j\,,\,m<n\,,\,p<q\\(i,j)<(m,n)<(p,q)}}^{A}\hat{l}_{ij}\hat{l}_{mn}\hat{l}_{pq}+O(\hat{l}^4)\Big)^{\dagger}\widehat{\mathcal{S}}^{\dagger}\Omega\,\widehat{\mathcal{S}}\\ &\qquad\Big(1+\sum_{r<s}^{A}\hat{l}_{rs}+\sum_{\substack{r<s\,,\,t<u\\(r,s)<(t,u)}}^{A}\hat{l}_{rs}\hat{l}_{tu}+\sum_{\substack{r<s\,,\,t<u\,,\,v<w\\(r,s)<(t,u)<(v,w)}}^{A}\hat{l}_{rs}\hat{l}_{tu}\hat{l}_{vw}+O(\hat{l}^4)\Big)\,.\end{aligned} \tag{2.24}$$

The low-order correlation approximation (LCA) amounts to truncating the expansion of $\widehat{\Omega}^{\text{eff}}$ (Eq. (2.24)) up to quadratic order in $\hat{l}$. Additionally, only the terms in which the correlation operators $\hat{l}$ act on the same nucleon pair are retained. Disconnected terms, in which the operator $\widehat{\Omega}$ acts on nucleons not affected by $\hat{l}$ are discarded. In the LCA a one(two)-body operator picks up two(three)-body correlation contributions.

$$\widehat{\Omega}^{\text{LCA}} = \widehat{\Omega}+\sum_{i<j}^{A}\hat{l}_{ij}^{\dagger}\widehat{\Omega}+\sum_{r<s}^{A}\widehat{\Omega}\,\hat{l}_{rs}+\sum_{i<j}^{A}\sum_{r<s}^{A}\delta_{ir}\delta_{js}\hat{l}_{ij}^{\dagger}\widehat{\Omega}\,\hat{l}_{rs} = \widehat{\Omega}+\sum_{i<j}^{A}\left(\hat{l}_{ij}^{\dagger}\widehat{\Omega}+\widehat{\Omega}\hat{l}_{ij}+\hat{l}_{ij}^{\dagger}\widehat{\Omega}\hat{l}_{ij}\right) . \tag{2.25}$$

The quadratic terms,

$$\sum_{\substack{i<j\,,\,m<n\\(i,j)<(m,n)}}^{A}\left(\frac{\hat{l}_{ij}^{\dagger}\hat{l}_{mn}^{\dagger}+\hat{l}_{mn}^{\dagger}\hat{l}_{ij}^{\dagger}}{2}\right)\widehat{\Omega}\,,\quad\sum_{\substack{r<s\,,\,t<u\\(r,s)<(t,u)}}^{A}\widehat{\Omega}\left(\frac{\hat{l}_{rs}\hat{l}_{tu}+\hat{l}_{tu}\hat{l}_{rs}}{2}\right),$$

are zero because of the requirement that both $\hat{l}$ operators act on the same nucleon pair and those terms do not appear in the summation.

With Eq. (2.25), a one-body operator $\widehat{\Omega}^{[1]}=\sum_i^A\widehat{\Omega}_i$ becomes

$$\begin{aligned}\widehat{\Omega}^{[1],\,\text{LCA}} &= \widehat{\Omega}^{[1]}+\sum_{j<k}^{A}\sum_{i}^{A}(\hat{l}_{jk}^{\dagger}\widehat{\Omega}_i+\widehat{\Omega}_i\hat{l}_{jk}+\hat{l}_{jk}^{\dagger}\widehat{\Omega}_i\hat{l}_{jk})(\delta_{ij}+\delta_{ik})\\ &= \widehat{\Omega}^{[1]}+\sum_{i,j\neq i}^{A}\left(\hat{l}_{ij}^{\dagger}\widehat{\Omega}_i+\widehat{\Omega}_i\hat{l}_{ij}+\hat{l}_{ij}^{\dagger}\widehat{\Omega}_i\hat{l}_{ij}\right) .\end{aligned} \tag{2.26}$$

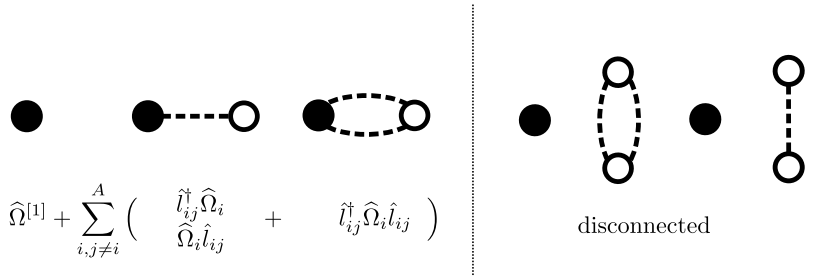

Figure 2.5 – The diagrammatic representation of the LCA expansion of a one-body operator (Eq. (2.26)). Below each diagram is their corresponding expression. The black dot represents the particle "i" on which the operator $\widehat{\Omega}_i$ is acting on. The dashed lines are the correlation operator $\hat{l}_{ij}$ acting the particle pair "ij". In the LCA, two dashed lines (correlation operators) are required to connect the same pair. Disconnected diagrams are not considered in the LCA.

The Kronecker deltas appearing in Eq. (2.26) make sure that the disconnected terms do not contribute to the effective operator. In similar vein, the LCA of Eq. (2.25) transforms a two-body operator $\widehat{\Omega}^{[2]} = \sum_{i<j} \widehat{\Omega}_{ij}$ to,

$$\begin{aligned}
\widehat{\Omega}^{[2],\,\mathrm{LCA}} &= \widehat{\Omega}^{[2]} + \sum_{m<n}^{A}\sum_{i<j}^{A}\Big(\hat{l}^\dagger_{mn}\widehat{\Omega}_{ij} + \widehat{\Omega}_{ij}\hat{l}_{mn} + \hat{l}^\dagger_{mn}\widehat{\Omega}_{ij}\hat{l}_{mn}\Big) \\
&\quad\times\left[(\delta_{mi}+\delta_{ni}+\delta_{mj}+\delta_{nj})(1-\delta_{mi}\delta_{nj})(1-\delta_{mj}\delta_{ni}) + \delta_{mi}\delta_{nj} + \delta_{mj}\delta_{ni}\right] \\
&= \widehat{\Omega}^{[2]} + \sum_{i<j}^{A}\Big[\hat{l}^\dagger_{ij}\widehat{\Omega}_{ij} + \widehat{\Omega}_{ij}\hat{l}_{ij} + \hat{l}^\dagger_{ij}\widehat{\Omega}_{ij}\hat{l}_{ij} \\
&\quad + \sum_{n\notin\{i,j\}}^{A}(\hat{l}^\dagger_{in}+\hat{l}^\dagger_{jn})\widehat{\Omega}_{ij} + \widehat{\Omega}_{ij}(\hat{l}_{in}+\hat{l}_{jn}) + \hat{l}^\dagger_{in}\widehat{\Omega}_{ij}\hat{l}_{in} + \hat{l}^\dagger_{jn}\widehat{\Omega}_{ij}\hat{l}_{jn}\Big]. \quad (2.27)
\end{aligned}$$

As in Eq. (2.26), the δ's guarantee that only connected terms contribute. Some care has to be taken to avoid double counting. Figures (2.5) and (2.6) provide a pictorial diagram of the LCA expansion corresponding to the one-body and two-body operators of Eqs. (2.26) and (2.27) respectively.

To preserve normalization the denominator of Eq. (2.21), $\mathcal{N} = \langle\Phi|\widehat{\mathcal{G}}^\dagger\mathcal{G}|\Phi\rangle$, should be expanded to the same order in $\hat{l}$ as the numerator. The normalisation factor $\mathcal{N}$ can be calculated by replacing $\widehat{\Omega}_i$ with $\frac{1}{A}$ in Eq. (2.26) or $\widehat{\Omega}_{ij}$ with $\frac{2}{A(A-1)}$ in Eq. (2.27),

$$\mathcal{N}^{[1]} = 1 + \frac{2}{A}\sum_{i<j}^{A}\langle\alpha_i\alpha_j|\hat{l}^\dagger_{ij} + \hat{l}_{ij} + \hat{l}^\dagger_{ij}\hat{l}_{ij}|\alpha_i\alpha_j\rangle\ , \quad (2.28)$$

$$\mathcal{N}^{[2]} = 1 + \frac{2(2A-3)}{A(A-1)}\sum_{i<j}^{A}\langle\alpha_i\alpha_j|\hat{l}^\dagger_{ij} + \hat{l}_{ij} + \hat{l}^\dagger_{ij}\hat{l}_{ij}|\alpha_i\alpha_j\rangle\ . \quad (2.29)$$

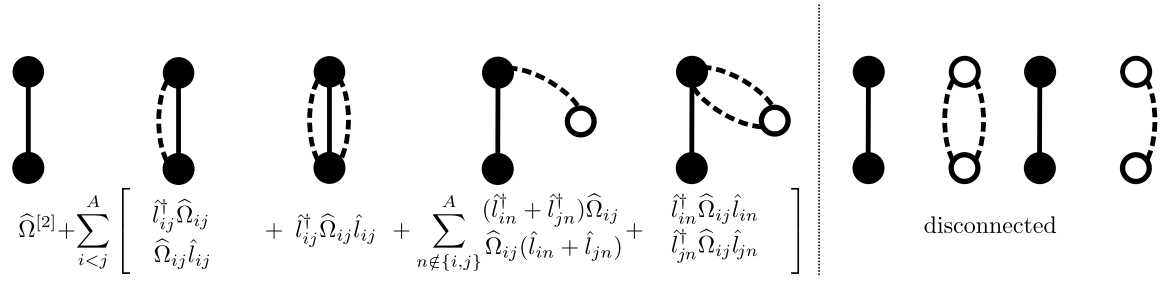

Figure 2.6 – The diagrammatic representation of the LCA expansion of a two-body operator (Eq. (2.26)). Below each diagram is their corresponding expression. The black dots represent the particle pair "ij" on which the operator $\widehat{\Omega}_{ij}$ is acting on. The dashed lines are the correlation operator $\hat{l}_{in}$ acting the particle pair "in". In the LCA, two dashed lines (correlation operators) are required to connect the same pair. Disconnected diagram are not considered in the LCA.

2.4.2 SRC momentum distributions

The effect of the correlations on nuclear momentum distributions can now be investigated. With Eq. (2.26) the LCA transforms the one-body momentum operator $\hat{n}^{[1]}(\vec{k}) = |\vec{k}\rangle\langle\vec{k}|$, into the effective operator $\hat{n}^{[1],\,\mathrm{LCA}}(\vec{k})$ given by

$$\hat{n}^{[1],\,\mathrm{LCA}}(\vec{k}) = \hat{n}^{[1]}(\vec{k}) + \sum_{i,j\neq i}^{A}\left(\hat{l}^{\dagger}_{ij}\hat{n}_i(\vec{k}) + \hat{n}_i(\vec{k})\hat{l}_{ij} + \hat{l}^{\dagger}_{ij}\hat{n}_i(\vec{k})\hat{l}_{ij}\right). \tag{2.30}$$

Using Eq. (2.27) the two-body momentum operator $\hat{n}^{[2]}(\vec{k}_1,\vec{k}_2) = |\vec{k}_1\vec{k}_2\rangle\langle\vec{k}_1\vec{k}_2|$ becomes,

$$\begin{aligned}\hat{n}^{[2]\,\mathrm{LCA}}(\vec{k}_1,\vec{k}_2) = \hat{n}^{[2]}(\vec{k}_1,\vec{k}_2) + \sum_{i<j}^{A}\Big[&\hat{l}^{\dagger}_{ij}\hat{n}_{ij}(\vec{k}_1,\vec{k}_2) + \hat{n}_{ij}(\vec{k}_1,\vec{k}_2)\hat{l}_{ij} + \hat{l}^{\dagger}_{ij}\hat{n}_{ij}(\vec{k}_1,\vec{k}_2)\hat{l}_{ij} + \\ \sum_{m\notin\{i,j\}}^{A}&(\hat{l}^{\dagger}_{im}+\hat{l}^{\dagger}_{jm})\hat{n}_{ij}(\vec{k}_1,\vec{k}_2) + \hat{n}_{ij}(\vec{k}_1,\vec{k}_2)(\hat{l}_{im}+\hat{l}_{jm}) + \hat{l}^{\dagger}_{im}\hat{n}_{ij}(\vec{k}_1,\vec{k}_2)\hat{l}_{im}\Big].\end{aligned} \tag{2.31}$$

The nuclear momentum distributions denoting the probability of finding a nucleon (two nucleons) with a given momentum $\vec{k}$ ($\vec{k}_1,\vec{k}_2$) are then given by,

$$n(\vec{k}) = \frac{\langle\Phi|\hat{n}^{[1],\,\mathrm{LCA}}(\vec{k})|\Phi\rangle}{\mathcal{N}^{[1]}}, \tag{2.32}$$

$$n(\vec{k}_1,\vec{k}_2) = \frac{\langle\Phi|\hat{n}^{[2],\,\mathrm{LCA}}(\vec{k}_1,\vec{k}_2)|\Phi\rangle}{\mathcal{N}^{[2]}}. \tag{2.33}$$

The normalization factors $\mathcal{N}^{[1]},\mathcal{N}^{[2]}$ are computed with the aid of Eqs. (2.28), (2.29).

Figure (2.7) shows the one-body momentum distribution calculated using Eq. (2.32), whereby the central (g_c), tensor (g_t) and spin-isospin ($g_{\tau\sigma}$) correlation functions of Eq. (2.34) have been included [12]. It is clear that the correlations induce high-momentum tails in the nuclear momentum distribution [12, 14, 15]. The probability of finding a nucleon with a momentum above the typical nuclear Fermi momentum ≈ 300 MeV is increased by several orders of magnitude when short-range correlations are included.

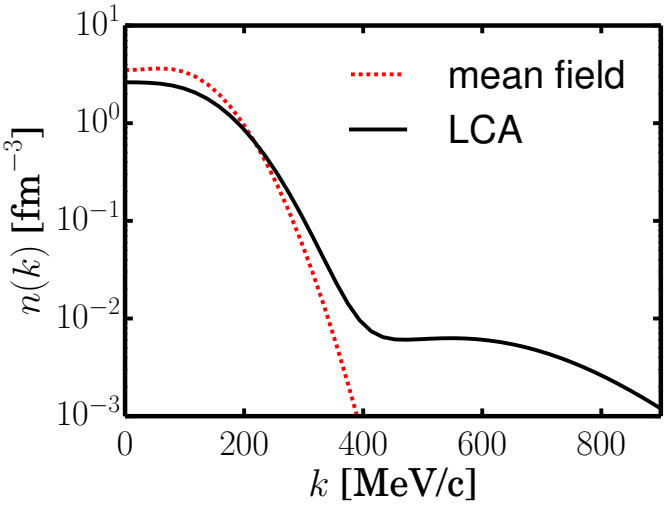

Figure 2.7 – The one-body momentum distribution $n(k) = \int \mathrm{d}^2\Omega_k n(\vec{k})$ of Eq. (2.26) with (LCA) and without correlations (mean field) for a ^{12}C nucleus. The mean-field Slater determinant $|\Phi\rangle$ is determined from an isotropic harmonic oscillator potential with $\hbar\omega = 45A^{-1/3} - 25A^{-2/3}$.

2.5 LCA recipe

The practical application of the LCA is outlined in this section. The LCA requires a choice for the single-particle wave functions $|\Phi\rangle$ of Eq. (2.18) and the correlation operator $\hat{\mathcal{G}}$ of Eq. (2.19). The determination of the correlation operator is discussed in Sec. 2.5.1. A convenient choice for the single-particle basis is outlined in Sec. 2.5.2.

2.5.1 Parameterization of the correlation operators

The correlation operators $\hat{l}_{ij}$ are often parameterized as

$$\begin{aligned}\hat{l}_{ij}(\vec{r}_{ij}) = &- g_c(r_{ij})\mathbb{1} + g_\sigma(r_{ij})\vec{\sigma}_i\cdot\vec{\sigma}_j + g_\tau(r_{ij})\vec{\tau}_i\cdot\vec{\tau}_j \\ &+ g_{\sigma\tau}(r_{ij})(\vec{\sigma}_i\cdot\vec{\sigma}_j)(\vec{\tau}_i\cdot\vec{\tau}_j) + g_t(r_{ij})\hat{S}_{ij} + g_{t\tau}(r_{ij})\hat{S}_{ij}(\vec{\tau}_i\cdot\vec{\tau}_j)\,,\end{aligned} \tag{2.34}$$

$\vec{r}_{ij} = \vec{r}_i - \vec{r}_j$ is the relative coordinate, $\vec{\sigma}$ ($\vec{\tau}$) is the (iso)spin operator and $\hat{S}_{ij}$ is the tensor operator,

$$\hat{S}_{ij} = \frac{3}{r_{ij}^2}(\vec{\sigma}_i\cdot\vec{r}_{ij})(\vec{\sigma}_j\cdot\vec{r}_{ij}) - (\vec{\sigma}_i\cdot\vec{\sigma}_j)\,. \tag{2.35}$$

The correlation functions $g(r_{ij})$ are introduced as a variational degree of freedom in the nuclear wave function [5, 16, 17]. In practice the correlation functions are parameterized and the parameters are determined by minimizing the energy-expectation value [18]. The determination of the ground-state energy and the correlation functions $g(r_{ij})$ requires a specific choice of the single-particle basis functions and the nucleon-nucleon interaction. Because of this, the correlation functions $g(r_{ij})$ are in principle scheme-dependent and can not be considered universal. However, the high-momentum components of SRC are generated by the

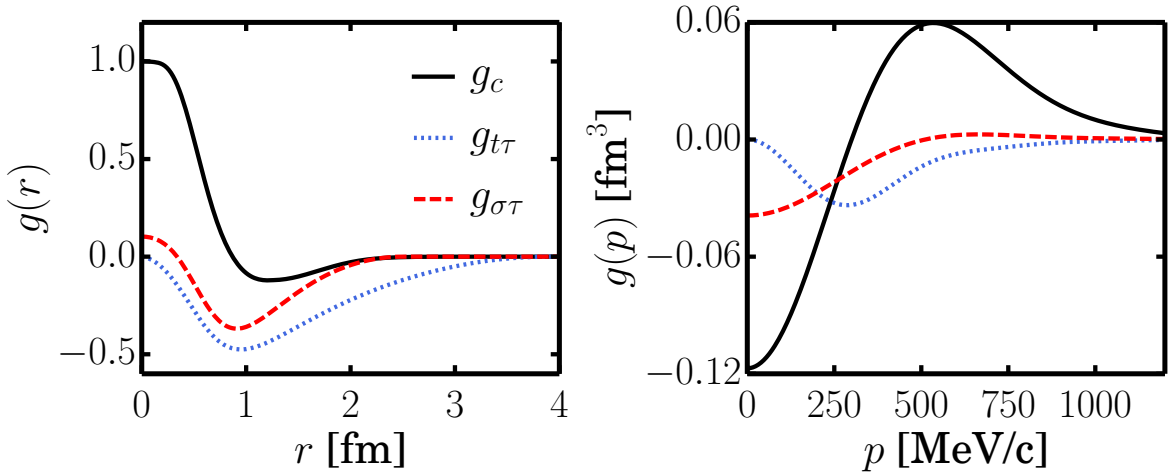

Figure 2.8 – The central g_c, tensor $g_{t\tau}$ and spin-isospin $g_{\sigma\tau}$ correlation functions in coordinate space (left) and momentum space (right). Note that $g_{t\tau}(r)$ and $g_{\sigma\tau}(r)$ have been multiplied by a factor of 10 in the left panel.

short-range structure of the nuclear wave function. This in turn is induced by the correlation operators, leading to the conclusion that the choice of single-particle basis functions should not have significant influence on the SRC high-momentum tails. The central correlation function $g_c(r_{ij})$ of Eq. (2.34) is difficult to constrain and shows large differences between different models for the nucleon-nucleon interaction in nuclei. The tensor correlation function $g_t(r_{ij})$ and spin-isospin correlation function $g_{\sigma\tau}(r_{ij})$ of Eq. (2.34) is better constrained and can be considered realistic [19]. Of the six terms in Eq. (2.34) it has been reported [16, 20–22] that the central $g_c(r_{ij})$, the spin-isospin $g_{\sigma\tau}(r_{ij})$ and the tensor $g_{t\tau}(r_{ij})$ terms yield the dominant contributions to the correlated operators. The central,spin-isospin and tensor correlation functions used in [12] are displayed in Fig. (2.8) in coordinate space and momentum space. It is clear that the effect of the inclusion of the correlations is to shift strength from the low-momentum to the high-momentum tails of the momentum distributions. This is prototypical for correlation corrections on mean-field properties. Whereas mean-field nuclear properties are often characterized by a certain momentum scale, correlations are often responsible for the spreading of the strength over a larger range in momenta. Roughly speaking, the correlations add fat tails to the mean-field momentum distributions.

2.5.2 Single-particle basis

The LCA is built upon pair correlations. The correlation functions contained in the correlation operators are used as an input to generate the correlated wave function. As such, there is no variational approach applied in the LCA. The correlation function depend on the relative coordinate of the pair. It is favourable to choose a single-particle basis $|\Phi\rangle$ that allows for an easy transformation to particle pairs. That is, a single-particle basis that accommodates for an efficient way of expressing two single-particle wavefunctions in function of the pair's center of mass (c.m.) and relative coordinates. The single-particle basis fulfilling this requirement is that of the isotropic harmonic oscillator, with the Hamiltonian

$\hat{H}$ given by

$$\hat{H} = -\frac{\hbar^2}{2m}\nabla^2 + \frac{1}{2}m\omega^2 r^2 \,. \tag{2.36}$$

The solutions of $\hat{H}\,|\alpha\rangle = E\,|\alpha\rangle$ are given by

$$\alpha(\vec{r}) = \langle\vec{r}|\alpha\rangle = \langle\vec{r}|nlm\rangle = \left[\frac{2n!}{\Gamma(n+l+\frac{3}{2})\nu^{l+\frac{3}{2}}}\right]^{\frac{1}{2}} r^l e^{-\frac{\nu r^2}{2}} L_n^{l+\frac{1}{2}}(\nu r^2) Y_{lm}(\Omega_r)\,, \tag{2.37}$$

with $L_n^{l+\frac{1}{2}}$ the generalized Laguerre polynomials and $\nu = m\omega/\hbar$. The harmonic oscillator Hamiltonian allows us to express a pair of single-particle states $|\alpha_1\alpha_2\rangle = |n_1 l_1 m_{l_1} n_2 l_2 m_{l_2}\rangle$ with total angular momentum Λ, M_Λ in terms of relative and c.m. states $|nlm_l NLM_L\rangle$ with the same total angular momentum Λ, M_Λ. The relative and c.m. state are again harmonic basis functions, that is, they are a solution to Eq. (2.36). The transformation is given in terms of the Moshinsky brakets [23]

$$|n_1 l_1 n_2 l_2; \Lambda M_\Lambda\rangle = \sum_{nl,NL} |nlNL; \Lambda M_\Lambda\rangle \,\langle nlNL; \Lambda|n_1 l_1 n_2 l_2; \Lambda\rangle \,. \tag{2.38}$$

Here, $\langle nlNL; \Lambda|n_1 l_1 n_2 l_2; \Lambda\rangle$ are the Moshinsky brakets and

$$|n_1 l_1 n_2 l_2; \Lambda M_\Lambda\rangle = \sum_{m_{l_1}, m_{l_2}} |n_1 l_1 m_{l_1} n_2 l_2 m_{l_2}\rangle \,\langle l_1 m_{l_1} l_2 m_{l_2}|\Lambda M_\Lambda\rangle \tag{2.39}$$

$$|nlNL; \Lambda M_\Lambda\rangle = \sum_{m_l, m_L} |nlm_l NLM_L\rangle \,\langle lm_l LM_L|\Lambda M_\Lambda\rangle \,. \tag{2.40}$$

The Clebsch-Gordan coefficient $\langle l_1 m_{l_1} l_2 m_{l_2}|\Lambda M_\Lambda\rangle$ ($\langle lm_l LM_L|\Lambda M_\Lambda\rangle$) couples the single-particle (relative and c.m.) states to total angular momentum Λ, M_Λ. The Moshinsky brakets in Eq. (2.38) are non-zero for only a few combinations of nl, NL limiting the summation over nl, NL in Eq. (2.38) to a handful of terms. Including the spin m_s and isospin m_t projections of the particles the full equation expressing a single-particle pair in terms of c.m. and relative states reads,

$$\begin{aligned}
|\alpha_1\alpha_2\rangle &= |n_1 l_1 m_{l_1} m_{s_1} m_{t_1} n_2 l_2 m_{l_2} m_{s_2} m_{t_2}\rangle \\
&= \sum_{\substack{nlm_l NLM_L \\ SM_S TM_T}} \langle nlm_l NLM_L SM_S TM_T|\alpha_1\alpha_2\rangle \,|nlm_l NLM_L SM_S TM_T\rangle \\
&= \sum_{\substack{A=\{nlm_l NLM_L \\ SM_S TM_T\}}} C^A_{\alpha_1\alpha_2}\,|A\rangle \,.
\end{aligned} \tag{2.41}$$

The quantum numbers S, T (M_S, M_T) denote the total spin and isospin (projections) of the particle pair. The expression for the coefficients $C^A_{\alpha_1\alpha_2}$ reads,

$$\begin{aligned}
C^{A=\{nlm_l NLM_L SM_S TM_T\}}_{\alpha_1\alpha_2} = \frac{1}{\sqrt{2}}\left[1-(-1)^{l+S+T}\right] &\langle\frac{1}{2}m_{t_1}\frac{1}{2}m_{t_2}|TM_T\rangle \,\langle\frac{1}{2}m_{s_1}\frac{1}{2}m_{s_2}|SM_S\rangle \\
&\sum_{\Lambda M_\Lambda} \langle l_1 m_{l_1} l_2 m_{l_2}|\Lambda M_\Lambda\rangle \,\langle nlNL; \Lambda|n_1 l_1 n_2 l_2; \Lambda\rangle \,\langle \Lambda M_\Lambda|nlm_l NLM_L\rangle \,.
\end{aligned} \tag{2.42}$$

The Moshinsky brakets allow the separation of the contribution from relative two-nucleon quantum states with specific quantum numbers nl. This powerful feature makes it possible to map the contributions from specific relative quantum states to the expectation value of any operator calculated in the LCA, shedding light on the structure of the pairs affecting the correlated operator.

2.6 How to probe high-momentum tails in quasi-free knockout reactions

The question that naturally arises is how the short-range correlations (SRC) can be measured in scattering reactions. The SRC-prone nucleon pairs are predominantly in a back-to-back configuration with a small center-of-mass (c.m.) and high relative momentum, where small and large are defined relative to the Fermi momentum. The high-momentum components in the relative-momentum distribution are induced by the correlation operators, acting on the relative coordinate of the SRC pair. This gives rise to fat tails in the one-body momentum distribution, inducing significant strength well above the Fermi momentum. In order to probe SRC a reaction is needed that allows one to identify initial high-momentum nucleons, generated by the fat tails in the one-body momentum distribution.

An ideal reaction to study SRC is the exclusive electrodinduced two-nucleon knockout reaction. The outgoing nucleons as well as the scattered electron are measured, fully determining the energy-momentum balance. This makes it a powerful tool to investigate SRC dynamics in nuclei. Information about the initial momenta of the knocked out nucleons can be inferred from the measured momenta of the final particles. This allows one to investigate the relative and c.m.-momentum distribution of the initial nucleon pair. However, it is not possible to directly connect the measured cross sections with the momentum distributions. In scattering reactions, both momentum and energy is exchanged by the probe. The cross section is proportional to the probability of finding an object with a certain momentum and energy. This is called the spectral function. In the case of exclusive two-nucleon knockout reactions, this is the probability of finding a nucleon pair with given initial four-momenta. In this work the initial energies of the nucleons are modelled using the discrete binding energies of the single-particle orbitals. More realistic spectral functions are continuous in the single-particle energies. As the SRC-driven two-nucleon knockout reaction targets nucleons with high initial and final momenta, with the corresponding kinetic energies much larger than the single-particle binding energies, it is expected that this has little or no influence.

In exclusive reactions all final particles are detected. The knocked-out nucleon pair has to traverse the recoiling nucleus, interacting with the $A-2$ nucleons. These interactions are denoted as final-state interactions (FSI). It is expected that FSI can have a significant influence on the cross section as they decrease the probability of the final particles reaching the detector. The importance of FSI can be quickly estimated using the classical mean free path length $\ell = 1/(\rho\sigma)$. The density of the recoiling nucleus is estimated using $\rho \approx \frac{A}{\frac{4\pi}{3}R^3} = \frac{A}{\frac{4\pi}{3}(1.21A^{1/3}\mathrm{fm})^3} = 0.138\ \mathrm{fm}^{-3}$. σ is the total elastic nucleon-nucleon cross section in the relevant energy range for SRC-driven knockout reactions ($\approx$ 300MeV up to a few GeV), $\sigma \in [2.0, 4.0]\ \mathrm{fm}^2$ (see Ref. [24]). The resulting mean free path length ℓ is then in the range $[1.8, 3.6]$ fm. As this is comparable to nuclear radii it can be expected that the FSI will

attenuate the two-nucleon knockout cross section significantly, as both escaping nucleons have to survive. It is straightforward to see that the attenuation should increase for larger nuclei.

The measurement of the electroinduced exclusive two-knockout process is very challenging as it requires the detection of the energy and momentum of the scattered projectile as well as the two ejected nucleons. Very few data is available for this highly exclusive reaction. Throughout this work the theoretical calculations are compared to experimental data obtained from the Jefferson Lab Hall B CEBAF Large Acceptance Spectrometer (CLAS) data mining initiative [25] and the Jefferson Lab Hall A collaboration [26, 27]. These two initiatives take different approaches in order to target SRC with the electroinduced two-nucleon knockout reaction. The CLAS results are obtained by a recent analysis [25] of data obtained in 2004 [28] with updated reconstruction software, cuts and corrections. This analysis is a part of the Jefferson Lab Hall B data mining project [29]. The project exploits the large acceptance and the wide open inclusive trigger of the CLAS detector to re-analyse the accumulated data for additional channels of interest. In particular it allows to extract information about the SRC-driven two-nucleon knockout reaction. There are ongoing efforts to uncover the dynamics of SRC, in particular, the properties of the SRC pair c.m.-momentum distribution are currently being investigated.

The Hall A experiment [26] on the other hand is a more recent experiment specifically designed to target two-nucleon knockout reactions. The detectors and kinematics are set up in a very specific configuration to constrain the phase-space of the reaction to the SRC-dominated regime. Thereby the detectors are placed in such a way that it is automatically ensured that the measured cross section is dominated by initially "back-to-back" moving nucleon pairs, a characteristic feature of SRC pairs.

The study of SRC-driven reactions is not limited to the exclusive electroinduced two-nucleon knockout scattering process. For example, in Ref. [30] the relative amount of SRC-pairs is extracted from inclusive electron scattering cross-section ratios of different nuclei. Additionally, SRC have been investigated in exclusive knockout reactions with a hadronic probe. At Brookhaven National Laboratory SRC have been studied where an incoming proton knocks out a proton-neutron pair from the target nucleus ^{12}C [31, 32]. It was demonstrated that the majority of SRC pairs consist of proton-neutron pairs.

2.7 References

[1] R. D. Amado, Phys. Rev. C **14**, 1264 (1976).
[2] O. Hen, L. B. Weinstein, E. Piasetzky, et al., Phys. Rev. C **92**, 045205 (2015).
[3] R. Schiavilla, R. B. Wiringa, S. C. Pieper, and J. Carlson, Phys. Rev. Lett. **98**, 132501 (2007).
[4] R. B. Wiringa, R. Schiavilla, S. C. Pieper, and J. Carlson, Phys. Rev. C **78**, 021001 (2008).
[5] H. Feldmeier, W. Horiuchi, T. Neff, and Y. Suzuki, Phys. Rev. C **84**, 054003 (2011).
[6] R. B. Wiringa, R. Schiavilla, S. C. Pieper, and J. Carlson, Phys. Rev. C **89**, 024305 (2014).
[7] M. Alvioli, C. Ciofi degli Atti, L. P. Kaptari, et al., Phys. Rev. C **87**, 034603 (2013).

[8] M. Alvioli, C. Ciofi degli Atti, and H. Morita, Phys. Rev. Lett. **100**, 162503 (2008).
[9] M. Alvioli, C. Ciofi degli Atti, L. P. Kaptari, et al., Phys. Rev. C **85**, 021001 (2012).
[10] F. Arias de Saavedra, C. Bisconti, G. Co', and A. Fabrocini, Phys.Rept. **450**, 1 (2007).
[11] C. Bisconti, F. A. d. Saavedra, and G. Co', Phys. Rev. C **75**, 054302 (2007).
[12] M. Vanhalst, "Quantifying short-range correlations in nuclei", `http://inwpent5.ugent.be`, PhD thesis (Ghent University, Sept. 2014).
[13] M. Gaudin, J. Gillespie, and G. Ripka, Nuclear Physics A **176**, 237 (1971).
[14] J. Ryckebusch, W. Cosyn, and M. Vanhalst, J. Phys. G **42**, 055104 (2015).
[15] C. Colle, W. Cosyn, J. Ryckebusch, and M. Vanhalst, Phys. Rev. C **89**, 024603 (2014).
[16] S. C. Pieper, R. B. Wiringa, and V. Pandharipande, Phys. Rev. C **46**, 1741 (1992).
[17] M. Alvioli, C. C. d. Atti, and H. Morita, Phys. Rev. C **72**, 054310 (2005).
[18] I. Lagaris and V. Pandharipande, Nuclear Physics A **359**, 349 (1981).
[19] M. Vanhalst, J. Ryckebusch, and W. Cosyn, Phys. Rev. C **86**, 044619 (2012).
[20] C. Ciofi degli Atti and D. Treleani, Phys. Rev. C **60**, 024602 (1999).
[21] O. Benhar, V. R. Pandharipande, and S. C. Pieper, Rev. Mod. Phys. **65**, 817 (1993).
[22] R. Guardiola, P. Moliner, J. Navarro, et al., Nucl. Phys. A **609**, 218 (1996).
[23] M. Moshinsky and Y. Smirnov, *The harmonic oscillator in modern physics* (Harwood Academic Publishers,Amsterdam, 1996).
[24] C. Lechanoine-LeLuc and F. Lehar, Rev. Mod. Phys. **65**, 47 (1993).
[25] O. Hen, H. Hakobyan, R. Shneor, et al., Phys. Lett. B **722**, 63 (2013).
[26] R. Shneor, P. Monaghan, R. Subedi, et al., Phys. Rev. Lett. **99**, 072501 (2007).
[27] R. Subedi, R Shneor, P. Monaghan, et al., Science **320**, 1476 (2008).
[28] B. Mecking, G. Adams, S. Ahmad, et al., Nuclear Instruments and Methods in Physics Research Section A: Accelerators, Spectrometers, Detectors and Associated Equipment **503**, 513 (2003).
[29] L. Weinstein and S. Kuhn, Short distance structure of nuclei: Mining the wealth of existing jefferson lab data, DOE Grant DE-SC0006801.
[30] N. Fomin, J. Arrington, R. Asaturyan, et al., Phys. Rev. Lett. **108**, 092502 (2012).
[31] J. Aclander, J. Alster, D. Barton, et al., Physics Letters B **453**, 211 (1999).
[32] A. Tang, J. W. Watson, J. Aclander, et al., Phys. Rev. Lett. **90**, 042301 (2003).

CHAPTER 3

Two-nucleon knockout reactions and their connection to SRC physics

3.1 Introduction

This chapter examines how two-nucleon knockout reactions can be connected to short-range correlation (SRC) physics. The framework modelling the exclusive electroinduced two-nucleon knockout reaction is outlined first. Further followed by the different articles containing the application and results of the reaction model.

In chapter 2 the SRC are generated by the LCA. In the LCA, the correlated wave functions are generated by letting a correlation operator $\mathcal{G}$ act on a A-body Slater determinant. In section 3.2 the SRC are selected using two approaches. On the one hand the LCA is proposed as a means to model SRC pairs, on the other hand the zero-range approximation (ZRA) is used to select SRC pairs. In the ZRA the relative coordinate $\vec{r}_{12}$ of the initial nucleon pair is set to zero, $\mathcal{G} \propto \delta(\vec{r}_{12})$. The SRC pairs are dominated by nucleon pairs with a nodeless relative radial wave function and vanishing relative orbital momentum, leading to a non-zero probability of finding the two nucleons at the same spatial coordinate. Therefore it is expected that the ZRA, which fixes the initial nucleon pair at the same spatial coordinate, is a good proxy for the more advanced correlation operators contained in the LCA. The LCA is derived in a non-relativistic framework. In order to incorporate the LCA methodology in the relativistic reaction model presented in this dissertation there are two possible approaches. (1) The reaction model is reduced to a non-relativistic version. However as the SRC-driven knockout reaction targets high-momentum nucleons, where the outgoing momentum is comparable to the rest mass of the nucleon, the validity of the non-relativistic approach should be carefully checked. This approach does not increase the difficulty of the numerical calculations. The LCA computations are under control, while the numerical aspect of the reaction model should not increase by the non-relativistic description. (2) Deriving a relativistic version of the LCA is a very challenging problem,

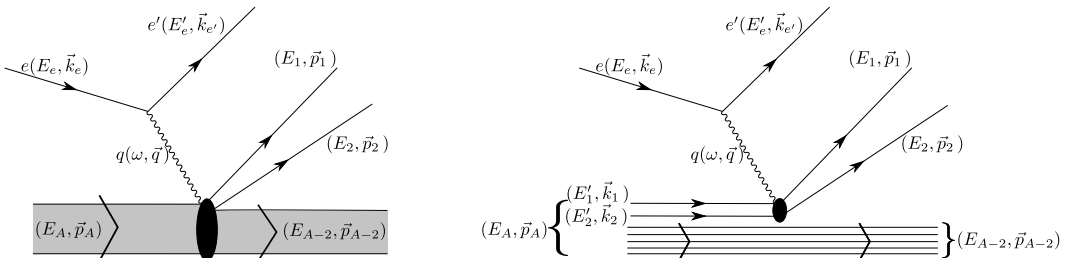

Figure 3.1 – A diagrammatic representation of the electroinduced two-nucleon knockout reaction. An incoming electron e with four-momentum $(E_e, \vec{k}_e)$ exchanges a virtual photon q with four momentum $(\omega, \vec{q})$ with a target nucleus $(E_A, \vec{p}_A)$, knocking two nucleons with initial four momenta k_1, k_2 out of the nucleus, leaving the recoiling nucleus with four momentum $(E_{A-2}, \vec{p}_{A-2})$. In the lab frame we have that the energy of the target nucleus is its rest mass, $E_A = M_A$. In an exclusive two-nucleon knockout reaction the final electron $(E'_e, \vec{k}'_e)$ and the two knocked out nucleons p_1, p_2 are detected. The diagram on the right shows the process where the correlated nucleon pair absorbs the exchanged four momentum q.

if not impossible. Major complications arise as there is no easy transformation to the relativistic c.m. and relative wave functions of the SRC nucleon pair, there is no relativistic extension of the Moshinsky brackets, accommodating for this transformation in the non-relativistic case. Additionally the formulation of correlation operators and corresponding correlation functions is a difficult question with no clear answer [1].

The reaction in which an incoming electron knocks out two nucleons out of a target nucleus is considered. The scattered electron as well as both outgoing nucleons are detected. The electron exchanges four momentum $q = (\omega, \vec{q})$ with the nucleus A, knocking a nucleon pair into continuum states, denoted p_1, p_2. Fig. 3.1 shows a diagrammatic representation of this reaction. It is assumed that one nucleon absorbs a large fraction of the three-momentum $\vec{q}$, exchanged by the projectile electron. When a nucleon pair with a large enough relative momentum is hit, the second, recoiling nucleon in the pair will leave the nucleus as well due to the high relative momentum. It is then possible to select nucleons with large initial momentum by making an appropriate cut on the final momenta of the nucleon pair. By demanding that $|\vec{q}| \gg 2|\vec{k}_F|$ we can identify which nucleon of the final pair absorbed the three-momentum $\vec{q}$. Choosing $|\vec{q}|$ large enough makes the case in which the slow, recoiling nucleon absorbed the virtual photon very unlikely. This would require an initial pair with relative momentum comparable to $|\vec{q}|$. As the distribution of the relative momentum of the SRC pairs is strongly decreasing for momenta above the Fermi momentum [2, 3] it is always possible to select an appropriate $|\vec{q}|$ value. The $A-2$ nucleons that do not participate in the hard scattering process remain unaffected. This is called the frozen spectator approximation, depicted by the right diagram of Fig. 3.1. The reference frame is taken to be the lab frame, where the target nucleus is stationary.

Several kinematical constraints are imposed in order to ensure that the process is dominated by knockout of SRC pairs. In a nucleus the nucleons with momenta above the Fermi momentum predominantly belong to SRC pairs with low center of mass (c.m.) momentum and high relative momentum, relative to the Fermi momentum. When assuming the exchanged four momentum q is largely absorbed by a single nucleon of the SRC pair, the

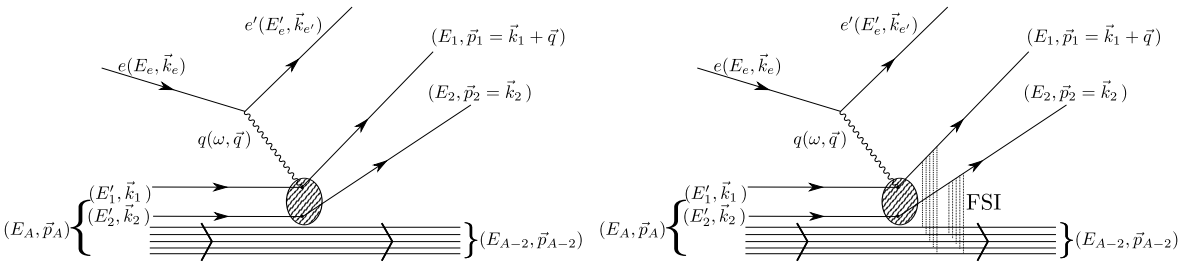

Figure 3.2 – A diagrammatic representation of the electroinduced two-nucleon knockout reaction as in Fig. 3.1 with the additional approximations whereby one nucleon of the correlated pair absorbs the four momentum q. The diagram on the right depicts the case where final-state interactions (FSI) between the knocked out nucleons and the recoiling nucleus are included.

initial three-momenta of the SRC pair $\vec{k}_1, \vec{k}_2$ can be reconstructed from the final momenta $\vec{p}_1, \vec{p}_2$ through $\vec{k}_1 = \vec{p}_1 - \vec{q}$, $\vec{k}_2 = \vec{p}_2$. In the exclusive reaction $\vec{p}_1, \vec{p}_2$ are measured and $\vec{q}$ can be reconstructed from the difference between the initial and final three-momentum of the projectile. This allows one to enforce restrictions on the initial three momenta of the nucleon pair. Knockout from SRC pairs can then be isolated by requiring the initial momenta to be larger than the Fermi momentum of the nucleus. The diagram corresponding to this process is shown in Fig. 3.2. The selection of SRC pairs can be reinforced by imposing the following additional restriction. Given that the SRC pairs have large relative momentum and small c.m. momentum it can be easily inferred that the initial momenta $\vec{k}_1, \vec{k}_2$ of the nucleon pair are biased towards a "back-to-back" configuration, whereby $\vec{k}_1$ and $\vec{k}_2$ are anti-parallel. As $\vec{k}_1, \vec{k}_2$ can be reconstructed, SRC pairs can be targeted by limiting the angle between $\vec{k}_1$ and $\vec{k}_2$ to back-to-back configurations, $(\vec{k}_1 \cdot \vec{k}_2)/(|\vec{k}_1||\vec{k}_2|) \sim -1$.

Final-state interactions (FSI) are an essential ingredient in the accurate description of exclusive nucleon knockout processes. They model the interactions between the particles in the "final" state. In this case this corresponds to the interactions between the knocked out nucleons and the recoiling $A-2$ nucleus (Fig. 3.2). The initial SRC pair, hit by the virtual photon, is brought into continuum states inside the nucleus. The knocked-out nucleons have to traverse the recoiling $A-2$ nucleus, possibly interacting with it. The FSI cause a significant reduction of the exclusive two-nucleon knockout cross section. The elastic and soft inelastic rescattering of the escaping nucleons is described using the Relativistic Multiple Scattering Glauber Approximation (RMSGA). The Glauber approximation is justified when the wavelength of the outgoing nucleon is sufficiently small in comparison to the distance-scale of the nucleon interaction with the residual nucleons. In the Glauber approximation the fast-moving particle interacts with fixed point scatterers, where the exchanged energy and momentum are small in comparison to the energy and momentum of the projectile. Each scatterer in the target adds to the eikonal phase factor, picked up by the wave function of the escaping particle. It the relativistic Glauber approximation the outgoing wave function is described by a relativistic plane wave, modified by an eikonal phase factor [4, 5]. The phase factor can be calculated starting from nucleon-nucleon scattering data. As such, it does not depend on the specific target nucleus, which makes the RMSGA readily applicable to the whole nuclear mass range. A detailed description of the RMSGA is provided in appendix A.3. Charge-exchange (CX) reactions, changing outgoing protons into neutrons and vice versa, are also included in the description of the FSI. This effect is calculated semi-classically. The influence of CX on the two-nucleon knockout reaction is described in

Sec. 3.3.

In this dissertation the contributions from inelastic processes such as excitations of the struck nucleon, multi-nucleon (> 2) knockout or fragmentation of the recoiling $A-2$ nucleus are not considered. When comparing to the theoretical results it is therefore imperative that these contributions are suppressed in the experimental data. In exclusive knockout reactions it is possible to suppress the inelastic contributions by imposing the appropriate conditions on the energy balance of the reaction, as outlined in the following. The four momenta of the target nucleus $p_A(E_A = M_A, \vec{0})$, the virtual photon $q(\omega, \vec{q})$ and the two ejected nucleons $p_1(E_1, \vec{p}_1), p_2(E_2, \vec{p}_2)$ are known (see Figs. 3.1,3.2). Without inelastic processes the energy conservation reads,

$$M_A + \omega - E_1 - E_2 - E_{A-2} = 0\,, \tag{3.1}$$

with $E_{A-2} = \sqrt{M^{*\,2}_{A-2} + |\vec{p}_{A-2}|^2}$ where M^*_{A-2} is the rest mass of the, possibly excited, recoiling nucleus. With $M_{A-2} \leqslant M^*_{A-2}$, where M_{A-2} the rest mass of the ground state of the $A-2$ nucleus Eq. (3.1) can be rewritten as,

$$M_A + \omega - E_1 - E_2 - \sqrt{M^2_{A-2} + |\vec{p}_{A-2}|^2} = E_X \geqslant 0\,, \tag{3.2}$$

E_X of Eq. (3.2) is at most equal to the excitation energy of the recoiling nucleus, $E_X \leq M^*_{A-2} - M_{A-2}$. Inelastic processes consume energy, making less energy available to be transferred to the ejected nucleons E_1, E_2. This will increase the value of E_X. In the reaction model used in this dissertation, the recoiling nucleus is left with little or no excitation energy. By limiting E_X below the threshold for pion production in the data, it is possible to allow for the mild excitations of the $A-2$ nucleus, originating from the knockout of two nucleons, while suppressing inelastic processes which require more energy.

In the following articles, it is shown that within the outlined reaction formalism, the two-nucleon knockout cross section $\sigma(e, e'NN)$ can be factorized into contributions depending on the relative and center-of-mass (c.m.) momentum of the initial nucleon pair. The factor depending on the relative momentum encodes the electron two-nucleon interaction, while the part that is a function of the c.m.-momentum holds the nuclear-structure information. The part of the cross section connected to the c.m. momentum is referred to as the distorted c.m. momentum distribution. It contains the distortion-effects of the final-state interactions (FSI). This factorization is a powerful tool in investigating the mass dependence of SRC features. When studying SRC across the whole nuclear mass range, the only quantity that changes is the distorted c.m. momentum distribution. Additionally, the factorization allows us to take cross section ratios of different nuclei which are independent of the electron two-nucleon interaction. The part containing the electron two-nucleon interaction is independent of the nuclear structure, reflecting the universality of the SRC, and is divided out when taking cross section ratios. It is expected that this approach leads to robust results as no model dependencies are introduced by modelling the electron two-nucleon interaction. A detailed derivation of the factorized cross section can be found in appendix B. There, the conditions for the factorization are examined in detail.

The articles presented in this chapter are arranged as follows. In Sec. 3.2 the factorization property of the exclusive two-nucleon knockout cross section is investigated, focussing upon the features of the distorted c.m. momentum distribution. Characteristics of the SRC pairs

contributing to the c.m. distribution are discussed, as well as the influence of FSI on the shape of the distribution.

The description of the FSI is the main focus of the second article (Sec. 3.3). The influence of charge-exchange processes on the two-nucleon knockout reaction is studied. Charge-exchange reactions change the isospin projection of the outgoing nucleons, transforming a proton in a neutron or vice versa. The calculation of the distorted c.m. momentum distribution is detailed and its decomposition into nucleon pairs with different isospin projections (proton-proton and proton-neutron pairs) is studied. The nuclear transparency, which is a measure of the FSI strength, across the nuclear mass range is investigated as well, in which the cross section ratios and the factorization property of the cross section play an important role.

Finally the third article of Sec. 3.4 addresses the issue of how the SRC properties in the ground state of atomic nuclei can be recovered from two-nucleon knockout cross sections. Theoretical predictions of SRC properties are compared to results extracted from measured cross sections that have been corrected for FSI, identifying the initial SRC dynamics.

3.2 Factorization of exclusive electroinduced 2N knockout

3.2.1 Introduction

In the following article, published as Ref. [2], the factorized expression for the exclusive two-nucleon knockout cross section is derived. The c.m. momentum distribution of SRC nucleon pairs is investigated in detail. The second, third and fourth moment (width, skewness and kurtosis) of the c.m. distribution are examined across the nuclear mass range. The c.m. momentum distribution as well as the relative momentum distribution are decomposed into the different contributions from SRC pairs with specific quantum numbers. This allows us to identify the dynamical behaviour of SRC pairs and their structure.

The calculated c.m. momentum distribution is then used as an input for Monte Carlo calculations, simulating an experimental scattering setup probing SRC pairs. In experimental measurements it is impossible to probe the full phase space uniformly. Due to kinematical constraints in scattering reactions, the c.m. momentum distribution is generally probed non-uniformly in a restricted part of the phase space. This paper investigates how the measured c.m. momentum distribution differs from the initial "true" distribution. Finally the effect of FSI on the c.m. momentum and the shape of the opening angle distribution is studied. The opening angle is defined as the relative angle between the individual initial momenta of the struck nucleon pair.

My specific contribution to this paper constitutes the computation and the discussion of the effect of the FSI on the c.m. momentum distribution and the opening-angle distribution of SRC pairs for different nuclei (section **V**). Additionally, an important message of the article is that the conditional c.m. momentum distribution, derived in the LCA framework, can be connected to the two-nucleon knockout cross section. The relation between the factorization function, appearing in the eightfold differential cross section $(e, e'NN)$, and the conditional

c.m. momentum distribution is stated, establishing the connection between SRC-pairs and the two-nucleon knockout cross section. This shows that SRC dynamics can be probed in the $(e, e'NN)$ reaction. The proof of the connection is quite involved. Therefore I derived the proof, included in Sec. (3.2.3)

Factorization of exclusive electroinduced two-nucleon knockout

Camille Colle,* Wim Cosyn,† Jan Ryckebusch,‡ and Maarten Vanhalst§
Department of Physics and Astronomy,
Ghent University, Proeftuinstraat 86, B-9000 Gent, Belgium
(Dated: 10 February 2014)

We investigate the factorization properties of the exclusive electroinduced two-nucleon knockout reaction $A(e, e'pN)$. A factorized expression for the cross section is derived and the conditions for factorization are studied. The $A(e, e'pN)$ cross section is shown to be proportional to the conditional center-of-mass (c.m.) momentum distribution for close-proximity pairs in a state with zero relative orbital momentum and zero radial quantum number. The width of this conditional c.m. momentum distribution is larger than the one corresponding with the full c.m. momentum distribution. It is shown that the final-state interactions (FSIs) only moderately affect the shape of the factorization function for the $A(e, e'pN)$ cross sections. Another prediction of the proposed factorization is that the mass dependence of the $A(e, e'pp)$ $[A(e, e'pn)]$ cross sections is much softer than $\frac{Z(Z-1)}{2}$ $[NZ]$.

PACS numbers: 25.30.Rw,25.30.Fj,24.10.-i

* Camille.Colle@UGent.be
† Wim.Cosyn@UGent.be
‡ Jan.Ryckebusch@UGent.be
§ Maarten.Vanhalst@UGent.be

I. INTRODUCTION

In recent years, substantial progress has been made in exploring the dynamics of short-range correlations (SRCs) in nuclei. On the experimental side, exclusive $A(p, 2p + n)$ [1] and $A(e, e'pN)$ [2–4] measurements have probed correlated pairs in nuclei and identified proton-neutron (pn) pairs as the dominant contribution. Inclusive $A(e, e')$ [5–7] measurements in kinematics favoring correlated pair knockout, have provided access to the mass dependence of the amount of correlated pairs relative to the deuteron. On the theoretical side, *ab initio* [8–11], cluster expansion [12–14], correlated basis function theory [15, 16], and low-momentum effective theory [17], calculations have provided insight in the fat high-momentum tails of the momentum distributions attributable to multinucleon correlations. Tensor correlations have been identified as the driving mechanism for the fat tails just above the Fermi momentum. The highest momenta in the tail of the momentum distribution are associated with the short-distance repulsive part of the nucleon-nucleon force and $N \geq 3$ correlations. Recent reviews of nuclear SRC can be found in Refs. [18, 19].

We have proposed a method to quantify the amount of correlated pairs in an arbitrary nucleus [20–22]. Thereby, we start from a picture of a correlated nuclear wave function as a product of a correlation operator acting on an independent-particle model (IPM) Slater determinant $\Psi_A^{\rm IPM}$ [17]. The SRC-susceptible pairs are identified by selecting those parts of $\Psi_A^{\rm IPM}$ that provide the largest contribution when subjected to typical nuclear correlation operators. It is found that IPM nucleon-nucleon pairs with vanishing relative orbital momentum and vanishing relative radial quantum numbers, receive the largest corrections from the correlation operators. This can be readily understood by realizing that IPM close-proximity pairs are highly susceptible to SRC corrections. This imposes constraints on the relative orbital and radial quantum numbers of the two-nucleon cluster components in the IPM wave functions which receive SRC corrections.

With the proposed method of quantifying SRC we can reasonably account for the mass dependence of the $\frac{A(e,e')}{d(e,e')}$ ratio under conditions of suppressed one-body contributions (Bjorken $x_B \gtrsim 1.2$) [21] and the mass dependence of the magnitude of the EMC effect [22, 23]. In connecting the SRC information to inclusive electron-scattering data at Bjorken $x_B \gtrsim 1.2$, there are complicating issues like the role of c.m. motion [21, 24] and final-state interactions (FSIs) [25]. More quantitative information on SRC and their mass and isospin dependence, is expected to come from exclusive electroinduced two-nucleon knockout which is the real fingerprint of nuclear SRC [26]. Reactions of this type are under investigation at Jefferson Laboratory (JLab) and results for ^{12}C$(e, e'pN)$ have been published [3, 4].

In this paper, we investigate the factorization properties of the exclusive $A(e, e'pN)$ reaction. Factorization is a particular result that emerges only under specific assumptions in the description of the scattering process. It results in an approximate expression for the cross section which becomes proportional to a specific function of selected dynamic variables. For exclusive quasielastic $A(e, e'p)$ processes, for example, the factorization function is the one-nucleon momentum distribution evaluated at the initial nucleon's momentum. It will be shown that for exclusive $A(e, e'pN)$ these roles are respectively played by the c.m. momentum distribution for close-proximity pairs and the c.m. momentum of the initial pair.

In Sec. II we present calculations for the pair c.m. momentum distribution in the IPM. It is shown that the correlation-susceptible IPM pairs have a broader c.m. width than those that are less prone to SRC corrections. In Sec. III, we show that after making a number of reasonable assumptions, the eightfold $A(e, e'pN)$ cross section factorizes with the conditional pair c.m. momentum distribution as the factorization function. In Sec. IV we report on results of Monte Carlo simulations for $A(e, e'pp)$ processes in kinematics corresponding to those accessible in the JLab Hall A and Hall B detectors. We study the effect of typically applied cuts on several quantities. In Sec. V it is investigated to what extent FSIs affect the factorization function of the exclusive $A(e, e'pN)$ process. Finally, our conclusions are stated in Sec. VI.

II. PAIR CENTER-OF-MASS MOMENTUM DISTRIBUTIONS

In this section we study the pp and pn pair c.m. momentum distribution for ^{12}C, ^{27}Al, ^{56}Fe and ^{208}Pb which we deem representative for the full mass range of stable nuclei. We introduce the relative and c.m. coordinates and momenta

$$\vec{r}_{12} = \vec{r}_1 - \vec{r}_2, \qquad \vec{R}_{12} = \frac{\vec{r}_1 + \vec{r}_2}{2} \,, \tag{1}$$

$$\vec{k}_{12} = \frac{\vec{k}_1 - \vec{k}_2}{2}, \qquad \vec{P}_{12} = \vec{k}_1 + \vec{k}_2 \,. \tag{2}$$

The corresponding two-body momentum density reads

$$P_2\left(\vec{k}_{12},\vec{P}_{12}\right) = \frac{1}{(2\pi)^6}\int d\vec{r}_{12}\int d\vec{r}\,'_{12}\int d\vec{R}_{12}\int d\vec{R}\,'_{12} \times e^{\imath\vec{k}_{12}\cdot\left(\vec{r}\,'_{12}-\vec{r}_{12}\right)}e^{\imath\vec{P}_{12}\cdot\left(\vec{R}\,'_{12}-\vec{R}_{12}\right)}\rho_2(\vec{r}\,'_{12},\vec{R}\,'_{12};\vec{r}_{12},\vec{R}_{12}), \quad (3)$$

where $\rho_2(\vec{r}\,'_{12},\vec{R}\,'_{12};\vec{r}_{12},\vec{R}_{12})$ is the non-diagonal two-body density (TBD) matrix

$$\rho_2(\vec{r}\,'_{12},\vec{R}\,'_{12};\vec{r}_{12},\vec{R}_{12}) = \int\{d\vec{r}_{3-A}\}\times\Psi_A^*(\vec{r}_1\,',\vec{r}_2\,',\vec{r}_3,\ldots,\vec{r}_A)\Psi_A(\vec{r}_1,\vec{r}_2,\vec{r}_3,\ldots,\vec{r}_A). \quad (4)$$

Here, Ψ_A is the normalized ground-state wave function of the nucleus A and $\{d\vec{r}_{i-A}\}\equiv d\vec{r}_i d\vec{r}_{i+1}\ldots d\vec{r}_A$. For a spherically symmetric system, $P_2\left(\vec{k}_{12},\vec{P}_{12}\right)$ depends on three independent variables, for example the magnitudes $\left|\vec{k}_{12}\right|$ and $\left|\vec{P}_{12}\right|$ and the angle between $\vec{k}_{12}$ and $\vec{P}_{12}$. In Ref. [13] two-body momentum distributions for ^{3}He and ^{4}He are shown to be largely independent of the angle between $\vec{k}_{12}$ and $\vec{P}_{12}$ for $P_{12}\lesssim 200$ MeV. Integrating over the directional dependence of Eq. (3), the quantity

$$\begin{aligned} &n_2(k_{12},P_{12})k_{12}^2dk_{12}P_{12}^2dP_{12} \\ &= k_{12}^2dk_{12}P_{12}^2dP_{12}\int d\Omega_{k_{12}}\int d\Omega_{P_{12}}P_2(\vec{k}_{12},\vec{P}_{12})\,, \end{aligned} \quad (5)$$

is connected to the probability of finding a nucleon pair with relative and c.m. momentum in $[k_{12},k_{12}+dk_{12}]$ and $[P_{12},P_{12}+dP_{12}]$. With the spherical-wave expansion for the two vector plane waves in Eq. (3) one obtains

$$n_2(k_{12},P_{12}) = \frac{4}{\pi^2}\sum_{lm_l}\sum_{\Lambda M_\Lambda} n_2^{lm_l\Lambda M_\Lambda}(k_{12},P_{12}), \quad (6)$$

with

$$\begin{aligned} &n_2^{lm_l\Lambda M_\Lambda}(k_{12},P_{12}) = \\ &\int dr\,'_{12}\;{r\,'_{12}}^2\int dR\,'_{12}\;{R\,'_{12}}^2\int dr_{12}\;r_{12}^2\int dR_{12}\;R_{12}^2 \\ &\times j_l(k_{12}r_{12})j_l(k_{12}r\,'_{12})j_\Lambda(P_{12}R_{12})j_\Lambda(P_{12}R\,'_{12}) \\ &\times \rho_2^{lm_l\Lambda M_\Lambda}(r\,'_{12},R\,'_{12};r_{12},R_{12}). \end{aligned} \quad (7)$$

Here, $\rho_2^{lm_l\Lambda M_\Lambda}(r\,'_{12},R\,'_{12};r_{12},R_{12})$ is the projection of the TBD matrix on relative and c.m. orbital angular-momentum states $|lm_l\rangle$ and $|\Lambda M_\Lambda\rangle$.

The pair c.m. momentum distribution is defined by

$$\begin{aligned} P_2(P_{12}) &= \int d\Omega_{P_{12}}\int d\vec{k}_{12}P_2(\vec{k}_{12},\vec{P}_{12}) \\ &= \int dk_{12}k_{12}^2n_2(k_{12},P_{12}), \end{aligned} \quad (8)$$

and the quantity $P_2(P_{12})\;P_{12}^2\;dP_{12}$ is related to the probability of finding a nucleon pair with $\left|\vec{P}_{12}\right|$ in $[P_{12},P_{12}+dP_{12}]$ irrespective of the magnitude and direction of $\vec{k}_{12}$. Similarly, the pair relative momentum distribution is defined as

$$n_2(k_{12}) = \int d\Omega_{k_{12}}\int d\vec{P}_{12}P_2(\vec{k}_{12},\vec{P}_{12})\,. \quad (9)$$

In the IPM, the ground-state wave function can be expanded in terms of single-particle wave functions ϕ_{α_i}

$$\Psi_A^{\rm IPM} = (A!)^{-1/2}\det\left[\phi_{\alpha_i}(\vec{x}_j)\right], \quad (10)$$

and the TBD matrix is given by

$$\rho_2^{\rm IPM}(\vec{r}_{12}',\vec{R}_{12}';\vec{r}_{12},\vec{R}_{12}) = \frac{2}{A(A-1)}\sum_{\alpha<\beta}\frac{1}{2}\left[\phi_\alpha^*(\vec{x}_1')\phi_\beta^*(\vec{x}_2') - \phi_\beta^*(\vec{x}_1')\phi_\alpha^*(\vec{x}_2')\right]\left[\phi_\alpha(\vec{x}_1)\phi_\beta(\vec{x}_2) - \phi_\beta(\vec{x}_1)\phi_\alpha(\vec{x}_2)\right]. \tag{11}$$

Here, $\vec{x} \equiv (\vec{r},\vec{\sigma},\vec{\tau})$ is a shorthand notation for the spatial, spin, and isospin coordinates. The summation $\sum_{\alpha<\beta}$ extends over all occupied single-particle levels and implicitly includes an integration over the spin and isospin degrees of freedom (d.o.f.).

In a HO basis the uncoupled single-particle states read

$$\phi_\alpha(\vec{x}) \equiv \psi_{n_\alpha l_\alpha m_{l_\alpha}}(\vec{r})\chi_{\sigma_\alpha}(\vec{\sigma})\,\xi_{\tau_\alpha}(\vec{\tau}). \tag{12}$$

The A dependence can be taken care of by means of the parameterization $\hbar\omega({\rm MeV}) = 45\ A^{\frac{1}{3}} - 25\ A^{\frac{2}{3}}$. A transformation from $(\vec{r}_1,\vec{r}_2)$ to $(\vec{r}_{12},\vec{R}_{12})$ for the uncoupled normalized-and-antisymmetrized (nas) two-nucleon states can be readily performed in a HO basis [20, 21]

$$\mid\alpha\beta\rangle_{\rm nas} = \sum_{\substack{nlm_lN\Lambda M_\Lambda\\ SM_STM_T}}\langle nlm_lN\Lambda M_\Lambda SM_STM_T \mid \alpha\beta\rangle \mid nlm_lN\Lambda M_\Lambda SM_STM_T\rangle = \sum_{\substack{A=\{nlm_lN\Lambda M_\Lambda\\ SM_STM_T\}}} C_{\alpha\beta}^A \mid A\rangle, \tag{13}$$

with the transformation coefficient $C_{\alpha\beta}^{nlm_lN\Lambda M_\Lambda SM_STM_T}$ given by

$$\begin{aligned} C_{\alpha\beta}^{nlm_lN\Lambda M_\Lambda SM_STM_T} =& \frac{1}{\sqrt{2}}\left[1-(-1)^{l+S+T}\right]\langle\frac{1}{2}\tau_\alpha\frac{1}{2}\tau_\beta \mid TM_T\rangle\langle\frac{1}{2}\sigma_\alpha\frac{1}{2}\sigma_\beta \mid SM_S\rangle \\ &\times\sum_{LM_L}\langle l_\alpha m_{l_\alpha} l_\beta m_{l_\beta} \mid LM_L\rangle\langle nlN\Lambda; L \mid n_\alpha l_\alpha n_\beta l_\beta; L\rangle_{\rm SMB}\langle LM_L \mid lm_l\Lambda M_\Lambda\rangle, \end{aligned} \tag{14}$$

where we use the Talmi-Moshinsky brackets $\langle|\rangle_{\rm SMB}$ [27] to separate out the relative and c.m. coordinates in the products of single-particle wave functions.

After performing the transformation of Eq. (13) for the TBD matrix of Eq. (11), $P_2(P_{12})$ can be written as

$$P_2(P_{12}) = \frac{2}{\pi}\sum_{nlm_l}\sum_{\Lambda M_\Lambda} P_2^{nlm_l\Lambda M_\Lambda}(P_{12}), \tag{15}$$

with

$$\begin{aligned} P_2^{nlm_l\Lambda M_\Lambda}(P_{12}) =& \frac{2}{A(A-1)}\sum_{\alpha<\beta}\sum_{NN'}\sum_{SM_STM_T}(C_{\alpha\beta}^{nlm_lN'\Lambda M_\Lambda SM_STM_T})^\dagger C_{\alpha\beta}^{nlm_lN\Lambda M_\Lambda SM_STM_T} \\ &\times\int dR_{12}'\ {R_{12}'}^2\int dR_{12}\ R_{12}^2\ \ j_\Lambda(P_{12}R_{12}')j_\Lambda(P_{12}R_{12})R_{N'\Lambda}(\sqrt{2}R_{12}')R_{N\Lambda}(\sqrt{2}R_{12}) \end{aligned} \tag{16}$$

A Woods-Saxon basis, for example, first needs to be expanded in a HO basis before a projection of the type (16) can be made. Using Eqs. (15) and (16), the conditional pair c.m. momentum distribution for a given relative radial quantum number n and relative orbital momentum l, can be defined as

$$P_2(P_{12}|nl=\nu\lambda) = \frac{2}{\pi}\sum_{m_l}\sum_{\Lambda M_\Lambda} P_2^{\nu\lambda m_l\Lambda M_\Lambda}(P_{12}). \tag{17}$$

Obviously, one has

$$P_2(P_{12}) = \sum_{\nu\lambda} P_2(P_{12}|nl=\nu\lambda) = \sum_\lambda P_2(P_{12}|l=\lambda), \tag{18}$$

where $P_2(P_{12}|l=\lambda)$ is the conditional pair c.m. momentum distribution for $l=\lambda$.

A symmetric correlation operator $\widehat{\mathcal{G}}$ can be applied to the IPM wave function of Eq. (10) in order to obtain a realistic ground-state wave function [15, 28–30]

$$\mid \Psi_A\rangle = \frac{1}{\sqrt{\langle\ \Psi_A^{\rm IPM} \mid \widehat{\mathcal{G}}^\dagger\widehat{\mathcal{G}} \mid \Psi_A^{\rm IPM}\ \rangle}}\ \widehat{\mathcal{G}} \mid \Psi_A^{\rm IPM}\ \rangle\ . \tag{19}$$

The operator $\widehat{\mathcal{G}}$ is complicated but as far as the SRC are concerned, it is dominated by the central, tensor and spin-isospin correlations [31, 32]

$$\widehat{\mathcal{G}} \approx \widehat{\mathcal{S}}\Big[\prod_{i<j=1}^{A}\Big(1+\hat{\imath}\,(\vec{x}_i,\vec{x}_j)\Big)\Big]\ , \tag{20}$$

with $\widehat{\mathcal{S}}$ the symmetrization operator and

$$\begin{aligned}\hat{\imath}\,(\vec{x}_1,\vec{x}_2) = &-g_c(r_{12}) + f_{t\tau}(r_{12})S_{12}\vec{\tau}_1\cdot\vec{\tau}_2\\ &+ f_{\sigma\tau}(r_{12})\vec{\sigma}_1\cdot\vec{\sigma}_2\vec{\tau}_1\cdot\vec{\tau}_2\,,\end{aligned} \tag{21}$$

where $g_c(r_{12})$, $f_{t\tau}(r_{12})$, $f_{\sigma\tau}(r_{12})$ are the central, tensor, and spin-isospin correlation functions, and S_{12} the tensor operator. The sign convention of $-g_c(r_{12})$ in Eq. (21) implies that $\lim\limits_{r_{12}\to 0} g_c(r_{12}) = g_0$ $(0 < g_0 \leq 1)$). We stress that the correlation functions cannot be considered as universal [29]. They depend for example on the choices made with regard to the nucleon-nucleon interaction, the single-particle basis and the many-body approximation scheme.

With Eq. (19), the intrinsic complexity stemming from the nuclear correlations is shifted from the wave functions to the transition operators. For example, the ground-state matrix element with a two-body operator $\hat{\mathcal{O}}^{[2]}$ adopts the form

$$\langle\Psi_A \mid \hat{\mathcal{O}}^{[2]} \mid \Psi_A\rangle = \frac{1}{\langle\ \Psi_A^{\rm IPM} \mid \widehat{\mathcal{G}}^\dagger\widehat{\mathcal{G}} \mid \Psi_A^{\rm IPM}\ \rangle}\langle\ \Psi_A^{\rm IPM} \mid \widehat{\mathcal{G}}^\dagger\hat{\mathcal{O}}^{[2]}\widehat{\mathcal{G}} \mid \Psi_A^{\rm IPM}\ \rangle\ , \tag{22}$$

whereby high-order many-body operators are generated. Throughout this work we adopt the two-body cluster (TBC) approximation, which amounts to discarding all terms in $\widehat{\mathcal{G}}^\dagger\hat{\mathcal{O}}^{[2]}\widehat{\mathcal{G}}$ except those in which the transition operator and the correlators act on the same pair of particles. In this lowest-order cluster expansion the matrix element of Eq. (22) becomes with the aid of Eq. (20)

$$\begin{aligned}\langle\Psi_A \mid \hat{\mathcal{O}}^{[2]} \mid \Psi_A\rangle &\approx \frac{1}{\langle\ \Psi_A \mid \Psi_A\ \rangle}\langle\ \Psi_A^{\rm IPM} \mid \sum_{i<j=1}^{A}\Big(1+\hat{\imath}\,(\vec{x}_i,\vec{x}_j)\Big)^\dagger\hat{\mathcal{O}}^{[2]}\,(i,j)\Big(1+\hat{\imath}\,(\vec{x}_i,\vec{x}_j)\Big) \mid \Psi_A^{\rm IPM}\rangle\\ &= \frac{1}{\langle\Psi_A \mid \Psi_A\ \rangle}\Big[\langle\ \Psi_A^{\rm IPM} \mid \hat{\mathcal{O}}^{[2]} \mid \Psi_A^{\rm IPM}\ \rangle + \text{TBC corrections}\Big]\ .\end{aligned} \tag{23}$$

In this expansion, the matrix element is written as the sum of the bare (or IPM) contribution and the TBC corrections to it. The $P_2(P_{12})$ and $n_2(k_{12})$ of Eqs. (8-9) can be computed with the aid of the Eq. (23) using the transition operators $\delta\left(\vec{P}_{ij} - (\vec{k}_i+\vec{k}_j)\right)$ and $\delta\left(\vec{k}_{ij} - \frac{\vec{k}_i-\vec{k}_j}{2}\right)$. As the $\hat{\imath}$ involves only relative coordinates, the $P_2(P_{12})$ is not affected by the SRC corrections in the TBC approximation. We define $n_2^{\rm IPM}(k_{12})$ as the IPM contribution of $n_2(k_{12})$ and $n_2^{\rm TBC}(k_{12})$ the result obtained with Eq. (23). Accordingly, $n_2^{\rm TBC}(k_{12}) = n_2^{\rm IPM}(k_{12}) + \text{TBC corrections}$. For $n_2^{\rm TBC}(k_{12})$ the denominator $\langle\ \Psi_A \mid \Psi_A\ \rangle$ in Eq. (23) can be numerically computed by imposing the normalization conditions: $\int dk_{12} n_2^{\rm TBC}(k_{12})k_{12}^2 = 1$. As in Eqs. (7) and (17), one can introduce projection operators, and select the contributions to $n_2^{\rm TBC}(k_{12})$ stemming from particular quantum numbers (nl) of the relative two-nucleon wave functions in $\Psi_A^{\rm IPM}$. We define $n_2^{2n+l}(k_{12})$ as the contribution to $n_2^{\rm TBC}$ considering only (nl) configurations in $\Psi_A^{\rm IPM}$ with constant $2n+l$. Obviously, one has

$$\sum_{2n+l} n_2^{2n+l}(k_{12}) = n_2^{\rm TBC}(k_{12}). \tag{24}$$

The computed n_2^{2n+l}, $n_2^{\rm TBC}$ and $n_2^{\rm IPM}$ for ^{56}Fe are shown in Fig. 1. Below the Fermi momentum k_F, the effect of the correlation operator is negligible and $n_2^{\rm IPM}(k_{12}) \approx n_2^{\rm TBC}(k_{12})$. For $k_{12} > k_F$, $n_2^{\rm IPM}(k_{12})$ drops rapidly while $n_2^{\rm TBC}(k_{12})$ exhibits the SRC related high momentum tail. The tail is dominated by the $2n+l=0$

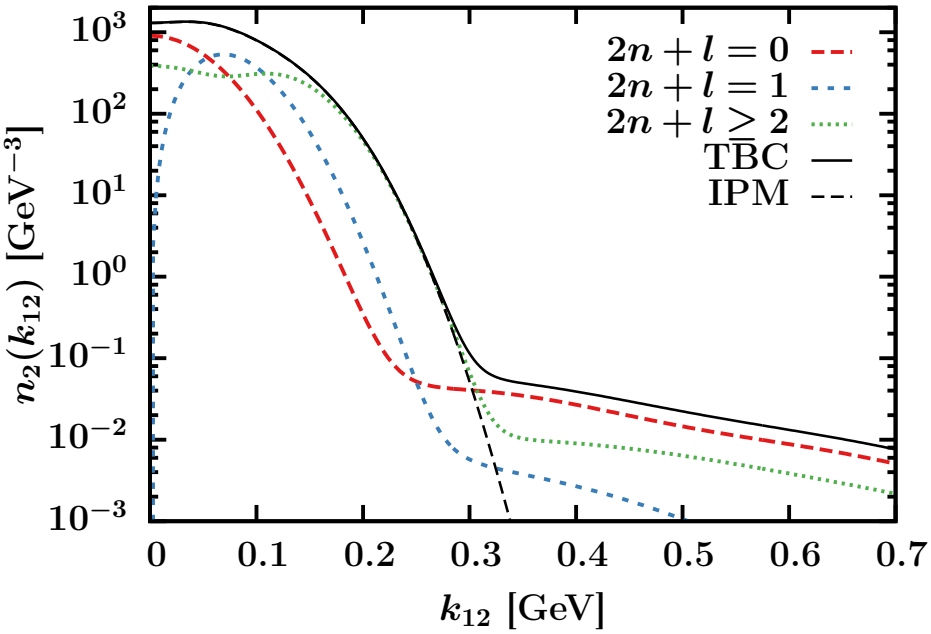

FIG. 1. (Color online) The momentum dependence of the computed $n_2^{2n+l}(k_{12})$, $n_2^{\rm TBC}(k_{12})$ and $n_2^{\rm IPM}(k_{12})$ for ^{56}Fe in a HO basis. In order to quantify the effect of SRC we have used the $g_c\,(r_{12})$ of Ref. [33] and the $f_{t\tau}\,(r_{12})$, $f_{\sigma\tau}(r_{12})$ of Ref. [28].

configurations. This indicates that most of the SRC are dynamically generated through the operation of the correlation operators on $nl = 00$ IPM pairs.

In Sec. III, it is shown that in the limit of vanishing FSIs the factorization function of the exclusive $A(e, e'pN)$ cross section is $P_2(P_{12}|nl = 00)$. In Figs. 2 and 3, we display the computed $P_2(P_{12})$ and $P_2(P_{12}|nl = 00)$ for the pp and pn pairs in ^{12}C, ^{27}Al, ^{56}Fe and ^{208}Pb. The relative weight of the $(nl = 00)$ in the total c.m. distribution decreases spectacularly with increasing mass number A. This will reflect itself in the mass dependence of the $A(e, e'NN)$ cross sections which are predicted to scale much softer than A^2. The $(nl = 00)$ pairs are strongly localized in space which enlarges the $P_2(P_{12}|nl = 00)$ width relative to the $P_2(P_{12})$ one. The mass dependence of the normalized $P_2(P_{12})$ reflects itself in a modest growth of the width of the distribution. For the light nuclei ^{12}C and ^{27}Al, the pp and pn c.m. distributions look very similar.

At first sight the computed $P_2(P_{12})$ for the pp and pn pairs in Figs. 2 and 3 look very Gaussian. In what follows, we use the moments to quantify the non-Gaussianity of the P_2. The first moment, or mean, of a distribution $F(x)$ is defined as

$$\mu_1 = \mu = \frac{\int_D xF(x)\mathrm{d}x}{\int_D F(x)\mathrm{d}x}, \tag{25}$$

where D is the domain of the distribution. For $m > 1$, we define the central moments as

$$\mu_m = \frac{\int_D (x-\mu)^m F(x)\mathrm{d}x}{\int_D F(x)\mathrm{d}x}\,. \tag{26}$$

The width is defined as $\sigma = \sqrt{\mu_2}$. With regard to μ_3 and μ_4, it is common practice to describe a distribution with the skewness γ_1 and excess kurtosis κ

$$\gamma_1 \equiv \frac{\mu_3}{\sigma^3} \tag{27}$$

$$\kappa \equiv \frac{\mu_4}{\sigma^4} - 3, \tag{28}$$

which are both vanishing for a Gaussian distribution.

For a spherically symmetric distribution, one can derive the distributions $P_{2,i}\,(P_{12,i})$ $(i = x, y, z)$ along the axes from $P_{12}^2 P_2\left(P_{12} = \sqrt{P_{12,x}^2 + P_{12,y}^2 + P_{12,z}^2}\right)$. Gaussian $P_{2,i}$ give rise to a $P_{12}^2 P_2\,(P_{12,i})$ of the Maxwell-Boltzmann type.

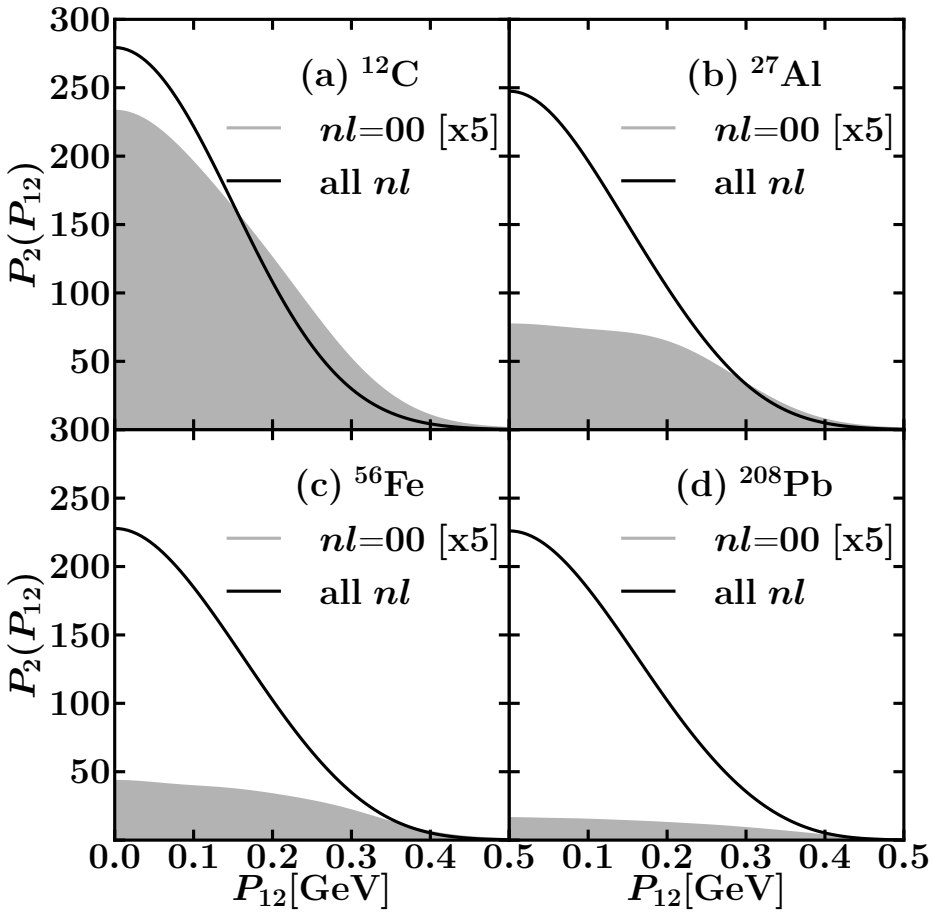

FIG. 2. The momentum dependence of $P_2(P_{12})$ and the $P_2\left(P_{12}|nl=00\right)$ for pp pairs in different nuclei. The adopted normalization convention is that $\int_0^\infty \mathrm{d}P_{12}\; P_{12}^2 P_2(P_{12}) = 1$. Note that only the pp contributions to $P_2(P_{12})$ are considered when performing the integral. The results are obtained in a HO basis.

		HO			WS		
		σ (MeV)	γ_1 [Eq. (27)]	κ [Eq. (28)]	σ (MeV)	γ_1 [Eq. (27)]	κ [Eq. (28)]
^{12}C	$P_{2,x}(P_{12,x}\|nl=00)$	156	0.00	−0.25	158	0.00	−0.28
^{12}C	$P_{2,x}(P_{12,x})$	140	−0.01	−0.12	142	−0.01	−0.05
^{27}Al	$P_{2,x}(P_{12,x}\|nl=00)$	164	0.00	−0.45	168	0.00	−0.45
^{27}Al	$P_{2,x}(P_{12,x})$	144	−0.01	−0.20	148	−0.01	−0.20
^{56}Fe	$P_{2,x}(P_{12,x}\|nl=00)$	172	0.00	−0.54	174	0.00	−0.54
^{56}Fe	$P_{2,x}(P_x)$	146	−0.01	−0.27	149	0.00	−0.26
^{208}Pb	$P_{2,x}(P_{12,x}\|nl=00)$	178	0.00	−0.58	177	0.00	−0.63
^{208}Pb	$P_{2,x}(P_{12,x})$	145	0.00	−0.31	146	0.00	−0.31

TABLE I. The moments of the $P_{2,x}\left(P_{12,x}\right)$ and the $P_{2,x}\left(P_{12,x}|nl=00\right)$ distributions for pp pairs as computed in a HO and WS single-particle basis for various nuclei.

Table I shows the computed moments of the $P_{2,x}(P_{12,x}|nl=00)$ and $P_{2,x}(P_{12,x})$ distributions for pp pairs. These results are obtained with HO and Woods-Saxon (WS) single-particle wave functions. We find that the c.m. distributions are not perfectly Gaussian and that the non-Gaussianity grows with A. The values of the widths are only moderately sensitive to the single-particle basis used. The WS widths are larger by a few percent than the HO ones.

In Fig. 4, the calculated widths of the $P_{2,x}(P_{12,x})$ and $P_{2,x}(P_{12,x}|l)$ are shown for pp, nn and np pairs. For the np pairs we discriminate between singlet ($S=0$) and triplet ($S=1$) spin states. From Fig. 4 we draw the following conclusions. The width of the $P_{2,x}(P_{12}|l)$ depends on l. For $l=0$ and np pairs, the width of $P_{2,x}(P|l)$ is almost independent of S. For heavy nuclei there is a substantial difference in the width

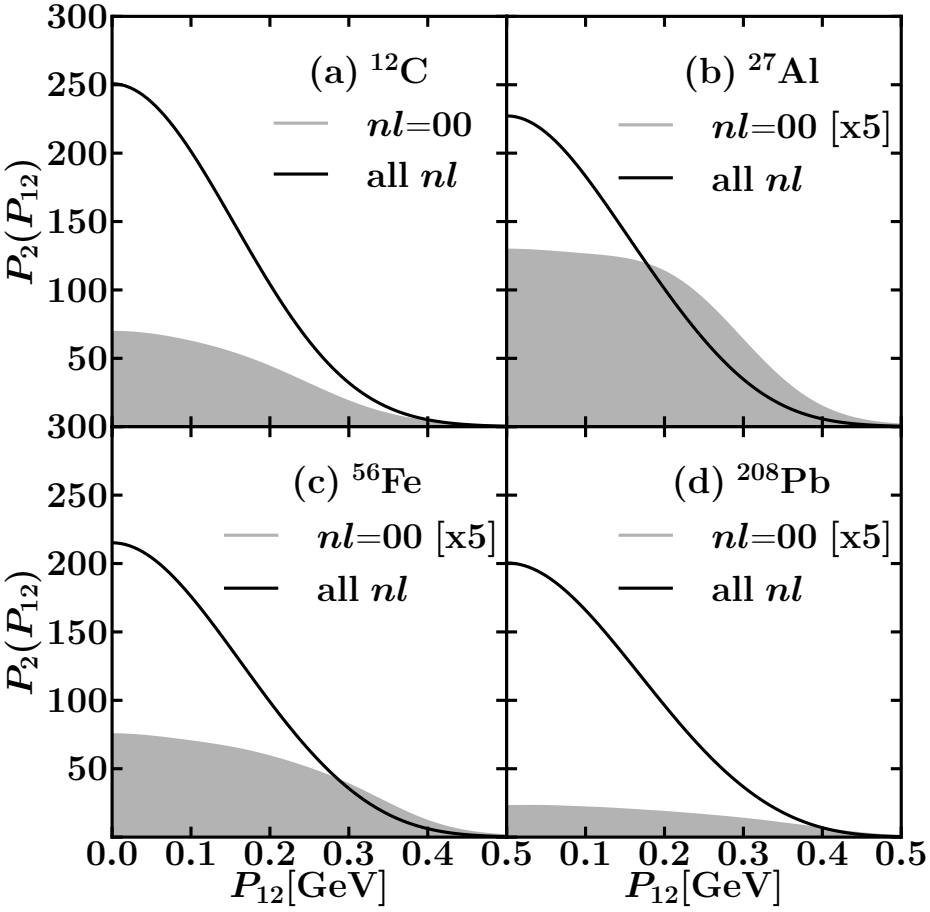

FIG. 3. As in Fig. 2 but for pn pairs.

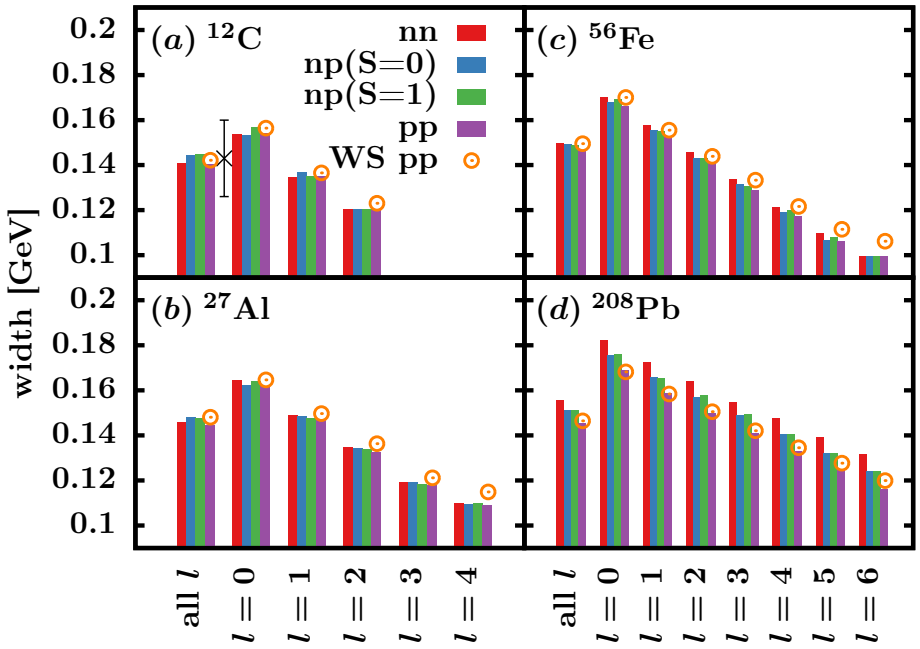

FIG. 4. (Color online) Computed widths of the $P_{2,x}\,(P_{12,x})$ (denoted as "all l") and $P_{2,x}\,(P_{12,x}|l)$ distributions for pp, nn, np($S=0$) and np($S=1$) pairs in ^{12}C, ^{27}Al, ^{56}Fe, ^{208}Pb. Unless stated otherwise the results are obtained in a HO basis. For pp pairs we also display results for a WS basis (denoted as "WS pp"). The black cross is the experimental result from Ref. [1].

of the $P_{2,x}(P|l=0)$ for pp, nn and np pairs but for light nuclei this is not the case. A similar but smaller dependence on the width is found for n at fixed l, the width of $P_2(P_{12}|nl)$ decreases for increasing n. We conclude that from the width of the c.m. distribution of the pairs one can infer information about their relative orbital momentum.

III. FACTORIZATION OF THE TWO-NUCLEON KNOCKOUT CROSS SECTION

It is well known that the fivefold differential cross section for the exclusive $A(e,e'p)A-1$ reaction under quasifree kinematics with $A-1$ spectators

$$\gamma^*\left(q\right)+A-1\left(p_{A-1}\right)+N\left(k_1\right)\longrightarrow A-1\left(p_{A-1}\right)+N\left(p_1\right)\ , \tag{29}$$

factorizes as

$$d^5\sigma(e,e'p)=K_{ep}\sigma_{ep}P_1(\vec{k}_m,E_m)\ . \tag{30}$$

Here, K_{ep} is a kinematical factor and σ_{ep} the off-shell electron-proton cross section. Further, $\vec{k}_m=-\vec{p}_{A-1}=\vec{k}_1$ is the missing momentum and $E_m=q^0-T_{p_1}-T_{A-1}$ the missing energy, whereby T_{A-1} and T_{p_1} are the kinetic energy of the recoiling nucleus and ejected nucleon. The $P_1(\vec{k},E)$ is the one-body spectral function and is associated with the combined probability of removing a proton with momentum $\vec{k}$ from the ground-state of A and of finding the residual $A-1$ nucleus at excitation energy E (measured relative to the ground-state of the target nucleus). The factorization is exact in a non-relativistic reaction model with $A-1$ spectators and vanishing FSIs [34]. The validity of the spectator approximation requires that the E_m is confined to low values, corresponding to states with a predominant one-hole character relative to the ground state of the target nucleus A.

Below, it is shown that also the $A(e,e'pN)$ differential cross section factorizes under certain assumptions. The factorization function is connected to the c.m. motion of close-proximity pairs. In Ref. [35] the factorization function is introduced as the so-called *decay function*. In Ref. [36] a factorized expression for the $A(e,e'pp)$ cross section has been derived. Thereby, in computing the matrix elements, all FSI effects have been neglected and the zero-range approximation ($\lim_{r_{12}\to 0}$) has been adopted. A ^{12}C$(e,e'pp)$ experiment conducted at the Mainz Microtron (MAMI) [37] showed very good quantitative agreement with the predicted diproton pair c.m. momentum factorization up to momenta of about 500 MeV. Here, the formalism of Ref. [36] is extended to include the effect of FSIs and to soften the zero-range approximation. Note that the limit $\lim_{r_{12}\to 0}$ effectively amounts to projecting on states with vanishing relative orbital momentum.

We consider exclusive $A(e,e'NN)$ reactions in the spectator approximation with a virtual photon coupling to a correlated pair $N\left(k_1\right)N\left(k_2\right)$

$$\gamma^*\left(q\right)+A-2\left(p_{A-2}\right)+N\left(k_1\right)N\left(k_2\right)\longrightarrow A-2\left(p_{A-2}\right)+N\left(p_1\right)+N\left(p_2\right)\ . \tag{31}$$

In a non-relativistic treatment, the corresponding matrix element is given by

$$\mathcal{M}^\mu=\int d\vec{x}_1\int d\vec{x}_2\Big[\chi^\dagger_{s_1}(\vec{\sigma}_1)\xi^\dagger_{t_1}\left(\vec{\tau}_1\right)\chi^\dagger_{s_2}(\vec{\sigma}_2)\xi^\dagger_{t_2}\left(\vec{\tau}_2\right)e^{-i\vec{p}_1\cdot\vec{r}_1}e^{-i\vec{p}_2\cdot\vec{r}_2}-(1\leftrightarrow 2)\Big]$$
$$\times\,\mathcal{F}^\dagger_{\rm FSI}(\vec{r}_1,\vec{r}_2)\hat{\mathcal{O}}^\mu(\vec{x}_1,\vec{x}_2)\phi_{\alpha_1}(\vec{x}_1)\phi_{\alpha_2}(\vec{x}_2)\,. \tag{32}$$

Here, $s_i(t_i)$ are the spin (isospin) projection of the outgoing nucleons. Further, $\mathcal{F}_{\rm FSI}(\vec{r}_1,\vec{r}_2)$ is an operator encoding the FSIs for a reaction where two nucleons are brought into the continuum at the spatial localizations $\vec{r}_1$ and $\vec{r}_2$ respectively. We assume that $\mathcal{F}_{\rm FSI}$ does not depend on the spin and isospin d.o.f, which is a fair approximation at higher energies. The amplitude of Eq. (32) refers to the physical situation whereby, as a result of virtual-photon excitation, two nucleons are excited from bound states $\alpha_1\alpha_2$ into continuum states.

In Eq. (32), the effect of the correlations is implemented in the TBC approximation by means of a symmetric two-body operator [29, 31]

$$\hat{\mathcal{O}}^\mu(\vec{x}_1,\vec{x}_2)=\left[e^{i\vec{q}\cdot\vec{r}_1}\Gamma^\mu_{\gamma^\star N}(\vec{x}_1)+e^{i\vec{q}\cdot\vec{r}_2}\Gamma^\mu_{\gamma^\star N}(\vec{x}_2)\right]\hat{\wr}\left(\vec{x}_1,\vec{x}_2\right)\ , \tag{33}$$

where the operator $\hat{\wr}\left(\vec{x}_1,\vec{x}_2\right)$ has been defined in Eq. (21) and $\vec{q}$ is the three-momentum of the virtual photon. The $\Gamma^\mu_{\gamma^\star N}(\vec{x}_i)$ denotes the one-body virtual photon coupling to a bound nucleon with coordinate

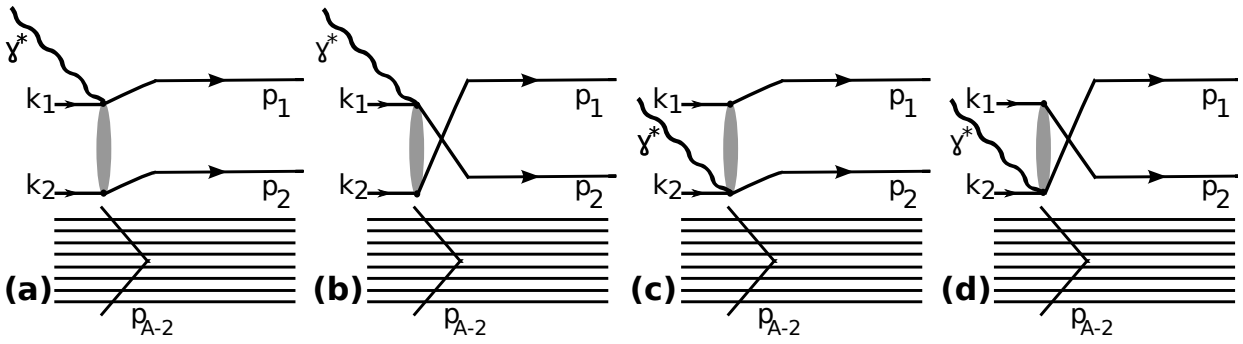

FIG. 5. The four contributions to the $A(e,e'NN)$ amplitude of Eq. (32).

$\vec{x}_i$ (includes the spatial, spin, and isospin d.o.f.). The Eq. (33) can be interpreted as the SRC-corrected photo-nucleon coupling which operates on IPM many-body wave functions.

The amplitude of Eq. (32) involves four contributions schematically shown in Fig. 5. For the sake of brevity, in the following we consider the term of Fig. 5(a) with a photon-nucleon coupling on coordinate $\vec{r}_1$ and the outgoing nucleon with momentum $\vec{p}_1$ directly attached to this vertex. The corresponding amplitude is denoted by $\mathcal{M}^\mu_a$. The other three terms in Fig. 5 follow a similar derivation.

In a HO single-particle basis, one can write

$$\mathcal{M}^\mu_a = \int d\vec{r}_1 \int d\vec{r}_2 e^{-i(\vec{p}_1-\vec{q})\cdot\vec{r}_1} e^{-i\vec{p}_2\cdot\vec{r}_2} \mathcal{F}^\dagger_{\rm FSI}(\vec{r}_1,\vec{r}_2) \times \langle s_1t_1, s_2t_2 \mid \Gamma^\mu_{\gamma^\star N}(\vec{x}_1)\,\hat{\imath}\,(\vec{x}_1,\vec{x}_2) \mid \sigma_1\tau_1,\sigma_2\tau_2\rangle \psi_{n_1l_1m_{l_1}}(\vec{r}_1)\psi_{n_2l_2m_{l_2}}(\vec{r}_2)\,, \quad (34)$$

where σ_i (τ_i) are the spin (isospin) quantum numbers of the bound states. Further, $\psi_{n_1l_1m_{l_1}}$ and $\psi_{n_2l_2m_{l_2}}$ are the radial HO wave functions as introduced in Eq. (12).

Similar to the Eq. (13), we apply the Talmi-Moshinsky brackets $\langle|\rangle_{\rm SMB}$ [27] to transform Eq. (34) to relative and c.m. radial coordinates to obtain

$$\mathcal{M}^\mu_a = \sum_{LM_L} \sum_{\substack{nlm_l \\ N\Lambda M_\Lambda}} \int d\vec{r}_{12} \int d\vec{R}_{12} e^{-i\vec{P}_{12}\cdot\vec{R}_{12}} e^{-i\vec{k}^-\cdot\vec{r}_{12}} \mathcal{F}^\dagger_{\rm FSI}(\vec{R}_{12}+\frac{\vec{r}_{12}}{2},\vec{R}_{12}-\frac{\vec{r}_{12}}{2}) \psi_{nlm_l}(\frac{\vec{r}_{12}}{\sqrt{2}}) \psi_{N\Lambda M_\Lambda}(\sqrt{2}\vec{R}_{12}) \times \langle l_1m_{l_1}l_2m_{l_2} \mid LM_L\rangle\langle lm_l\Lambda M_\Lambda \mid LM_L\rangle\langle nlN\Lambda; L \mid n_1l_1n_2l_2; L\rangle_{\rm SMB} \times \langle s_1t_1, s_2t_2 \mid \Gamma^\mu_{\gamma^\star N}(\vec{x}_1)\,\hat{\imath}\,(\vec{x}_1,\vec{x}_2) \mid \sigma_1\tau_1,\sigma_2\tau_2\rangle\,, \quad (35)$$

where $\vec{P}_{12} = \vec{p}_1 + \vec{p}_2 - \vec{q}$, $\vec{k}^\mp = \frac{\vec{p}_1-\vec{p}_2}{2} \mp \frac{\vec{q}}{2}$.

In Eq. (35) the sum over the relative quantum numbers is dominated by $(nl = 00)$. This is based on the observation that typical correlation operators act over relatively short internucleon distances and mostly affect the $(nl = 00)$ components of the ψ_{nlm_l} wave functions. For a more detailed explanation we refer to the discussion of Fig. 1 in Sect. II and Refs. [20, 21].

For close-proximity nucleons one can set $\vec{r}_{12} \approx \vec{0}$ in the FSI operator:

$$\mathcal{F}_{\rm FSI}(\vec{r}_1,\vec{r}_2) = \mathcal{F}_{\rm FSI}(\vec{R}_{12}+\frac{\vec{r}_{12}}{2},\vec{R}_{12}-\frac{\vec{r}_{12}}{2}) \approx \mathcal{F}_{\rm FSI}(\vec{R}_{12},\vec{R}_{12})\,. \quad (36)$$

This approximation amounts to computing the effect of FSIs as if the the two nucleons are brought into the continuum at the same spatial point (determined by the c.m. coordinate of the pair), which is very reasonable for close-proximity nucleons. With the above assumptions one arrives at the expression for the matrix element

$$\mathcal{M}^\mu_a \approx \langle s_1t_1, s_2t_2 \mid \widehat{\Gamma}^\mu_{\gamma^\star N}(\vec{k}^-) \mid \sigma_1\tau_1,\sigma_2\tau_2\rangle \times \sum_{N\Lambda M_\Lambda} \langle l_1m_{l_1}l_2m_{l_2} \mid \Lambda M_\Lambda\rangle\langle 00N\Lambda; \Lambda \mid n_1l_1n_2l_2; \Lambda\rangle_{\rm SMB} \times \int d\vec{R}_{12} e^{-i\vec{P}_{12}\cdot\vec{R}_{12}} \mathcal{F}^\dagger_{\rm FSI}(\vec{R}_{12},\vec{R}_{12}) \psi_{N\Lambda M_\Lambda}(\sqrt{2}\vec{R}_{12})\,,$$

with

$$\widehat{\Gamma}^{\mu}_{\gamma^\star N}(\vec{p}) \equiv \int d\vec{r}_{12} e^{-i\vec{p}\cdot\vec{r}_{12}} \psi_{000}(\frac{\vec{r}_{12}}{\sqrt{2}}) \Gamma^{\mu}_{\gamma^\star N}(\vec{x}_1) \hat{\lambda}(\vec{x}_1, \vec{x}_2)\,. \tag{37}$$

In deriving the Eq. (37), we have separated the integration over the spatial and spin-isospin d.o.f.. In addition, use has been made of the fact that the operator $\hat{\lambda}(\vec{x}_1, \vec{x}_2)$ of Eq. (21) does not depend on the c.m. coordinate $\vec{R}_{12}$. The most striking feature of Eq. (37) is the factorization of the amplitude in a term connected to the c.m. motion of the initial pair and a term which contains the full complexity of the photon-nucleon coupling to a correlated pair.

After summing the four terms that contribute to Eq. (32) and squaring the matrix element, the eightfold differential cross section factorizes according to

$$d^8\sigma(e, e'NN) = K_{eNN}\sigma_{e2N} F^{D}_{n_1 l_1, n_2 l_2}(\vec{P}_{12}), \tag{38}$$

with K_{eNN} a kinematic factor. Further, the off-shell electron-two-nucleon cross section is given by

$$\sigma_{e2N} \propto L_{\mu\nu} \sum_{\substack{s_1 s_2 \sigma_1 \sigma_2 \\ \tau_1 \tau_2}} J^{\mu} \left(J^{\nu}\right)^{\dagger}\,, \tag{39}$$

with $L_{\mu\nu}$ the leptonic tensor and J^{μ} the hadronic current given by

$$\begin{aligned} J^{\mu} = &\langle s_1 t_1, s_2 t_2 \mid \widehat{\Gamma}^{\mu}_{\gamma^\star N}(\vec{k}^{-}) \mid \sigma_1\tau_1, \sigma_2\tau_2\rangle \\ &- \langle s_2 t_2, s_1 t_1 \mid \widehat{\Gamma}^{\mu}_{\gamma^\star N}(\vec{k}^{+}) \mid \sigma_1\tau_1, \sigma_2\tau_2\rangle \\ &+ \langle s_1 t_1, s_2 t_2 \mid \widehat{\Gamma}^{\mu}_{\gamma^\star N}(\vec{k}^{+}) \mid \sigma_1\tau_1, \sigma_2\tau_2\rangle \\ &- \langle s_2 t_2, s_1 t_1 \mid \widehat{\Gamma}^{\mu}_{\gamma^\star N}(\vec{k}^{-}) \mid \sigma_1\tau_1, \sigma_2\tau_2\rangle\,. \end{aligned} \tag{40}$$

The factorization function $F^{D}_{n_1 l_1, n_2 l_2}(\vec{P}_{12})$ in Eq. (38) can be associated with the distorted c.m. momentum distribution of pairs in a relative $(nl = 00)$ state of the nucleus A

$$\begin{aligned} F^{D}_{n_1 l_1, n_2 l_2}(\vec{P}_{12}) = 4 \sum_{m_{l_1} m_{l_2}} \Big| \sum_{N\Lambda M_\Lambda} \int d\vec{R}_{12} e^{-i\vec{P}_{12}\cdot\vec{R}_{12}} \langle l_1 m_{l_1} l_2 m_{l_2} \mid \Lambda M_\Lambda\rangle \langle n_1 l_1 n_2 l_2; \Lambda \mid 00 N\Lambda; \Lambda\rangle_{\rm SMB} \\ \times \mathcal{F}^{\dagger}_{\rm FSI}(\vec{R}_{12}, \vec{R}_{12}) \psi_{N\Lambda M_\Lambda}(\sqrt{2}\vec{R}_{12}) \Big|^2\,, \end{aligned} \tag{41}$$

where the factor 4 accounts for the spin degeneracy of the HO states.

In the limit of vanishing FSIs ($\mathcal{F}_{\rm FSI} \equiv 1$), one has

$$P_2(P_{12}|nl = 00) = \frac{1}{A(A-1)} \frac{3}{(2\pi)^3} \sum_{n_\alpha l_\alpha n_\beta l_\beta} \int d\Omega_{P_{12}} F^{D}_{n_\alpha l_\alpha, n_\beta l_\beta}(\vec{P}_{12})\,. \tag{42}$$

This establishes a connection between the $A(e, e'NN)$ factorization function and the contribution of pairs with quantum numbers $(n_1 l_1 n_2 l_2)$ to $P_2(P_{12}|nl = 00)$, illustrated for pp pairs in ^{12}C in Fig. 6.

In the naive IPM, each two-hole (2h) state $(n_1 l_1)^{-1}(n_2 l_2)^{-1}$ can be associated with a sharp excitation energy in the $A-2$ system. In reality, the 2h strength corresponding with $(n_1 l_1)^{-1}(n_2 l_2)^{-1}$ extends over a wide energy range [38]. Current $A(e, e'pN)$ measurements are performed at Q^2-values of the order of GeV^2 not allowing one to measure cross sections for real exclusive processes as could be done at lower Q^2 values [26, 39, 40]. Accordingly, rather than probing the individual 2h contributions to P_2, the measured semi-inclusive $A(e, e'pN)$ cross sections can be linked to the $P_2(P_{12} \mid nl = 00)$ which involves a summation over the 2h states. From Fig. 6 it can be appreciated that in high-resolution $A(e, e'pN)$ measurements the c.m. distribution depends on the two-hole structure of the discrete final A-2 state [38, 39].

The $A(e, e'p)$ reaction allows one to access the $P_1(\vec{k}_m, E_m)$ modulo corrections from FSIs. It is worth stressing that there is no simple analogy for the $A(e, e'pN)$ reaction and that a direct connection with the two-body spectral function $P_2(\vec{P}_{12}, \vec{k}_{12}, E_{2m})$ is by no means evident, if not impossible.

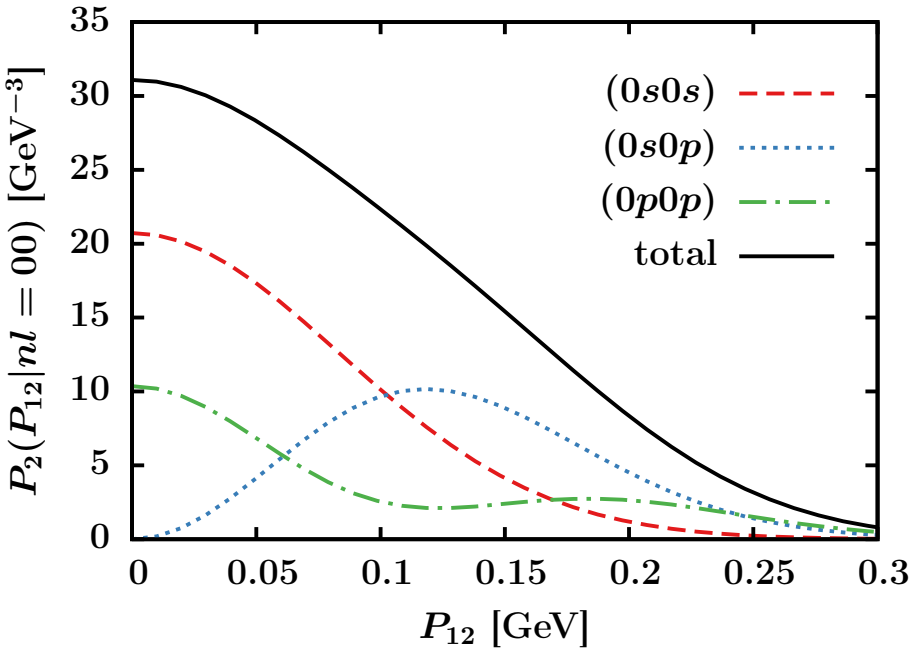

FIG. 6. (Color online) The contribution of the different shell-model pair combinations to the $P_2\,(P_{12}|nl = 00)$ for pp pairs in ^{12}C.

IV. MONTE CARLO SIMULATIONS

In this section, we investigate the implications of the proposed factorization of Eq. (38) for the $A(e, e'pp)$ opening-angle and c.m. distributions accessible in typical measurements. We present Monte Carlo simulations for $A(e, e'pp)$ building on the expression (38) suggesting that the magnitude of the cross section is proportional to $P_2(P_{12}|nl = 00)$. In this section the effects of FSIs are neglected. Its impact will be the subject of Sect. V.

The data-mining effort at CLAS in Jlab [41, 42] is analyzing exclusive $(e, e'pN)$ for ^{12}C, ^{27}Al, ^{56}Fe, and ^{208}Pb for a 5.014 GeV unpolarized electron beam [41]. In order to guarantee the exclusive character of the events, cuts are applied to the leading proton: $0.62 < \frac{|\vec{p}_1|}{|\vec{q}|} < 0.96$, $\theta_{\vec{p}_1,\vec{q}} < 25°$ and $k_1 > 300\,\mathrm{MeV}$. To increase the sensitivity to SRC-driven processes one imposes the kinematic constraints $x_B = \frac{Q^2}{2M_N\omega} > 1.2$ and $Q^2 > 1.4\ \mathrm{GeV}^2$. We have performed $(e, e'pp)$ simulations for all 4 target nuclei. The electron kinematics are drawn from the measured $x_B - Q^2$ distributions. We then generate two protons from the phase space by adoping a reaction picture of the type (31) whereby we assume that one nucleon absorbs the virtual photon. This results in a fast leading proton $p_1(E_1, \vec{p}_1 = \vec{k}_1 + \vec{q})$ and a recoil proton $p_2(E_2, \vec{p}_2 = \vec{k}_2)$, where $\vec{k}_1$ and $\vec{k}_2$ are the initial proton momenta. The initial c.m. momentum $\vec{P}_{12} = \vec{k}_1 + \vec{k}_2$ is drawn from the computed HO pp pair c.m. momentum distribution $P_2(P_{12}|nl = 00)$ of Table I. We choose $\vec{k}_1$ along the z-axis and $\vec{q}$ in the xz plane. The recoil $A-2$ nucleus can have excitation energies between 0 and 80 MeV. All $A(e, e'pp)$ results of this section are obtained for 10^5 events which comply with the kinematic cuts.

First, we investigate in how far the factorization function can be addressed after applying kinematic cuts. This can be done by comparing the input and extracted pp c.m. distributions. Fig. 7 shows the extracted c.m. distribution from the simulated ^{12}C$(e, e'pp)$ events. The kinematic cuts have a narrowing effect (less than 10 %) on the distributions along the x- and y-axis. In addition, one observes a shift of roughly 100 MeV and an increase in the non-Gaussianity of the c.m. distribution along the z-axis. Similar observations have been made for the other three target nuclei.

We now address the issue whether the extracted c.m. distributions can provide information about the relative quantum numbers of the pairs. To this end, we have performed simulations starting from the assumption that the $(e, e'pp)$ cross section factorizes with $P_2(P_{12}|nl)$ for various nl combinations. The results of the simulations are summarized in Table II. The narrowing effect attributed to the kinematic cuts is less significant for $l > 0$ pairs. Photon absorption on $l = 0$ and $l = 1$ pairs leads to differences in the extracted widths of the c.m. momentum distributions of the order of 20 MeV, which leads us to conclude that high-accuracy $A(e, e'pp)$ experiments could indeed provide information about the relative

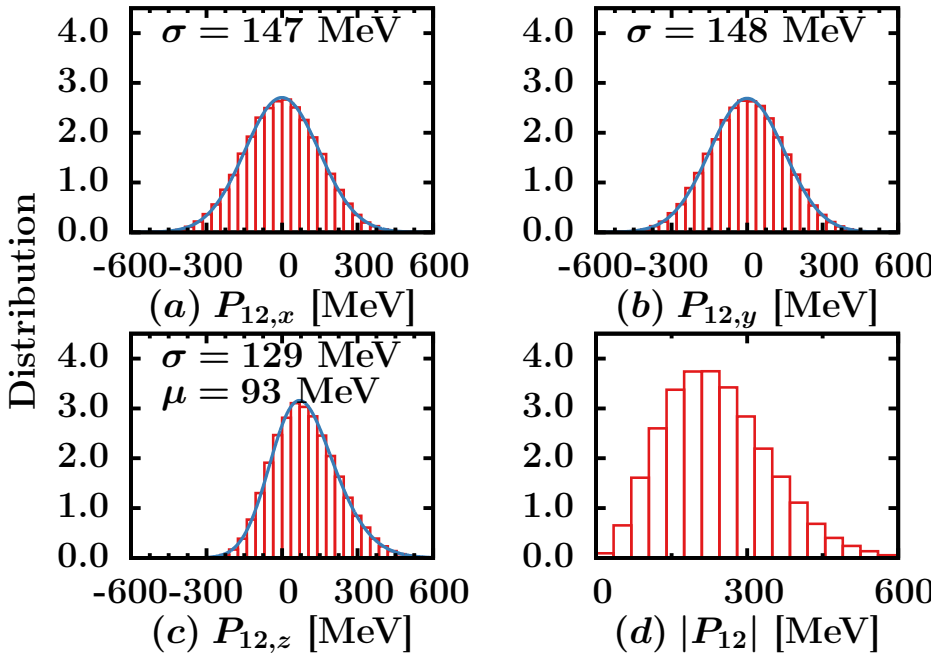

FIG. 7. (Color online) Total (bottom right) and directional pp c.m. distributions extracted from the ^{12}C$(e,e'pp)$ simulations in the CLAS kinematics described in the text. The blue solid line is a fit with a skew normal distribution.

	$nl=00$	$l=0$	$l=1$	$l=2$	all l
$\sigma_x^i(MeV)$	156	154	135	121	140
$\sigma_x^f(MeV)$	147	145	130	118	134

TABLE II. The width of the c.m. distribution along the x-axis for pp pairs with different relative orbital momentum l. σ_x^i is the width used as input parameter in the ^{12}C$(e,e'pp)$ simulations. The σ_x^f is the width extracted after the simulation.

orbital angular momentum of the correlated pairs.

Fig. 8 shows the simulated opening-angle (γ) distributions of the initial-state protons for all four target nuclei considered. The A$(e,e'pp)$ simulations starting from the computed $P_2(P_{12}|nl=00)$ and $P_2(P_{12})$ provide very similar backwardly peaked $\cos\gamma$ distributions. The peak is not due to the kinematic cuts as a uniform c.m. momentum distributions gives rise to a flat $\cos\gamma$ distribution. The shape of the simulated $\cos\gamma$ distributions is hardly target-mass dependent. The peak at 180 degrees in the $\cos\gamma$ distributions conforms with the picture of correlated nucleons moving back to back with high relative and low c.m. momentum.

We now turn our attention to an ^{12}C$(e,e'pp)$ measurement probing a restricted part of phase space. The JLab Hall-A ^{12}C$(e,e'pp)$ experiment of Refs. [3, 4], used an incident electron beam of 4.672 GeV and three spectrometers. We consider the kinematic settings with $\omega = 0.865$ GeV, $Q^2 = 2$ GeV^2, $x_B = 1.2$ and a median missing momentum $p_m = 0.55$ GeV. Figure 9 shows the shapes of the simulated and measured $\cos\gamma$ simulations. The proposed factorization for the $A(e,e'pp)$ cross section accounts for the shape of the measured $\cos\gamma$ distribution. We stress that the computed pair c.m. distributions (Table I) are the sole input to the simulations.

V. FINAL STATE INTERACTIONS

In this section the impact of FSIs on the proposed factorization function of Eq. (38) is investigated. In order to keep computing times reasonable we limit ourselves to some particular kinematic cases and introduce an additional approximation. We start from Eq. (41) for the distorted momentum distribution $F^D_{n_1l_1,n_2l_2}(\vec{P}_{12})$ and apply the zero-range approximation [36, 43] which amounts to setting $\psi_{\alpha_1}(\vec{r}_1)\psi_{\alpha_2}(\vec{r}_2) \approx$

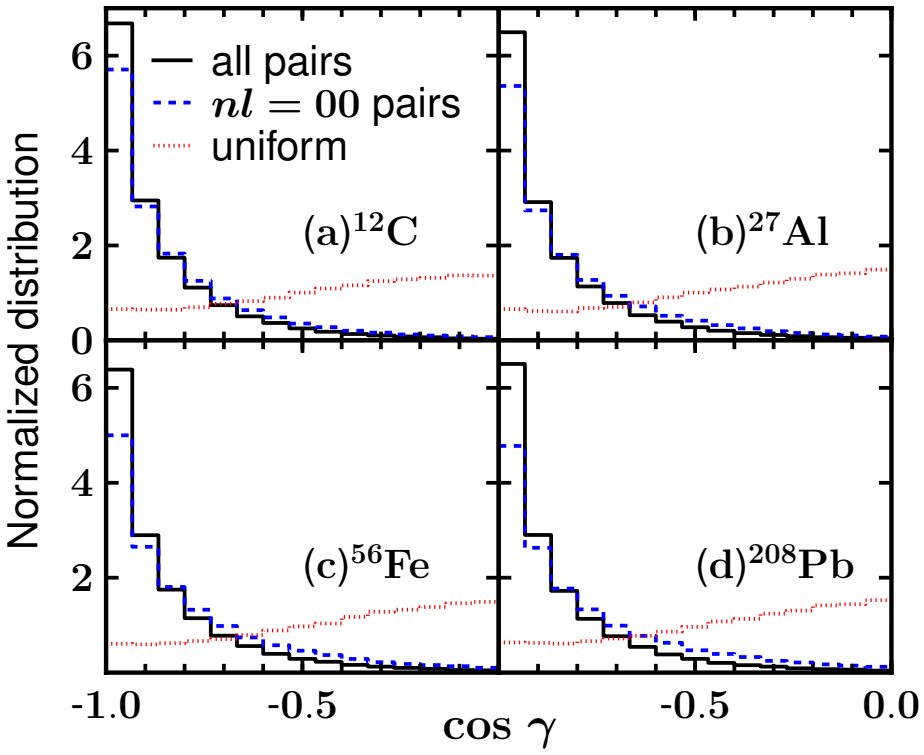

FIG. 8. (Color online) The opening angle distribution of the simulated A$(e, e'pp)$ events in the kinematics described in the text. The black solid, blue dashed and red dotted line is for a reaction picture with an $(e, e'pp)$ cross section proportional to $P_2(P_{12})$, to $P_2(P_{12}|nl = 00)$, and to a uniform pair c.m. distribution.

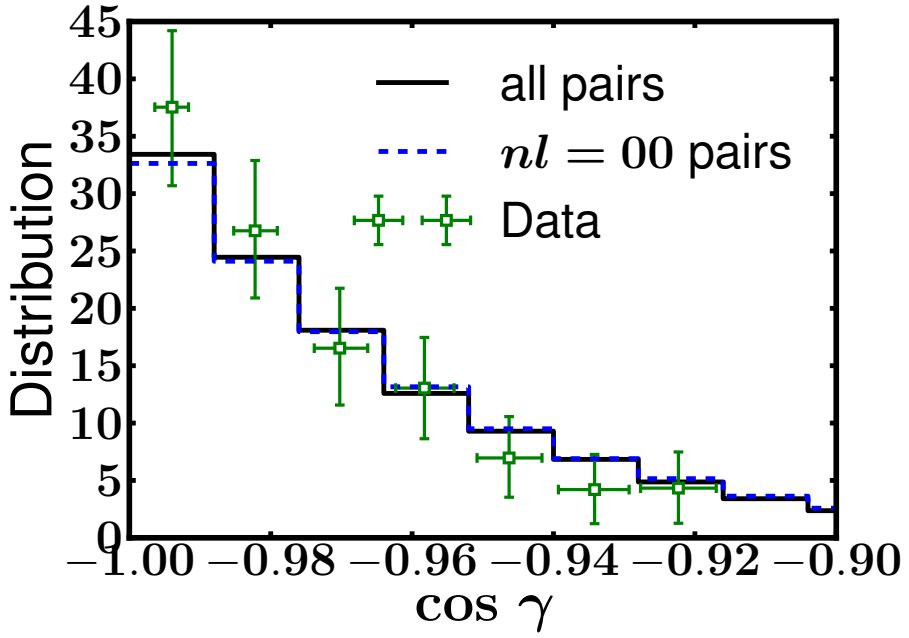

FIG. 9. (Color online) The opening angle distribution of the ^{12}C$(e, e'pp)$ reaction in the kinematics of Ref. [3]. Curve notations of Fig. 8 are used.

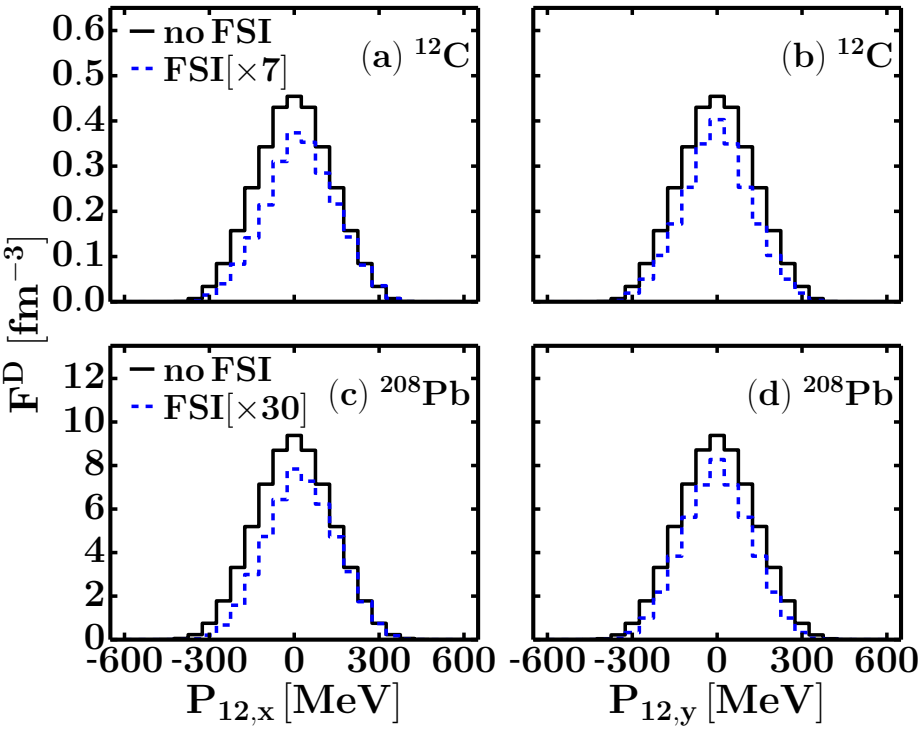

FIG. 10. (Color online) The two-body c.m. momentum distribution for ^{12}C$(e,e'pp)$ (top) and ^{208}Pb$(e,e'pp)$ (bottom) with (RMSGA) and without (no-FSI) inclusion of FSIs. We consider the kinematics $|\vec{q}| = 1.4$ GeV, $|\vec{p}_1| = 0.82|\vec{q}|$ and $\theta_{\vec{p}_1,\vec{q}} = 10^\circ$. The FSI results have been multiplied by a factor of 7 for ^{12}C$(e,e'pp)$ and by a factor of 30 for ^{208}Pb$(e,e'pp)$.

$\psi_{\alpha_1}(\vec{R}_{12})\psi_{\alpha_2}(\vec{R}_{12})$ in Eq. (34). Consequently, we can write

$$F^D_{n_1l_1,n_2l_2}(\vec{P}_{12}) = 4\sum_{m_{l_1}m_{l_2}}\left|\int d\vec{R}_{12}e^{-i\vec{P}_{12}\cdot\vec{R}_{12}}\mathcal{F}^\dagger_{\rm FSI}(\vec{R}_{12},\vec{R}_{12})\psi_{n_1l_1m_{l_1}}(\vec{R}_{12})\psi_{n_2l_2m_{l_2}}(\vec{R}_{12})\right|^2. \quad (43)$$

It is possible to derive a relativized version of this expression [43]

$$F^D_{n_1\kappa_1,n_2\kappa_2}(\vec{P}_{12}) = \sum_{s_1,s_2,m_1,m_2}\left|\int d\vec{R}_{12}\, e^{i\vec{P}_{12}\cdot\vec{R}_{12}}\bar{u}(\vec{k}_1,s_1)\psi_{n_1\kappa_1m_1}(\vec{R}_{12})\bar{u}(\vec{k}_2,s_2)\psi_{n_2\kappa_2m_2}(\vec{R}_{12})\mathcal{F}_{\rm FSI}(\vec{R}_{12},\vec{R}_{12})\right|^2. \quad (44)$$

Here, $u(\vec{k},s)$ are positive-energy Dirac spinors and $\psi_{n\kappa m}$ are relativistic mean-field wave functions [44] with quantum numbers $(n, j = |\kappa|/2, m)$. We neglect the projections on the lower components of the plane-wave Dirac spinors. The FSIs of the ejected pair with the remaining $A-2$ spectators, encoded in $\mathcal{F}_{\rm FSI}$, can be computed in a relativistic multiple-scattering Glauber approximation (RMSGA) [45, 46]. As the c.m. momentum is conserved in interactions among the two ejected nucleons, we discard those. This approximation does not affect the shape of $F^D_{n_1\kappa_1,n_2\kappa_2}(\vec{P}_{12})$.

We include FSIs for the JLab data mining kinematics considered in Sec. IV. We have computed the distorted c.m. momentum distribution of Eq. (44) for the kinematics that yields the most events in the simulations of Sec. IV: $|\vec{q}| = 1.4$ GeV, $|\vec{p}_1| = 0.82|\vec{q}|, \theta_{\vec{p}_1,\vec{q}} = 10^\circ$. As in Sec. IV, $\vec{k}_1$ lies along the z-axis and the $\vec{q}$ is located in the xz plane. The results of the FSI calculations are summarized in Figs. 10 and 11.

In Fig. 10 we compare the RMSGA c.m. momentum distributions $F^D(\vec{P}_{12,x}) = \sum_{n_1\kappa_1,n_2\kappa_2} F^D_{n_1\kappa_1,n_2\kappa_2}(\vec{P}_{12,x})$ and $F^D(\vec{P}_{12,y})$ with their respective plane-wave (no-FSI) limit. First, the FSIs are responsible for a substantial reduction of the cross sections: a factor of about 7 for carbon and about 30 in lead. The effects of FSIs on the shape of $F^D(\vec{P}_{12})$, however, are rather modest. Gaussian fits to the $F^D(\vec{P}_{12,i=x,y})$ result in widths which are less than 10% smaller than in the plane-wave limit. The effects of FSIs on the shape of

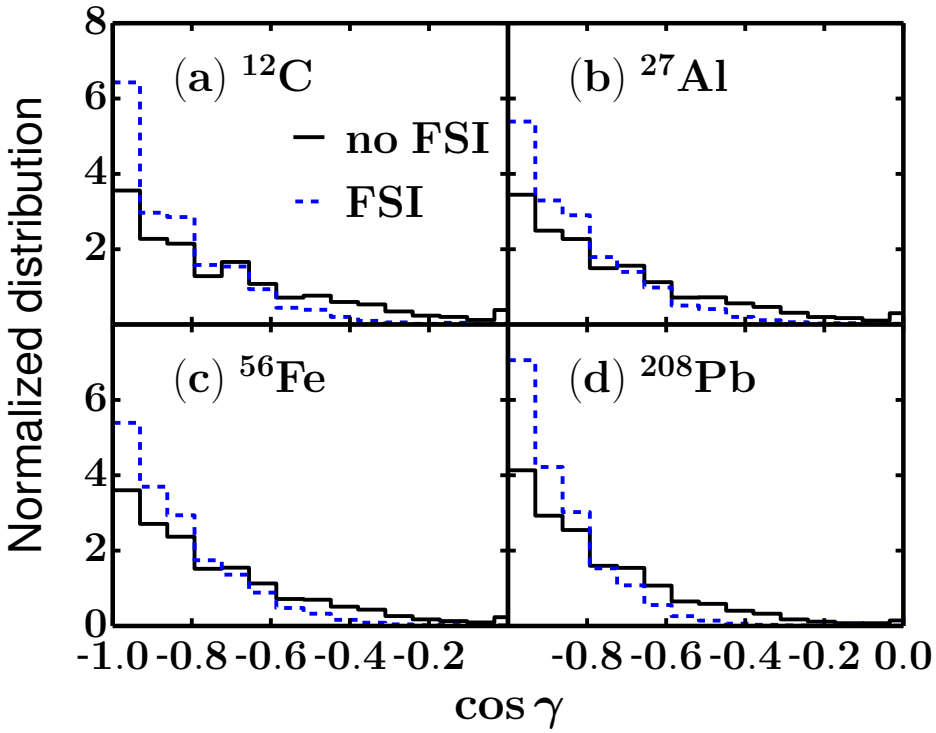

FIG. 11. (Color online) The normalized opening angle distributions for A$(e, e'pp)$ for ^{12}C, ^{27}Al, ^{56}Fe and ^{208}Pb in the kinematics of Fig. 10.

the c.m. distributions in Fig. 10 can be qualitatively understood considering that the nucleons undergoing FSIs are slowed down on average: $(\vec{p}_1, \vec{p}_2) \xrightarrow{\text{FSI}} \zeta\,(\vec{p}_1, \vec{p}_2)$ with $0 < \zeta \leq 1$. It is straightforward to show that for the adopted conventions this results in $P_{12,x} \to \zeta P_{12,x} - (1-\zeta)p_{1,x}$, and $P_{12,y} \to \zeta P_{12,y}$. This explains the observed contraction and shift to the right in the $P_{12,x}$ distribution, and the contraction of the $P_{12,y}$ distributions.

The effect of FSIs on the shape of the normalized opening angle distributions is studied in Fig. 11 for four target nuclei. It is clear that they become even more forwardly peaked after including FSIs.

VI. SUMMARY

Summarizing, we have shown that in the plane-wave limit the factorization function for the exclusive SRC-driven $A(e, e'pN)$ reaction is the conditional c.m. distribution $P_2(P_{12}|nl = 00)$ for pN pairs in a nodeless relative state with a vanishing orbital momentum. We have illustrated that in a two-body cluster expansion the correlated part of the momentum distribution originates mainly from correlation operators acting on IPM pairs with $(nl = 00)$ quantum numbers, supporting the assumptions underlying the proposed factorization of the $A(e, e'pN)$ reaction. Numerical calculations indicate that the $P_2(P_{12}|nl = 00)$ has a wider distribution than the unconditional $P_2(P_{12})$ one. An important implication of the proposed factorization is that the mass dependence of the $A(e, e'pp)$ and $A(e, e'pn)$ cross section is predicted to be much softer than $\frac{Z(Z-1)}{2}$ and NZ respectively.

We have examined the robustness of the proposed factorization of the two-nucleon knockout cross sections against kinematic cuts and FSIs. Both mechanisms modestly affect the shape of the c.m. distributions which leads us to conclude that they can be accessed in $A(e, e'pN)$ measurements. The FSIs bring about a mass-dependent reduction of the cross sections which is of the order of 10 for carbon and 30 for lead.

ACKNOWLEDGMENTS

The authors wish to thank Or Hen, Eli Piasetzky, and Larry Weinstein for stimulating discussions and suggestions. This work is supported by the Research Foundation Flanders (FWO-Flanders) and by the

Interuniversity Attraction Poles Programme P7/12 initiated by the Belgian Science Policy Office. The computational resources (Stevin Supercomputer Infrastructure) and services used in this work were provided by Ghent University, the Hercules Foundation and the Flemish Government.

[1] A. Tang, J. W. Watson, J. Aclander, J. Alster, G. Asryan, Y. Averichev, D. Barton, V. Baturin, N. Bukhtoyarova, A. Carroll, et al., Phys. Rev. Lett. **90**, 042301 (2003).
[2] R. A. Niyazov, L. B. Weinstein, G. Adams, P. Ambrozewicz, E. Anciant, M. Anghinolfi, B. Asavapibhop, G. Asryan, G. Audit, T. Auger, et al. (CLAS Collaboration), Phys. Rev. Lett. **92**, 052303 (2004).
[3] R. Shneor, P. Monaghan, R. Subedi, B. D. Anderson, K. Aniol, J. Annand, J. Arrington, H. Benaoum, F. Benmokhtar, P. Bertin, et al. (Jefferson Lab Hall A Collaboration), Phys. Rev. Lett. **99**, 072501 (2007).
[4] R. Subedi, R. Shneor, P. Monaghan, B. Anderson, K. Aniol, J. Annand, J. Arrington, H. Benaoum, F. Benmokhtar, W. Boeglin, et al., Science **320**, 1476 (2008).
[5] K. S. Egiyan, N. Dashyan, M. Sargsian, S. Stepanyan, L. B. Weinstein, G. Adams, P. Ambrozewicz, E. Anciant, M. Anghinolfi, B. Asavapibhop, et al. (CLAS Collaboration), Phys. Rev. C **68**, 014313 (2003).
[6] K. S. Egiyan, N. B. Dashyan, M. M. Sargsian, M. I. Strikman, L. B. Weinstein, G. Adams, P. Ambrozewicz, M. Anghinolfi, B. Asavapibhop, G. Asryan, et al. (CLAS Collaboration), Phys. Rev. Lett. **96**, 082501 (2006).
[7] N. Fomin, J. Arrington, R. Asaturyan, F. Benmokhtar, W. Boeglin, P. Bosted, A. Bruell, M. H. S. Bukhari, M. E. Christy, E. Chudakov, et al., Phys. Rev. Lett. **108**, 092502 (2012).
[8] R. Schiavilla, R. B. Wiringa, S. C. Pieper, and J. Carlson, Phys. Rev. Lett. **98**, 132501 (2007).
[9] R. B. Wiringa, R. Schiavilla, S. C. Pieper, and J. Carlson, Phys. Rev. C **78**, 021001 (2008).
[10] H. Feldmeier, W. Horiuchi, T. Neff, and Y. Suzuki, Phys. Rev. C **84**, 054003 (2011).
[11] R. B. Wiringa, R. Schiavilla, S. C. Pieper, and J. Carlson, Phys. Rev. **C89**, 024305 (2014), URL {http://link.aps.org/doi/10.1103/PhysRevC.89.024305}.
[12] M. Alvioli, C. Ciofi degli Atti, and H. Morita, Phys. Rev. Lett. **100**, 162503 (2008).
[13] M. Alvioli, C. Ciofi degli Atti, L. P. Kaptari, C. B. Mezzetti, H. Morita, and S. Scopetta, Phys. Rev. C **85**, 021001 (2012).
[14] M. Alvioli, C. Ciofi degli Atti, L. P. Kaptari, C. B. Mezzetti, and H. Morita, Phys. Rev. C **87**, 034603 (2013).
[15] F. Arias de Saavedra, C. Bisconti, G. Co', and A. Fabrocini, Phys.Rept. **450**, 1 (2007).
[16] C. Bisconti, F. A. d. Saavedra, and G. Co', Phys. Rev. C **75**, 054302 (2007).
[17] S. Bogner and D. Roscher, Phys. Rev. **C86**, 064304 (2012).
[18] J. Arrington, D. Higinbotham, G. Rosner, and M. Sargsian, Prog. Part. Nucl. Phys. **67**, 898 (2012).
[19] L. Frankfurt, M. Sargsian, and M. Strikman, Int. J. Mod. Phys. **A23**, 2991 (2008).
[20] M. Vanhalst, W. Cosyn, and J. Ryckebusch, Phys. Rev. **C84**, 031302 (2011).
[21] M. Vanhalst, J. Ryckebusch, and W. Cosyn, Phys. Rev. **C86**, 044619 (2012).
[22] M. Vanhalst, J. Ryckebusch, and W. Cosyn (2012), 1210.6175.
[23] W. Cosyn, M. Vanhalst, and J. Ryckebusch (2013), 1308.5583.
[24] J. Arrington, A. Daniel, D. Day, N. Fomin, D. Gaskell, et al., Phys. Rev. **C86**, 065204 (2012).
[25] O. Benhar, Phys. Rev. **C87**, 024606 (2013).
[26] R. Starink, M. van Batenburg, E. Cisbani, W. Dickhoff, S. Frullani, F. Garibaldi, C. Giusti, D. Groep, P. Heimberg, W. Hesselink, et al., Phys.Lett. **B474**, 33 (2000).
[27] M. Moshinsky and Y. Smirnov, *The harmonic oscillator in modern physics* (Harwood Academic Publishers,Amsterdam, 1996).
[28] S. C. Pieper, R. B. Wiringa, and V. Pandharipande, Phys. Rev. C **46**, 1741 (1992).
[29] J. Engel, J. Carlson, and R. Wiringa, Phys. Rev. **C83**, 034317 (2011).
[30] R. Roth, T. Neff, and H. Feldmeier, Prog. Part. Nucl. Phys. **65**, 50 (2010).
[31] S. Janssen, J. Ryckebusch, W. Van Nespen, and D. Debruyne, Nucl. Phys. A **672**, 285 (2000).
[32] J. Ryckebusch, V. Van der Sluys, K. Heyde, H. Holvoet, W. Van Nespen, M. Waroquier, and M. Vanderhaegen, Nucl. Phys. A **624**, 581 (1997).
[33] C. Gearheart, Ph.D. thesis, Washington University, St. Louis (1994).
[34] J. Caballero, T. Donnelly, E. Moya de Guerra, and J. Udias, Nucl. Phys. **A632**, 323 (1998).
[35] L. L. Frankfurt and M. I. Strikman, Phys. Rept. **160**, 235 (1988).
[36] J. Ryckebusch, Phys. Lett. **B383**, 1 (1996).
[37] K. I. Blomqvist et al., Phys. Lett. **B421**, 71 (1998).
[38] C. Barbieri, C. Giusti, F. Pacati, and W. Dickhoff, Phys. Rev. **C70**, 014606 (2004).
[39] J. Ryckebusch and W. Van Nespen, Eur. Phys. J. **A20**, 435 (2004).
[40] D. Middleton, J. Annand, C. Barbieri, C. Giusti, P. Grabmayr, et al., Eur. Phys. J. **A43**, 137 (2010).
[41] L. Weinstein, S. Kuhn, et al., Short distance structure of nuclei: Mining the wealth of existing jefferson lab data, DOE Grant DE-SC0006801 (2009).
[42] O. Hen et al. (CLAS Collaboration), Phys. Lett. **B722**, 63 (2013).
[43] W. Cosyn and J. Ryckebusch, Phys. Rev. **C80**, 011602 (2009).
[44] R. J. Furnstahl, B. D. Serot, and H.-B. Tang, Nucl. Phys. **A615**, 441 (1997).

[45] J. Ryckebusch, D. Debruyne, P. Lava, S. Janssen, B. Van Overmeire, and T. Van Cauteren, Nucl. Phys. **A728**, 226 (2003).
[46] W. Cosyn and J. Ryckebusch, Phys. Rev. **C87**, 064608 (2013).

3.2.3 Supplementary material

Connecting the factorization function with the conditional pair c.m. momentum distribution

In Sec. **II** of Sec. 3.2.2 the conditional c.m. momentum distribution $P_2(P_{12}|nl = 00)$ is derived in the LCA. The single-particle wave functions are coupled to nucleon pairs described in function of their c.m. and relative coordinates. The c.m. momentum distribution $P_2(P_{12})$ of Eq. (8) is then calculated using the Fourier transform of the TBD ρ_2 of Eq. (4). Restricting the contributions to $P_2(P_{12})$ of the SRC pairs with relative quantum numbers $nl = 00$ gives the conditional c.m. momentum distribution $P_2(P_{12}|nl = 00)$ of Eq. (17).

In Sec. **III** the reaction model describing the two-nucleon knockout process is outlined. It is shown that the two-nucleon knockout cross section can be factorized into c.m. and relative momentum of the initial nucleon pair. The factor containing the c.m. momentum $\vec{P}_{12}$ is denoted the factorization function $F^D(\vec{P}_{12})_{n_1l_1,n_2l_2}$ (Eq. (41)).

In the limit of vanishing FSI, the factorization function F^D and the conditional c.m. momentum distribution can be connected, their relation is given by Eq. (42) and reads,

$$P_2(P_{12}|nl = 00) = \frac{1}{A(A-1)} \frac{3}{(2\pi)^3} \sum_{n_\alpha l_\alpha n_\beta l_\beta} \int d\Omega_{P_{12}} F^D_{n_\alpha l_\alpha, n_\beta l_\beta}(\vec{P}_{12}) \,. \tag{3.3}$$

This relation is proven by starting from the left and right hand side and connecting them midway.

The conditional c.m. momentum probability distribution $P_2(P_{12}|nl = 00)$ as defined by Eqs. (15) and (17) of Sec. 3.2 reads,

$$P_2(P_{12}|nl = 00) = \frac{2}{\pi} \sum_{nlm_l} \sum_{\Lambda M_\Lambda} \delta_{n\,0}\delta_{l\,0} P_2^{nlm_l\Lambda M_\Lambda}(P_{12}) = \frac{2}{\pi} \sum_{\Lambda M_\Lambda} P_2^{000\Lambda M_\Lambda}(P_{12}) \,,$$

with,

$$P_2^{000\Lambda M_\Lambda}(P_{12}) = \frac{2}{A(A-1)} \sum_{\alpha<\beta} \sum_{NN'} \sum_{SM_STM_T} \left(C_{\alpha\beta}^{000N'\Lambda M_\Lambda SM_STM_T} \right)^\dagger C_{\alpha\beta}^{000N\Lambda M_\Lambda SM_STM_T}$$
$$\int \mathrm{d}R'_{12} R'^2_{12} \int \mathrm{d}R_{12} R^2_{12} j_\Lambda(P_{12}R'_{12}) j_\Lambda(P_{12}R_{12}) R_{N'\Lambda}(\sqrt{2}R'_{12}) R_{N\Lambda}(\sqrt{2}R_{12}) \,, \tag{3.4}$$

and

$$C_{\alpha\beta}^{000N\Lambda M_\Lambda SM_STM_T} = \frac{1}{\sqrt{2}} \left[1 - (-1)^{S+T}\right] \langle \frac{1}{2} t_\alpha \frac{1}{2} t_\beta | TM_T \rangle \langle \frac{1}{2} \sigma_\alpha \frac{1}{2} \sigma_\beta | SM_S \rangle$$
$$\sum_{LM_L} \langle l_\alpha m_{l_\alpha} l_\beta m_{l_\beta} | LM_L \rangle \langle 00N\Lambda; L | n_\alpha l_\alpha n_\beta l_\beta; L \rangle_{\mathrm{SMB}} \underbrace{\langle LM_L | 00\Lambda M_\Lambda \rangle}_{\delta_{LM_L,\Lambda M_\Lambda}} \,.$$

The summation over spin S, M_S and isospin T, M_T of Eq. (3.4) is performed first. The spin

and isospin quantum numbers only appear in the coefficients $C_{\alpha\beta}$.

$$\sum_{SM_STM_T} \left(C_{\alpha\beta}^{000N'\Lambda M_\Lambda SM_STM_T}\right)^\dagger C_{\alpha\beta}^{000N\Lambda M_\Lambda SM_STM_T} =$$
$$\frac{1}{2}\sum_{ST}\left[1-(-1)^{S+T}\right]^2 \sum_{M_T}\left|\langle\frac{1}{2}t_\alpha\frac{1}{2}t_\beta|TM_T\rangle\right|^2 \sum_{M_S}\left|\langle\frac{1}{2}\sigma_\alpha\frac{1}{2}\sigma_\beta|SM_S\rangle\right|^2$$
$$\left|\langle l_\alpha m_{l_\alpha} l_\beta m_{l_\beta}|\Lambda M_\Lambda\rangle\right|^2 \langle 00N'\Lambda;\Lambda|n_\alpha l_\alpha n_\beta l_\beta;\Lambda\rangle^*_{\mathrm{SMB}}\langle 00N\Lambda;\Lambda|n_\alpha l_\alpha n_\beta l_\beta;\Lambda\rangle_{\mathrm{SMB}}\,. \quad (3.5)$$

The following summation over spin and isospin appearing in Eq. (3.5) can be simplified,

$$\sum_{ST}\left[1-(-1)^{S+T}\right]^2 \sum_{M_T}\left|\langle\frac{1}{2}t_\alpha\frac{1}{2}t_\beta|TM_T\rangle\right|^2 \sum_{M_S}\left|\langle\frac{1}{2}\sigma_\alpha\frac{1}{2}\sigma_\beta|SM_S\rangle\right|^2 .$$

As we are dealing with two nucleons we have $S,T\in\{0,1\}$. Only the terms where S and T have opposite even-odd parity survive, that is $S=0,T=1$ and $S=1,T=0$,

$$\sum_{ST}\left[1-(-1)^{S+T}\right]^2 \sum_{M_T}\left|\langle\frac{1}{2}t_\alpha\frac{1}{2}t_\beta|TM_T\rangle\right|^2 \sum_{M_S}\left|\langle\frac{1}{2}\sigma_\alpha\frac{1}{2}\sigma_\beta|SM_S\rangle\right|^2$$
$$= 4\left|\langle\frac{1}{2}t_\alpha\frac{1}{2}t_\beta|00\rangle\right|^2 \sum_{M_S=-1}^{1}\left|\langle\frac{1}{2}\sigma_\alpha\frac{1}{2}\sigma_\beta|1M_S\rangle\right|^2 + 4\left|\langle\frac{1}{2}\sigma_\alpha\frac{1}{2}\sigma_\beta|00\rangle\right|^2 \sum_{M_T=-1}^{1}\left|\langle\frac{1}{2}t_\alpha\frac{1}{2}t_\beta|1M_T\rangle\right|^2$$
$$= (1-\delta_{t_\alpha t_\beta})(1+\delta_{\sigma_\alpha\sigma_\beta}) + (1-\delta_{\sigma_\alpha\sigma_\beta})(1+\delta_{t_\alpha t_\beta}) = 2(1-\delta_{\sigma_\alpha\sigma_\beta}\delta_{t_\alpha t_\beta})\,.$$

Eq. (3.5) then reads,

$$\sum_{SM_STM_T}\left(C_{\alpha\beta}^{000N'\Lambda M_\Lambda SM_STM_T}\right)^\dagger C_{\alpha\beta}^{000N\Lambda M_\Lambda SM_STM_T} = (1-\delta_{\sigma_\alpha\sigma_\beta}\delta_{t_\alpha t_\beta})$$
$$\left|\langle l_\alpha m_{l_\alpha} l_\beta m_{l_\beta}|\Lambda M_\Lambda\rangle\right|^2 \langle 00N'\Lambda;\Lambda|n_\alpha l_\alpha n_\beta l_\beta;\Lambda\rangle^*_{\mathrm{SMB}}\langle 00N\Lambda;\Lambda|n_\alpha l_\alpha n_\beta l_\beta;\Lambda\rangle_{\mathrm{SMB}}\,. \quad (3.6)$$

With Eq. (3.4) and Eq. (3.5) the conditional c.m. momentum distribution of $P_2(P_{12}|nl=00)$ can be written as,

$$P_2(P_{12}|nl=00) = \frac{2}{\pi}\sum_{\Lambda M_\Lambda} P_2^{000\Lambda M_\Lambda}(P_{12})$$
$$= \frac{2}{A(A-1)}\frac{2}{\pi}\sum_{\Lambda M_\Lambda}\sum_{\alpha<\beta}\sum_{NN'}(1-\delta_{\sigma_\alpha,\sigma_\beta}\delta_{t_\alpha,t_\beta})\left|\langle l_\alpha m_{l_\alpha} l_\beta m_{l_\beta}|\Lambda M_\Lambda\rangle\right|^2$$
$$\langle 00N'\Lambda;\Lambda|n_\alpha l_\alpha n_\beta l_\beta;\Lambda\rangle^*_{\mathrm{SMB}}\langle 00N\Lambda;\Lambda|n_\alpha l_\alpha n_\beta l_\beta;\Lambda\rangle_{\mathrm{SMB}}$$
$$\int \mathrm{d}R'_{12}R'^2_{12}\int \mathrm{d}R_{12}R^2_{12}j_\Lambda(P_{12}R'_{12})j_\Lambda(P_{12}R_{12})R_{N'\Lambda}(\sqrt{2}R'_{12})R_{N\Lambda}(\sqrt{2}R_{12})\,. \quad (3.7)$$

This expression is invariant under the interchange $\alpha\leftrightarrow\beta$ allowing us to write the summation $\sum_{\alpha<\beta}$ as $\frac{1}{2}\sum_{\alpha\neq\beta}$. The factor $(1-\delta_{\sigma_\alpha,\sigma_\beta}\delta_{t_\alpha,t_\beta})$ ensures that the term with $\alpha=\beta$ is zero and the restriction $\alpha\neq\beta$ in the summation can be dropped. With

$$\sum_{\alpha,\beta}(1-\delta_{\sigma_\alpha,\sigma_\beta}\delta_{t_\alpha,t_\beta}) = \sum_{\substack{n_\alpha l_\alpha m_{l_\alpha}\\ n_\beta l_\beta m_{l_\beta}}}\sum_{\substack{\sigma_\alpha t_\alpha\\ \sigma_\beta t_\beta}}(1-\delta_{\sigma_\alpha,\sigma_\beta}\delta_{t_\alpha,t_\beta}) = 12\sum_{\substack{n_\alpha l_\alpha m_{l_\alpha}\\ n_\beta l_\beta m_{l_\beta}}},$$

Eq. (3.7) can be written as,

$$
\begin{aligned}
P_2(P_{12}|nl=00) &= \frac{2}{\pi}\sum_{\Lambda M_\Lambda} P_2^{000\Lambda M_\Lambda}(P_{12}) \\
&= \frac{12}{A(A-1)}\frac{2}{\pi}\sum_{n_\alpha l_\alpha, n_\beta l_\beta}\sum_{m_{l_\alpha}, m_{l_\beta}}\sum_{\Lambda M_\Lambda}\sum_{NN'}\left|\langle l_\alpha m_{l_\alpha} l_\beta m_{l_\beta}|\Lambda M_\Lambda\rangle\right|^2 \\
&\quad \langle 00N'\Lambda;\Lambda|n_\alpha l_\alpha n_\beta l_\beta;\Lambda\rangle^*_{\rm SMB}\langle 00N\Lambda;\Lambda|n_\alpha l_\alpha n_\beta l_\beta;\Lambda\rangle_{\rm SMB} \\
&\int {\rm d}R'_{12}R'^2_{12}\int {\rm d}R_{12}R^2_{12} j_\Lambda(P_{12}R'_{12}) j_\Lambda(P_{12}R_{12}) R_{N'\Lambda}(\sqrt{2}R'_{12}) R_{N\Lambda}(\sqrt{2}R_{12})\,. \quad (3.8)
\end{aligned}
$$

Starting from the right hand side of Eq. (3.3) the same expression is now derived, proving that identity. The factorization function of Eq. (41) with vanishing FSI ($\mathcal{F}_{\rm FSI}\equiv 1$) is given by,

$$
\begin{aligned}
F^D_{n_\alpha l_\alpha, n_\beta l_\beta}(\vec{P}_{12}) = 4\sum_{m_{l_\alpha}, m_{l_\beta}}\Big|\sum_{N\Lambda M_\Lambda}\int d\vec{R}_{12} e^{-i\vec{P}_{12}\cdot\vec{R}_{12}} \\
\langle l_\alpha m_{l_\alpha} l_\beta m_{l_\beta}|\Lambda M_\Lambda\rangle\,\langle n_\alpha l_\alpha n_\beta l_\beta;\Lambda|00N\Lambda;\Lambda\rangle_{\rm SMB}\,\psi_{N\Lambda M_\Lambda}(\sqrt{2}\vec{R}_{12})\Big|^2 .
\end{aligned}
$$

Expanding the exponential using the plane wave expansion,

$$
e^{i\vec{k}\cdot\vec{r}} = 4\pi\sum_{l,m_l} i^l j_l(kr) Y^*_{lm_l}(\Omega_k) Y_{lm_l}(\Omega_r)\,,
$$

and splitting the HO wave functions $\psi_{N\Lambda M_\Lambda}$ in their (real) radial $R_{N\Lambda}$ and angular $Y_{\Lambda M_\Lambda}$ part yields,

$$
\begin{aligned}
F^D_{n_\alpha l_\alpha, n_\beta l_\beta}(\vec{P}_{12}) = 4\sum_{m_{l_\alpha}, m_{l_\beta}}\Big|\sum_{N\Lambda M_\Lambda}\langle l_\alpha m_{l_\alpha} l_\beta m_{l_\beta}|\Lambda M_\Lambda\rangle\,\langle n_\alpha l_\alpha n_\beta l_\beta;\Lambda|00N\Lambda;\Lambda\rangle_{\rm SMB} \\
(4\pi)\int R^2_{12}dR_{12}\int d\Omega_{R_{12}}\sum_{l,m_l}(-i)^l j_l(P_{12}R_{12}) Y_{lm_l}(\Omega_{P_{12}}) Y^*_{lm_l}(\Omega_{R_{12}}) R_{N\Lambda}(\sqrt{2}R_{12}) Y_{\Lambda M_\Lambda}(\Omega_{R_{12}})\Big|^2 .
\end{aligned}
$$

The integration over the solid angle $\Omega_{R_{12}}$ gives $\delta_{\Lambda l}\delta_{M_\Lambda, m_l}$, leading to,

$$
\begin{aligned}
F^D_{n_\alpha l_\alpha, n_\beta l_\beta}(\vec{P}_{12}) = 4(4\pi)^2\sum_{m_{l_\alpha}, m_{l_\beta}}\Big|\sum_{N\Lambda M_\Lambda}(-i)^\Lambda\,\langle l_\alpha m_{l_\alpha} l_\beta m_{l_\beta}|\Lambda M_\Lambda\rangle\,\langle n_\alpha l_\alpha n_\beta l_\beta;\Lambda|00N\Lambda;\Lambda\rangle_{\rm SMB} \\
Y_{\Lambda M_\Lambda}(\Omega_{P_{12}})\int R^2_{12}dR_{12} j_\Lambda(P_{12}R_{12}) R_{N\Lambda}(\sqrt{2}R_{12})\Big|^2 .
\end{aligned}
$$

Expanding the modulus squared, the integration over the solid angle $\Omega_{P_{12}}$ produces the

result,

$$\begin{aligned}
\int d\Omega_{P_{12}} F^D_{n_\alpha l_\alpha, n_\beta l_\beta}(\vec{P}_{12}) = 4(4\pi)^2 \sum_{m_{l_\alpha}, m_{l_\beta}} \sum_{N\Lambda M_\Lambda} \sum_{N'\Lambda' M'_\Lambda} i^{\Lambda'+\Lambda}(-1)^\Lambda \\
\langle l_\alpha m_{l_\alpha} l_\beta m_{l_\beta} | \Lambda M_\Lambda \rangle \langle l_\alpha m_{l_\alpha} l_\beta m_{l_\beta} | \Lambda' M'_\Lambda \rangle^* \\
\langle n_\alpha l_\alpha n_\beta l_\beta; \Lambda | 00 N \Lambda; \Lambda \rangle_{\mathrm{SMB}} \langle n_\alpha l_\alpha n_\beta l_\beta; \Lambda' | 00 N' \Lambda'; \Lambda' \rangle^*_{\mathrm{SMB}} \\
\underbrace{\int d\Omega_{P_{12}} Y^*_{\Lambda' M'_\Lambda}(\Omega_{P_{12}}) Y_{\Lambda M_\Lambda}(\Omega_{P_{12}})}_{\delta_{\Lambda,\Lambda'}\delta_{M_\Lambda, M'_\Lambda}} \\
\int R'^2_{12} dR'_{12} \int R^2_{12} dR_{12} j_{\Lambda'}(P_{12}R'_{12}) j_\Lambda(P_{12}R_{12}) R_{N'\Lambda'}(\sqrt{2}R'_{12}) R_{N\Lambda}(\sqrt{2}R_{12}) \\
= 4(4\pi)^2 \sum_{m_{l_\alpha}, m_{l_\beta}} \sum_{NN'} \sum_{\Lambda M_\Lambda} \left| \langle l_\alpha m_{l_\alpha} l_\beta m_{l_\beta} | \Lambda M_\Lambda \rangle \right|^2 \\
\langle n_\alpha l_\alpha n_\beta l_\beta; \Lambda | 00 N' \Lambda; \Lambda \rangle^*_{\mathrm{SMB}} \langle n_\alpha l_\alpha n_\beta l_\beta; \Lambda | 00 N \Lambda; \Lambda \rangle_{\mathrm{SMB}} \\
\int R'^2_{12} dR'_{12} \int R^2_{12} dR_{12} j_\Lambda(P_{12}R'_{12}) j_\Lambda(P_{12}R_{12}) R_{N'\Lambda}(\sqrt{2}R'_{12}) R_{N\Lambda}(\sqrt{2}R_{12}) \,. \quad (3.9)
\end{aligned}$$

Comparing the Eqs. (3.9) and (3.8) results in,

$$P_2(P_{12}|nl=00) = \frac{1}{A(A-1)} \frac{3}{(2\pi)^3} \sum_{n_\alpha l_\alpha, n_\beta l_\beta} \int d\Omega_{P_{12}} F^D_{n_\alpha l_\alpha, n_\beta l_\beta}(\vec{P}_{12}) \,.$$

This is identical to Eq. (3.3), proving the identity.

Note that the expression given by Eq. (3.9), or equivalently Eq. (3.8), can be simplified further by making use of $\sum_{m_1 m_2} |\langle j_1 m_1 j_2 m_2 | JM \rangle|^2 = 1$,

$$\begin{aligned}
\sum_{n_\alpha l_\alpha, n_\beta l_\beta} \sum_{m_{l_\alpha}, m_{l_\beta}} \sum_{\Lambda M_\Lambda} \sum_{NN'} \left| \langle l_\alpha m_{l_\alpha} l_\beta m_{l_\beta} | \Lambda M_\Lambda \rangle \right|^2 \\
\langle 00 N' \Lambda; \Lambda | n_\alpha l_\alpha n_\beta l_\beta; \Lambda \rangle^*_{\mathrm{SMB}} \langle 00 N \Lambda; \Lambda | n_\alpha l_\alpha n_\beta l_\beta; \Lambda \rangle_{\mathrm{SMB}} \\
\int \mathrm{d}R'_{12} R'^2_{12} \int \mathrm{d}R_{12} R^2_{12} j_\Lambda(P_{12}R'_{12}) j_\Lambda(P_{12}R_{12}) R_{N'\Lambda}(\sqrt{2}R'_{12}) R_{N\Lambda}(\sqrt{2}R_{12}) \\
= \sum_{n_\alpha l_\alpha, n_\beta l_\beta} \sum_\Lambda (2\Lambda+1) \sum_{NN'} \langle 00 N' \Lambda; \Lambda | n_\alpha l_\alpha n_\beta l_\beta; \Lambda \rangle^*_{\mathrm{SMB}} \langle 00 N \Lambda; \Lambda | n_\alpha l_\alpha n_\beta l_\beta; \Lambda \rangle_{\mathrm{SMB}} \\
\int \mathrm{d}R'_{12} R'^2_{12} \int \mathrm{d}R_{12} R^2_{12} j_\Lambda(P_{12}R'_{12}) j_\Lambda(P_{12}R_{12}) R_{N'\Lambda}(\sqrt{2}R'_{12}) R_{N\Lambda}(\sqrt{2}R_{12})
\end{aligned}$$

3.3 Final-state interactions in two-nucleon knockout cross sections

3.3.1 Introduction

The c.m. momentum distribution of SRC pairs is the main focus of the article outlined in Sec. 3.2, published as Ref. [2]. The effect of final-state interactions (FSI) on the c.m. momentum distribution and the opening angle distribution of the SRC pairs is briefly discussed. In the article of Ref. [6] presented in this section the description of final-state interaction (FSI) in exclusive two-nucleon knockout reactions is discussed in more detail and additional FSI processes are considered compared to Sec. 3.2. The difficulties regarding the practical computation of the FSI are addressed as well.

Within the approximations used in our model, the inclusion of the FSI, describing the interaction of the outgoing nucleons with the recoiling nucleus, only affects the c.m. momentum distribution. This means that the factorization of the cross section is preserved and the electron two-nucleon coupling can still be divided out in cross-section ratios. Charge-exchange reactions are included in the description of the FSI and the effect on the cross-section ratios and the shape of the c.m. momentum and the opening angle distribution is studied. The mass dependence of the charge-exchange probabilities and the nuclear transparency is studied across the whole nuclear mass range. A simple geometric model is developed to gain more insight into the nuclear transparency mass dependence. This geometric model allows to set predictive bounds on the nuclear mass dependence.

The calculation of the cross section ratios for two-nucleon knockout reactions are time-consuming due to the large kinematical phase space that has to be covered. In the supplementary material of Sec. 3.3.3 the sampling of this high-dimensional phase space is described.

My contribution in the article presented here [6] consists of substantial contributions to the text as well as producing the computer code, leading to the presented numerical results and figures.

3.3 Final-state interactions in two-nucleon knockout reactions

Camille Colle,* Wim Cosyn,† and Jan Ryckebusch‡

Department of Physics and Astronomy,

Ghent University, Proeftuinstraat 86, B-9000 Gent, Belgium

(Dated: 7 March 2016)

Background: Exclusive two-nucleon knockout after electroexcitation of nuclei ($A(e,e'NN)$ in brief) is considered to be a primary source of information about short-range correlations (SRC) in nuclei. For a proper interpretation of the data, final-state interactions (FSI) need to be theoretically controlled.

Purpose: Our goal is to quantify the role of FSI effects in exclusive $A(e,e'pN)$ reactions for four target nuclei representative for the whole mass region. Our focus is on processes that are SRC driven. We investigate the role of FSI for two characteristic detector setups corresponding with a "small" and "large" coverage of the available phase space.

Method: Use is made of a factorized expression for the $A(e,e'pN)$ cross section that is proportional to the two-body center-of-mass (c.m.) momentum distribution of close-proximity pairs. The $A(e,e'pp)$ and $A(e,e'pn)$ reactions for the target nuclei ^{12}C, ^{27}Al, ^{56}Fe and ^{208}Pb are investigated. The elastic attenuation mechanisms in the FSI are included using the relativistic multiple-scattering Glauber approximation (RMSGA). Single-charge exchange (SCX) reactions are also included. We introduce the nuclear transparency T_A^{pN}, defined as the ratio of exclusive $(e,e'pN)$ cross sections on nuclei to those on "free" nucleon pairs, as a measure for the aggregated effect of FSI in pN knockout reactions from nucleus A. A toy model is introduced in order to gain a better understanding of the A dependence of T_A^{pN}.

Results: The transparency T_A^{pN} drops from $0.2-0.3$ for ^{12}C to $0.04-0.07$ for ^{208}Pb. For all considered kinematics, the mass dependence of the T_A^{pN} can be captured by the power law $T_A^{pN} \propto A^{-\lambda}$ with $0.4 \lesssim \lambda \lesssim 0.5$. Apart from an overall reduction factor, we find that FSI only modestly affects the distinct features of SRC-driven $A(e,e'pN)$ which are dictated by the c.m. distribution of close-proximity pairs.

Conclusion: The SCX mechanisms represent a relatively small (order of a few percent) contribution of SRC-driven $A(e,e'pN)$ processes. The mass dependence of FSI effects in exclusive $A(e,e'pN)$ can be captured in a robust power law and is in agreement with the predictions obtained in a toy model.

PACS numbers: 25.30.Rw, 25.30.Fj, 24.10.i

* Camille.Colle@UGent.be

† Wim.Cosyn@UGent.be

‡ Jan.Ryckebusch@UGent.be

I. INTRODUCTION

Nuclear SRC are an essential ingredient of the dynamics of nuclei at large momenta and energies. The short- and medium-range components of the nucleon-nucleon interaction induce beyond mean-field high-momentum and high-density fluctuations in the nuclear medium, thereby giving rise to fat tails in the nuclear momentum distributions [1–3]. The magnitude of nuclear SRC has been linked to plateaus in ratios of cross sections of inclusive electron scattering off different nuclei [4–6], and to the size of the EMC effect [7].

Nuclear SRC can be studied in exclusive two-nucleon knockout processes with hadronic and electroweak probes. In appropriately selected kinematics, those reactions give access to the dynamics and isospin composition of the initial nucleon pair. In the 1990s, high-resolution $A(e,e'pp)$ measurements carried out at MAMI [8, 9] and NIKHEF [10–12] could determine the transition to a specific final state of the residual $A-2$ nucleus. When comparing to data for the $^{16}\mathrm{O}(e,e'pp)$ transition to the 0^+ ground state of $^{14}\mathrm{C}$, model calculations [13–15] showed the clear dominance of SRC contributions to the cross section at low c.m. pair momentum, where the initial pair is in a relative S-state. The EVA collaboration at Brookhaven National Laboratory (BNL) measured the $^{12}\mathrm{C}(p,ppn)$ reaction [16] as a function of the initial neutron momentum. For neutron momenta above the Fermi surface ($\sim$ 220 MeV) the data showed a clear angular correlation between the initial proton and neutron momenta with backward angles ($> 90°$) dominating. For momenta below the Fermi surface the angular correlation between the two nucleon momenta is almost random. This picture was later confirmed by a $^{3}\mathrm{He}(e,e'pp)$ experiment performed in Jefferson Lab [17]. More recently, $^{12}\mathrm{C}(e,e'pN)$ [18, 19] and $^{4}\mathrm{He}(e,e'pN)$ [20] measurements (both at Jefferson Lab) provided proof that in the probed kinematics about 20% of the nucleons in nuclei form correlated pairs. Of those, about 90% is of the proton-neutron type [21], illustrating the dominance of tensor correlations in the nucleon momentum region of 300-500 MeV/c. A feature that emerges from all those experimental investigations, is that SRC pairs are mostly in a back-to-back configuration with a high relative and small c.m. momentum, whereby small and large are defined relative to the Fermi momentum.

In this paper we focus on the effect of FSI in SRC-driven high-virtuality $A(e,e'pN)$ cross sections. In Sec. II, we discuss the approximations underlying the factorized form of the $A(e,e'pN)$ cross section (detailed in Ref. [22]) and how we implement the FSI. Using the factorized $A(e,e'pN)$ cross-section expression, we show in Sec. II C that cross-section ratios can be directly related to the ratios of the integrated distorted two-body c.m. momentum distributions of close-proximity nucleon pairs. In Sec. III, we apply the developed model to four different target nuclei (^{12}C, ^{27}Al, ^{56}Fe, ^{208}Pb) and two very different kinematics probing SRC pairs. First, the kinematics of the $A(e,e'pp)$ cross-section measurements with the CEBAF Large Acceptance Spectrometer (CLAS) [21] covering a very large phase space. Second, the kinematics of an experimental setup with a very restricted phase-space coverage [18]. We extract the nuclear transparencies for two-nucleon knockout and compare them to single-particle knockout transparencies extracted from $A(e,e'p)$ measurements. We propose parameterizations for the mass dependence of the $A(e,e'pN)$ transparencies in the form of a power law and study its robustness. The opening-angle distribution for the initial correlated nucleon pair is shown to be dominated by backward angles, with little modification after the inclusion of FSI. A toy model that captures the essential features of elastic attenuation mechanisms in $A(e,e'NN)$ is

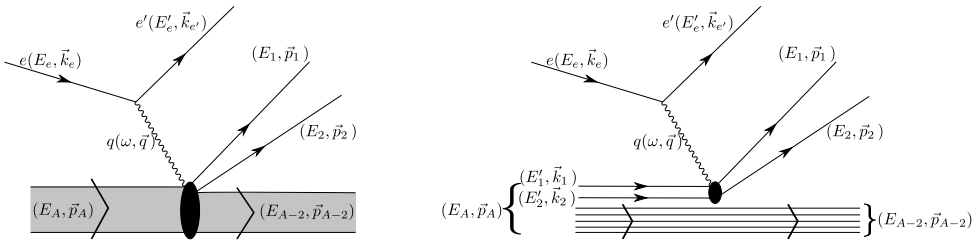

FIG. 1. (left) Sketch of the exclusive $A(e, e'pN)$ reaction with all kinematic variables. (right) The $A(e, e'pN)$ reaction in the impulse- and spectator approximation.

proposed. This toy model allows us to gain a more qualitative understanding of the mass dependence of the nuclear transparency. Conclusions are given in Sec. IV.

II. MODEL

A. Factorization of the $A(e, e'pN)$ cross section

We consider exclusive electroinduced knockout of a correlated proton-nucleon (pN) pair from the target nucleus A

$$e + A \to e' + (A-2)^* + p + N\,. \tag{1}$$

In this paper we solely deal with reactions whereby the residual $(A-2)^*$ is left with little or no excitation energy. This condition is essential for keeping the number of contributing reaction mechanisms under control.

Let $(\vec{k}_1, \vec{k}_2)$ and $(\vec{p}_1, \vec{p}_2)$ be the initial and final three-momenta of the nucleon pair. We label the struck proton with "1" and the recoiling nucleon with "2". In the impulse approximation, in which the exchanged momentum is absorbed by a single nucleon, we have that $\vec{p}_1 = \vec{k}_1 + \vec{q}$ with $\vec{q}$ the transferred three-momentum of the virtual photon (Fig. 1). We define the c.m. $\vec{P}_{12}$ and relative momentum $\vec{k}_{12}$ of the initial pair as,

$$\vec{P}_{12} = \vec{k}_1 + \vec{k}_2, \qquad \vec{k}_{12} = \frac{\vec{k}_1 - \vec{k}_2}{2}\,. \tag{2}$$

The corresponding c.m. and relative coordinates are denoted by $\vec{R}_{12}$ and $\vec{r}_{12}$.

By selecting events with a large $|\vec{q}|$ (large in comparison to the initial momenta $(\vec{k}_1, \vec{k}_2)$ of the nucleon pair) and requiring that one of the measured nucleons carries a significant fraction of the exchanged momentum $|\vec{q}|$, the contribution from the exchange term in which nucleon "2" absorbs the photon can be made negligible. Indeed, above the Fermi momentum, the $\vec{k}_{12}$ distribution of the pairs is strongly decreasing with increasing $|\vec{k}_{12}|$ [22, 23]. This makes it highly unlikely that the fast nucleon in the final state is not the one that absorbed the virtual photon.

As outlined in Refs. [22, 24], in kinematics probing SRC pairs, it is possible to factorize the $A(e, e'pN)$ cross section in a product of a function depending on the relative momentum $\vec{k}_{12}$, and a part depending on

the c.m. momentum $\vec{P}_{12}$ of the initial pN pair

$$\frac{\mathrm{d}^8\sigma(e,e'pN)}{\mathrm{d}^2\Omega_{k_{e'}}\mathrm{d}^3\vec{p}_1\mathrm{d}^3\vec{p}_2} = \frac{M_A M_{A-2}}{E_A E_{A-2}} \frac{1}{(2\pi)^3} f_{\mathrm{rec}} \sigma_{epN}(\vec{k}_{12}) F_A^{pN,D}(\vec{P}_{12})\,, \tag{3}$$

with $\Omega_{k_{e'}}$ the solid angle of the scattered electron, f_{rec} the recoil factor,

$$f_{\mathrm{rec}} = \frac{\left|1 - \frac{E_{e'}}{E_2}\frac{\vec{p}_2\cdot\vec{k}_{e'}}{|\vec{k}_{e'}|^2}\right|}{\left|1 + \frac{E_{e'}}{E_{A-2}}\frac{\vec{P}\cdot\vec{k}_{e'}}{|\vec{k}_{e'}|^2}\right|}\,, \tag{4}$$

and M_A, E_A (M_{A-2},E_{A-2}) the rest mass and energy of the initial (recoiling $A-2$) nucleus. $\sigma_{epN}(\vec{k}_{12})$ encodes the virtual-photon coupling to a correlated pN pair with relative momentum $\vec{k}_{12}$. $F_A^{pN,D}(\vec{P}_{12})$ is the distorted c.m. momentum distribution of the close-proximity pair that absorbs the photon. The factorized cross-section expression of Eq. (3) hinges on the validity of the zero-range approximation (ZRA), which amounts to putting the relative pair coordinate $\vec{r}_{12}$ to zero (Fig. 2). Thereby, the amplitude for photo-absorption on a close-proximity pair that involves the product of two IPM wave functions $\psi_\alpha(\vec{R}_{12}+\frac{\vec{r}_{12}}{2})$ and $\psi_\beta(\vec{R}_{12}-\frac{\vec{r}_{12}}{2})$ and a two-body operator $\widehat{O}^{[2]}(\vec{R}_{12},\vec{r}_{12})$ (left panel of Fig. 2) is written as a product of a one-body operator $\widehat{O}^{[1]}$ evaluated at the c.m. coordinate $\vec{R}_{12}$ and a correlation operator $\widehat{\ell}$ that depends only on the relative coordinate $\vec{r}_{12}$ (right panel of Fig. 2). In nuclei, $\widehat{\ell}$ has a complicated spin and isospin structure. The ZRA acts as a projection operator on the short-range components of the wave function corresponding with the relative motion of the pair. Throughout this paper the factorized cross section of Eq. (3) is used. The validity of this expression (3) has been experimentally verified. The proposed factorization of the cross section in terms of $F_A^{pp,D}$ was first confirmed in ^{12}C$(e,e'pp)$ measurements back in the late 1990s [9]. An effort is on its way to extract the width of the $F_A^{pp,D}$ distribution in $A(e,e'pp)$ measurements on ^{12}C, ^{27}Al, ^{56}Fe and ^{208}Pb [25, 26], and compare them with the theoretical predictions [22]. Another striking prediction of the expression (3) is that the $A(e,e'pN)$ cross section is proportional to the number of close-proximity pN pairs in the target nucleus. As a result, it can be inferred that the A dependence of the $A(e,e'pp)$ cross section is much softer than naive FSI-corrected $Z(Z-1)/2$ counting. Recent measurements of the $A(e,e'pp)/^{12}$C$(e,e'pp)$ ratios are completely in line with those predictions [27]. The measured and predicted ^{208}Pb/^{12}C $(e,e'pp)$ cross section ratio, for example, is a mere five whereas the naive prediction is over two hundred.

B. Final-state interactions

We include two FSI mechanisms in our model. First, attenuation (ATT) of the outgoing nucleons upon traversing the recoiling nucleus. Second, single-charge exchange (SCX), i.e. an outgoing proton (neutron) rescattering into a neutron (proton). The attenuation effect is calculated in the relativistic multiple-scattering Glauber approximation (RMSGA) [28, 29]. The RMSGA is based on high-energy diffractive scattering. It uses an eikonal form for the rescattering amplitude dominated by the central term, neglecting spin-dependent attenuation. The RMSGA is fully parameterized in terms of nucleon-nucleon scattering data. We systematically use "FSI" upon referring to the combined effect of attenuation and single-charge exchange. Throughout this paper, we refer to $A(e,e'pN)$ results that ignore the effect of FSI as "ZRA" results.

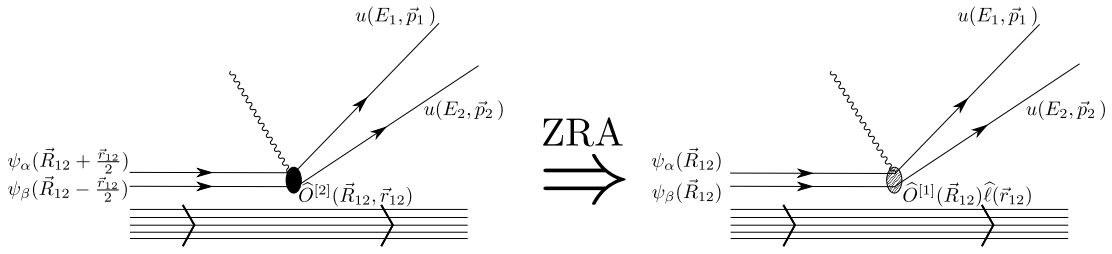

FIG. 2. A sketch of the zero-range approximation (ZRA) which underlies the factorized expression of the exclusive $A(e,e'pN)$ cross section.

The distorted c.m. momentum distribution $F_A^{pN,D}(\vec{P}_{12})$ in Eq. (3) is defined in the following way

$$F_A^{pN,D}(\vec{P}_{12}) = \sum_{\alpha,\beta} F_A^{pN,D;\alpha\beta}(\vec{P}_{12}) \\ = \sum_{\substack{s_1,s_2\\ \alpha\beta}} \left| \int d\vec{R}_{12}\, e^{i\vec{P}_{12}\cdot\vec{R}_{12}} \bar{u}(\vec{k}_1,s_1)\psi_\alpha(\vec{R}_{12})\bar{u}(\vec{k}_2,s_2)\psi_\beta(\vec{R}_{12})\mathcal{F}_{\rm RMSGA}(\vec{R}_{12}) \right|^2 . \quad (5)$$

Here, $u(\vec{k},s)$ is the positive-energy free Dirac spinor and $(\psi_\alpha,\,\psi_\beta)$ are relativistic mean-field wave functions with IPM quantum numbers (α,β) computed in the Serot-Walecka model [30]. The contribution from a specific IPM nucleon pair with quantum numbers (α,β) is denoted as $F_A^{pN,D;\alpha\beta}(\vec{P}_{12})$. We consider experimental conditions whereby the precise state of the residual $A-2$ nucleus is not resolved. As a result, the sum over (α,β) extends over all occupied pN pairs. In the practical implementation of Eq. (5), we neglect the projection on the lower components of the plane-wave Dirac spinors. The rescattering of the ejected pair with the remaining $A-2$ spectators, encoded in the standard Glauber phase $\mathcal{F}_{\rm RMSGA}$, is computed in the RMSGA [28]. The interactions among the two ejected nucleons do not affect $F_A^{pN,D}(\vec{P}_{12})$ due to c.m. momentum conservation, and they are effectively included in $\sigma_{epN}(\vec{k}_{12})$. The implementation of reinteractions between the ejected nucleons is not addressed in this article, as $\sigma_{epN}(\vec{k}_{12})$ drops out in the cross section ratios defined in Sec. II C.

The SCX mechanisms are treated in a semi-classical manner. The joint probability for the struck proton, labelled "1", undergoing SCX while the recoiling nucleon of the SRC pair, labelled "2", is not undergoing any SCX, is given by

$$P_{\rm CX,A}^{[\mathbf{1}]2,pN} = \sum_{\alpha,\beta} \frac{\int {\rm d}^3\vec{R}_{12}\, P_{\rm CX}^{[\boldsymbol{\alpha}]\beta}(\vec{R}_{12}) \left[1 - P_{\rm CX}^{\alpha[\boldsymbol{\beta}]}(\vec{R}_{12})\right] F_A^{pN,D;\alpha\beta}(\vec{R}_{12})}{\int {\rm d}^3\vec{R}_{12}\, F_A^{pN,D;\alpha\beta}(\vec{R}_{12})} . \quad (6)$$

As in Eq. (5), the sum over (α,β) extends over all the occupied pN pairs. Further, the square bracket $[\mathbf{1}]$ identifies the nucleon subject to SCX. In Eq. (6), the probability that an initial nucleon with quantum numbers α (with correlated partner with quantum numbers β) has undergone a SCX after a hard interaction at c.m. coordinate $\vec{R}_{12}$ is given by $P_{\rm CX}^{[\boldsymbol{\alpha}]\beta}(\vec{R}_{12})$, and is weighted with the RMSGA-corrected probability $F_A^{pN,D;\alpha\beta}(\vec{R}_{12})$ of finding the two nucleons at c.m. coordinate $\vec{R}_{12}$. Similar expressions to Eq. (6) can be

written for the situations where only the recoil nucleon "2" is subject to SCX ($P_{\rm CX,A}^{1[\mathbf{2}],pN}$), both nucleons in the pair are subject to SCX ($P_{\rm CX,A}^{[\mathbf{12}],pN}$) or none of the nucleons in the pair are subject to SCX ($P_{\rm CX,A}^{12,pN}$). In those situations, the factor $P_{\rm CX}^{[\boldsymbol{\alpha}]\beta}(\vec{R}_{12})\left[1-P_{\rm CX}^{\alpha[\boldsymbol{\beta}]}(\vec{R}_{12})\right]$ in the numerator of Eq. (6), is replaced by respectively the factor $\left[1-P_{\rm CX}^{[\boldsymbol{\alpha}]\beta}(\vec{R}_{12})\right]P_{\rm CX}^{\alpha[\boldsymbol{\beta}]}(R_{12})$, $P_{\rm CX}^{[\boldsymbol{\alpha}]\beta}(\vec{R}_{12})P_{\rm CX}^{\alpha[\boldsymbol{\beta}]}(R_{12})$, and $[1-P_{\rm CX}^{[\boldsymbol{\alpha}]\beta}(\vec{R}_{12})][1-P_{\rm CX}^{\alpha[\boldsymbol{\beta}]}(\vec{R}_{12})]$. One has $P_{\rm CX,A}^{[\mathbf{1}]2,pN}+P_{\rm CX,A}^{1[\mathbf{2}],pN}+P_{\rm CX,A}^{[\mathbf{12}],pN}+P_{\rm CX,A}^{12,pN}=1$.

The SCX probabilities $P_{\rm CX}^{[\boldsymbol{\alpha}]\beta}(\vec{R}_{12})$ are calculated in a semi-classical approximation. Thereby, the probability of charge-exchange rescattering for a nucleon with bound-state IPM quantum numbers α that is brought in a continuum state at the coordinate $\vec{r}$ is modelled by

$$P_{\rm CX}^{[\boldsymbol{\alpha}]\beta}(\vec{r})=1-\exp\left[-\sigma_{\rm CX}(s)\int_z^{+\infty}{\rm d}z'\rho_{A-2}^{\alpha\beta}(z')\right]. \tag{7}$$

The z-axis is chosen along the direction of propagation of the nucleon undergoing SCX ($[\boldsymbol{\alpha}]$). The $\rho_{A-2}^{\alpha\beta}$ is the one-body density of the recoiling $A-2$ nucleus that contributes to the SCX reaction. For an ejected proton (neutron) only the neutron (proton) density of the recoiling nucleus affects SCX reactions. The parameter $\sigma_{\rm CX}(s)$ in Eq. (7) can be extracted from elastic proton-neutron scattering data [31], with s the total c.m. energy squared of the two nucleons involved in the SCX. In Ref. [32], it was shown that $\sigma_{\rm CX}(s)$ obeys the relation

$$\sigma_{\rm CX}(s)=0.424\frac{s}{s_{800}}\ {\rm fm}^2\,, \tag{8}$$

where s_{800} is the c.m. energy squared for a collision between a neutron with 800 MeV kinetic energy and a stationary proton. The value 0.424 fm^2 is obtained by integrating the elastic pn differential cross section with s=s_{800} at backward scattering angles dominated by charge-exchange [31]. The parameterization of Eq. (8) is valid for lab frame momenta in the interval $[0.1,100]$ GeV/c.

In Eq. (6), the weight factor $F_{\rm A}^{pN,D;\alpha\beta}(\vec{R}_{12})$ gives the attenuation corrected probability to find a pair (α,β) at a coordinate $\vec{R}_{12}$

$$F_A^{pN,D;\alpha\beta}(\vec{R}_{12})=\lim_{\vec{r}_{12}\to\vec{0}}|\psi_\alpha(\vec{R}_{12}+\frac{\vec{r}_{12}}{2})|^2|\psi_\beta(\vec{R}_{12}-\frac{\vec{r}_{12}}{2})|^2|\mathcal{F}_{\rm RMSGA}(\vec{R}_{12}\pm\frac{\vec{r}_{12}}{2})|^2\,. \tag{9}$$

Note that $F_A^{pN,D;\alpha\beta}(\vec{R}_{12})$ is the Fourier transform of $F_A^{pN,D;\alpha\beta}(\vec{P}_{12})$ appearing in Eq. (3). In the limit of vanishing FSI ($\mathcal{F}_{\rm RMSGA}\equiv 1$) Eq. (9) reduces to the probability of finding two IPM nucleons at the same coordinate $\vec{R}_{12}$.

The flow diagram in Fig. 3 shows an overview of the different FSI mechanisms that are included in the $A(e,e'pN)$ reactions considered in this article. The initial plane-wave (vanishing FSI) ZRA $A(e,e'pN)$ cross section (σ_A^{pN}) is positioned at the center. The partner nucleon can be a proton (σ_A^{pp}) or a neutron (σ_A^{pn}). The observable cross sections are denoted with $\widetilde{\sigma}_A^{pp}$ and $\widetilde{\sigma}_A^{pn}$. The sources and sinks between the different $\widetilde{\sigma}_A^{NN}$ through the SCX mechanism are denoted with the solid arrows. The dashed arrows denote the RMSGA attenuation contribution, quantified by means of the nuclear transparency T_A^{pN}, defined as the ratio of the $A(e,e'pN)$ cross section with and without the RMSGA attenuations (see Eq. (14)). It is a measure for attenuation caused by the nuclear medium. The different contributions to the final cross sections $\widetilde{\sigma}_A^{pp}$, $\widetilde{\sigma}_A^{pn}$ can be visually deduced by following all possible paths from σ_A^{pN} to $\widetilde{\sigma}_A^{pp}$ or $\widetilde{\sigma}_A^{pn}$ in Fig. (3). Because we only account for single-charge exchange, the SCX arrows can only be used at most once for each particle

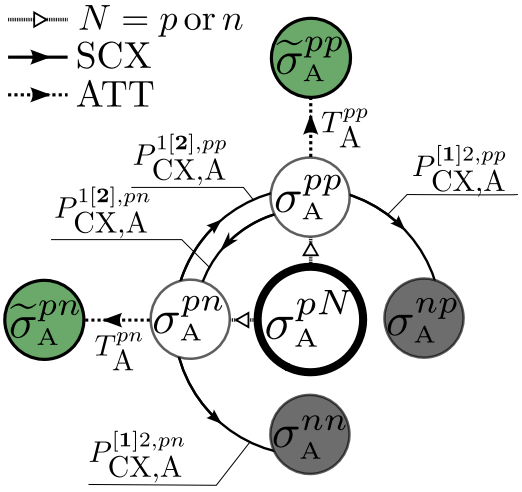

FIG. 3. (Color online) A flow diagram illustrating the different FSI effects included in our model calculations. The center of the diagram ($\sigma^{pN}_{\rm A}$) denotes the plane-wave ZRA $A(e,e'pN)$ cross section. The $\widetilde{\sigma}^{pp}_{\rm A}$ and $\widetilde{\sigma}^{pn}_{\rm A}$ correspond with the observed $A(e,e'pp)$ and $A(e,e'pn)$ cross sections. The solid arrows denote SCX reactions. The dashed arrows denote the attenuation (ATT).

in every path, meaning $P^{1[\mathbf{2}],pN}_{\rm CX,A}P^{[\mathbf{1}]2,pN}_{\rm CX,A}$ is allowed but $P^{[\mathbf{1}]2,pN}_{\rm CX,A}P^{[\mathbf{1}]2,pN}_{\rm CX,A}$ or $P^{1[\mathbf{2}],pN}_{\rm CX,A}P^{1[\mathbf{2}],pN}_{\rm CX,A}$ are not. The missing SCX arrows (from and between σ^{nn}_A, σ^{np}_A) are neglected as we assume that the struck nucleon is a proton. We argue that this is a valid approximation. First, the photon-neutron coupling is a fraction of the photon-proton one. Second, an SCX reaction is a necessary condition to end up with a leading proton in the final state. We find that those SCX probabilities are very small (Sec. III).

C. $A(e,e'pN)$ cross-section ratios

Most often, it is extremely challenging to measure $A(e,e'pN)$ cross sections. A lot of information regarding nuclear SRC has been obtained by measuring cross-section rations over extended ranges of the phase space [4, 5, 21, 25, 27]. Using the factorized form of the differential cross section from Eq. (3), one can investigate $A(e,e'pN)$ cross-section ratios relative to ^{12}C. Let $\widetilde{R}^{pN}_A$ (R^{pN}_A) be the cross-section ratios with (without) the inclusion of FSI,

$$\widetilde{R}^{pN}_A = \frac{\widetilde{\sigma}^{pN}_A}{\widetilde{\sigma}^{pN}_{^{12}\rm C}} \approx \frac{\int {\rm d}^2\Omega_{k_{e'}}{\rm d}^3\vec{k}_{12}\sigma_{epN}(\vec{k}_{12})\int {\rm d}^3\vec{P}_{12}F^{pN,D}_A(\vec{P}_{12})}{\int {\rm d}^2\Omega_{k_{e'}}{\rm d}^3\vec{k}_{12}\sigma_{epN}(\vec{k}_{12})\int {\rm d}^3\vec{P}_{12}F^{pN,D}_{^{12}\rm C}(\vec{P}_{12})} = \frac{\int {\rm d}^3\vec{P}_{12}F^{pN,D}_A(\vec{P}_{12})}{\int {\rm d}^3\vec{P}_{12}F^{pN,D}_{^{12}\rm C}(\vec{P}_{12})}\,. \tag{10}$$

The $\widetilde{\sigma}^{pN}_A$ denotes the FSI-corrected $A(e,e'pN)$ cross section. The cross-section ratios are independent of the information contained in the photon-nucleon coupling $\sigma_{epN}(\vec{k}_{12})$. Therefore, we use cross-section ratios to quantify the effect of SRC as those are less model dependent.

In the limit of vanishing FSI the integrated c.m. momentum distribution $\int {\rm d}^3\vec{P}_{12}\,F^{pN,D}_A(\vec{P}_{12})$ is proportional to the amount of SRC-susceptible pN pairs. The relative amount of SRC pairs for nucleus A relative to ^{12}C is then given by $R_{pN} = \sigma^{pN}_A/\sigma^{pN}_{^{12}\rm C}$, where σ^{pN}_A denotes the $A(e,e'pN)$ cross section in the limit of vanishing FSI. It is well established that the tensor correlation [3, 19] induces a heavy dominance of SRC pn

pairs over SRC pp pairs. This dominance is not automatically generated in the ZRA without introducing additional assumptions with regard to the dynamical mechanisms underlying the SRC. The pn- over pp-pair dominance can be included for nucleus A using the measured pn/pp pair ratio (18 ± 5) in ^{12}C [19], in the following way

$$\frac{\sigma_A^{pn}}{\sigma_A^{pp}} = \frac{\sigma_A^{pn}}{\sigma_{^{12}\mathrm{C}}^{pn}} \frac{\sigma_{^{12}\mathrm{C}}^{pn}}{\sigma_{^{12}\mathrm{C}}^{pp}} \frac{\sigma_{^{12}\mathrm{C}}^{pp}}{\sigma_A^{pp}} \approx \frac{\sigma_A^{pn}}{\sigma_{^{12}\mathrm{C}}^{pn}} \frac{\#pn\text{-pairs}\,(^{12}\mathrm{C})}{2 \cdot \#pp\text{-pairs}\,(^{12}\mathrm{C})} \frac{\sigma_{^{12}\mathrm{C}}^{pp}}{\sigma_A^{pp}} \approx \frac{\sigma_A^{pn}}{\sigma_{^{12}\mathrm{C}}^{pn}} \left(\frac{18 \pm 5}{2}\right) \frac{\sigma_{^{12}\mathrm{C}}^{pp}}{\sigma_A^{pp}} \,. \tag{11}$$

The exchanged photon can couple to both protons in a pp pair and to one in a pn pair leading to the factor 2 in the denominator of Eq. (11). The expressions for the FSI-corrected cross-section ratios, $\widetilde{R}^{pN} = \widetilde{\sigma}_A^{pN}/\widetilde{\sigma}_{^{12}\mathrm{C}}^{pN}$, are then given by (see Fig. 3)

$$\widetilde{R}_A^{pp} = \frac{\widetilde{\sigma}_A^{pp}}{\widetilde{\sigma}_{^{12}\mathrm{C}}^{pp}} = \frac{P_{\mathrm{CX,A}}^{12,pp} T_A^{pp} \sigma_A^{pp} + P_{\mathrm{CX,A}}^{1[\mathbf{2}],pn} T_A^{p*} \sigma_A^{pn}}{P_{\mathrm{CX}^{12}\mathrm{C}}^{12,pp} T_{^{12}\mathrm{C}}^{pp} \sigma_{^{12}\mathrm{C}}^{pp} + P_{\mathrm{CX}^{12}\mathrm{C}}^{1[\mathbf{2}],pn} T_{^{12}\mathrm{C}}^{p*} \sigma_{^{12}\mathrm{C}}^{pn}} = \frac{P_{\mathrm{CX,A}}^{12,pp} T_A^{pp} R_A^{pp} + P_{\mathrm{CX,A}}^{1[\mathbf{2}],pn} T_A^{p*} \frac{\sigma_A^{pn}}{\sigma_{^{12}\mathrm{C}}^{pp}}}{P_{\mathrm{CX}^{12}\mathrm{C}}^{12,pp} T_{^{12}\mathrm{C}}^{pp} + P_{\mathrm{CX}^{12}\mathrm{C}}^{1[\mathbf{2}],pn} T_{^{12}\mathrm{C}}^{p*} \frac{\sigma_{^{12}\mathrm{C}}^{pn}}{\sigma_{^{12}\mathrm{C}}^{pp}}}$$

$$= \frac{P_{\mathrm{CX,A}}^{12,pp} T_A^{pp} R_A^{pp} + P_{\mathrm{CX,A}}^{1[\mathbf{2}],pn} T_A^{p*} R_A^{pn} \frac{18\pm5}{2}}{P_{\mathrm{CX}^{12}\mathrm{C}}^{12,pp} T_{^{12}\mathrm{C}}^{pp} + P_{\mathrm{CX}^{12}\mathrm{C}}^{1[\mathbf{2}],pn} T_{^{12}\mathrm{C}}^{p*} \frac{18\pm5}{2}} \,. \tag{12}$$

Here, $\widetilde{\sigma}_A^{pN}$ is the FSI corrected $A(e,e'pN)$ cross section. The first term in the numerator and denominator consists of the $A(e,e'pp)$ cross section (σ_A^{pp}) corrected for attenuation (T_A^{pp}) given that no SCX occurred ($P_{\mathrm{CX,A}}^{12,pp}$). The second term is the contribution from an initial $A(e,e'pn)$ (σ_A^{pn}) multiplied by the attenuation factor (T_A^{p*}) given that the recoiling partner changes to a proton ($P_{\mathrm{CX,A}}^{1[\mathbf{2}],pn}$). These two terms correspond with the two possible paths to $\widetilde{\sigma}_A^{pp}$ in Fig. 3 :

$$\sigma_A^{pN} \to \sigma_A^{pp} \xrightarrow{P_{\mathrm{CX,A}}^{12,pp} T_A^{pp}} \widetilde{\sigma}_A^{pp} \quad \text{and,} \quad \sigma_A^{pN} \to \sigma_A^{pn} \xrightarrow{P_{\mathrm{CX,A}}^{1[\mathbf{2}],pn} T_A^{p*}} \widetilde{\sigma}_A^{pp} \,. \tag{13}$$

In the ZRA, the nuclear $A(e,e'pN)$ transparency T_A^{pN} can be calculated as,

$$T_A^{pN} \approx \frac{\int \mathrm{d}^3\vec{P}_{12}\, F_A^{pN,D}(\vec{P}_{12})}{\int \mathrm{d}^3\vec{P}_{12}\, F_A^{pN}(\vec{P}_{12})} \,. \tag{14}$$

Here, $F_A^{pN}(\vec{P}_{12})$ is the c.m. momentum distribution in the limit of vanishing attenuation ($\mathcal{F}_{\mathrm{RMSGA}} \equiv 1$ in Eq. (5)). We stress that the transparency depends on the sampled phase space, i.e. the integration volume of $\vec{P}_{12}$ in Eq. (14).

In estimating the attenuation effect for the SCX contribution we use the averaged transparency $T_A^{p*} = \frac{1}{2}(T_A^{pp} + T_A^{pn})$. The reason is that in our model we have no information about the time ordering of the SCX and attenuation mechanisms. Therefore, starting from initial pp knockout followed by $p \to n$ SCX, one can adopt the averaged attenuation $\frac{T_A^{pn}+T_A^{pp}}{2}$. Note that the difference between T_A^{pp} and T_A^{pn} is rather small for the kinematics addressed in this paper (2% for ^{12}C and about 20% for ^{208}Pb).

For the $A(e,e'pn)$ cross-section ratios we get,

$$\widetilde{R}_A^{pn} = \frac{\widetilde{\sigma}_A^{pn}}{\widetilde{\sigma}_{^{12}\mathrm{C}}^{pn}} = \frac{P_{\mathrm{CX,A}}^{12,pn} T_A^{pn} \sigma_A^{pn} + P_{\mathrm{CX,A}}^{1[\mathbf{2}],pp} T_A^{p*} \sigma_A^{pp}}{P_{\mathrm{CX}^{12}\mathrm{C}}^{12,pn} T_{^{12}\mathrm{C}}^{pn} \sigma_{^{12}\mathrm{C}}^{pn} + P_{\mathrm{CX}^{12}\mathrm{C}}^{1[\mathbf{2}],pp} T_{^{12}\mathrm{C}}^{p*} \sigma_{^{12}\mathrm{C}}^{pp}} = \frac{P_{\mathrm{CX,A}}^{12,pn} T_A^{pn} R_A^{pn} + P_{\mathrm{CX,A}}^{1[\mathbf{2}],pp} T_A^{p*} R_A^{pp} \frac{2}{18\pm5}}{P_{\mathrm{CX}^{12}\mathrm{C}}^{12,pn} T_{^{12}\mathrm{C}}^{pn} + P_{\mathrm{CX}^{12}\mathrm{C}}^{1[\mathbf{2}],pp} T_{^{12}\mathrm{C}}^{p*} \frac{2}{18\pm5}} \,. \tag{15}$$

As in Eq. (12) each term can be identified with a certain path to $\widetilde{\sigma}_A^{pn}$ in Fig. 3. The experimental values for $\widetilde{R}_A^{pn}$ are not known if the outgoing neutrons are not detected. In kinematics tuned so that the $A(e,e'p)$

signal is dominated by $A(e,e'pN)$ events it is possible to deduce $\widetilde{R}_A^{pn}$ from the $A(e,e'p)$ cross section ratios ($\widetilde{R}_A^{p}$) measured for the same kinematical settings

$$\widetilde{R}_A^{p} = \frac{\widetilde{\sigma}_A^{p}}{\widetilde{\sigma}_{^{12}\mathrm{C}}^{p}} \approx \frac{2\widetilde{\sigma}_A^{pp} + \widetilde{\sigma}_A^{pn}}{2\widetilde{\sigma}_{^{12}\mathrm{C}}^{pp} + \widetilde{\sigma}_{^{12}\mathrm{C}}^{pn}} = \frac{2\widetilde{R}_A^{pp} + \widetilde{R}_A^{pn}\widetilde{R}_{^{12}\mathrm{C}}^{\frac{pn}{pp}}}{2 + \widetilde{R}_{^{12}\mathrm{C}}^{\frac{pn}{pp}}} \,. \tag{16}$$

The $^{12}\mathrm{C}(e,e'pn)$ over $^{12}\mathrm{C}(e,e'pp)$ cross-section ratio $\widetilde{R}_{^{12}\mathrm{C}}^{\frac{pn}{pp}}$ can be extracted in the following way

$$\widetilde{R}_{^{12}\mathrm{C}}^{\frac{pn}{pp}} = \frac{\widetilde{\sigma}_{^{12}\mathrm{C}}^{pn}}{\widetilde{\sigma}_{^{12}\mathrm{C}}^{pp}} = \frac{P_{\mathrm{CX}^{12}\mathrm{C}}^{12,pn} T_{^{12}\mathrm{C}}^{pn} \sigma_{^{12}\mathrm{C}}^{pn} + P_{\mathrm{CX}^{12}\mathrm{C}}^{1[\mathbf{2}],pp} T_{^{12}\mathrm{C}}^{p*} \sigma_{^{12}\mathrm{C}}^{pp}}{P_{\mathrm{CX}^{12}\mathrm{C}}^{12,pp} T_{^{12}\mathrm{C}}^{pp} \sigma_{^{12}\mathrm{C}}^{pp} + P_{\mathrm{CX}^{12}\mathrm{C}}^{1[\mathbf{2}],pn} T_{^{12}\mathrm{C}}^{p*} \sigma_{^{12}\mathrm{C}}^{pn}} = \frac{P_{\mathrm{CX}^{12}\mathrm{C}}^{12,pn} T_{^{12}\mathrm{C}}^{pn} \frac{18\pm5}{2} + P_{\mathrm{CX}^{12}\mathrm{C}}^{1[\mathbf{2}],pp} T_{^{12}\mathrm{C}}^{p*}}{P_{\mathrm{CX}^{12}\mathrm{C}}^{12,pp} T_{^{12}\mathrm{C}}^{pp} + P_{\mathrm{CX}^{12}\mathrm{C}}^{1[\mathbf{2}],pn} T_{^{12}\mathrm{C}}^{p*} \frac{18\pm5}{2}} \,. \tag{17}$$

Hence from Eq. (16),

$$\widetilde{R}_A^{pn} = \frac{1}{\widetilde{R}_{^{12}\mathrm{C}}^{\frac{pn}{pp}}} \left[\widetilde{R}_A^{p} \left(2 + \widetilde{R}_{^{12}\mathrm{C}}^{\frac{pn}{pp}} \right) - 2\widetilde{R}_A^{pp} \right] \,. \tag{18}$$

The relations for $\widetilde{R}_A^{pp}$ and $\widetilde{R}_A^{pn}$ can be inverted to extract the FSI-uncorrected cross section ratios (which are proportional to the ratios of SRC prone pairs) R_A^{pp}, R_A^{pn} from the measured values for $\widetilde{R}^{pp}$ and $\widetilde{R}^{pn}$ [27].

III. RESULTS

In this section we present the results of the numerical $A(e,e'pN)$ calculations for four representative target nuclei and two representative but distinct kinematic settings. First, we apply the formalism developed in the previous section to the $A(e,e'pN)$ reaction in the kinematics covered by the Jefferson Lab CLAS detector [21]. The latter is a "4π" detector, which results in a very large phase-space coverage. We systematically refer to this kinematics as "KinB". Kinematics approaching a "4π" layout pose challenges for the calculations and require dedicated sampling techniques that are outlined below. After the discussion of the "4π" KinB results we present two-nucleon knockout calculations in kinematics in very narrow solid angles for all detected particles (coined "KinA").

In dealing with the KinB situation, we define a reference frame with the z-axis along the initial momentum $\vec{k}_1$ of the proton and the exchanged photon-momentum $\vec{q}$ in the $x-z$ plane. A two-nucleon knockout event is uniquely characterized by the set of 6 kinematical variables $\{Q^2 \equiv |\vec{q}|^2 - \omega^2, x_B = \frac{Q^2}{2m_N\omega}, \theta_q, \vec{P}_{12}\}$. Here, θ_q is the direction of $\vec{q}$ relative to the z axis.

Upon numerically computing the distorted c.m. momentum distribution of Eq. (5), we generate phase space samples by drawing (x_B,Q^2) from the experimentally measured (x_B, Q^2) distribution [25]. We draw the θ_q and the $\vec{P}_{12}$ uniformly from the relevant ranges. In order to guarantee that the virtual photon primarily probes correlated pairs a number of kinematic constraints are imposed

$$\theta_{\vec{p}_1,\vec{q}} \leq 25^\circ \; ; \; 0.62 < \frac{|\vec{p}_1|}{|\vec{q}|} < 0.96 \; ; \; x_B \geq 1.2; \tag{19}$$

$$|\vec{k}_1| \geq 300 \text{ MeV}; |\vec{p}_2| \geq 350 \text{ MeV} \,. \tag{20}$$

The first two cuts select events where the virtual photon has mainly interacted with the struck (leading) proton. The $x_B \geq 1.2$ cut selects events with a high $|\vec{q}|$ and relatively low ω, suppressing for example pion production through intermediate Δ production. The last two cuts impose high-momentum conditions (larger than the Fermi momentum) for the initial nucleon pair.

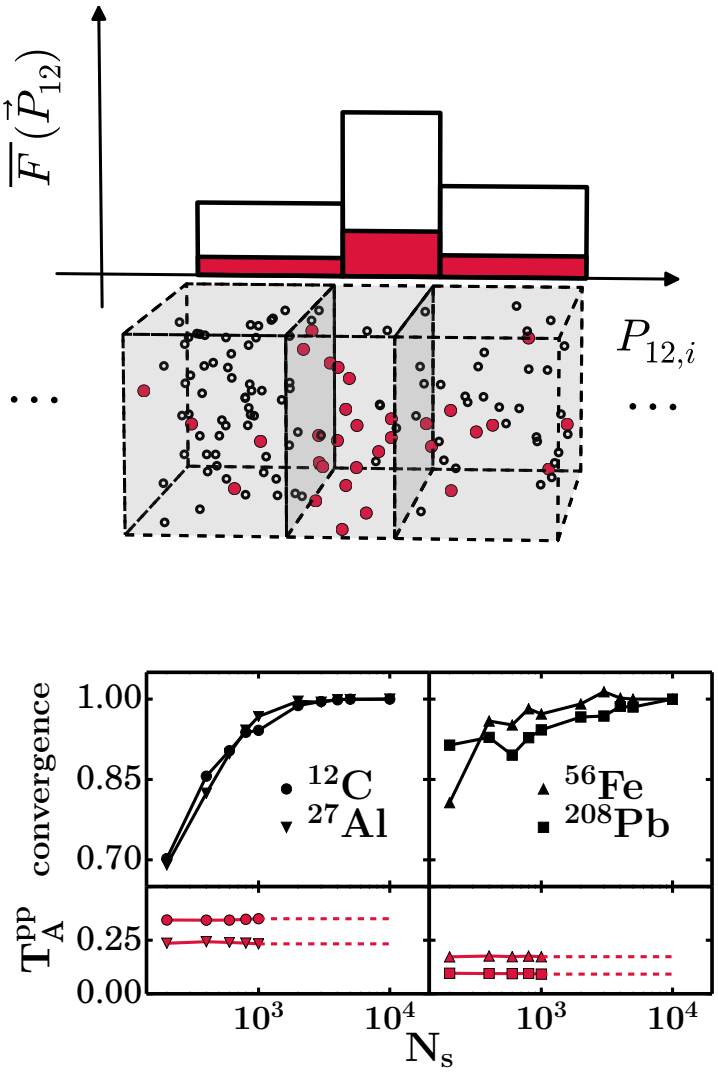

FIG. 4. (Color online) (Top) A schematic representation of the sampling procedure adopted in the $A(e,e'pN)$ calculations in kinematics covering a large phase space. The gray cubes are $\vec{P}_{12}$ bins. The black circles are those points in $\vec{P}_{12}$ space for which $A(e,e'pN)$ calculations with vanishing FSI ($\mathcal{F}_{\rm RMSGA} \equiv 1$) are done. The red dots represent the sampled points for which the RMSGA $A(e,e'pN)$ calculations are performed. The sampling weight of each bin is the bin-averaged c.m. momentum distribution $\overline{F}_A^{pN}(\vec{P}_{12})$ indicated by the white bars. The resulting bin-averaged c.m. momentum distribution including FSI is indicated by the red bars. (Bottom) The convergence as defined in Eq. (22) and the transparency T_A^{pp} of Eq. (14) as a function of the sample size N_s for $(e,e'pp)$ from ^{12}C, ^{27}Al, ^{56}Fe and ^{208}Pb in the kinematics defined by Eq. (20).

Sampling over the complete $\{x_B,Q^2,\theta_q,\vec{P}_{12}\}$ space is computationally very demanding in the RMSGA calculations. Therefore, we use stratified sampling on the binned plane-wave result $F_A^{pN}(\vec{P}_{12})$ ($\mathcal{F}_{\rm RMSGA} \equiv 1$), to generate the events in phase space (see Fig. 4 for an illustration). Thereby, after calculating $F_A^{pN}(\vec{P}_{12})$ for a large number of events, we bin the events in the $\vec{P}_{12}$ space. Next, we sample phase-space events from the bins using the bin-averaged value $\overline{F}_A^{pN}(\vec{P}_{12})$ of $F_A^{pN}(\vec{P}_{12})$ as bin weights. We then include the effect of attenuation by calculating $F_A^{pN,D}(\vec{P}_{12})$ in the RMSGA, for the sampled phase-space events. It is assumed

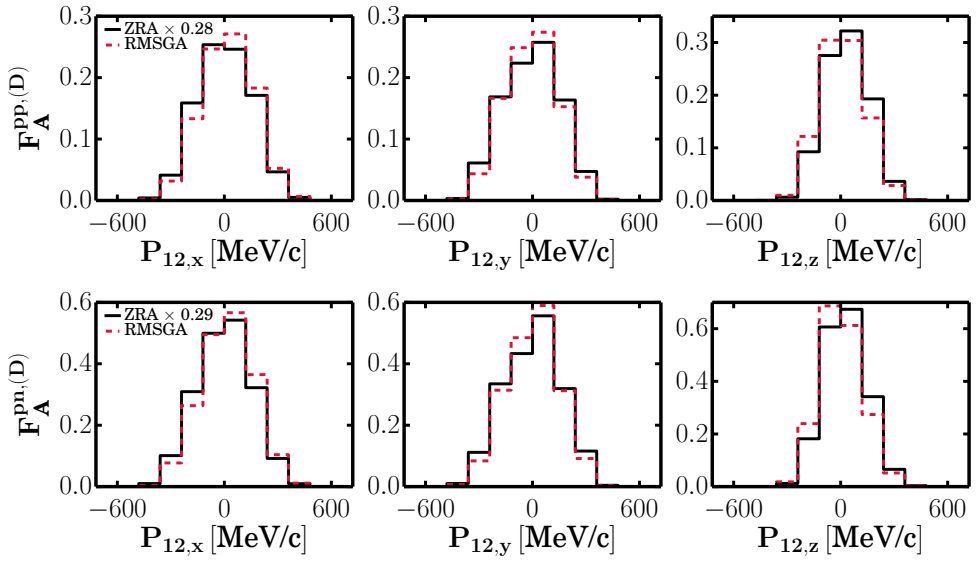

FIG. 5. (Color online) The $P_{12,x}$,$P_{12,y}$,$P_{12,z}$ dependence of the c.m. momentum distribution $F_A^{pN}(\vec{P}_{12})$ (ZRA in the plane-wave limit of the ejected nucleons) and $F_A^{pN,D}(\vec{P}_{12})$ (including elastic attenuation of the ejected nucleons) for ^{12}C$(e,e'pp)$ (top) and ^{12}C$(e,e'pn)$ (bottom) in KinB kinematics. The solid lines, obtained in the ZRA are multiplied with the nuclear transparency for ^{12}C (Table I).

that the bin averaged $\overline{F}_A^{pN,D}(\vec{P}_{12})$ of the function $F_A^{pN,D}(\vec{P}_{12})$ of the sampled events is representative for the real bin average. Using this procedure, the integrals in Eq. (10) are determined in the following way:

$$\int \mathrm{d}^3\vec{P}_{12} F_A^{pN,D}(\vec{P}_{12}) \approx \frac{V_{\vec{P}_{12}}}{N_s} \sum_{n\in\text{bins}} \overline{F}_{A,n}^{pN,D}(\vec{P}_{12}) N_n \,, \tag{21}$$

with N_n the number of events in the n-th bin, N_s the total number of phase-space events and $V_{\vec{P}_{12}}$ the considered phase-space volume in $\vec{P}_{12}$.

Fig. 4 displays the convergence of the plane-wave integrated c.m. distribution, defined as,

$$\frac{\left[\int \mathrm{d}^3\vec{P}_{12} F_A^{pN}(\vec{P}_{12})\right]_{N_s}}{\left[\int \mathrm{d}^3\vec{P}_{12} F_A^{pN}(\vec{P}_{12})\right]_{N_s=10^4}} \,, \tag{22}$$

and the nuclear transparency T_A^{pp} (Eq. (14)) as a function of the number of sampled events N_s. The convergence at a 1000 samples is between 94% and 97% for all nuclei. We perform the RMSGA calculations for this sample size. From Fig. 4 it is clear that the nuclear transparency is almost independent of the sample size. This indicates that the ZRA and RMSGA (≡ZRA+RMSGA) have almost identical convergence behavior as a function of the sample size N_s.

Figures 5 and 6 show the computed c.m. distribution for $A(e,e'pp)$ and $A(e,e'pn)$. Both undistorted (ZRA, $F^{pN}(\vec{P}_{12})$) and distorted (RMSGA, $F^{pN,D}(\vec{P}_{12})$) results are shown. It is clear that for all target nuclei considered, attenuation effects on the ejected nucleons marginally affect the shape of the c.m. momentum distribution. Note that the shape of the c.m. momentum distribution is fairly similar for all four nuclei considered. This illustrates that SRC are connected with the local and "universal" short-distance behavior of nucleon pairs [3].

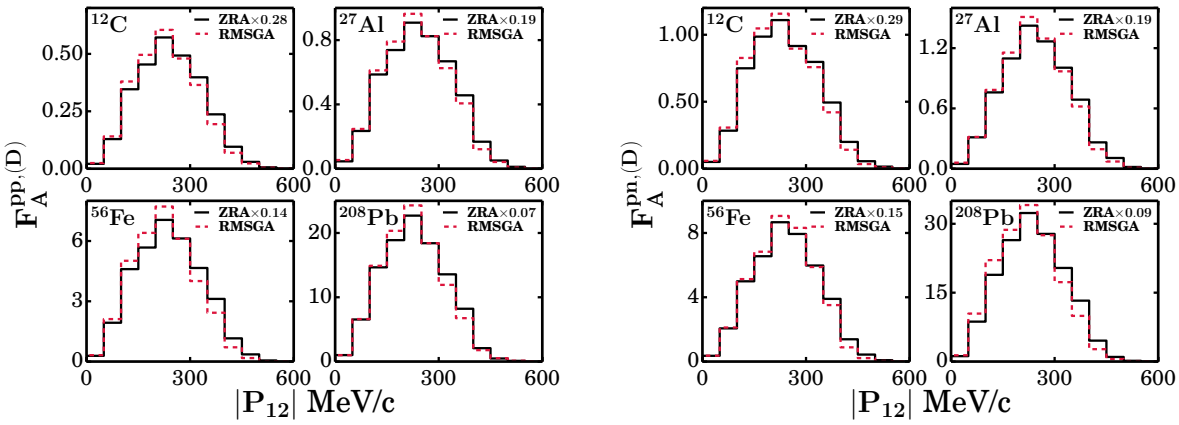

FIG. 6. (Color online) The c.m. momentum distribution in the ZRA $F_A^{pN,(D)}(\vec{P}_{12})$ with and without RMSGA attenuation corrections for $A(e,e'pp)$ (left) and $A(e,e'pn)$ (right) in KinB kinematics. As in Fig. 5 the ZRA results are multiplied with the corresponding T_A^{pN} (see Table I).

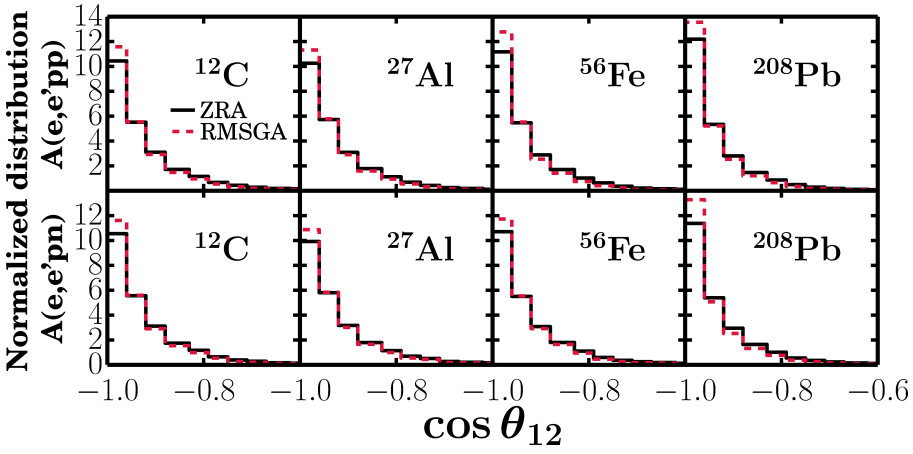

FIG. 7. (Color online) The normalized θ_{12} distributions for $A(e,e'pp)$ (top) and $A(e,e'pn)$ (bottom) in KinB kinematics.

The opening angle θ_{12} is defined as the angle between the two initial nucleon momenta, $\cos\theta_{12} = \left(\vec{k}_1 \cdot \vec{k}_2\right) / \left(|\vec{k}_1||\vec{k}_2|\right)$. Nucleon pairs susceptible to SRC have a high relative momentum and a small c.m momentum, reminiscent of "back-to-back" motion. This causes the opening-angle distribution of SRC pairs to be biased towards backward angles. Figure 7 displays the normalized θ_{12} distributions as they can be extracted from the undistorted and distorted distributions $F^{pN}(\vec{P}_{12})$ and $F^{pN,D}(\vec{P}_{12})$ for the different nuclei. The inclusion of elastic attenuation mechanisms as computed in the RMSGA framework, has a relatively small effect on the opening-angle distribution. A slight tendency to effectively increase the contributions of the $\cos\theta_{12} \approx -1$ events is observed.

Charge-exchange reactions in the final state will mix the c.m. momentum distribution and the opening-angle distribution of the initial pp- and pn-pairs. For example initial pp-pairs, with a c.m. momentum distribution $F_A^{pp,D}(\vec{P}_{12})$, can change into pn-pairs, contaminating $F_A^{pn,D}(\vec{P}_{12})$ and vice versa. From Figs. 5

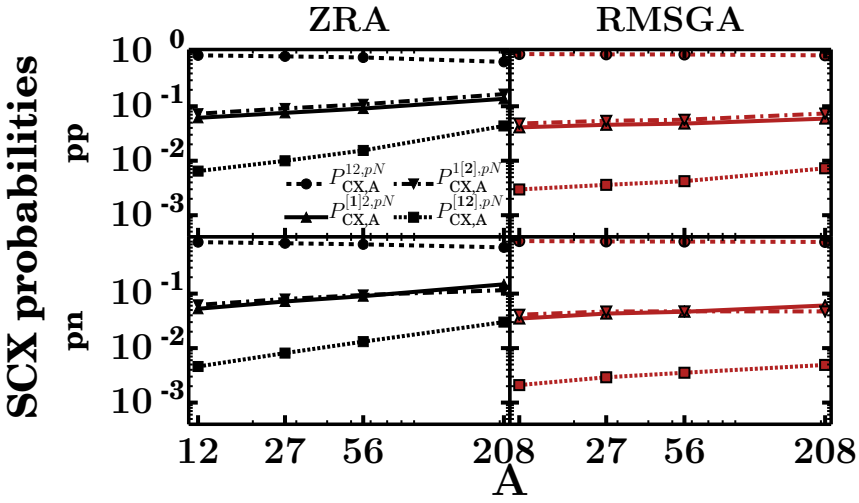

FIG. 8. (Color online) The mass dependence of the SCX probabilities for $A(e,e'pp)$ (top) and $A(e,e'pn)$ (bottom) for KinB. $P^{12,pN}_{\rm CX,A}$ is the probability that no charge exchange scattering occurs. $P^{[\mathbf{1}],2,pN}_{\rm CX,A}$, $P^{1,[\mathbf{2}],pN}_{\rm CX,A}$ are the probabilities that either the leading or the recoil nucleon undergoes charge exchange. $P^{[\mathbf{1},\mathbf{2}],pN}_{\rm CX,A}$ is the probability that both the leading proton and recoiling nucleon undergo charge exchange. The black lines (left) are calculated in the ZRA, the red ones (right) include RMSGA attenuation.

	R_A^{pp}	T_A^{pp}	$\widetilde{R}_A^{pp}$	R_A^{pn}	T_A^{pn}	$\widetilde{R}_A^{pn}$	$(T_A^p)^2$
^{12}C	1.00	0.280	1.00	1.00	0.286	1.00	0.26
^{27}Al	2.89	0.186	$1.91^{+0.01}_{-0.01}$	2.52	0.186	$1.65^{+0.01}_{-0.01}$	–
^{56}Fe	5.89	0.138	$2.85^{+0.01}_{-0.01}$	4.82	0.150	$2.49^{+0.01}_{-0.01}$	0.10
^{208}Pb	17.44	0.073	$4.96^{+0.11}_{-0.14}$	18.80	0.093	$6.00^{+0.01}_{-0.01}$	0.05

TABLE I. The numerical results for the cross-section ratios R_A^{pN} (ZRA) and the corresponding transparencies (Eq. 14) calculated with the RMSGA. $\widetilde{R}_A^{pN}$ are the cross section ratios corrected for FSI (RMSGA and SCX). For vanishing SCX probabilities $\widetilde{R}_A^{pN}$ is equal to $R_A^{pN}T_A^{pN}/T_{^{12}\rm C}^{pN}$. T_A^p is the measured $A(e,e'p)$ transparency [29].

to 7 it is clear that throughout the mass table the $A(e,e'pp)$ and $A(e,e'pn)$ c.m. momentum distributions as well as the opening angle distributions are very similar. The effect of SCX on the shape of these distributions is close to negligible. The SCX probabilities calculated in the ZRA and ZRA+RMSGA (Eq. 6) are displayed in Fig. 8. The RMSGA clearly diminishes the SCX probabilities. This can be understood in the following way: the events most susceptible to SCX reactions are those whereby the ejected nucleon pair traverses large distances in the recoiling nucleus. These events are most suppressed by the attenuation, causing the SCX probabilities to decrease.

Table I lists the cross-section ratios R_A^{pN} calculated in the ZRA. These are approximately equal to the SRC pair ratios. The nuclear transparencies T_A^{pN} calculated in the RMSGA (Eq. (14)) and the FSI (RMSGA+SCX) corrected cross section ratios $\widetilde{R}_A^{pN}$ are listed as well. The RMSGA attenuates the cross sections significantly, ranging from a factor of four for ^{12}C to fourteen for ^{208}Pb. The inclusion of SCX has a very modest effect on the cross section ratios $\widetilde{R}_A^{pN}$, the largest effect is approximately 8% for $\widetilde{R}^{pp}_{^{208}\rm Pb}$.

The mass dependence of the calculated transparencies for the "4π" kinematics KinB follow a power law

($T_A^{pN} \propto A^{\lambda}$) and are displayed in Fig. 9. Up to now we concentrated on the kinematics accessed in the experiment of Ref. [21].

We test the robustness of our methodology by applying it to the kinematics accessed in the ^{12}C$(e, e'pp)$ measurements of Ref. [18], denoted KinA. It corresponds with a very selective phase space whereby the scattered electron and leading proton are detected with two high resolution spectrometers at the fixed central angles 19.5° (electron) and -35.8° (leading proton) relative to the incoming electron beam. The angular acceptance is ±0.03 mrad (±0.06 mrad) in the horizontal (vertical) plane. The initial (final) electron momentum is fixed at 4.627 GeV/c (3.724 GeV/c). The leading proton momentum is $1.42 \pm 4\%$ GeV/c. The recoiling proton is detected at the central angle -99° with an angular acceptance of 96 msr. These kinematics are finely tuned and optimized to select knockout reactions of initial back-to-back pairs. For example, more than 80% of the available phase space has opening angle $\cos\theta_{12} < -0.9$.

The power-law dependencies of the T_A^{pN} transparencies in KinA and KinB kinematics are very similar and are included in Fig. 9. We find $T_A^{pp} \propto A^{-0.46\pm0.02}$ (KinB), $T_A^{pp} \propto A^{-0.49\pm0.06}$ (KinA), $T_A^{pn} \propto A^{-0.38\pm0.03}$ (KinB) and $T_A^{pn} \propto A^{-0.42\pm0.05}$ (KinA). This indicates that the mass dependence of the transparency is robust. The absolute value of the KinA transparencies is lower by approximately a factor of 2 compared to the KinB results. Given the small phase space of KinA we cannot make a detailed study of the c.m. momentum distribution $F_A^{pN,(D)}$ and the opening-angle distribution, as was done for KinB. Indeed, KinA kinematics only covers restricted ranges in $\vec{P}_{12}$ and $\cos\theta_{12}$.

Next, we outline an alternative method to account for the mass dependence of T_A^{pN}. The transparency T_A^p of $A(e, e'p)$ processes can be interpreted as the probability of a single proton leaving the nucleus after virtual photon excitation. Recent measurements [25] have confirmed that the A dependence of the T_A^p can be captured by the power-law $A^{-0.33}$ [33] . One could naively expect that $T_A^{pp} \approx T_A^p T_A^p \approx A^{-0.66}$. Upon squaring the T_A^p one assumes that the two protons are independent. This is in obvious contradiction with the ZRA picture for SRC-driven two-nucleon knockout reaction where the nucleon pair is maximally correlated: finding one nucleon at the spatial coordinate $\vec{R}_{12}$ fixes the second nucleon's spatial coordinate. To obtain a deeper and more intuitive understanding of the A dependence of T_A^{pN} we have developed a toy model detailed in Appendix A. Thereby the nucleus is treated as a uniform sphere with radius $R = 1.2A^{-\frac{1}{3}}$ fm and density $\rho = \frac{A}{4/3\pi R^3} = 0.138$ fm^{-3}. We calculate the transparencies using a semi-classical approach analogous to the method used to compute the SCX probabilities. The attenuation is derived using the scattering probabilities as in Eq. (7), where the scattering cross section is treated as a model parameter. We derive a range $\lambda \in [-0.37, -0.78]$ for the exponent λ in $T_A^{pN} \propto A^{\lambda}$. This range is established by varying two parameters: (1) the nucleon-nucleus cross section describing the attenuation, (2) the θ_{12} distribution for the nucleon pair is varied from a uniform distribution (no angular correlation) to a back-to-back delta function $\delta(\theta_{12} - \pi)$. The exponents derived involving the full calculations (Fig. 9) are well in agreement with the toy model. The toy model predicts that for increasingly backward peaked θ_{12} distributions the exponent λ becomes more negative. The toy model also explains why the T_A^{pN} diminishes as one increasingly selects back-to-back nucleons.

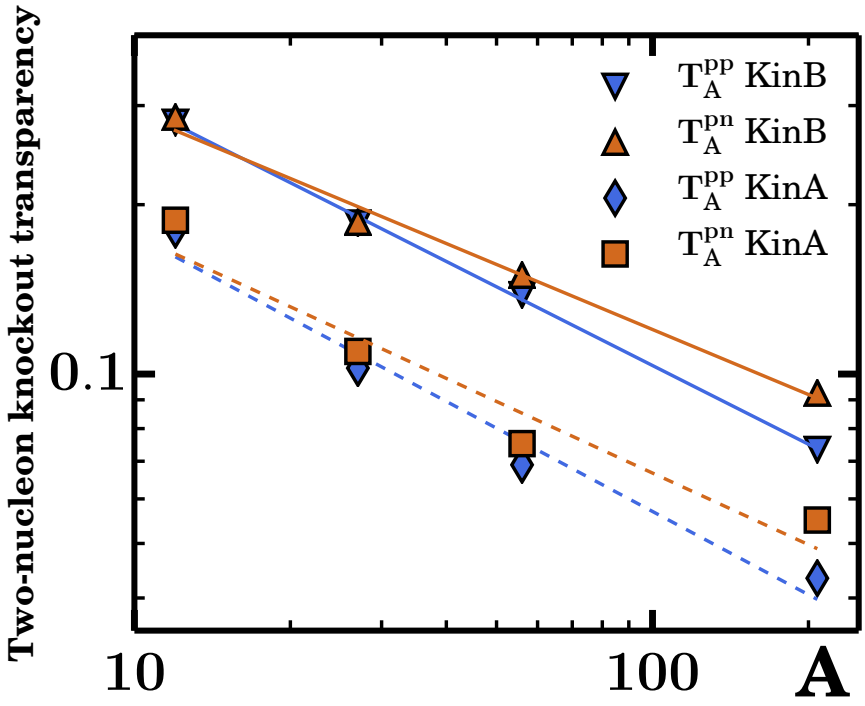

FIG. 9. (Color online) Mass dependence of the two-nucleon knockout transparency calculated according to Eq. (14). The lines are power-law fits ($\sim A^{\lambda}$) to the numerical predictions. KinB denotes the results for the $A(e,e'pN)$ kinematics accessed in Ref. [21] covering a large phase space. KinA are the transparencies calculated for $A(e,e'pN)$ in the kinematics accessed in Ref. [18] with very selective phase space.

IV. SUMMARY

We have studied the impact of final-state interactions in SRC-driven exclusive $A(e,e'pN)$ processes. Attenuation through elastic and soft inelastic rescattering as well as single-charge exchange processes are included in the description of the FSI. We applied our model to two very different kinematics probing SRC pairs and four target nuclei from carbon to lead. It is shown that the inclusion of FSI has a limited effect on the extracted shapes of the c.m. momentum and opening-angle distributions of the correlated nucleon pair. The cross section, however, is significantly attenuated by the FSI. The absolute values of the transparencies depend on the kinematics and we find $T_A^{pN} \approx 0.2 - 0.3$ for a light nucleus like ^{12}C and $T_A^{pN} \approx 0.04 - 0.07$ for a heavy nucleus like ^{208}Pb. The mass dependence of the nuclear transparency is more robust. We find $T_A^{pp} \propto A^{-0.46\pm0.02}$ and $T_A^{pn} \propto A^{-0.38\pm0.03}$ in "4π" kinematics. For the highly selective kinematics, that exclusively probes back-to-back nucleons, we find $T_A^{pp} \propto A^{-0.49\pm0.06}$ and $T_A^{pn} \propto A^{-0.42\pm0.05}$. Both are softer than one would expect from a doubling of the power found for single-nucleon knockout ($T_A^{p} \propto A^{-0.33}$). The values for the exponent λ in the power-law dependence of $T_A^{pN} \propto A^{\lambda}$ are tested against the results of a toy model which allows us to set bounds on values for λ. We find the calculated values to be well within these bounds, $\lambda \in [-0.37, -0.78]$.

It is well known that exclusive $A(e,e'p)$ reactions, populating low-lying states in the residual $(A-1)^*$ nucleus, are proportional to the FSI corrected single-particle momentum distributions for specific hole states.

Along similar lines, the SRC-driven $A(e,e'pN)$ cross section is proportional to the c.m. distribution of close-proximity pairs. We find that the FSI only modestly affect the shape of the c.m. distribution, with the width of the distribution barely changing. In essence, to a reasonable degree of accuracy, the aggregated effect of FSI for exclusive $A(e,e'pN)$ processes is a sizeable reduction of the plane-wave cross sections. This is a remarkable result that could help to quantify the effect of two-nucleon knockout contributions to quasi-elastic neutrino-nucleus and anti-neutrino nucleus responses [34].

ACKNOWLEDGMENTS

This work is supported by the Research Foundation Flanders (FWO-Flanders) and by the Interuniversity Attraction Poles Programme P7/12 initiated by the Belgian Science Policy Office. The computational resources (Stevin Supercomputer Infrastructure) and services used in this work were provided by Ghent University, the Hercules Foundation and the Flemish Government.

[1] R. B. Wiringa, R. Schiavilla, S. C. Pieper, and J. Carlson, Phys. Rev. C **89**, 024305 (2014), URL `http://link.aps.org/doi/10.1103/PhysRevC.89.024305`.

[2] A. Rios, A. Polls, and W. H. Dickhoff, Phys. Rev. C **89**, 044303 (2014), URL `http://link.aps.org/doi/10.1103/PhysRevC.89.044303`.

[3] J. Ryckebusch, W. Cosyn, and M. Vanhalst, J. Phys. **G42**, 055104 (2015), 1405.3814.

[4] K. S. Egiyan, N. Dashyan, M. Sargsian, S. Stepanyan, L. B. Weinstein, G. Adams, P. Ambrozewicz, E. Anciant, M. Anghinolfi, B. Asavapibhop, et al. (CLAS Collaboration), Phys. Rev. C **68**, 014313 (2003), nucl-ex/0301008, URL `http://link.aps.org/doi/10.1103/PhysRevC.68.014313`.

[5] K. S. Egiyan, N. B. Dashyan, M. M. Sargsian, M. I. Strikman, L. B. Weinstein, G. Adams, P. Ambrozewicz, M. Anghinolfi, B. Asavapibhop, G. Asryan, et al. (CLAS Collaboration), Phys. Rev. Lett. **96**, 082501 (2006), nucl-ex/0508026, URL `http://link.aps.org/doi/10.1103/PhysRevLett.96.082501`.

[6] N. Fomin, J. Arrington, R. Asaturyan, F. Benmokhtar, W. Boeglin, P. Bosted, A. Bruell, M. H. S. Bukhari, M. E. Christy, E. Chudakov, et al., Phys. Rev. Lett. **108**, 092502 (2012), 1107.3583, URL `http://link.aps.org/doi/10.1103/PhysRevLett.108.092502`.

[7] O. Hen, D. W. Higinbotham, G. A. Miller, E. Piasetzky, and L. B. Weinstein, Int. J. Mod. Phys. **E22**, 1330017 (2013), 1304.2813.

[8] G. Rosner, Prog. Part. Nucl. Phys. **44**, 99 (2000), ISSN 0146-6410, URL `http://www.sciencedirect.com/science/article/pii/S0146641000000636`.

[9] K. I. Blomqvist et al., Phys. Lett. B **421**, 71 (1998).

[10] C. J. G. Onderwater, K. Allaart, E. C. Aschenauer, T. S. Bauer, D. J. Boersma, E. Cisbani, S. Frullani, F. Garibaldi, W. J. W. Geurts, D. L. Groep, et al., Phys. Rev. Lett. **78**, 4893 (1997), URL `http://link.aps.org/doi/10.1103/PhysRevLett.78.4893`.

[11] C. J. G. Onderwater, K. Allaart, E. C. Aschenauer, T. S. Bauer, D. J. Boersma, E. Cisbani, W. H. Dickhoff, S. Frullani, F. Garibaldi, W. J. W. Geurts, et al., Phys. Rev. Lett. **81**, 2213 (1998), URL `http://link.aps.org/doi/10.1103/PhysRevLett.81.2213`.

[12] R. Starink, M. van Batenburg, E. Cisbani, W. Dickhoff, S. Frullani, F. Garibaldi, C. Giusti, D. Groep, P. He-

imberg, W. Hesselink, et al., Phys. Lett. B **474**, 33 (2000).

[13] J. Ryckebusch and W. Van Nespen, Eur. Phys. J. A **20**, 435 (2004), ISSN 1434-6001, URL http://dx.doi.org/10.1140/epja/i2003-10175-2.

[14] J. Ryckebusch, V. V. der Sluys, K. Heyde, H. Holvoet, W. V. Nespen, M. Waroquier, and M. Vanderhaeghen, Nucl. Phys. A **624**, 581 (1997), ISSN 0375-9474, URL http://www.sciencedirect.com/science/article/pii/S0375947497003850.

[15] C. Giusti, F. D. Pacati, K. Allaart, W. J. W. Geurts, W. H. Dickhoff, and H. Müther, Phys. Rev. C **57**, 1691 (1998), URL http://link.aps.org/doi/10.1103/PhysRevC.57.1691.

[16] A. Tang, J. W. Watson, J. Aclander, J. Alster, G. Asryan, Y. Averichev, D. Barton, V. Baturin, N. Bukhtoyarova, A. Carroll, et al., Phys. Rev. Lett. **90**, 042301 (2003), nucl-ex/0206003, URL http://link.aps.org/doi/10.1103/PhysRevLett.90.042301.

[17] R. A. Niyazov, L. B. Weinstein, G. Adams, P. Ambrozewicz, E. Anciant, M. Anghinolfi, B. Asavapibhop, G. Asryan, G. Audit, T. Auger, et al. (CLAS Collaboration), Phys. Rev. Lett. **92**, 052303 (2004), nucl-ex/0308013, URL http://link.aps.org/doi/10.1103/PhysRevLett.92.052303.

[18] R. Shneor, P. Monaghan, R. Subedi, B. D. Anderson, K. Aniol, J. Annand, J. Arrington, H. Benaoum, F. Benmokhtar, P. Bertin, et al. (Jefferson Lab Hall A Collaboration), Phys. Rev. Lett. **99**, 072501 (2007), nucl-ex/0703023, URL http://link.aps.org/doi/10.1103/PhysRevLett.99.072501.

[19] R. Subedi, R. Shneor, P. Monaghan, B. Anderson, K. Aniol, J. Annand, J. Arrington, H. Benaoum, F. Benmokhtar, W. Boeglin, et al., Science **320**, 1476 (2008).

[20] I. Korover, N. Muangma, O. Hen, R. Shneor, V. Sulkosky, A. Kelleher, S. Gilad, D. W. Higinbotham, E. Piasetzky, J. W. Watson, et al. (Jefferson Lab Hall A Collaboration), Phys. Rev. Lett. **113**, 022501 (2014), URL http://link.aps.org/doi/10.1103/PhysRevLett.113.022501.

[21] O. Hen, M. Sargsian, L. B. Weinstein, E. Piasetzky, H. Hakobyan, D. W. Higinbotham, M. Braverman, W. K. Brooks, S. Gilad, K. P. Adhikari, et al., Science **346**, 614 (2014), http://www.sciencemag.org/content/346/6209/614.full.pdf, URL http://www.sciencemag.org/content/346/6209/614.abstract.

[22] C. Colle, W. Cosyn, J. Ryckebusch, and M. Vanhalst, Phys. Rev. C **89**, 024603 (2014), URL http://link.aps.org/doi/10.1103/PhysRevC.89.024603.

[23] Cosyn, Wim, Vanhalst, Maarten, and Ryckebusch, Jan, EPJ Web of Conferences **66**, 02022 (2014), URL http://dx.doi.org/10.1051/epjconf/20146602022.

[24] J. Ryckebusch, Phys. Lett. B **383**, 1 (1996), ISSN 0370-2693, URL http://www.sciencedirect.com/science/article/pii/0370269396007253.

[25] O. Hen, H. Hakobyan, R. Shneor, E. Piasetzky, L. Weinstein, W. Brooks, S. M.-T. Beck, S. Gilad, I. Korover, A. Beck, et al., Phys. Lett. B **722**, 63 (2013), ISSN 0370-2693, URL http://www.sciencedirect.com/science/article/pii/S0370269313002906.

[26] O. Hen and E. Piasetzky, (private communication).

[27] C. Colle, O. Hen, W. Cosyn, I. Korover, E. Piasetzky, J. Ryckebusch, and L. B. Weinstein, Phys. Rev. C **92**, 024604 (2015), URL http://link.aps.org/doi/10.1103/PhysRevC.92.024604.

[28] J. Ryckebusch, D. Debruyne, P. Lava, S. Janssen, B. Van Overmeire, and T. Van Cauteren, Nucl. Phys. A **728**, 226 (2003), nucl-th/0305066.

[29] W. Cosyn and J. Ryckebusch, Phys. Rev. C **87**, 064608 (2013), 1301.1904.

[30] R. J. Furnstahl, B. D. Serot, and H.-B. Tang, Nucl. Phys. A **615**, 441 (1997), nucl-th/9608035.

[31] M. Jain, M. L. Evans, G. Glass, J. C. Hiebert, R. A. Kenefick, L. C. Northcliffe, B. E. Bonner, J. E. Simmons,

C. W. Bjork, P. J. Riley, et al., Phys. Rev. C **30**, 566 (1984), URL http://link.aps.org/doi/10.1103/PhysRevC.30.566.

[32] W. R. Gibbs and B. Loiseau, Phys. Rev. C **50**, 2742 (1994), URL http://link.aps.org/doi/10.1103/PhysRevC.50.2742.

[33] P. Lava, M. Martinez, J. Ryckebusch, J. Caballero, and J. Udias, Phys. Lett. B **595**, 177 (2004), ISSN 0370-2693, URL http://www.sciencedirect.com/science/article/pii/S0370269304007646.

[34] R. Acciarri, C. Adams, J. Asaadi, B. Baller, T. Bolton, C. Bromberg, F. Cavanna, E. Church, D. Edmunds, A. Ereditato, et al., Phys. Rev. D **90**, 012008 (2014), URL http://link.aps.org/doi/10.1103/PhysRevD.90.012008.

Appendix A: Qualitative model for the mass dependence of nuclear transparencies

In order to gain a qualitative understanding of the mass dependence of the transparency in knockout reactions we develop a toy model. In Sec. A 1 we introduce several scenarios each of which provides predictions for the mass dependence of the nuclear transparency. We display the numerical results in Sec. A 2.

1. Model

We model the nucleus as a homogeneous sphere with radius $R = 1.20A^{\frac{1}{3}}$ fm and constant density $\rho(\vec{r}) = 0.138$ fm^{-3}. Without attenuation the $A(e,e'N)$ cross section is proportional to the integrated density $\int \mathrm{d}^3\vec{r}\rho(\vec{r}) = A$. The attenuation with the nuclear medium is calculated with the aid of a classical survival probability $P(\vec{r})$. Given a nucleon brought into an energy continuum state at the coordinate $\vec{r}$, $P(\vec{r})$ is

$$P(\vec{r}) = \exp\left[-\sigma \int_z^{+\infty} \mathrm{d}z' \rho(\vec{r}')\right] . \tag{A1}$$

Let $\vec{r} = (x,y,z)$ and $\vec{r}' = (x,y,z')$. The integration variable z' runs along the direction of the momentum $\vec{p}$ of the outgoing nucleon. The cross section describing the scattering of the outgoing nucleon with the nuclear medium is denoted by σ. It is a measure for the aggregated effect of the attenuation. For a sphere with radius R and homogeneous density ρ the survival probability of Eq. (A1) becomes,

$$P(\vec{r}) = \exp\left[-\sigma\rho(\sqrt{R^2 - r^2\sin^2\xi} - r\cos^2\xi)\right] .$$

Here, ξ is the angle between $\vec{r}$ and $\vec{e}_p = \frac{\vec{p}}{p}$. The $A(e,e'N)$ nuclear transparency T_A^N, defined as the cross section including attenuation divided by the cross section without attenuation, is

$$T_A^N[\text{single}] \propto \frac{\int \mathrm{d}^2\Omega_p \int \mathrm{d}^3\vec{r}\rho(\vec{r})P(\vec{r})}{\int \mathrm{d}^2\Omega_p \int \mathrm{d}^3\vec{r}\rho(\vec{r})} = \frac{8\pi^2\rho \int_0^R \mathrm{d}r\, r^2 \int_{-1}^1 \mathrm{d}x \exp\left[-\sigma\rho(\sqrt{R^2 - r^2(1-x^2)} - rx)\right]}{4\pi A} . \tag{A2}$$

The integration $\int \mathrm{d}^2\Omega_p$ covers all possible outgoing-momentum directions.

For uncorrelated two-nucleon knockout the cross section is proportional to the total number of pairs $\int \mathrm{d}^3\vec{r}_1\rho(\vec{r}_1) \int \mathrm{d}^3\vec{r}_2\rho(\vec{r}_2) = A^2$. The attenuation-corrected cross section is obtained by including the survival probability for both nucleons, and one finds for the two-nucleon knockout transparency $T_A^{NN}[\text{double}]$,

$$T_A^{NN}[\text{double}] \propto \frac{\int \mathrm{d}^2\Omega_{p_1} \int \mathrm{d}^3\vec{r}_1\rho(\vec{r}_1)P(\vec{r}_1) \int \mathrm{d}^2\Omega_{p_2} \int \mathrm{d}^3\vec{r}_2\rho(\vec{r}_2)P(\vec{r}_2)}{\int \mathrm{d}^2\Omega_{p_1} \int \mathrm{d}^3\vec{r}_1\rho(\vec{r}_1) \int \mathrm{d}^2\Omega_{p_2} \int \mathrm{d}^3\vec{r}_2\rho(\vec{r}_2)} = T_A^N[\text{single}] \cdot T_A^N[\text{single}] \tag{A3}$$

Next we investigate two-nucleon knockout in the ZRA, which serves as a proxy for identifying SRC-prone nucleon pairs. The ZRA is introduced by requiring that the initial nucleons are found at the same spatial coordinate. The cross section without attenuation is proportional to,

$$\int \mathrm{d}^2\Omega_{p_1} \int \mathrm{d}^2\Omega_{p_2} \int \mathrm{d}^3\vec{r}_1 \rho(\vec{r}_1) \int \mathrm{d}^3\vec{r}_2 \rho(\vec{r}_2)\delta(\vec{r}_1-\vec{r}_2) = (4\pi)^2 \int \mathrm{d}^3\vec{r}\rho(\vec{r})^2 = (4\pi)^3\rho^2 \int_0^R \mathrm{d}r\, r^2 = (4\pi)^2\rho A \tag{A4}$$

We find that in the ZRA the two-nucleon knockout cross section is proportional to A as opposed to A^2 in the uncorrelated case. Including attenuation gives,

$$\begin{aligned}&\int \mathrm{d}^3\vec{r}\rho(\vec{r})^2 \int \mathrm{d}^2\Omega_{p_1} P_1(\vec{r}) \int \mathrm{d}^2\Omega_{p_2} P_2(\vec{r}) = \\ &16\pi^3\rho^2 \int_0^R \mathrm{d}r\, r^2 \int_{-1}^1 \mathrm{d}x \exp\left[-\sigma\rho(\sqrt{R^2-r^2(1-x^2)}-rx)\right] \int_{-1}^1 \mathrm{d}y \exp\left[-\sigma\rho(\sqrt{R^2-r^2(1-y^2)}-ry)\right]\end{aligned} \tag{A5}$$

The transparency mass dependence is then given by the ratio of Eqs. (A5) and (A4),

$$\begin{aligned}&T_A^{NN}[\mathrm{ZRA}] \propto \\ &\frac{\pi\rho}{A} \int_0^R \mathrm{d}r\, r^2 \int_{-1}^1 \mathrm{d}x \exp\left[-\sigma\rho(\sqrt{R^2-r^2(1-x^2)}-rx)\right] \int_{-1}^1 \mathrm{d}y \exp\left[-\sigma\rho(\sqrt{R^2-r^2(1-y^2)}-ry)\right]\end{aligned} \tag{A6}$$

It is well established that SRC pairs prefer back-to-back motion with anti-parallel momenta of the initial nucleon pair [16, 27]. After introducing the following angular constraints in the ZRA cross sections of Eqs. (A4),(A5),

$$\delta(\phi_1-\phi_2+\pi)\delta(\theta_1+\theta_2-\pi)\,,$$

the transparency becomes,

$$T_A^{NN}[\mathrm{ZRA+SRC}] \propto \frac{2\pi\rho}{A} \int_0^R \mathrm{d}r\, r^2 \int_{-1}^1 \mathrm{d}\cos\theta_1 \exp\left[-\sigma\rho(\sqrt{R^2-r^2(1-\cos^2\theta_1)}-r\cos\theta_1)\right] \tag{A7}$$

$$\times \int_{-1}^1 \mathrm{d}\cos\theta_2 \exp\left[-\sigma\rho(\sqrt{R^2-r^2(1-\cos^2\theta_2)}-r\cos\theta_2)\right] \delta(\theta_1+\theta_2-\pi)\,. \tag{A8}$$

With the substitution $(r,\cos\theta_1) \to (r, \ell = \sqrt{R^2-r^2(1-\cos^2\theta_1)})$, and further manipulations one finds,

$$T_A^{NN}[\mathrm{ZRA+SRC}] \propto \frac{2\pi\rho}{A} \int_0^R \mathrm{d}\ell\, \ell \exp(-2\rho\sigma\ell)\sqrt{R^2-\ell^2} \ln\left(\frac{R+\ell}{R-\ell}\right)\,. \tag{A9}$$

2. Results

The mass dependence of the T_A^N, T_A^{NN} of Eqs. (A2),(A3),(A6),(A9) is investigated by varying the mass number A in the range $[12, 208]$. A power law is fitted to the numerical results $T_A \propto A^\lambda$. Figure 10 displays the numerical results for the exponent λ as a function of σ. In the limit of vanishing attenuation ($\sigma \to 0$) the cross section equals the plane-wave one and one has $T_A \approx A^0$.

For $\sigma > 10$ fm^2 we find that the λ values approach a limit value corresponding with an extremely opaque nucleus. In this limit one expects that the single-nucleon knockout cross section is surface dominated $\propto A^{\frac{2}{3}}$

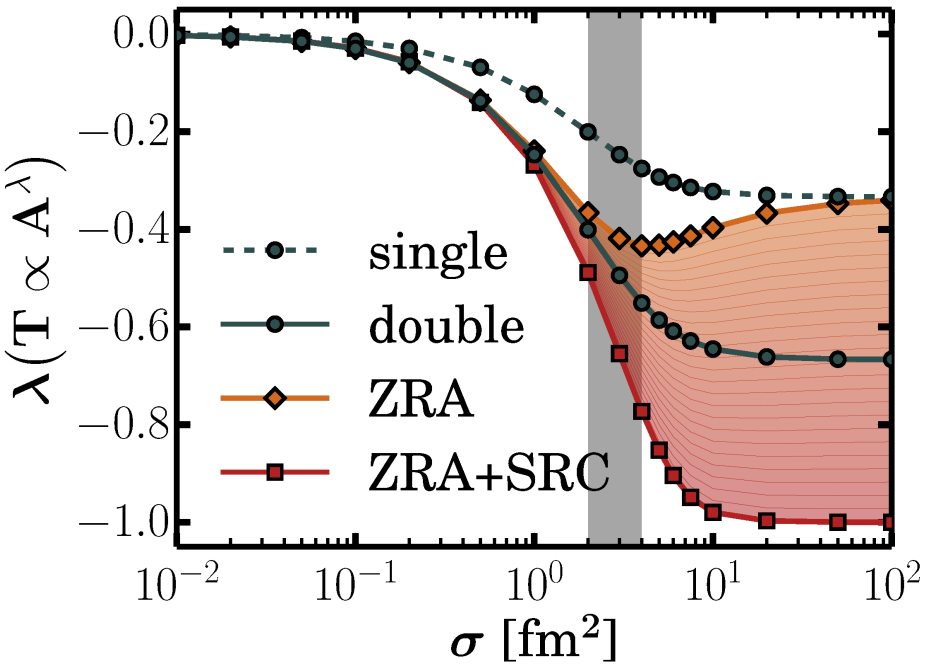

FIG. 10. (Color online) The exponents λ in $T_A^{N(N)} \propto A^{\lambda}$ as a function of the nucleon-nucleus cross section σ. The gray band corresponds with the σ of outgoing nucleon momenta $0.3 \leq p \leq 10$ GeV/c. With "single" we denote the T_A^N[single] results of Eq. (A2). With "double" we refer to the T_A^{NN}[double] results obtained with Eq. (A3) which corresponds to uncorrelated two-nucleon knockout. The "ZRA" ("ZRA+SRC") results for T_A^{NN}[ZRA] (T_A^{NN}[ZRA+SRC]) are obtained with the expressions of Eq. (A6)[Eq. (A9)].

as no nucleons originating from within the nucleus are able to escape. The mass dependence of T_A^N[single] then becomes,

$$\lim_{\sigma\to+\infty} T_A^N[\text{single}] \propto \frac{A^{\frac{2}{3}}}{A} = A^{-\frac{1}{3}}\,, \tag{A10}$$

which complies with the measured value [25, 33]. For T_A^{NN}[double], we have,

$$\lim_{\sigma\to+\infty} T_A^{NN}[\text{double}] = \lim_{\sigma\to+\infty} T_A^N[\text{single}] \cdot T_A^N[\text{single}] \propto A^{-\frac{2}{3}}\,. \tag{A11}$$

In the case of two-nucleon knockout in the ZRA the two nucleons originate from the same spatial coordinate. We again expect a surface dominated cross section as in the single nucleon knockout case, leading to the exponent $\lim_{\sigma\to+\infty}\lambda = -\frac{1}{3}$.

Including the additional constraint of back-to-back angles (ZRA+SRC in Fig. 10) will strongly favour the situation in which $(\vec{r} \perp \vec{e}_{p_1} \Leftrightarrow \vec{r} \perp \vec{e}_{p_2}) \wedge (r \approx R)$. When investigating the mass dependence of the transparency in the strong attenuation limit one finds (Fig. 10),

$$T_A^{NN}[\text{ZRA+SRC}] \propto \frac{A^0}{A^1} = A^{-1}\,. \tag{A12}$$

The cross section in the strong attenuation limit becomes **independent** of A.

3.3.3 Supplementary material

Sampling the high-dimensional phase space of exclusive two-nucleon knockout events

In this section a more detailed overview is given concerning the calculation of the distorted c.m. momentum distribution $F_A^{pN,D}(\vec{P}_{12})$, given by Eq. (5) in Sec. 3.3. Computing the $F_A^{pN,D}(\vec{P}_{12})$ for the kinematics described in [7] requires the sampling of a highly-dimensional phase space. The calculation of $F_A^{pN,D}(\vec{P}_{12})$ is computationally very demanding. This calls for an efficient way of dealing with the high-dimensionality of the phase space. First the generation of the phase space for two-nucleon knockout events is discussed, followed by the determination of $F_A^{pN,D}(\vec{P}_{12})$ over this large phase space.

As in Sec. 3.3 the scattering reaction whereby a correlated proton-nucleon pair is knocked out of the target nucleus with a hard electromagnetic probe exchanging four momentum $q = (\omega, \vec{q})$ is considered. In the impulse approximation, the exchanged three momentum $\vec{q}$ is absorbed by a single nucleon, labelled "1". The recoiling nucleon is labelled "2". Let $(\vec{k}_1, \vec{k}_2)$ and $(\vec{p}_1 = \vec{k}_1 + \vec{q}, \vec{p}_2)$ be the initial and final three-momenta of the nucleon pair. The c.m. $\vec{P}_{12}$ and relative momentum $\vec{k}_{12}$ are given by Eq. (2) in Sec. 3.3.

Choosing the reference frame with the z-axis along the momentum $\vec{k}_1$ and $\vec{q}$ in the $x-z$ plane, a two-nucleon knockout event can be characterized by 6 variables $\{Q^2 = -q^2, x_B = \frac{Q^2}{2m_N\omega}, \theta_q, \vec{P}_{12}$. θ_q is the angle of $\vec{q}$ relative to the z-axis and m_N is the nucleon mass. To ensure knockout events of SRC pairs the following kinematic constraints are imposed,

$$\theta_{\vec{p}_1,\vec{q}} \leq 25^\circ \; ; \; 0.62 < \frac{|\vec{p}_1|}{|\vec{q}|} < 0.96 \; ; \; x_B \geq 1.2; \tag{3.10}$$

$$|\vec{k}_1| \geq 300 \text{ MeV}; |\vec{p}_2| \geq 350 \text{ MeV}\,. \tag{3.11}$$

The phase space can then be sampled with the following procedure,

- draw x_B, Q^2 from the experimental (x_B, Q^2) distribution, $|\vec{q}|, \omega$ can then be calculated from x_B, Q^2.
- draw $|\vec{k}_1|$ uniformly
- draw the c.m. momentum $\vec{P}_{12}$ uniformly

θ_q is then calculated from energy conservation,

$$\begin{aligned} M_A + \omega - E_{A-2} - E_2 = E_1 = \sqrt{m_1 + (\vec{q} + \vec{k}_1)^2} \\ \cos\theta_q = \frac{E_1^2 - m_1^2 - |\mathbf{k}_1|^2 - |\mathbf{q}|^2}{2|\mathbf{k}_1||\mathbf{q}|}\,. \end{aligned} \tag{3.12}$$

Stratified importance sampling

The calculation of the distorted c.m. momentum distribution $F_A^{pN,D}(\vec{P}_{12})$ over the whole phase space is computationally very demanding. Specifically the effect of final-state interactions (FSI) calculated in the RMSGA require intensive numerical integrations. As shown

in Sec. 3.3 the major effect of including FSI on the c.m. momentum distribution is an overall attenuation of the distribution. This means that the $F_A^{pN,D}(\vec{P}_{12})$ with vanishing FSI, denoted $F_A^{pN}(\vec{P}_{12})$, is a suitable candidate for the use in importance sampling where the individual events are weighted according to the corresponding value of $F_A^{pN}(\vec{P}_{12})$. The distorted c.m. momentum distribution $F_A^{pN,D}(\vec{P}_{12})$ is then calculated for the sampled events. Rather than sampling the events directly they are first binned in the three-dimensional $\vec{P}_{12}$-space. The importance sampling procedure is then applied on these bins whereby the sampling weights are given by the bin average of $F_A^{pN}(\vec{P}_{12})$. The $F_A^{pN,D}(\vec{P}_{12})$ calculated for the limited set of sampled events is then extrapolated to the whole phase space by assuming that bin-averaged value of $F_A^{pN,D}(\vec{P}_{12})$ of the sampled events is representative for the real bin average. In other words, the mean of $F_A^{pN,D}(\vec{P}_{12})$ for a selected bin n, denoted with $\overline{F}_{A,n}^{pN,D}(\vec{P}_{12})$ is assumed to be equal to the value that would be obtained by calculating and averaging $F_A^{pN,D}(\vec{P}_{12})$ for all the events in that bin. This procedure is illustrated in Fig. 3.3. As shown in Sec. 3.3, the validity of this assumption can be investigated by examining the convergence $\int \mathrm{d}^3\vec{P}_{12} F_A^{pN,D}(\vec{P}_{12})$ (Eq. (21) in Sec. 3.3) as a function of the number of sampled events. The binning and sampling procedure can be written as approximating the integral $\int \mathrm{d}^3\vec{P}_{12} F_A^{pN,D}(\vec{P}_{12})$ in the following way,

$$\int \mathrm{d}^3\vec{P}_{12} F_A^{pN,D}(\vec{P}_{12}) = V_{\vec{P}_{12}} \langle F_A^{pN,D} \rangle = \frac{V_{\vec{P}_{12}}}{N_s} \sum_{i=1}^{N_s} F_{A,i}^{pN,D}(\vec{P}_{12,i})\,. \tag{3.13}$$

The total number of events is denoted with N_s. The summation over the individual events i is rewritten as a sum over the bins in $\vec{P}_{12}$-space. The value for $F_{A,i}^{pN,D}(\vec{P}_{12,i})$ of each event in a certain bin n is set to the average calculated from the sampled events inside that bin, $\overline{F}_{A,n}^{pN,D}(\vec{P}_{12})$,

$$\begin{aligned} \sum_{i=1}^{N_s} F_{A,i}^{pN,D}(\vec{P}_{12,i}) &= \sum_{n\in\text{bins}} \sum_{i\in n} F_{A,i}^{pN,D}(\vec{P}_{12,i}) \approx \sum_{n\in\text{bins}} \sum_{i\in n} \overline{F}_{A,n}^{pN,D}(\vec{P}_{12}) \\ &= \sum_{n\in\text{bins}} \overline{F}_{A,n}^{pN,D}(\vec{P}_{12}) \sum_{i\in n} = \sum_{n\in\text{bins}} \overline{F}_{A,n}^{pN,D}(\vec{P}_{12}) N_n\,. \end{aligned} \tag{3.14}$$

The number of events in a bin n, $\sum_{i\in n}$, is denoted as N_n. Eq. (3.13) can then be written as,

$$\int \mathrm{d}^3\vec{P}_{12} F_A^{pN,D}(\vec{P}_{12}) = \frac{V_{\vec{P}_{12}}}{N_s} \sum_{n\in\text{bins}} \overline{F}_{A,n}^{pN,D}(\vec{P}_{12}) N_n \tag{3.15}$$

From the investigated convergence behaviour of this expression in function of the number of sampled events, displayed in Fig. 4 of the article [6], it can be concluded that the approximation is very close to the true value of the integral.

Alternative approaches to calculating the integral should use importance sampling or equivalent strategies as covering the whole phase space is computationally infeasible. In order to infer the value of $F_{A,i}^{pN,D}(\vec{P}_{12,i})$ of the unsampled events from the sampled events, any multidimensional interpolation algorithm can be used, for example radial basis function (RBF) interpolation.

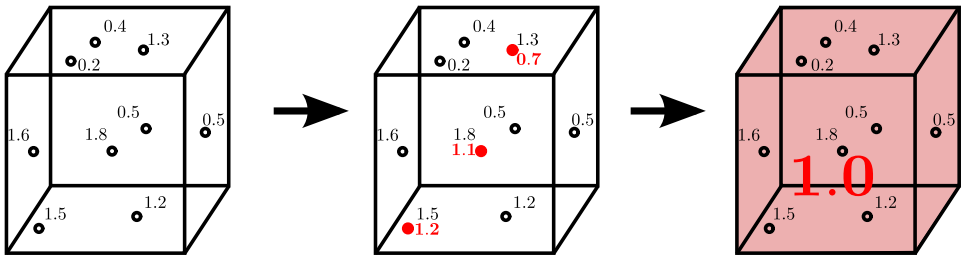

Figure 3.3 – An illustration of the sampling procedure for a specific bin in c.m. momentum ($\vec{P}_{12}$) space. The numbers are arbitrary values. The left hand side figure shows the events in the bin with their values calculated for the c.m. momentum distribution $F_A^{pN}(\vec{P}_{12})$ with vanishing FSI. The bin weight is 1.0 in this case. The centre shows three events which were sampled and for which the distorted c.m. momentum distribution $F_A^{pN,D}(\vec{P}_{12})$, including FSI, was calculated, denoted with the red fictional values offset downward. The right hand side shows a representation of the assumption that the average of $F_A^{pN,D}(\vec{P}_{12})$ is the "true" bin average which would be obtained by calculating $F_A^{pN,D}(\vec{P}_{12})$ for all the events in the bin.

3.4 Extracting the mass and isospin dependence of SRC of 2N knockout reactions

3.4.1 Introduction

In Sec. 3.1 the connection of the exclusive two-nucleon knockout reaction and SRC momentum distributions is discussed. The c.m. and relative momentum distributions are computed in Sec. 3.2 and it is shown that the SRC pairs induce high-momentum tails in the relative momentum distribution. Sec. 3.3 then follows up on how these SRC pairs with high-relative momentum can be probed in two-nucleon knockout scattering reactions. It is shown that FSI cause a large attenuation on the final cross section.

In order to infer the properties of initial SRC-pairs from the experimental two-nucleon knockout reaction, the measured cross section has to be corrected for FSI. This issue is addressed in this section [8]. The mass dependence of the number of initial SRC-prone pairs present in the ground state of a nucleus is investigated. The theoretical predictions are compared to the values extracted from the measured cross section. In order to identify the probed initial SRC pairs the measured cross sections are corrected for the attenuation and the charge-exchange effects caused by the FSI. Given the mass dependence of the initial SRC pairs it is possible to infer their internal structure

My contributions to the article presented here, published in [8], are significant contributions to the text, predominantly in sections **III**,**IV** and **V**. The results and figures presented in those sections are a part of my input as well.

Extracting the Mass Dependence and Quantum Numbers of Short-Range Correlated Pairs from A(e, e′p) and A(e, e′pp) Scattering

C. Colle,[1] O. Hen,[2] W. Cosyn,[1] I. Korover,[2] E. Piasetzky,[2] J. Ryckebusch,[1] and L.B. Weinstein[3]

[1] *Ghent University, Ghent, Belgium.*
[2] *School of Physics and Astronomy, Tel Aviv University, Tel Aviv 69978, Israel.*
[3] *Old Dominion University, Norfolk VA, USA.*

(Dated: 6 August 2015)

The nuclear mass dependence of the number of short-range correlated (SRC) proton-proton (pp) and proton-neutron (pn) pairs in nuclei is a sensitive probe of the dynamics of short-range pairs in the ground state of atomic nuclei. This work presents an analysis of electroinduced single-proton and two-proton knockout measurements off ^{12}C, ^{27}Al, ^{56}Fe, and ^{208}Pb in kinematics dominated by scattering off SRC pairs. The nuclear mass dependence of the observed $A(e,e'pp)/^{12}\mathrm{C}(e,e'pp)$ cross-section ratios and the extracted number of pp- and pn-SRC pairs are much softer than the mass dependence of the total number of possible pairs. This is in agreement with a physical picture of SRC affecting predominantly nucleon-nucleon pairs in a nodeless relative-S state of the mean-field basis.

PACS numbers: 25.30.Rw, 25.30.Fj, 24/10.-i

I. INTRODUCTION

The nuclear momentum distribution (NMD) is often quoted as being composed of two separate parts [1–3]. Below the Fermi momentum ($k_F \approx 250$ MeV/c) single nucleons move as independent particles in a mean field created by their mutual interactions. Above the Fermi momentum ($k > k_F$) nucleons predominantly belong to short-range correlated (SRC) pairs with high relative and low center-of-mass (c.m.) momenta, where high and low are relative to the Fermi momentum [4–8]. In addition to its intrinsic interest, the NMD and its division into mean-field and correlated parts is relevant to two-component Fermi systems [9], neutrino physics [10, 11], and the symmetry energy of nuclear matter [12].

The mean-field and long-range aspects of nuclear dynamics have been studied extensively since the dawn of nuclear physics. The effect of long-range correlations on the NMDs is limited to momenta which do not extend far beyond k_F [13]. Study of the short-range aspects of nuclear dynamics has blossomed with the growing availability of high-energy high-intensity electron and proton accelerators. Recent experiments confirm the predictions that SRC pairs dominate the high-momentum tails ($k > k_F$) of the NMDs [4–7], accounting for 20-25 % of the NMD probability density [14–17]. These high-momentum tails have approximately the same shape for all nuclei [2, 3, 9, 14–18], differing only by scale factors which can be interpreted as a measure of the relative number of SRC pairs in the different nuclei. In this work, we aim at understanding the underlying dynamics which give rise to this universal behavior of the high-momentum tail.

An intuitive picture describing the dynamics of nuclei including SRCs is that of independent bound nucleons moving in the nucleus, occasionally getting sufficiently close to each other to temporarily fluctuate into SRC-induced nucleon-nucleon pairs. This picture can be formally implemented in a framework in which one shifts the complexity of the nuclear SRC from the wave functions to the operators by calculating independent-particle model (IPM) Slater determinant wave functions and acting on them with correlation operators to include the effect of SRCs [18–20]. The observed number of proton-proton (pp) and proton-neutron (pn) SRC pairs in various nuclei can then be used to constrain the amount and the quantum numbers of the initial-state IPM nucleon-nucleon (SRC-prone) pairs that can fluctuate dynamically into SRC pairs through the action of correlation operators.

In this paper, we will extract the relative number of pp-SRC and pn-SRC pairs in different nuclei from measurements of electroinduced two-proton and one-proton knockout cross-section ratios for medium and heavy nuclei (^{27}Al, ^{56}Fe, and ^{208}Pb) relative to ^{12}C in kinematics dominated by scattering off SRC pairs [8, 21]. In these kinematics in the plane-wave approximation $A(e,e'pp)$ cross sections are proportional to the number of pp-pairs in the nucleus and $A(e,e'p)$ cross sections are proportional to twice the number of pp pairs plus the number of pn pairs (2pp+pn). Therefore, after correcting the measured cross sections for rescattering of the outgoing nucleons from the residual nucleus (final state interactions or FSI), the relative number of pp and pn pairs will be extracted from measurements of $A(e,e'pp)/^{12}\mathrm{C}(e,e'pp)$ and $A(e,e'p)/^{12}\mathrm{C}(e,e'p)$ cross-section ratios [8].

We will then compare the $A(e,e'pp)/^{12}\mathrm{C}(e,e'pp)$ cross-section ratios and the extracted number of pp and pn pairs to factorized calculations using different models of nucleon pairs in order to deduce the quantum

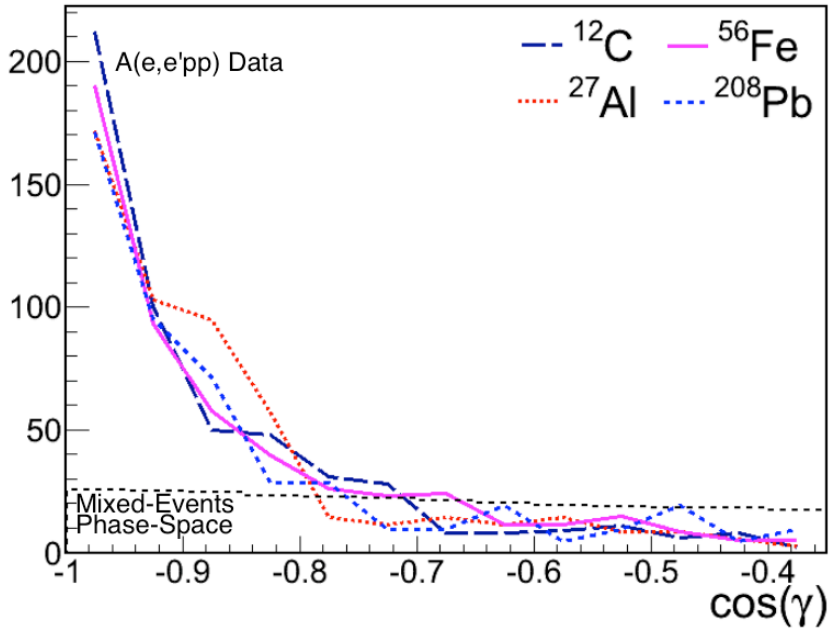

FIG. 1: (color online). The distribution (in arbitrary units) of the cosine of the angle γ between the missing momentum of the leading proton and the recoil proton for ^{12}C (dark blue long-dashed line), ^{27}Al (red dotted line), ^{56}Fe (purple solid line), and ^{208}Pb (blue dashed line). The black dashed line shows the distribution of the random phase-space extracted from mixed events.

numbers of the IPM SRC-prone pairs. We will provide strong evidence that the relative quantum numbers of the majority of the SRC-susceptible pairs are $^1S_0(1)$ for pp and $^3S_1(0)$ for pn. Hereby, we used the notation $^{2J+1}L_S(T)$ to identify the pair's quantum state (T is the total isospin).

This paper is structured as follows. The one- and two-proton knockout experiments analyzed in this paper are described in Sec. II. In Sec. III we introduce the model to calculate the FSI-corrected two-nucleon knockout cross-section ratios. Results and discussions are presented in Sec. IV. Section V contains the concluding remarks.

II. EXPERIMENT

The one- and two-proton knockout measurements analyzed in this paper were described in [8] and its supplemental information. They were carried out using the CEBAF Large Acceptance Spectrometer (CLAS) [22], located in Hall-B of the Thomas Jefferson National Accelerator Facility (Jefferson Lab) in Newport News, Virginia. The data were collected in 2004 using a 5.014 GeV electron beam incident on ^{12}C, ^{27}Al, ^{56}Fe and ^{208}Pb targets. The scattered electron and knocked out proton(s) were measured with CLAS. We selected $A(e,e'p)$ events in which the electron interacts with a single fast proton from a SRC nucleon-nucleon pair in the nucleus by requiring large four-momentum transfer ($Q^2 > 1.5$ GeV^2), Bjorken scaling parameter $x_B = \frac{Q^2}{2m_N\omega} > 1.2$ and missing momentum $300 < |\vec{p}_{\rm miss}| < 600$ MeV/c. The four-momentum transfer $Q^2 = \vec{q}\cdot\vec{q} - \left(\frac{\omega}{c}\right)^2$ where $\vec{q}$ and ω are the three-momentum and energy transferred to the nucleus respectively; m_N is the nucleon mass; the missing momentum $\vec{p}_{\rm miss} = \vec{p}_p - \vec{q}$, and $\vec{p}_p$ is the knockout proton three-momentum. We also required that the knockout proton was detected within a cone of 25° of the momentum transfer $\vec{q}$ and that it carried at least 60% of its momentum (i.e. $\frac{|\vec{p}_p|}{|\vec{q}|} \geq 0.6$). To suppress contributions from inelastic excitations of the struck nucleon we limited the reconstructed missing mass of the two-nucleon system $m_{\rm miss} < 1.1$ GeV/c^2.

The $A(e,e'pp)$ event sample contains all $A(e,e'p)$ events in which a second, recoil, proton was detected with momentum greater than 350 MeV/c. Fig. 1 shows the distribution of the cosine of the angle between the initial momentum of the knockout proton and the recoil proton for these events [8]. The recoil proton is emitted almost diametrically opposite to the missing-momentum direction. The observed backward-peaked angular distributions are very similar for all nuclei and are not due to acceptance effects as shown by the

angular distribution of mixed events. These distributions are a signature of scattering on a nucleon in a SRC pair, indicating that the two emitted protons were largely back-to-back in the initial state, having large relative momentum and small c.m. momentum [6, 23]. Further evidence of scattering on a SRC nucleon pair is that the recoil proton was emitted at forward angles (i.e., angles in the range 20-60° with respect to $\vec{q}$).

The $A(e,e'p)/^{12}\mathrm{C}(e,e'p)$ and $A(e,e'pp)/^{12}\mathrm{C}(e,e'pp)$ cross-section ratios are obtained from the ratio of the measured number of events, normalized by the incident integrated electron flux and the nuclear density of each target. During the experiment all solid targets were held in the same location, the detector instantaneous rate was kept constant, and the kinematics of the measured events from all target nuclei were almost identical [8, 21]. Therefore detector acceptance effects cancel almost entirely in the $A(e,e'pp)/\mathrm{C}(e,e'pp)$ cross section ratios. Due to the large acceptance of CLAS, radiative effects affect mainly the electron kinematics. These corrections were calculated in Ref. [21] for the extraction of the $A(e,e'p)/\mathrm{C}(e,e'p)$ cross section ratio. As the electron kinematics is the same for the $A(e,e'p)$ and $A(e,e'pp)$ reactions, the same corrections are used here to extract the $A(e,e'pp)/\mathrm{C}(e,e'pp)$ cross-section ratios. See Ref. [8] for additional details.

III. FSI AND CROSS-SECTION MODEL

In order to extract the underlying relative number of pp and pn SRC pairs in nuclei from the measured cross-section ratios, we must correct the data for FSI effects [8]. Alternatively, in order to compare the measured ratios to calculations, we must correct either the data or the calculation for FSI effects. The two dominant contributions are: (1) attenuation of the outgoing nucleon(s) upon traversing the residual $A-1$ or $A-2$ nucleus, and (2) rescattering of a neutron into a proton (i.e., single charge-exchange (SCX)). SCX can lead to a pp final state which originates from a pn pair.

The effect of FSIs of the ejected pair with the remaining $A-2$ spectators was computed in a relativistic multiple-scattering Glauber approximation (RMSGA) [24, 25]. The RMSGA is a multiple-scattering formalism based on the eikonal approximation with spin-independent NN interactions. We have included both the elastic and the SCX rescattering of the outgoing nucleons with the $A-2$ spectators. The three parameters entering in the RMSGA model are taken from NN scattering data and yield an excellent description of the world's $\mathrm{A}(e,e'p)$ transparency data [25]. In this work no free parameters are tuned to model the FSI effects in the $A(e,e'p)$ and $A(e,e'pp)$ data under study. The RMSGA yields attenuation coefficients that are similar to the power-law results obtained in nuclear transparency measurements [21]. For those reasons, we estimate the systematic uncertainty related to the FSI calculation as small.

The SCX probabilities are calculated in a semi-classical approximation. The probability of charge-exchange re-scattering for a nucleon with initial IPM quantum numbers α which is brought in a continuum state at the coordinate $\vec{r}$ is modeled by,

$$P_{\mathrm{CX}}^{\alpha(\beta)}(\vec{r}\,) = 1 - \exp[-\sigma_{\mathrm{CX}}(s) \int_z^{+\infty} \mathrm{d}z' \rho^{\alpha\beta}(z')] \,. \tag{1}$$

The z-axis is chosen along the direction of propagation of the nucleon with initial quantum numbers α. The quantum numbers of the correlated partner in the SRC pair are denoted with β. The $\rho^{\alpha\beta}$ is the IPM one-body density of the residual nucleus available for SCX reactions. The $\rho^{\alpha\beta}$ is determined as the IPM density of the target nucleus, minus the contribution from the single-particle orbitals α and β. Obviously, for an ejected proton (neutron) only the neutron (proton) density of the residual nucleus affects SCX reactions. $\sigma_{\mathrm{CX}}(s)$ in Eq. (1), with s the total c.m. energy squared of the two nucleons involved in the SCX [26], can be extracted from elastic proton-neutron scattering data [27].

As outlined in Refs. [23, 28], in the spectator approximation it is possible to factorize the $A(e,e'pN)$ cross section in kinematics probing short-range correlated pairs as

$$\frac{\mathrm{d}^8\sigma\,[A(e,e'pN)]}{\mathrm{d}^2\Omega_{e'}\mathrm{d}^3\vec{P}_{12}\mathrm{d}^3\vec{k}_{12}} = K_{epN}\sigma_{epN}(\vec{k}_{12})F_{\mathrm{A}}^{pN(D)}(\vec{P}_{12})\,, \tag{2}$$

where $\Omega_{e'}$ is the solid angle of the scattered electron, and $\vec{k}_{12}$ and $\vec{P}_{12}$ are the relative and c.m. momenta of the nucleon pair that absorbed the virtual-photon. The K_{epN} is a kinematic factor and $\sigma_{epN}(\vec{k}_{12})$ is the cross section for virtual-photon absorption on a correlated pN pair. The $F_{\mathrm{A}}^{pN(D)}(\vec{P}_{12})$ is the distorted two-body c.m. momentum distribution of the correlated pN pair. In the limit of vanishing FSIs, it is the conditional c.m. momentum distribution of a pN pair with relative $\mathrm{S}_{n=0}$ quantum numbers. Distortions of $F_{\mathrm{A}}^{pN(D)}(\vec{P}_{12})$

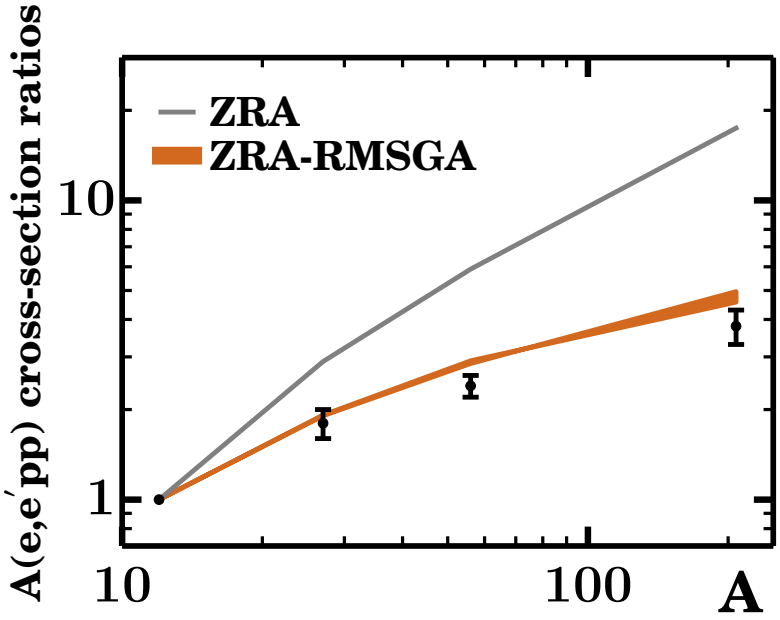

FIG. 2: (color online). The mass dependence of the $A(e,e'pp)/^{12}\mathrm{C}(e,e'pp)$ cross-section ratios. The points show the measured, uncorrected, cross section ratios. The lower orange band and upper grey line denote ZRA reaction-model calculations for ^{12}C, ^{27}Al, ^{56}Fe, and ^{208}Pb based on Eq. (3) with and without FSI corrections respectively. The width of the ZRA-RMSGA band reflects the maximum possible effect of SCX.

due to FSI are calculated in the RMSGA. The factorized cross-section expression of Eq. (2) hinges on the validity of the zero-range approximation (ZRA), which amounts to putting the relative pair coordinate $\vec{r}_{12}$ to zero. The ZRA works as a projection operator for selecting the very short-range components of the IPM relative pair wave functions.

The probability for charge-exchange reactions in pN knockout is calculated on an event per event basis, using the SRC pair probability density $F_{\mathrm{A}}^{pN(D)}(\vec{R}_{12})$ in the ZRA corrected for FSI. With the aid of the factorized cross-section expression of Eq. (2), the phase-space integrated $A(e,e'pN)$ to $^{12}\mathrm{C}(e,e'pN)$ cross-section ratios can be approximately expressed as integrals over distorted c.m. momentum distributions,

$$\frac{\sigma\left[A(e,e'pN)\right]}{\sigma\left[^{12}\mathrm{C}(e,e'pN)\right]} \approx \frac{\int \mathrm{d}^2\Omega_{e'}\mathrm{d}^3\vec{k}_{12}K_{epN}\sigma_{epN}(\vec{k}_{12})\int \mathrm{d}^3\vec{P}_{12}F_{\mathrm{A}}^{pN(D)}(\vec{P}_{12})}{\int \mathrm{d}^2\Omega_{e'}\mathrm{d}^3\vec{k}_{12}K_{epN}\sigma_{epN}(\vec{k}_{12})\int \mathrm{d}^3\vec{P}_{12}F_{\mathrm{C}}^{pN(D)}(\vec{P}_{12})} = \frac{\int \mathrm{d}^3\vec{P}_{12}F_{\mathrm{A}}^{pN(D)}(\vec{P}_{12})}{\int \mathrm{d}^3\vec{P}_{12}F_{\mathrm{C}}^{pN(D)}(\vec{P}_{12})}. \quad (3)$$

In the absence of FSI, the integrated c.m. momentum distributions $\int \mathrm{d}^3\vec{P}_{12}F_{\mathrm{A}}^{pN(D)}(\vec{P}_{12})$ equal the total number of SRC-prone pN pairs in the nucleus A. Hence, the cross section ratios of Eq. (3) provide access to the relative number of SRC pN-pairs up to corrections stemming from FSI. We have evaluated the ratios of the distorted c.m. momentum distributions of Eq. (3) over the phase space covered in the experiment. Given the almost 4π phase space and the high computational requirement of multidimensional FSI calculations, we use an importance-sampling approach. The major effect on the c.m. momentum distribution $F_{\mathrm{A}}^{pN(D)}(\vec{P}_{12})$ when including FSIs is an overall attenuation, the shape is almost unaffected [23]. Motivated by this, we used the c.m. momentum distributions without FSI as sampling distribution for the importance sampling in the FSI calculations. When convergence is reached, the computed impact of FSI is extrapolated to the whole phase space.

	pp			pn		
	$S_{n=0}$	ZRA	expt.	$S_{n=0}$	ZRA	expt.
^{27}Al / ^{12}C	3.10	2.89	$2.47^{+0.55}_{-0.67}$	2.99	2.52	$2.99^{+0.26}_{-0.22}$
^{56}Fe / ^{12}C	8.60	5.89	$3.98^{+0.99}_{-1.19}$	7.72	4.82	$6.03^{+0.60}_{-0.51}$
^{208}Pb/ ^{12}C	45.29	17.44	$7.73^{+5.92}_{-7.23}$	37.62	18.80	$24.87^{+3.89}_{-3.42}$

TABLE I: The relative number of SRC pp and pn pairs calculated using $S_{n=0}$ counting and the ZRA reaction model compared to the extracted values from the measured $A(e,e'p)$ and $A(e,e'pp)$ ratios after correcting for FSI effects. The error includes the uncertainties on the cross-section ratios and FSI calculations.

IV. RESULTS AND DISCUSSIONS

Figure 2 shows the measured uncorrected $\frac{\sigma[A(e,e'pp)]}{\sigma[^{12}C(e,e'pp)]}$ cross-section ratios compared with the ZRA reaction-model calculation with and without RMSGA FSI corrections. The first striking observation is that the measured cross-section ratios increase very slowly with A (e.g., the Pb/C ratio is only 3.8 ± 0.5). For contrast, combinatorial scaling based on the number of pp pairs leads to a ratio of over 200. The ZRA-RMSGA calculations agree well with the measured data, yielding a Pb/C ratio of $4.96^{+0.11}_{-0.14}$. The ZRA and ZRA-RMSGA calculations assume that only pairs with a finite probability density at relative coordinate zero contribute to the cross-section. This is consistent with assuming that only IPM pairs in a relative $S_{n=0}$ state contribute.

Figure 3 shows the number of pp- and pn-SRC pairs in various nuclei relative to Carbon extracted from the measured $A(e,e'pp)/C(e,e'pp)$ and $A(e,e'p)/C(e,e'p)$ cross-section ratios following the method outlined in Ref. [8] with RMSGA corrections for FSI and SCX. The extracted number of pp pairs are very sensitive to SCX. If the virtual photon is absorbed on a pn pair and the neutron subsequently undergoes a single charge exchange reaction with a proton, two protons will be detected in the final state. These events must be subtracted in order to extract the number of pp-SRC pairs. As the contribution from these pn pairs to the pp final state is comparable to the number of initial pp pairs, this leads to a large uncertainty in the number of pp pairs, especially for heavy nuclei.

Figure 3 also shows the expected number of pp and pn SRC pairs relative to Carbon for different quantum numbers of the IPM pairs that can dynamically form SRC pairs through the action of correlation operators. These include (a) all possible NN pairs (i.e. $Z(Z-1)/(6\cdot 5)$ and $ZN/(6\cdot 6)$ for pp and pn pairs respectively), (b) pairs in a nodeless relative S state (i.e. $S_{n=0}$), and (c) $L \leq 1$ pairs (i.e. both S and P state pairs). Those "$S_{n=0}$" pairs are characterized by the $(n=0, L=0)$ quantum numbers for their relative orbital motion. Of all possible states for the pairs, the $S_{n=0}$ pairs have the highest probability for the two nucleons in the pair to approach each other closely. Close-proximity IPM pn pairs in a $^3S_1(0)$ state are highly susceptible to the tensor correlation operator that creates SRC pairs in a spin-triplet state with predominantly deuteron-like quantum numbers ($L=0,2; T=0; S=1$).

We determine the number of pairs in each case using an IPM harmonic-oscillator basis and performing a standard transformation to relative and center-of-mass coordinates as detailed in Ref. [29]. The relative number of pairs are displayed in Fig. 3 and listed in Table I. As can be seen, both (a) the naive combinatorial assumption and (c) the calculations that include IPM S and P pairs contributions both drastically overestimate the increase in the number of pairs with A. The ZRA and $S_{n=0}$ pairs counting calculations are in fair agreement with the extracted number of pp and pn pairs.

As both the ZRA and the $S_{n=0}$ pair counting project IPM states onto close-range pairs, we expect the two methods to produce a similar mass dependence of the number of SRC pairs The ZRA predicts a somewhat softer mass dependence ($\propto A^{1.01\pm0.02}$ vs $A^{1.12\pm0.02}$). This can be explained by the fact that the ZRA is a more restrictive projection on close-proximity pairs than the $S_{n=0}$ counting which accounts also for $\vec{r}_{12} \neq 0$ contributions.

The observed agreement with the experimental data indicates that correlation operators acting on IPM $S_{n=0}$ pairs are responsible for the largest fraction of the high-momentum nucleons in nuclei. This gives further support to the assumption that the number of IPM pairs with quantum numbers $S_{n=0}$ is a good proxy for the number of correlated pairs in any nucleus A [18, 29, 30]. This is also consistent with an analysis of the cross section of the ground-state to ground-state transition in high-resolution $^{16}O(e,e'pp)^{14}C$ measurements [31, 32] which provided evidence for the $^1S_0(1)$ dominance in SRC-prone pp pairs.

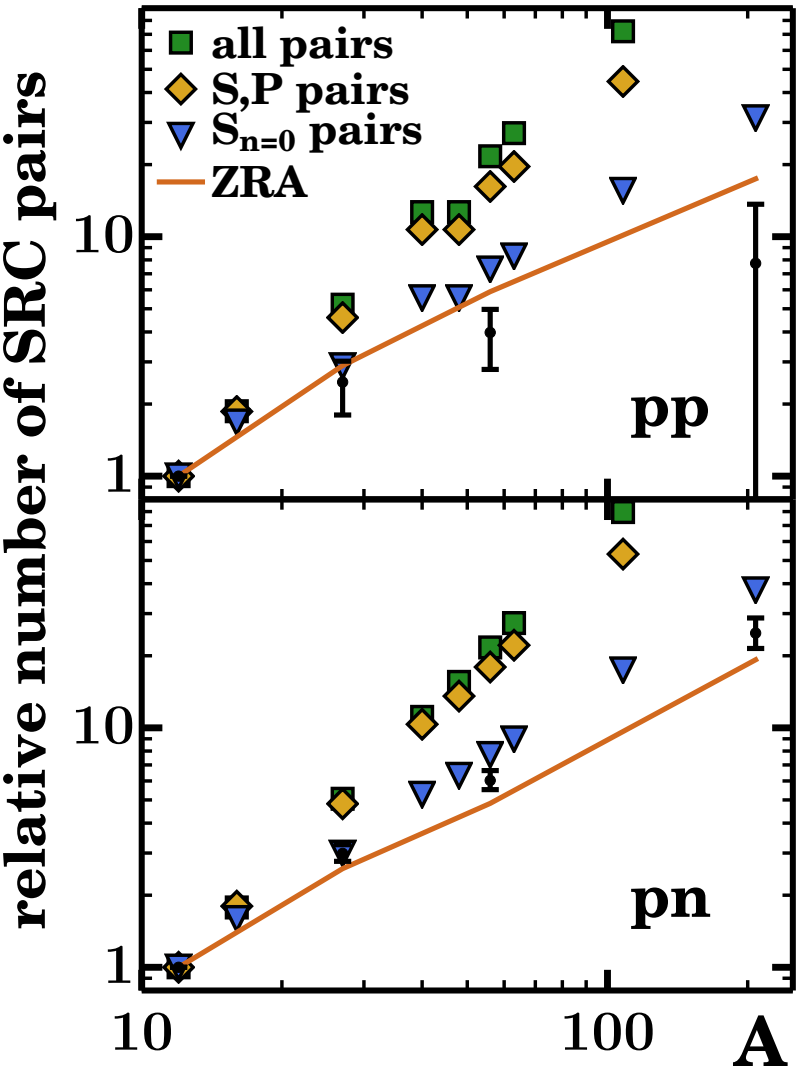

FIG. 3: (color online). The mass dependence of the number of pp (top panel) and pn (bottom panel) SRC pairs of nucleus A relative to ^{12}C. Data are extracted from the measured CLAS $A(e,e'p)$ and $A(e,e'pp)$ cross section ratios [8, 21] after correcting for FSI. Error bars include the estimated uncertainty on the cross-section ratios and the FSI corrections. The green squares correspond with unconditional counting of the pp pairs i.e. (Z(Z-1)/30 in the upper panel) and pn pairs (ZN/36 in the bottom panel) for the nuclei ^{12}C, ^{16}O, ^{27}Al, ^{40}Ca, ^{48}Ca, ^{56}Fe, ^{63}Cu, ^{108}Ag and ^{208}Pb. The yellow diamonds are the ratios obtained by counting IPM pairs in a relative S and P state. The blue triangles count IPM $S_{n=0}$ pairs. The solid line denotes the result of a reaction-model calculation for scattering from close-proximity pairs (Eq. (3)) which takes full account of the experimental phase space. This calculation does not include FSI corrections as these are applied to the data, see text for details.

V. CONCLUSIONS

We have extracted the relative number of np and pp SRC correlated pairs in nucleus A relative to Carbon from previously published measured $A(e,e'pp)/\mathrm{C}(e,e'pp)$ and $A(e,e'p)/\mathrm{C}(e,e'p)$ cross section ratios corrected for final state interactions. The relative number of np and pp pairs increases much more slowly with A than expected from simple combinatorics.

We calculated the cross section in a framework which shifts the complexity of the nuclear SRC from the wave functions to the operators by calculating independent-particle model (IPM) Slater determinant wave functions and acting on them with correlation operators to include the effect of SRCs [18–20]. The uncorrected $A(e,e'pp)/\mathrm{C}(e,e'pp)$ cross section ratios are consistent with a zero range approximation (ZRA) calculation including the effects of FSI.

Due to factorization, the ratio of calculated cross sections is approximately equal to the ratio of the distorted c.m. momentum distributions. In the absence of FSI, the integrated c.m. momentum distribution equals the total number of SRC-prone pairs in that nucleus. We compared three choices of SRC-prone pairs to the data: (a) all pairs, (b) pairs in a nodeless relative S state ($S_{n=0}$), and (c) $L \leq 1$ pairs (i.e., both S and P).

We found that the soft mass dependence of the measured $A(e, e'pp)$ cross-section ratios agrees with scattering from highly selective close-proximity pairs (i.e., only IPM relative $S_{n=0}$ pairs). The mass dependence of the extracted ratios of the number of short-range correlated pp and pn pairs provides additional support for this conclusion. All these results consistently hint at a physical picture whereby the aggregated effect of SRC in the nuclear wave function is determined to a large extent by mass-independent correlation operators on $S_{n=0}$ pairs. This provides additional evidence for the scale separation between the mean-field and SRC dynamics that has, for example, been used in calculations of NMD of Refs. [18–20]. Amongst other things, these conclusions are likely to affect the models used to estimate the effect of correlated pairs on neutrino-nucleus cross sections [33] and studies of the nuclear equation-of-state in conditions of increased density—enhanced sensitivity of SRC [34].

Acknowledgments

We acknowledge the efforts of the Jefferson Lab staff that made this experiment possible and the EG2 group and CLAS Collaboration. The Ghent group is supported by the Research Foundation Flanders (FWO-Flanders) and by the Interuniversity Attraction Poles Programme P7/12 initiated by the Belgian Science Policy Office. For the theoretical calculations, the computational resources (Stevin Supercomputer Infrastructure) and services used in this work were provided by Ghent University, the Hercules Foundation and the Flemish Government. O. Hen and E. Piasetzky are supported by the Israeli Science Foundation. L.B. Weinstein is supported by the US Department of Energy under grant de-SC00006801 and DOE-FG02-96ER40960.

[1] O. Benhar, A. Fabrocini, S. Fantoni, and I. Sick, Nucl. Phys. **A579**, 493 (1994).
[2] M. Alvioli, C. Ciofi degli Atti, L. P. Kaptari, C. B. Mezzetti, and H. Morita, Phys. Rev. C **87**, 034603 (2013).
[3] R. B. Wiringa, R. Schiavilla, S. C. Pieper, and J. Carlson, Phys. Rev. C **89**, 024305 (2014), URL `http://link.aps.org/doi/10.1103/PhysRevC.89.024305`.
[4] A. Tang, J. W. Watson, J. Aclander, J. Alster, G. Asryan, Y. Averichev, D. Barton, V. Baturin, N. Bukhtoyarova, A. Carroll, et al., Phys. Rev. Lett. **90**, 042301 (2003), nucl-ex/0206003.
[5] E. Piasetzky, M. Sargsian, L. Frankfurt, M. Strikman, and J. Watson, Phys. Rev. Lett. **97**, 162504 (2006), nucl-th/0604012.
[6] R. Subedi, R. Shneor, P. Monaghan, B. Anderson, K. Aniol, J. Annand, J. Arrington, H. Benaoum, F. Benmokhtar, W. Boeglin, et al., Science **320**, 1476 (2008).
[7] I. Korover, N. Muangma, O. Hen, R. Shneor, V. Sulkosky, A. Kelleher, S. Gilad, D. W. Higinbotham, E. Piasetzky, J. W. Watson, et al. (Jefferson Lab Hall A Collaboration), Phys. Rev. Lett. **113**, 022501 (2014).
[8] O. Hen, M. Sargsian, L. B. Weinstein, E. Piasetzky, H. Hakobyan, D. W. Higinbotham, M. Braverman, W. K. Brooks, S. Gilad, K. P. Adhikari, et al., Science **346**, 614 (2014), http://www.sciencemag.org/content/346/6209/614.full.pdf, URL `http://www.sciencemag.org/content/346/6209/614.abstract`.
[9] O. Hen, L. Weinstein, E. Piasetzky, G. Miller, M. Sargsian, and Y. Sagi (2014), 1407.8175.
[10] L. Fields et al., Phys. Rev. Lett. **111**, 022501 (2013), URL `http://link.aps.org/doi/10.1103/PhysRevLett.111.022501`.
[11] G. A. Fiorentini et al., Phys. Rev. Lett. **111**, 022502 (2013), URL `http://link.aps.org/doi/10.1103/PhysRevLett.111.022502`.
[12] O. Hen, B.-A. Li, W.-J. Guo, L. Weinstein, and E. Piasetzky, Phys. Rev. C **91**, 025803 (2015).
[13] W. Dickhoff and C. Barbieri, Prog. Part. Nucl. Phys. **52**, 377 (2004).
[14] L. Frankfurt, M. Strikman, D. Day, and M. Sargsian, Phys. Rev. C **48**, 2451 (1993).
[15] K. S. Egiyan, N. Dashyan, M. Sargsian, S. Stepanyan, L. B. Weinstein, G. Adams, P. Ambrozewicz, E. Anciant, M. Anghinolfi, B. Asavapibhop, et al. ((CLAS Collaboration)), Phys. Rev. C **68**, 014313 (2003), nucl-ex/0301008, URL `http://link.aps.org/doi/10.1103/PhysRevC.68.014313`.
[16] K. S. Egiyan, N. B. Dashyan, M. M. Sargsian, M. I. Strikman, L. B. Weinstein, G. Adams, P. Ambrozewicz, M. Anghinolfi, B. Asavapibhop, G. Asryan, et al. (CLAS Collaboration), Phys. Rev. Lett. **96**, 082501 (2006), nucl-ex/0508026, URL `http://link.aps.org/doi/10.1103/PhysRevLett.96.082501`.

[17] N. Fomin, J. Arrington, R. Asaturyan, F. Benmokhtar, W. Boeglin, P. Bosted, A. Bruell, M. H. S. Bukhari, M. E. Christy, E. Chudakov, et al., Phys. Rev. Lett. **108**, 092502 (2012), 1107.3583, URL `http://link.aps.org/doi/10.1103/PhysRevLett.108.092502`.
[18] J. Ryckebusch, M. Vanhalst, and W. Cosyn, J. Phys. G **42**, 055104 (2015), 1405.3814.
[19] R. Roth, T. Neff, and H. Feldmeier, Prog. Part. Nucl. Phys. **65**, 50 (2010), 1003.3624.
[20] S. Bogner and D. Roscher, Phys. Rev. C **86**, 064304 (2012), 1208.1734.
[21] O. Hen et al. (CLAS Collaboration), Phys. Lett. **B722**, 63 (2013), 1212.5343.
[22] B. Mecking et al. (CLAS Collaboration), Nucl. Instr. Meth. **A503**, 513 (2003).
[23] C. Colle, W. Cosyn, J. Ryckebusch, and M. Vanhalst, Phys. Rev. C **89**, 024603 (2014).
[24] J. Ryckebusch, D. Debruyne, P. Lava, S. Janssen, B. Van Overmeire, and T. Van Cauteren, Nucl. Phys. **A728**, 226 (2003), nucl-th/0305066.
[25] W. Cosyn and J. Ryckebusch, Phys. Rev. C 87, **064608** (2013), 1301.1904.
[26] W. R. Gibbs and B. Loiseau, Phys. Rev. C **50**, 2742 (1994).
[27] M. Jain, M. L. Evans, G. Glass, J. C. Hiebert, R. A. Kenefick, L. C. Northcliffe, B. E. Bonner, J. E. Simmons, C. W. Bjork, P. J. Riley, et al., Phys. Rev. C **30**, 566 (1984).
[28] J. Ryckebusch, Phys. Lett. **B383**, 1 (1996), nucl-th/9605043.
[29] M. Vanhalst, W. Cosyn, and J. Ryckebusch, Phys. Rev. C **84**, 031302 (2011), 1105.1038.
[30] M. Vanhalst, J. Ryckebusch, and W. Cosyn, Phys.Rev. **C86**, 044619 (2012), 1206.5151.
[31] C. J. G. Onderwater et al., Phys. Rev. Lett. **78**, 4893 (1997).
[32] R. Starink, M. van Batenburg, E. Cisbani, W. Dickhoff, S. Frullani, F. Garibaldi, C. Giusti, D. Groep, P. Heimberg, W. Hesselink, et al., Phys. Lett. **B474**, 33 (2000).
[33] R. Acciarri, C. Adams, J. Asaadi, B. Baller, T. Bolton, C. Bromberg, F. Cavanna, E. Church, D. Edmunds, A. Ereditato, et al., Phys. Rev. D **90**, 012008 (2014).
[34] Xin Zhang, Chang Xu, Zhongzhou Ren, Eur. Phys. J. **A50**, 113 (2014).

3.5 References

[1] P. K. Panda, D. P. Menezes, C. Providência, and J. d. Providência, Brazilian Journal of Physics **35**, 873 (2005).
[2] C. Colle, W. Cosyn, J. Ryckebusch, and M. Vanhalst, Phys. Rev. C **89**, 024603 (2014).
[3] W. Cosyn, M. Vanhalst, J. Ryckebusch, and LALA, EPJ Web of Conferences **66**, 02022 (2014).
[4] C. J. Joachain, *Quantum collision theory* (North-Holland, Amsterdam, 1975).
[5] J. Ryckebusch, D. Debruyne, P. Lava, et al., Nucl. Phys. **A728**, 226 (2003).
[6] C. Colle, W. Cosyn, and J. Ryckebusch, Phys. Rev. C **93**, 034608 (2016).
[7] O. Hen, M. Sargsian, L. B. Weinstein, et al., Science **346**, 614 (2014).
[8] C. Colle, O. Hen, W. Cosyn, et al., Phys. Rev. C **92**, 024604 (2015).

CHAPTER 4

Summary and outlook

A complete description of the nucleus is a major goal of nuclear physics. The search of how the nuclear observables are generated from the complex nucleon-nucleon interaction is a very difficult one and has been studied since the dawn of nuclear physics. An early model that successfully describes many nuclear properties is the independent-particle model (IPM) whereby the nucleons move in a mean-field potential, encoding the average effect of the individual nucleon-nucleon interactions [1, 2]. It is well known that the nucleon-nucleon force induces correlations in the nucleus. These correlations can not be described in mean-field models, whereby the nucleons are considered as independent particles. The nuclear correlations can be divided into long-range correlations (LRC) and short range correlations (SRC). The LRC are connected to the low-lying collective excitations of the nucleus. The effects of LRC do not extend far beyond the Fermi momentum k_F in the nucleus. SRC are generated by the short-range repulsive core and tensor interaction of the nucleon-nucleon force. SRC create nucleon pairs with high relative momentum and low c.m. momentum compared to k_F [3–6]. The dominant effects of SRC happen above the Fermi momentum k_F. They induce high-momentum components in the nuclear momentum distribution (NMD). This separation of LRC and SRC in momentum space [7–9] allows us to isolate the SRC and focus on the short-range dynamics inside the nucleus. Finding nucleons with momenta well above k_F is a clear signature of SRC.

In order to measure SRC effects, the SRC nucleons have to be probed in scattering reactions. The exclusive two-nucleon knockout reaction is an ideal choice for probing SRC. Thereby a hard probe interacts with a correlated nucleon pair with high relative momentum, that is subsequently knocked out of the nucleus. Both ejected nucleons as well as the scattered projectile are measured. The kinematics for this reaction can be tuned in such a way that it can be ensured that the scattering process is dominated entirely by SRC pairs. The measurement of the electroinduced exclusive two-knockout process is very challenging as it requires the detection of the energy and momentum of the scattered projectile as well as the two ejected nucleons. Very few data is available for this highly exclusive reaction. Throughout this work

the theoretical calculations are compared to experimental data obtained from the Jefferson Lab Hall B CEBAF Large Acceptance Spectrometer (CLAS) data mining initiative [10] and the Jefferson Lab Hall A collaboration [5, 11]. However, the study of SRC-driven reactions is not limited to the exclusive electroinduced two-nucleon knockout scattering process. For example, in Ref. [12] the relative amount of SRC-pairs is extracted from inclusive electron scattering cross-section ratios of different nuclei. Additionally, SRC have been investigated in exclusive knockout reactions with a hadronic probe. At Brookhaven National Laboratory SRC have been studied whereby an incoming proton knocks out a proton-neutron pair from the target nucleus ^{12}C [3, 13]. It was demonstrated that the majority of SRC pairs consist of proton-neutron pairs.

In this work a reaction model for the electroinduced two-nucleon knockout scattering process has been developed [5, 14–16]. This reaction model is used to investigate the SRC dynamics inside the nucleus. A factorized expression for the electroinduced two-nucleon knockout cross section is used to study SRC properties across the entire nuclear mass range. The factorized cross section allows the calculation of cross-section ratios that are independent of the electron two-nucleon coupling. It is expected that this leads to robust results. Final-state interactions (FSI) are included in the calculation of the cross section. It is established that the FSI have a large effect on the cross section, predominantly causing a significant attenuation [14]. The mass dependence of the two-nucleon knockout cross section is determined. It is found to be very soft, whereby the FSI play a significant role in softening the mass dependence. The effect of including charge-exchange reactions in the FSI does not significantly alter the computed results. It can be concluded that FSI are an essential ingredient in a realistic description of the two-nucleon knockout process. The calculated cross-section ratios are found to be in agreement with the measured ratios. The nuclear transparency, which is a measure of the attenuation strength caused by the FSI, is examined across the nuclear mass range. With the factorized cross section the nuclear transparency can be calculated independently of the electron two-nucleon coupling, increasing the robustness of the results. Given the mass dependence of the nuclear transparency, the magnitude of the attenuation caused by the FSI can be quickly estimated across the nuclear mass range.

Furthermore, the framework developed in this dissertation allows us to reconstruct properties of initial SRC pairs from the measured exclusive two-nucleon knockout cross section. The measured cross section is corrected for FSI to infer the SRC in the initial nucleus. The synergy between theory and experiment has resulted in improved knowledge about short-distance dynamics of nuclei. We have established the fraction of the nucleon-nucleon pairs that are subject to SRC corrections. The investigation of the mass dependence of this fraction allows us to deduce the internal structure of the SRC pairs, identifying their relative quantum numbers and isospin. The mass dependence of the amount of SRC-prone pairs is much softer than a naive combinatorial prediction whereby one assumes that the SRC-pairs are a fixed fraction of the total number of nucleon-nucleon pairs available in a nucleus ($\propto A(A-1)$). We find that the theoretical predictions and the results reconstructed from the measured cross sections are in agreement.

Outlook

In the two-nucleon knockout reaction model outlined in this dissertation, the initial SRC pairs are selected using the zero-range approximation (ZRA). The ZRA fixes the nucleon pair to the same spatial coordinate. It sets the relative distance of the nucleon pair to zero. The ZRA is used as a proxy for the more advanced correlation operators used in the LCA framework. The possibility of introducing the LCA in the electroinduced two-nucleon knockout reaction model as outlined in Sec. 3.2 [16] can be considered in future work. Additionally the reaction model can be extended by including the photon two-nucleon coupling. This will enable the calculations of absolute cross section instead of cross-section ratios. Ideally the model-dependence introduced by the description of photon-two nucleon coupling should be investigated.

Improved knowledge of the nuclear SRC will be of great help to quantify the effect of SRC-governed multi-nucleon signal to neutrino-nucleus response [17–19]. In its turn this will further help in improving the extracted neutrino-oscillation parameters. This is an active area of research. In the ArgoNeuT experiment neutrino-induced knockout back-to-back moving nucleon pairs has been directly observed [20]. Other neutrino experiments, such as MicroBooNE, DUNE, MINERvA and NOvA, will benefit from a better understanding of SRC dynamics as well.

It is expected that SRC play an important role in asymmetric nuclei with "exotic" neutron-to-proton fractions. The framework outlined in this dissertation can be used to model the scattering reactions off these asymmetric nuclei, leading to new probes investigating nuclear short-range dynamics. This will shed light on the the persistence of the robust SRC properties in unstable nuclei. Scattering reactions involving unstable nuclei are typically performed in inverse kinematics, whereby the unstable nucleus is impinging on a hadronic target. For knockout reactions, the target hadron induces the two-nucleon knockout. Due to the hadronic probe it is expected that the importance of (initial-) final-state interactions will grow even larger compared to the electroninduced two-nucleon knockout reactions. The attenuation effect will increase, softening the mass-dependence of the cross-section. The framework used in this dissertation to describe the final-state interactions can be readily applied to this type of reactions.

References

[1] M. G. Mayer, Phys. Rev. **74**, 235 (1948).
[2] O. Haxel, J. H. D. Jensen, and H. E. Suess, Phys. Rev. **75**, 1766 (1949).
[3] A. Tang, J. W. Watson, J. Aclander, et al., Phys. Rev. Lett. **90**, 042301 (2003).
[4] E. Piasetzky, M. Sargsian, L. Frankfurt, et al., Phys. Rev. Lett. **97**, 162504 (2006).
[5] R. Subedi, R Shneor, P. Monaghan, et al., Science **320**, 1476 (2008).
[6] O. Hen, M. Sargsian, L. B. Weinstein, et al., Science **346**, 614 (2014).
[7] O. Benhar, A. Fabrocini, S. Fantoni, and I. Sick, Nuclear Physics A **579**, 493 (1994).
[8] M. Alvioli, C. Ciofi degli Atti, L. P. Kaptari, et al., Phys. Rev. C **87**, 034603 (2013).
[9] R. B. Wiringa, R. Schiavilla, S. C. Pieper, and J. Carlson, Phys. Rev. C **89**, 024305 (2014).
[10] O. Hen, H. Hakobyan, R. Shneor, et al., Phys. Lett. B **722**, 63 (2013).

[11] R. Shneor, P. Monaghan, R. Subedi, et al., Phys. Rev. Lett. **99**, 072501 (2007).
[12] N. Fomin, J. Arrington, R. Asaturyan, et al., Phys. Rev. Lett. **108**, 092502 (2012).
[13] J. Aclander, J. Alster, D. Barton, et al., Physics Letters B **453**, 211 (1999).
[14] C. Colle, W. Cosyn, and J. Ryckebusch, Phys. Rev. C **93**, 034608 (2016).
[15] C. Colle, O. Hen, W. Cosyn, et al., Phys. Rev. C **92**, 024604 (2015).
[16] C. Colle, W. Cosyn, J. Ryckebusch, and M. Vanhalst, Phys. Rev. C **89**, 024603 (2014).
[17] T. Van Cuyck, N. Jachowicz, R. González-Jiménez, et al., Phys. Rev. C **94**, 024611 (2016).
[18] T. Katori and M. Martini, (2016).
[19] L Alvarez-Ruso, Y Hayato, and J Nieves, New Journal of Physics **16**, 075015 (2014).
[20] R. Acciarri, C. Adams, J. Asaadi, et al., Phys. Rev. D **90**, 012008 (2014).

APPENDIX A

The eikonal approximation

The eikonal approximation is used extensively in this dissertation. It is an essential ingredient of our description of the final-state interactions (FSI) in nuclear reactions. The majority of the results involving FSI presented in chapter 3 have been obtained by adopting the eikonal approximation in the description of the FSI. In this chapter we investigate the eikonal approximation and its applications. We start with a short discussion of the eikonal approximation in one and three dimensions. This paves the way to the introduction of the Relativistic Multiple Scattering Glauber Approximation (RMSGA) in Sec. A.3. The RMSGA can be categorized as an eikonal approximation. The RMSGA can be used to describe realistic FSI in nuclear reactions involving sufficiently energetic nucleons. In the simulation of realistic scattering reactions off nuclei it is often necessary to make additional approximations to keep the RMSGA calculations computationally feasible. The RMSGA and possible additional approximations are evaluated using a test model in Sec. A.3.

A.1 The eikonal approximation in 1D

Here, we report a succinct derivation of the eikonal approximation for potential scattering in one dimension. The extension to higher dimensions is straightforward. A more rigorous derivation can be found in [1] (p188).

We start from the one-dimensional time-independent Schrödinger equation

$$\frac{\mathrm{d}^2}{\mathrm{d}x^2}\psi(x) - U(x)\psi(x) + k^2\psi(x) = 0\,, \tag{A.1}$$

with $U(x) = 2m/\hbar^2 V(x)$ and $k^2 = 2m/\hbar^2 E$. The eikonal approximation adopts the following assumptions:

- The length scale a of the potential $V(x)$ is much larger than the wavelength $\lambda = 2\pi/k$ of the particle, $(ka \gg 1)$.
- The energy of the particle is much larger than the potential strength $E \gg V(x)$.

From these assumptions one can infer that the wave function will be adequately described by a plane wave modulated by some position-dependent factor

$$\psi(x) = \frac{1}{\sqrt{2\pi}} e^{ikx} \eta(x) \,.$$

Inserting this expression into Eq. (A.1) gives,

$$-k^2 e^{ikx}\eta(x) + 2ike^{ikx}\eta'(x) + e^{ikx}\eta''(x) - U(x)e^{ikx}\eta(x) + k^2 e^{ikx}\eta(x) = 0 \,.$$

The second-order derivative of $\eta(x)$ can be neglected by considering that $\eta(x)$ is a slowly varying function, consistent with the assumption $ka \gg 1$. This results in,

$$\begin{aligned} \eta'(x) &= \frac{1}{2ik} U(x)\eta(x) \\ \ln(\eta(x)) - \ln(\eta(-\infty)) &= -\frac{i}{2k} \int_{-\infty}^{x} U(x')\mathrm{d}x' \,. \end{aligned}$$

Assuming that the potential approaches zero at $-\infty$ it is easy to see that $\eta(-\infty) = 1$ and,

$$\eta(x) = e^{-\frac{i}{2k}\int_{-\infty}^{x} U(x')\mathrm{d}x'} \,.$$

The above derivations lead to the following approximate expression for the wave function,

$$\psi(x) = \frac{1}{\sqrt{2\pi}} e^{ikx} e^{-\frac{i}{2k}\int_{-\infty}^{x} U(x')\mathrm{d}x'} \,. \tag{A.2}$$

A.1.1 1D step potential barrier

Eq. (A.2) is applied to the potential step barrier $V(x) = |V_0|\theta(x)$ in the case $E > |V_0|$, for particles impinging from the left $(x < 0)$ as illustrated in [2] (p145). It is an easy exercise to show that $k'/k = \sqrt{1 - V_0/E}$, with k the wave number in the region $x < 0$ and k' the wave number in the region $x > 0$.

The eikonal approximation is applied to construct the wave function. Using Eq. (A.2) the wave function is described by,

$$\begin{aligned} \psi(x) &= \frac{1}{\sqrt{2\pi}} e^{ikx} e^{-\frac{i}{2k}\int_{-\infty}^{x} U(x')\mathrm{d}x'} \\ &= \frac{1}{\sqrt{2\pi}} e^{ikx} e^{-\frac{i2mV_0}{2k\hbar^2}\int_{-\infty}^{x} \theta(x')\mathrm{d}x'} \,. \end{aligned}$$

For $x < 0$ the wave function reduces to the plane wave $\frac{1}{\sqrt{2\pi}} e^{ikx}$, only describing *forward propagation*, an inherent feature of the eikonal description. Note that the exact solution also contains a term $\propto e^{-ikx}$ in the region $x < 0$. For $x > 0$ the wave function is given by,

$$\begin{aligned} \psi(x > 0) &= \frac{1}{\sqrt{2\pi}} e^{ikx} e^{-\frac{imV_0}{k\hbar^2}x} \\ &= \frac{1}{\sqrt{2\pi}} e^{ik(1-\frac{mV_0}{k^2\hbar^2})x} \,. \end{aligned}$$

Using $E = \frac{\hbar^2 k^2}{2m}$ this becomes,

$$\psi(x > 0) = \frac{1}{\sqrt{2\pi}} e^{ik(1-\frac{V_0}{2E})x} .$$

Identifying the factor $k(1 - \frac{V_0}{2E})$ with k', the wave number of the particle after it has crossed the potential barrier it follows that,

$$\frac{k'}{k} = 1 - \frac{V_0}{2E} .$$

This is the first-order expansion of the exact solution, given by $\sqrt{1 - V_0/E}$, in the high energy limit ($E \gg V_0$). The eikonal approximation gives the correct result in the region where it is expected to work ($E \gg V_0$).

A.2 The eikonal approximation in 3D

As in the one-dimensional case we assume that the wave function of the particle is described by

$$\psi(\vec{r}) = \frac{1}{(2\pi)^{\frac{3}{2}}} e^{i\vec{k}\cdot\vec{r}} \eta(\vec{r}) , \tag{A.3}$$

where $\eta(\vec{r})$ is a slowly varying function in a range comparable to the wavelength of the particle λ. Inserting the eikonal ansatz of Eq. (A.3) into the 3D Schrödinger equation one obtains,

$$\begin{aligned} \left(\nabla^2 + k^2\right) \psi(\vec{r}) &= U(\vec{r})\psi(\vec{r}) \\ 2i\vec{k}\cdot\nabla\eta(\vec{r}) + \nabla^2\eta(\vec{r}) &= U(\vec{r})\eta(\vec{r}) \end{aligned}$$

Neglecting the second-order derivative of $\eta(\vec{r})$ and choosing the z-axis along the momentum $\vec{k}$ results in,

$$\begin{aligned} \frac{\partial}{\partial z}\eta(\vec{r}) &= \frac{1}{2ik} U(\vec{r})\eta(\vec{r}) \\ \Rightarrow \ln(\eta(\vec{b}, z)) - \ln(\eta(\vec{b}, -\infty)) &= \frac{1}{2ik} \int_{-\infty}^{z} \mathrm{d}z' U(\vec{b}, z')\eta(\vec{b}, z') , \end{aligned}$$

$\vec{b}, z$ are the transversal and longitudinal components or $\vec{r} = (x, y, z) = (\vec{b}, z)$. From Eq. (A.3) it is clear that $\eta(\vec{b}, -\infty) = 1$,

$$\eta(\vec{b}, z) = \exp\left(\frac{1}{2ik} \int_{-\infty}^{z} \mathrm{d}z' U(\vec{b}, z')\eta(\vec{b}, z')\right) \tag{A.4}$$

$$\psi(\vec{r}) = \frac{1}{(2\pi)^{\frac{3}{2}}} \exp\left(-i\vec{k}\cdot\vec{r} - \frac{i}{2k} \int_{-\infty}^{z} \mathrm{d}z' U(\vec{b}, z')\eta(\vec{b}, z')\right) . \tag{A.5}$$

After defining the *eikonal phase-shift function* $\chi(\vec{r}) = -\frac{1}{2k}\int_{-\infty}^{z} \mathrm{d}z' U(\vec{b}, z')$ [1], the wave function adopts the short-hand form,

$$\psi(\vec{r}) = \frac{e^{-i\vec{k}\cdot\vec{r}}}{(2\pi)^{\frac{3}{2}}} e^{i\chi(\vec{r})}\,. \tag{A.6}$$

It is possible to derive Eq. (A.5) in a more mathematically rigorous fashion, described in for example Ref. [1]. The key feature is that the propagator $G_0(\vec{r}, \vec{r}')$ in the Lipmann-Schwinger equation,

$$\psi(\vec{r}) = \frac{e^{i\vec{k}\cdot\vec{r}}}{(2\pi)^{\frac{3}{2}}} + \int \mathrm{d}\vec{r}'\, G_0(\vec{r}, \vec{r}') U(\vec{r}')\psi(\vec{r}') \tag{A.7}$$

can be expanded as,

$$\begin{aligned}
G_0(\vec{r}, \vec{r}') &= -\frac{1}{(2\pi)^3} \lim_{\varepsilon\to 0} \int \mathrm{d}\vec{k}' \frac{e^{i\vec{k}'\cdot(\vec{r}-\vec{r}')}}{k'^2 - k^2 - i\varepsilon} \\
= G_0(\vec{R}) &= -\frac{e^{i\vec{k}\cdot\vec{R}}}{(2\pi)^3} \lim_{\varepsilon\to 0} \int \mathrm{d}\vec{p} \frac{e^{i\vec{p}\cdot\vec{R}}}{p^2 + 2\vec{k}\cdot\vec{p} - i\varepsilon} \\
&= -\frac{e^{i\vec{k}\cdot\vec{R}}}{(2\pi)^3} \lim_{\varepsilon\to 0} \int \mathrm{d}\vec{p} \frac{e^{i\vec{p}\cdot\vec{R}}}{2\vec{k}\cdot\vec{p} - i\varepsilon} \left(1 - \frac{p^2}{2\vec{p}\cdot\vec{k} - i\varepsilon} + \frac{p^4}{(2\vec{p}\cdot\vec{k} - i\varepsilon)^2} - \dots\right) \\
&= -\frac{e^{i\vec{k}\cdot\vec{R}}}{(2\pi)^3} \lim_{\varepsilon\to 0} \int \mathrm{d}\vec{p} \frac{e^{i\vec{p}\cdot\vec{R}}}{2\vec{k}\cdot\vec{p} - i\varepsilon} \left(1 - \frac{p/k}{2\vec{e}_p\cdot\vec{e}_k - i\varepsilon} + \frac{(p/k)^2}{(2\vec{e}_p\cdot\vec{e}_k - i\varepsilon)^2} - \dots\right) \\
&\approx -\frac{e^{i\vec{k}\cdot\vec{R}}}{(2\pi)^3} \lim_{\varepsilon\to 0} \int \mathrm{d}\vec{p} \frac{e^{i\vec{p}\cdot\vec{R}}}{2\vec{k}\cdot\vec{p} - i\varepsilon} + \mathcal{O}(p/k)\,.
\end{aligned} \tag{A.8}$$

In the above derivation the following vectors have been introduced, $\vec{R} = \vec{r} - \vec{r}'$, $\vec{p} = \vec{k}' - \vec{k}$, $\vec{e}_k = \vec{k}/k$ and $\vec{e}_p = \vec{p}/p$. The validity of the expansion in p/k is not apparent at first sight. In order to justify the expansion the eikonal ansatz of Eq. (A.3) is substituted into Eq. (A.7),

$$\begin{aligned}
\eta(\vec{r}) &= 1 + \int \mathrm{d}\vec{r}' G_0(\vec{r}, \vec{r}') e^{i\vec{k}\cdot(\vec{r}'-\vec{r})} U(\vec{r}')\eta(\vec{r}') \\
&= 1 + \int \mathrm{d}\vec{R}\, G_0(R) e^{-i\vec{k}\cdot\vec{R}} U(\vec{r} - \vec{R})\eta(\vec{r} - \vec{R}) \\
&= 1 - \frac{1}{(2\pi)^3} \lim_{\varepsilon\to 0} \int \mathrm{d}\vec{p} \frac{1}{p^2 + 2\vec{k}\cdot\vec{p} - i\varepsilon} \int \mathrm{d}\vec{R}\, e^{i\vec{p}\cdot\vec{R}} U(\vec{r} - \vec{R})\eta(\vec{r} - \vec{R})\,.
\end{aligned} \tag{A.9}$$

It is a general feature of Fourier transformations that for a given function $f(\vec{x})$ which varies over a distance scale a, the Fourier transformation $f(\vec{p})$ will have most of its strength up to $p \approx 1/a$. Applying this argument to the integral over $\mathrm{d}\vec{R}$ in Eq. (A.9) it follows that the largest contribution to the integral over $\mathrm{d}\vec{p}$ stems from momenta $p \lesssim 1/a$, with a the distance scale of $U(\vec{r})\eta(\vec{r})$. With the condition $ka \gg 1$ it follows that $1 \ll ka \lesssim k/p$, or $p/k \ll 1$. This validates the expansion in powers of p/k. As shown in Ref. [1] this approximation (Eq. (A.8)) leads to Eq. (A.5).

A.3 Relativistic Multiple Scattering Glauber Approximation

A.3.1 Introduction

Here the assumptions underlying the Relativistic Multiple Scattering Glauber Approximation (RMSGA) [3] are briefly discussed. The RMSGA is an eikonal approximation as the wave function of a scattered particle is described by a plane wave modulated by a position dependent factor. It describes forward propagation of the scattered particle. This means that the RMSGA can be applied to high-energy small-angle scattering reactions. Where high energy means that the energy of the projectile should be large compared to the interaction energy of the system.

The incoming particle is described as a plane wave with momentum $\vec{k}_i$ ($k = |\vec{k}_i|$). The wave function of the scattered particle picks up a complex phase $\chi(\vec{r})$ (Eq. (A.6)),

$$\begin{aligned} \psi(\vec{r}) &= \frac{e^{i\vec{k}_i \cdot \vec{r}}}{(2\pi)^{\frac{3}{2}}} e^{i\chi(\vec{r})}\,, \\ \chi(\vec{r}) &= -\frac{1}{2k}\int_{-\infty}^{z} \mathrm{d}z'\, U(\vec{b}, z')\,. \end{aligned} \tag{A.10}$$

The vector $\vec{r}$ can be written as $(\vec{b}, z)$ where z is the coordinate along the z-axis and $\vec{b}$ is the perpendicular component. The orientation of the z-axis is chosen to be parallel to the momentum $\vec{k}_i$. The scattering amplitude $f(\Omega)$ can be expressed as a function of the eikonal phase-shift function $\chi(k, \vec{b})$ (Eq. (A.10)),

$$\begin{aligned} f(\vec{\Delta}) &= \frac{k}{2\pi i}\int \mathrm{d}^2\vec{b} \exp(i\vec{\Delta}\cdot\vec{b}) \left[\exp(i\chi(k,\vec{b})) - 1\right] \\ &= \frac{k}{2\pi i}\int \mathrm{d}^2\vec{b} \exp(i\vec{\Delta}\cdot\vec{b})\Gamma(k,\vec{b})\,. \end{aligned} \tag{A.11}$$

In Eq. (A.13) the *profile function* $\Gamma(k, \vec{b}) = \exp(i\chi(k, \vec{b})) - 1$ is introduced. Further, $\vec{\Delta}$ is the transferred three momentum $\vec{k}_i - \vec{k}_f$ with $\vec{k}_i$ and $\vec{k}_f$ the initial and final momentum of the particle. Eq. (A.13) can be easily inverted to,

$$\Gamma(k,\vec{b}) = \frac{i}{2\pi k}\int \mathrm{d}^2\vec{\Delta} e^{-i\vec{\Delta}\cdot\vec{b}} f(\vec{\Delta})\,. \tag{A.12}$$

For high-energy diffractive scattering the scattering amplitude can be parameterized as,

$$f(\vec{\Delta}) \approx A e^{-\frac{\beta^2\Delta^2}{2}}\,. \tag{A.13}$$

Using the optical theorem $\mathrm{Im}f(\vec{\Delta} = \vec{0}) = \frac{k\sigma_{\mathrm{tot}}}{4\pi}$ we can rewrite this as,

$$f(\vec{\Delta}) \approx \frac{k\sigma_{\mathrm{tot}}}{4\pi}(i+\varepsilon)e^{-\frac{\beta^2\Delta^2}{2}}\,,$$

where ε is defined as $\varepsilon = \mathrm{Re}f(\vec{\Delta} = \vec{0})/\mathrm{Im}f(\vec{\Delta} = \vec{0})$. Inserting this parameterization into Eq. (A.12) gives,

$$\Gamma(k, \vec{b}) = \frac{\sigma_{\mathrm{tot}}}{8\pi^2}(i\varepsilon - 1) \int \mathrm{d}^2\vec{\Delta}\, \exp\left(-\frac{\beta^2\Delta^2}{2} - i\vec{\Delta}\cdot\vec{b}\right) = \frac{\sigma_{\mathrm{tot}}}{4\pi\beta^2}(1 - i\varepsilon) \exp\left(-\frac{\vec{b}^2}{2\beta^2}\right) \quad \text{(A.14)}$$

A major advantage of this approach is that for a particular scattering reaction, the profile function can be calculated from the forward-scattering amplitude $f(\vec{\Delta})$ (Eq. (A.13)) of that reaction, without the need of introducing a potential describing the interaction between the projectile and the target. The introduction of a potential induces model-dependency and often has a limited energy-range of applicability.

A.3.2 Nucleon-Nucleus scattering

The application of RMSGA in scattering reactions off many-body systems is discussed in this section. A nucleon-nucleus scattering reaction is considered here. Constraining the parameters of the nucleon-nucleus potential is challenging. Often a large numbers of parameters are needed to describe the interaction adequately. Moreover it requires elastic scattering data at specific energies. Because of this the nuclear potential parameterizations have a limited energy range of validity. With the RMSGA it is possible to describe the scattering process without the need of a potential. Within the RMSGA the scattering with a composite system (nucleus) can be described as a superposition of scattering events with the individual constituents (nucleons), this formalism can then be readily applied to the whole mass range. This is very advantageous and a large fraction for the research presented in this dissertation hinges on this assumption. It is expected that because of this the calculations across the entire nuclear mass range are robust. The RMSGA is a high-energy, eikonal approximation. The de Broglie wavelength of the particle should be small compared to the distance scale of the interaction. In the context of single-proton knockout reactions it was shown in Ref. [4] that the RMSGA is a realistic approach for proton kinetic energies down to 300 MeV, corresponding with a de Broglie wavelength of 1.5 fm. For medium to large nuclei ($A \geq 12$) the dimensionality of the RMSGA equations combined with a large kinematical phase space makes the numerical calculations very computationally intensive. Additional approximations, lessening the computational burden, can be made. In what follows several approximations that reduce the dimensionality of the numerical calculations are examined and their performance is checked using a test model. For the RMSGA calculations of chapter 3 the thickness approximation (outlined below) is used.

A scattering reaction with an incoming nucleon scattering off a nucleus, consisting of individual nucleons, is considered. The incoming particle can scatter with the A nucleons present in the nucleus. The total phase shift function χ_{tot} (Eq. (A.6)) is given by the sum of the phase shifts χ_j contributed by the A individual scatterers in the target. The A constituents are fixed during the scattering process. This means that their positions and quantum numbers remain unchanged during the collision process. This combination of assumptions is often

referred to as the frozen approximation. The above assumptions imply,

$$\chi_{\rm tot}(k,\vec{b},\vec{b}_1,\ldots,\vec{b}_A) = \sum_{j=1}^{A}\chi_j(k,\vec{b}-\vec{b}_j)\,, \tag{A.15}$$

$$\begin{aligned}\Gamma_{\rm tot}(k,\vec{b},\vec{b}_1,\ldots,\vec{b}_A) &= 1-\prod_{j=1}^{A}\Big(1-\Gamma_j(k,\vec{b}-\vec{b}_j)\Big)\\ &= \sum_{j=1}^{A}\Gamma_j(k,\vec{b}-\vec{b}_j) - \sum_{j<l}^{A}\Gamma_j(k,\vec{b}-\vec{b}_j)\Gamma_l(k,\vec{b}-\vec{b}_l)+\ldots\end{aligned} \tag{A.16}$$

This phase-shift additivity is a consequence of the purely forward motion of the projectile and the frozen approximation.

Elastic scattering nucleon-nucleus scattering is considered. The initial and final state of the nucleus is the ground state $|\Phi\rangle$, a Slater determinant of orthonormal single-particle wave functions,

$$\begin{aligned}|\Phi\rangle &= |\alpha_1\alpha_2\ldots\alpha_A\rangle\ ,\\ \langle\vec{r}_1|\,\langle\vec{r}_2|\ldots\langle\vec{r}_A|\,|\Phi\rangle &= \frac{1}{\sqrt{A!}}\sum_P(-1)^P\phi_{P(\alpha_1)}(\vec{r}_1)\phi_{P(\alpha_2)}(\vec{r}_2)\ldots\phi_{P(\alpha_A)}(\vec{r}_A)\,,\end{aligned}$$

with P a permutation of the set $\{\alpha_1,\alpha_2,\ldots\alpha_A\}$, we get,

$$\begin{aligned}\Gamma^{\rm el}_{\rm tot}(k,\vec{b}) &= \langle\Phi|\hat{\Gamma}_{\rm tot}(k,\vec{b})|\Phi\rangle = \langle\Phi|1-\prod_i^A(1-\hat{\Gamma}_i(k,\vec{b}))|\Phi\rangle\\ &= \int \mathrm{d}\vec{r}_1\ldots\mathrm{d}\vec{r}_A\,\langle\alpha_1\alpha_2\ldots\alpha_A|\,|\vec{r}_A\rangle\ldots|\vec{r}_2\rangle\,|\vec{r}_1\rangle\,\langle\vec{r}_1|\,\langle\vec{r}_2|\ldots\langle\vec{r}_A|\,1-\prod_i^A(1-\hat{\Gamma}_i(k,\vec{b}))\,|\alpha_1\alpha_2\ldots\alpha_A\rangle\\ &= \frac{1}{A!}\int \mathrm{d}\vec{r}_1\ldots\mathrm{d}\vec{r}_A\sum_{P_n,P_m}(-1)^{P_n+P_m}\phi^\dagger_{P_n(\alpha_1)}(\vec{r}_1)\phi^\dagger_{P_n(\alpha_2)}(\vec{r}_2)\ldots\phi^\dagger_{P_n(\alpha_A)}(\vec{r}_A)\\ &\quad\left[1-\prod_i^A(1-\Gamma_i(k,\vec{b}-\vec{b}_i))\right]\phi_{P_m(\alpha_1)}(\vec{r}_1)\phi_{P_m(\alpha_2)}(\vec{r}_2)\ldots\phi_{P_m(\alpha_A)}(\vec{r}_A)\\ &= 1-\frac{1}{A!}\sum_{P_n,P_m}(-1)^{P_n+P_m}\prod_i\int\mathrm{d}\vec{r}_i\phi^\dagger_{P_n(\alpha_i)}(\vec{r}_i)(1-\Gamma_i(k,\vec{b}-\vec{b}_i))\phi_{P_m(\alpha_i)}(\vec{r}_i)\end{aligned} \tag{A.17}$$

The superscript "el" in $\Gamma^{\rm el}_{\rm tot}(k,\vec{b})$ of Eq. (A.17) emphasizes the fact that elastic scattering is considered. With $\hat{\Gamma}(k,\vec{b})$ defined as $\langle\vec{r}\,'|\hat{\Gamma}(k,\vec{b})|\phi\rangle = \Gamma(k,\vec{b}-\vec{b}\,')\phi(\vec{r}\,')$. The frozen approximation amounts to requiring that the bound nucleons have fixed quantum numbers during the collision process. This can be translated into the condition $P_n = P_m \Leftrightarrow P_n(\alpha_i) = P_m(\alpha_i)$, $i\in\{1,2,\ldots A\}$.

$$\begin{aligned}\Gamma^{\rm el}_{\rm tot}(k,\vec{b}) &= 1-\prod_i^A\int\mathrm{d}\vec{r}_i\phi^\dagger_{\alpha_i}(\vec{r}_i)(1-\Gamma_i(k,\vec{b}-\vec{b}_i))\phi_{\alpha_i}(\vec{r}_i)\\ &= 1-\prod_i^A\left[1-\int\mathrm{d}\vec{r}_i|\phi_{\alpha_i}(\vec{r}_i)|^2\Gamma_i(k,\vec{b}-\vec{b}_i)\right] = 1-\prod_i\Big[1-G_i(k,\vec{b})\Big]\,.\end{aligned} \tag{A.18}$$

The function $G_i(k,\vec{b})$ is defined as $\int\mathrm{d}\vec{r}_i|\phi_{\alpha_i}(\vec{r}_i)|^2\Gamma_i(k,\vec{b}-\vec{b}_i)$.

Zero-range approximation

In nuclear physics the zero-range approximation is often used. Thereby the nucleon-nucleon interaction is described by a "contact" interaction with a vanishing range. This means that it is proportional to a delta function in the relative distance. The profile function in Eq. (A.18) can then be replaced by a delta function with the appropriate energy dependent normalization factor $A(k)$. The elements of the $G(k,\vec{b})$ vector are then given by,

$$G_i(k,\vec{b}) \approx \int \mathrm{d}\vec{r}_i |\phi_{\alpha_i}(\vec{r}_i)|^2 A(k)\delta(\vec{b}-\vec{b}_i)\,. \tag{A.19}$$

This reduces the dimensionality of the integrals from three to one.

N-scattering approximation

The profile function $\Gamma^{\mathrm{el}}_{\mathrm{tot}}(k,\vec{b})$ of Eq. (A.18) can be expanded as,

$$\begin{aligned}\Gamma^{\mathrm{el}}_{\mathrm{tot}}(k,\vec{b}) \approx \sum_i^A G_i(k,\vec{b}) - \sum_{i<j}^A G_i(k,\vec{b})G_j(k,\vec{b}) + \sum_{i<j<k}^A G_i(k,\vec{b})G_j(k,\vec{b})G_k(k,\vec{b}) - \ldots \\ - (-1)^N \sum_{i_1<i_2<\ldots<i_N}^A G_{i_1}(k,\vec{b})G_{i_2}(k,\vec{b})\ldots G_{i_N}(k,\vec{b}) + \mathcal{O}(G^{N+1})\,.\end{aligned} \tag{A.20}$$

This is an expansion in powers of $\hat{\Gamma}(k,\vec{b})$ (Eq. (A.17)) and can be interpreted as an expansion in the amount of active scatterers in the target. Truncating this expression up to first order in G_i ($N \leq 1$) is called the single-scattering approximation. Including the second order ($N \leq 2$) is denoted the double-scattering approximation. This expansion converges rapidly if the individual G_i's are small. With Eq. (A.14) and Eq. (A.18) this can be translated into the condition that the product of the nucleon-nucleon scattering cross section (σ in Eq.(A.14)) and the total integrated density seen by the projectile ($\propto \int \mathrm{d}\vec{r}_i |\phi_{\alpha_i}(\vec{r}_i)|^2 e^{-\frac{\vec{b}^2}{2\beta^2}}$) is much smaller than 1. As the nuclear density rises for increasing mass number A the convergence of Eq. (A.20) is expected to become worse for increasing A.

Thickness approximation

In the thickness approximation the single-particle densities $\rho_i = |\phi_{\alpha_i}|^2$ are replaced by an average density $\bar{\rho} = \frac{1}{A}\sum_{i=1}^A \rho_i$. As a result the expression for G_i becomes,

$$G_i(k,\vec{b}) = \int \mathrm{d}\vec{r}_i \bar{\rho}(\vec{r}_i)\Gamma_i(k,\vec{b}-\vec{b}_i)$$

Assuming that the interaction with the A scatterers can be modelled with one and the same profile function Γ (which is not necessarily the case, considering the difference between protons and neutrons for example) Eq. (A.18) is simplified to,

$$\begin{aligned}\Gamma^{\mathrm{el}}_{\mathrm{tot}}(k,\vec{b}) &= 1 - \prod_i^A \left[1 - \int \mathrm{d}\vec{r}_i \bar{\rho}(\vec{r}_i)\Gamma(k,\vec{b}-\vec{b}_i)\right] = 1 - \left[1 - \int \mathrm{d}\vec{r}_i \bar{\rho}(\vec{r}_i)\Gamma(k,\vec{b}-\vec{b}_i)\right]^A \\ &= 1 - \left[1 - G(k,\vec{b})\right]^A\,.\end{aligned} \tag{A.21}$$

$G(k,\vec{b})$ is defined as $\int \mathrm{d}\vec{r}_i\bar{\rho}(\vec{r}_i)\Gamma(k,\vec{b}-\vec{b}_i)$. The zero-range (Eq. (A.19)) and thickness approximation (Eq. (A.21)) can be combined to yield the following expression for the profile function,

$$\Gamma^{\mathrm{el}}_{\mathrm{tot}}(k,\vec{b}) = 1 - \prod_i \left[1 - \int \mathrm{d}\vec{r}_i\bar{\rho}(\vec{r}_i)A(k)\delta(\vec{b}-\vec{b}_i)\right] = 1 - \left[1 - A(k)\int \mathrm{d}\vec{r}\,'\bar{\rho}(\vec{r})\delta(\vec{b}-\vec{b}\,')\right]^A \tag{A.22}$$

Cross section

The elastic scattering amplitude $f^{\mathrm{el}}(k,\vec{\Delta})$ can be calculated using Eq. (A.13),

$$f^{\mathrm{el}}(k,\vec{\Delta}) = \frac{k}{2\pi i}\int \mathrm{d}^2\vec{b}\, e^{i\vec{\Delta}\cdot\vec{b}}\Gamma^{\mathrm{el}}_{\mathrm{tot}}(k,\vec{b})\,.$$

The total integrated cross section is then given by,

$$\sigma^{\mathrm{el}}(k) = \int \mathrm{d}^2\vec{\Delta}|f(k,\vec{\Delta})|^2 = \int \mathrm{d}^2\vec{b}|\Gamma^{\mathrm{el}}_{\mathrm{tot}}(k,\vec{b})|^2\,. \tag{A.23}$$

A.3.3 Effect of the approximations on the elastic cross section

In the previous section several approximations have been introduced that simplify the numerical calculations in the RMSGA. In order to gain further insight into the accuracy and characteristics of the approximations introduced above, they are applied to a toy model detailed below.

We consider a bound system consisting of A spin-less neutrons with mass m_N trapped in an isotropic harmonic oscillator potential $V(r) = \frac{1}{2}m_N\omega^2r^2$, $\hbar\omega = 15$ MeV. The single-particle wave functions are given by,

$$\phi_{nlm}(\vec{r}) \equiv \langle\vec{r}|nlm\rangle = R_{nl}(r)Y_{lm}(\Omega) \tag{A.24}$$

where $Y_{lm}(\Omega)$ are the spherical harmonics and the radial wave functions are given by

$$R_{nl}(r) = \left[\frac{2n!}{\Gamma(n+l+\frac{3}{2})}\nu^{l+\frac{3}{2}}\right]^{\frac{1}{2}} r^l e^{-\frac{\nu r^2}{2}} L_n^{l+\frac{1}{2}}(\nu r^2)\,. \tag{A.25}$$

Here, $L_n^{\alpha}(r)$ are the generalized Laguerre polynomials and

$$\nu = \frac{m_N\omega}{\hbar}\,. \tag{A.26}$$

The single-particle levels are populated up to a specific energy $E = \hbar\omega(2n+l+\frac{3}{2})$. Only closed shells are considered. Degenerate energy-levels are filled with the highest l value first.

The projectile is taken to be a proton with momentum $k = 500$ MeV. Details about the parameterization of the profile function for proton-neutron scattering can be found in Refs. [3, 5]. The total profile function (Eq. (A.18)) and the total cross section (Eq. (A.23)) are calculated in the RMSGA and following additional approximations,

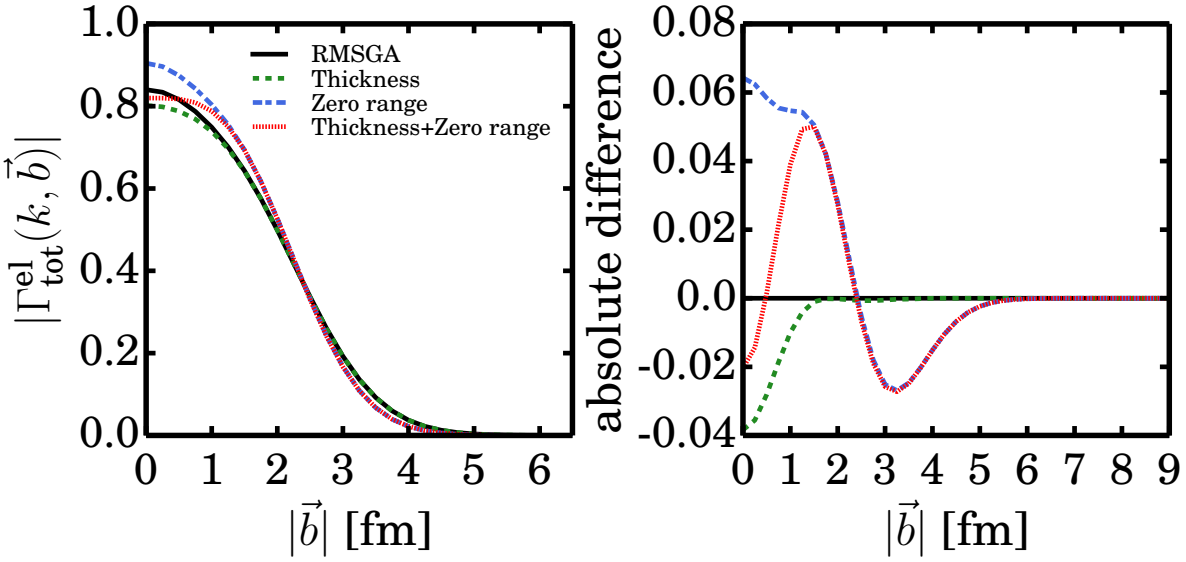

Figure A.1 – The total profile function $|\Gamma^{\rm el}_{\rm tot}(k = 500\ {\rm MeV}, \vec{b})|$ of Eq. (A.18) for $A = 4$. This system has a closed $n = 0, l = 1$ valence shell. The results obtained with different approximations are displayed. The right hand side figure shows the absolute difference of the the approximations compared to the full-fledged RSMGA result.

- The zero-range approximation of Eq. (A.19).
- The thickness approximation of Eq. (A.21) can be used.
- The combination of the zero-range and thickness approximation, (Eq. (A.22)).
- In the RMSGA and other above approximations the N-scattering approximation of Eq. (A.20) can be investigated.

Figures A.1,A.2,A.3 and A.4 show the calculated profile function $|\Gamma^{\rm el}_{\rm tot}(k, \vec{b})|$ of Eq. (A.18) with the different approximations listed above. From Figures A.1 and A.3 it is concluded that the thickness approximation performs the best, especially for larger systems. For larger systems the zero-range approximation underestimates the tails of $\Gamma^{\rm el}_{\rm tot}(k, \vec{b})$. The result for $\sigma^{\rm el}(k)$ (Eq. (A.23)) is depicted in Figure (A.5). The thickness approximation is very accurate while the zero-range approximation underestimates the cross section slightly.

From Fig. A.2 it is clear that for $A = 4$ the N-scattering approximation is converged for $N \leq 2$. For $A = 84$ (Fig. A.4) convergence is reached for $N \leq 20$. Lower-order approximations over-estimate the profile function $|\Gamma^{\rm el}_{\rm tot}(k = 500\ {\rm MeV}, \vec{b})|$ dramatically. It is worth to note that the N-scattering approximation converges fast in the tails of the profile function, corresponding with areas of low densities.

Numerical implications

From Eq. (A.18) it is clear that the fully-fledged RMSGA requires the evaluation of A three-dimensional integrals for each value of the momentum k of the particle and its impact parameter $\vec{b}$. The zero-range approximation of Eq. (A.19) reduces the dimensionality of those integrals from three to one. It can therefore be expected that the speed of the numerical

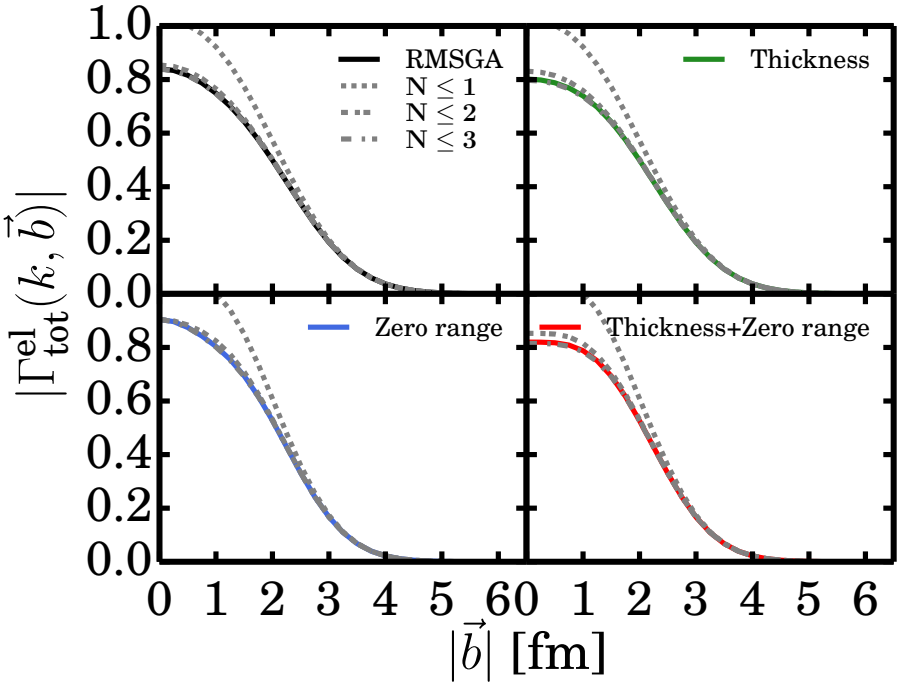

Figure A.2 – The total profile function $|\Gamma^{\rm el}_{\rm tot}(k = 500\ \text{Mev}, \vec{b})|$ of Eq. (A.18) for $A = 4$. This system has a closed $n = 0, l = 1$ valence shell. The results obtained with different approximations are displayed. The N-scattering expansion of Eq. (A.20) is represented with the dashed lines, where N denotes the order of the expansion.

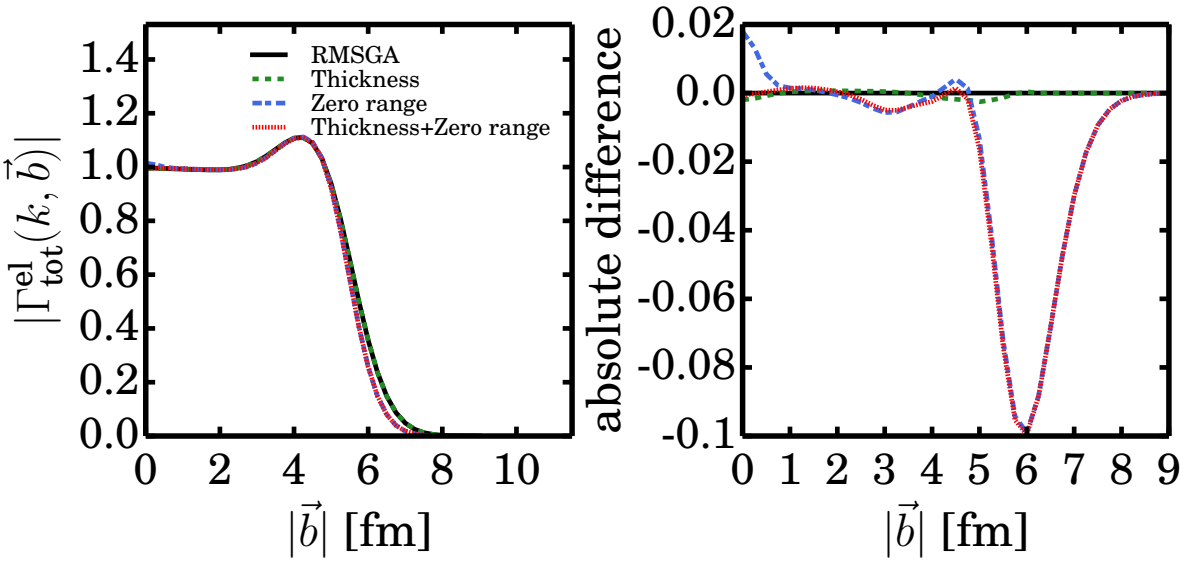

Figure A.3 – The total profile function $|\Gamma^{\rm el}_{\rm tot}(k = 500\ \text{MeV}, \vec{b})|$ of Eq. (A.18) for $A = 84$. This system has a closed $n = 3, l = 0$ valence shell. The results obtained with different approximations are displayed. The right hand side figure shows the absolute difference of the the approximations compared to the full-fledged RSMGA result.

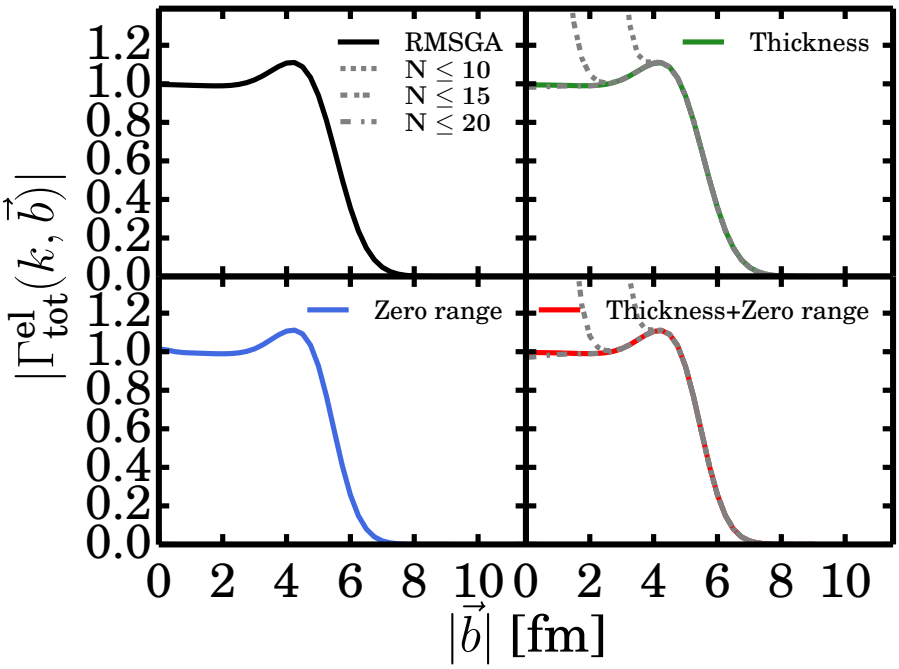

Figure A.4 – The total profile function $|\Gamma^{\rm el}_{\rm tot}(k = 500\ \text{MeV}, \vec{b})|$ of Eq. (A.18) for $A = 84$. This system has a closed $n = 3, l = 0$ valence shell. The results obtained with different approximations are displayed. The N-scattering expansion of Eq. (A.20) is represented with the dashed lines, where N denotes the order of the expansion. The N-scattering approximation is not calculated here when the thickness approximation is not used (i.e. "RMSGA" and "Zero range"). For a given order N the number of terms in Eq. (A.20) without the thickness approximation is equal to $\frac{A!}{N!(A-N)!}$. For large A this number quickly becomes infeasibly large.

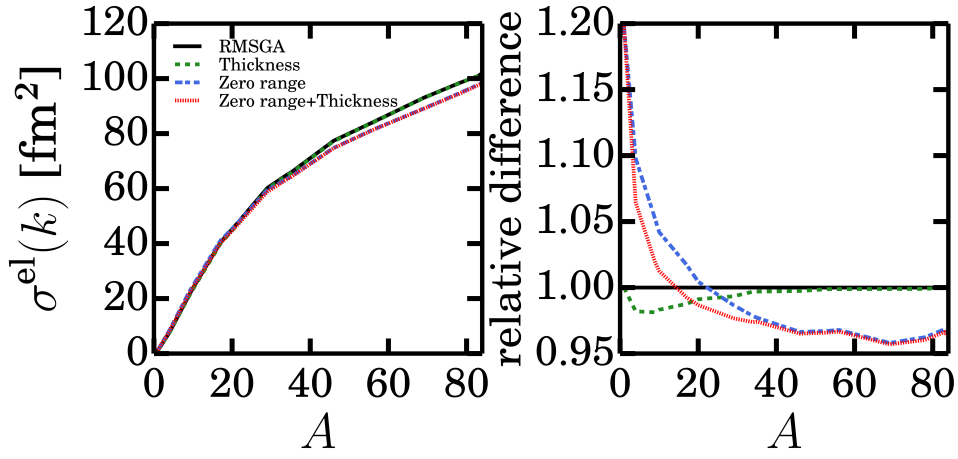

Figure A.5 – The elastic cross section of Eq (A.23) in function of the mass number A is displayed. The right hand side shows the relative difference of the different approximations compared to the full-fledged RSMGA result.

calculations improve considerably: A times the time saved by calculating a one-dimensional integral as opposed to a three-dimensional one. The thickness approximation of Eq. (A.21), replaces the single-particle densities with an averaged density. For this approximation only one three-dimensional integral has to be calculated, decreasing the computational effort by a factor of A. Combining the zero-range approximation with the thickness approximation leaves a single one-dimension integral to be calculated for each value of k and $\vec{b}$. The computation time is expected to decrease by a factor of A multiplied with the speed-up from reducing the dimensionality of the integral from three to one. The N-scattering approximation is very illustrative and allows for an easy interpretation of the number of active scatterers involved in the scattering process. However, it is not of any benefit in terms of computation intensity, as it does not decrease the numerical complexity. Additionally it is in general infeasible to apply in medium to large nuclei as the number of terms quickly becomes insurmountably large.

From the results presented in this chapter it is clear that the thickness approximation is by far the best choice when the fully-fledged RMSGA calculations are too computationally intensive. It benefits in general a larger speed-up than the zero-range approximation, especially for larger nuclei, while being the most accurate.

A.4 References

[1] C. J. Joachain, *Quantum collision theory* (North-Holland, Amsterdam, 1975).
[2] J. C. Bransden B., *Quantum mechanics*, 2ed (Pearson, 2000).
[3] J. Ryckebusch, D. Debruyne, P. Lava, et al., Nucl. Phys. **A728**, 226 (2003).
[4] P. Lava, M. Martinez, J. Ryckebusch, et al., Phys. Lett. B **595**, 177 (2004).
[5] W. Cosyn, "Exploring the limits of the hadronic picture of nuclei through pion and nucleon removal reactions", `http://inwpent5.ugent.be`, PhD thesis (Ghent University, May 2009).

APPENDIX B

Factorization of exclusive two-nucleon knockout cross sections

The use of a realistic factorized expression for the cross section of the two-nucleon knockout process is a key ingredient of the research presented in this dissertation. It allows us to write cross-section ratios which are independent of the complicated photon two-nucleon coupling, which would introduce a considerable model dependence. This is a strong argument for the robustness of the results derived using this factorized cross section.

The factorization procedure outlined here is strikingly different from the one presented in Sec. 3.2.2. In the article of Sec. 3.2.2 the cross section is factorized within the non-relativistic LCA framework. Here, the factorization property is proven in a relativistic treatment.

Final-state interactions (FSI) are included in the description of the two-nucleon knockout process. After the bound nucleon pair is brought into continuum states within the nucleus, they can interact and rescatter with the recoiling nucleus on their path through it. These interaction are denoted as FSI. Soft FSI are considered here. Thereby the rescattering events are elastic or mildly inelastic. This means that the exchanged three-momentum and energy are small compared to the three-momentum and energy of the escaping nucleons. In that case the RSMGA (Sec. A.3) provides a realistic framework for the description of the FSI.

In this appendix the necessary conditions are outlined in detail to arrive at a factorized expression for the exclusive electroinduced two-nucleon knockout cross section. We consider an electron exchanging four momentum $q = k'_e - k_e$, ($Q^2 = -q^2$) with a correlated nucleon pair in a nucleus $|P_A\rangle$. The correlated nucleon pair is knocked out leaving the recoiling nucleus $|P_{A-2}\rangle$ with little or no excitation energy in a well defined quantum state ($P^2_{A-2} \approx M^2_{A-2}$). A diagram of this reaction is displayed in Fig. (B.1). The matrix element M_{fi} for such a process is given by,

$$M_{fi} = e^2 \frac{j_\mu J^\mu}{Q^2} \,. \tag{B.1}$$

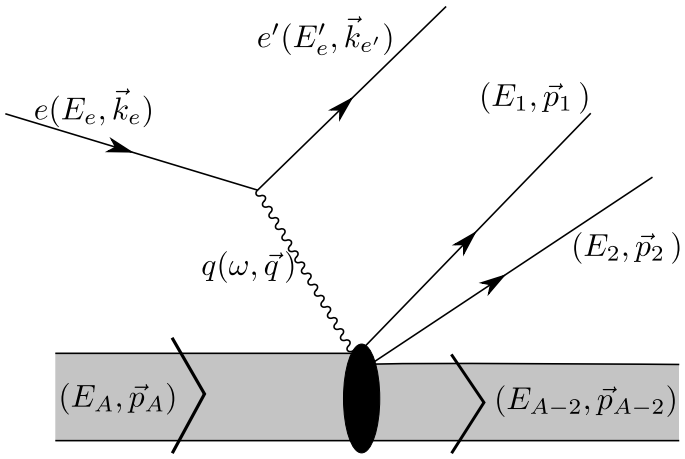

Figure B.1 – A sketch of the exclusive electrodinduced two-nucleon knockout reaction with all kinematic variables.

$j_\mu = \langle k'_e|\gamma_\mu|k_e\rangle$ is the lepton current and J^μ is the hadron current. The lepton current reads,

$$j_\mu = \bar{u}^{(r')}(k'_e)\gamma_\mu u^{(r)}(k_e)\,. \tag{B.2}$$

For the hadron current an expression of the form

$$J^\mu = \langle p_1 p_2 P_{A-2}|\mathcal{O}^{\mu,[2]}|P_A\rangle \tag{B.3}$$

is proposed, with $\mathcal{O}^{\mu,[2]}$ a two-body operator that accounts for the electromagnetic coupling to the correlated nucleon pair. Further, $|p_1\rangle\,|p_2\rangle$ are the momentum states of the ejected nucleons. The initial (final) state $|P_A\rangle$ ($|p_1 p_2 P_{A-2}\rangle$) is described by a Slater determinant of single-particle wave functions ϕ_{α_i} ($\langle\vec{r}\,|\alpha_i\rangle = \phi_{\alpha_i}(\vec{r}), \langle\vec{r}\,|p_i\rangle = \phi_{p_i}(\vec{r}) = u_{s_i}(p_i)e^{i\vec{r}\cdot\vec{p}_i}$),

$$\langle\vec{r}_1\vec{r}_2\ldots\vec{r}_A|P_A\rangle = \frac{1}{\sqrt{A!}}\sum_{P_m}(-1)^{P_m}\phi_{P_m(\alpha_1)}(\vec{r}_1)\phi_{P_m(\alpha_2)}(\vec{r}_2)\ldots\phi_{P_m(\alpha_A)}(\vec{r}_A)$$
$$\langle\vec{r}_1\vec{r}_2\ldots\vec{r}_A|p_1p_2P_{A-2}\rangle = \frac{1}{\sqrt{A!}}\sum_{P_n}(-1)^{P_n}\phi_{P_n(p_1)}(\vec{r}_1)\phi_{P_n(p_2)}(\vec{r}_2)\phi_{P_n(\alpha_3)}(\vec{r}_3)\ldots\phi_{P_n(\alpha_A)}(\vec{r}_A)\,.$$

P_m (P_n) permutes the set $\{\alpha_1, \alpha_2, \ldots \alpha_A\}$ ($\{p_1, p_2, \alpha_3, \ldots \alpha_A\}$). The choice of replacing α_1, α_2 with p_1, p_2 corresponds with a particular choice of the final quantum state of the residual $A-2$ system. The recoiling nucleus $|P_{A-2}\rangle$ is left with the α_1, α_2 orbitals empty as those particles are excited into continuum states. If the orbitals of the initial nucleon-pair α_1, α_2 can not be resolved, the sum over all possible single-particle quantum numbers has to appear in the summation over the final states. The hadron current (Eq. (B.3)) can now be written as,

$$J^\mu = \frac{A(A-1)}{A!}\sum_{P_nP_m}(-1)^{P_n+P_m}\prod_{i=1}^{A}\int \mathrm{d}\vec{r}_i$$
$$\phi^\dagger_{P_n(p_1)}(\vec{r}_1)\phi^\dagger_{P_n(p_2)}(\vec{r}_2)\mathcal{O}^\mu(\vec{r}_1,\vec{r}_2)\phi_{P_m(\alpha_1)}(\vec{r}_1)\phi_{P_m(\alpha_2)}(\vec{r}_2)$$
$$\phi^\dagger_{P_n(\alpha_3)}(\vec{r}_3)\phi_{P_m(\alpha_3)}(\vec{r}_3)\ldots\phi^\dagger_{P_n(\alpha_A)}(\vec{r}_A)\phi_{P_m(\alpha_A)}(\vec{r}_A)\,. \tag{B.4}$$

The identity $\sum_{ij}^{A} \langle C|\mathcal{O}_{ij}|D\rangle = A(A-1)\,\langle C|\mathcal{O}_{12}|D\rangle$ has been used. It is valid for a two-body operator inserted between A-particle antisymmetric states C, D.

In the frozen spectator approximation it is assumed that the nucleons not taking part in the scattering process remain fixed. That is, their quantum numbers do not change during the collision of the virtual photon with the bound nucleon pair. This condition can be enforced by inserting $\delta_{P_n(\alpha_3),P_m(\alpha_3)} \ldots \delta_{P_n(\alpha_A),P_m(\alpha_A)}$ in Eq. (B.4). J^μ is then invariant under the $(A-2)!$ permutations of $P_m(\alpha_3) \ldots P_m(\alpha_A)$,

$$J^\mu = \prod_{i=1}^{A} \int \mathrm{d}\vec{r}_i \left[\phi^\dagger_{p_1}(\vec{r}_1)\phi^\dagger_{p_2}(\vec{r}_2) - \phi^\dagger_{p_2}(\vec{r}_1)\phi^\dagger_{p_1}(\vec{r}_2)\right] \\ \mathcal{O}^\mu(\vec{r}_1,\vec{r}_2)\left[\phi_{\alpha_1}(\vec{r}_1)\phi_{\alpha_2}(\vec{r}_2) - \phi_{\alpha_2}(\vec{r}_1)\phi_{\alpha_1}(\vec{r}_2)\right]|\phi_{\alpha_3}(\vec{r}_3)|^2 \ldots |\phi_{\alpha_A}(\vec{r}_A)|^2 \,.$$

After including the effect of final-state interactions (FSI) using the RMSGA (Sec. A.3), the outgoing wave functions pick up a phase $\chi(\vec{r},\vec{r}_1,\ldots\vec{r}_A)$ (Eq. (A.16)), with Eq. (A.3) they adopt the form,

$$\phi_{p_1}(\vec{r}_1) \to \phi_{p_1}(\vec{r}_1)\eta(\vec{r}_1;\vec{r}_3\ldots\vec{r}_A) \\ \phi_{p_2}(\vec{r}_2) \to \phi_{p_2}(\vec{r}_2)\eta(\vec{r}_2;\vec{r}_3\ldots\vec{r}_A)$$

Defining $\mathscr{F}_{\mathrm{FSI}}$ as,

$$\mathscr{F}_{\mathrm{FSI}}(\vec{r}_1,\vec{r}_2) = \prod_{i=3}^{A} \int \mathrm{d}\vec{r}_i\, |\phi_{\alpha_i}(\vec{r}_i)|^2 \eta(\vec{r}_1;\vec{r}_3\ldots\vec{r}_A)\eta(\vec{r}_2;\vec{r}_3\ldots\vec{r}_A)\,,$$

the hadron current J^μ can be written as,

$$\begin{aligned} J^\mu &= \int \mathrm{d}\vec{r}_1 \int \mathrm{d}\vec{r}_2 \mathscr{F}_{\mathrm{FSI}}(\vec{r}_1,\vec{r}_2)\left[\phi^\dagger_{p_1}(\vec{r}_1)\phi^\dagger_{p_2}(\vec{r}_2) - \phi^\dagger_{p_2}(\vec{r}_1)\phi^\dagger_{p_1}(\vec{r}_2)\right] \\ &\qquad \mathcal{O}^\mu(\vec{r}_1,\vec{r}_2)\left[\phi_{\alpha_1}(\vec{r}_1)\phi_{\alpha_2}(\vec{r}_2) - \phi_{\alpha_2}(\vec{r}_1)\phi_{\alpha_1}(\vec{r}_2)\right] \\ &= \int \mathrm{d}\vec{r}_1 \int \mathrm{d}\vec{r}_2 \mathscr{F}_{\mathrm{FSI}}(\vec{r}_1,\vec{r}_2)\left[\phi^\dagger_{p_1}(\vec{r}_1)\phi^\dagger_{p_2}(\vec{r}_2) - \phi^\dagger_{p_2}(\vec{r}_1)\phi^\dagger_{p_1}(\vec{r}_2)\right] \\ &\qquad \left[\mathcal{O}^\mu(\vec{r}_1,\vec{r}_2) + \mathcal{O}^\mu(\vec{r}_2,\vec{r}_1)\right]\phi_{\alpha_1}(\vec{r}_1)\phi_{\alpha_2}(\vec{r}_2)\,. \end{aligned} \tag{B.5}$$

The operator $\mathcal{O}^\mu(\vec{r}_1,\vec{r}_2)$ is considered to be of the form $\Gamma^\mu_{\gamma N^*} e^{i\vec{q}\cdot\vec{r}_1} g(\vec{r}_1,\vec{r}_2)$. The exponential $e^{i\vec{q}\cdot\vec{r}_1}$ follows from the part of the photon propagator attached to the hadron vertex $\vec{r}_1$. $g(\vec{r}_1,\vec{r}_2)$ is a correlation function for which the property $g(\vec{r}_1,\vec{r}_2) \equiv g(\vec{r}_2,\vec{r}_1)$ is assumed. With this description of the operator $\mathcal{O}^\mu(\vec{r}_1,\vec{r}_2)$ Eq. (B.5) becomes,

$$\begin{aligned} J^\mu &= \int \mathrm{d}\vec{r}_1 \int \mathrm{d}\vec{r}_2 \mathscr{F}_{\mathrm{FSI}}(\vec{r}_1,\vec{r}_2)\left[\bar{u}_{s_1}(p_1)e^{-i\vec{p}_1\cdot\vec{r}_1}\bar{u}_{s_2}(p_2)e^{-i\vec{p}_2\cdot\vec{r}_2} - \bar{u}_{s_2}(p_2)e^{-i\vec{p}_2\cdot\vec{r}_1}\bar{u}_{s_1}(p_1)e^{-i\vec{p}_1\cdot\vec{r}_2}\right] \\ &\qquad \left[\Gamma^\mu_{\gamma N^*}e^{i\vec{q}\cdot\vec{r}_1} + \Gamma^\mu_{\gamma N^*}e^{i\vec{q}\cdot\vec{r}_2}\right] g(\vec{r}_1,\vec{r}_2)\phi_\alpha(\vec{r}_1)\phi_{\alpha_2}(\vec{r}_2) \\ &= \int \mathrm{d}\vec{r}_1 \int \mathrm{d}\vec{r}_2 \mathscr{F}_{\mathrm{FSI}}(\vec{r}_1,\vec{r}_2) g(\vec{r}_1,\vec{r}_2)\Big\{ \\ &\quad e^{-i(\vec{p}_1-\vec{q})\cdot\vec{r}_1}e^{-i\vec{p}_2\cdot\vec{r}_2}\bar{u}_{s_1}(p_1)\Gamma^\mu_{\gamma N^*}\phi_{\alpha_1}(\vec{r}_1)\bar{u}_{s_2}(p_2)\phi_{\alpha_2}(\vec{r}_2) \\ &\quad + e^{-i\vec{p}_1\cdot\vec{r}_1}e^{-i(\vec{p}_2-\vec{q})\cdot\vec{r}_2}\bar{u}_{s_1}(p_1)\phi_{\alpha_1}(\vec{r}_1)\bar{u}_{s_2}(p_2)\Gamma^\mu_{\gamma N^*}\phi_{\alpha_2}(\vec{r}_2) \\ &\quad - e^{-i(\vec{p}_2-\vec{q})\cdot\vec{r}_1}e^{-i\vec{p}_1\cdot\vec{r}_2}\bar{u}_{s_2}(p_2)\Gamma^\mu_{\gamma N^*}\phi_{\alpha_1}(\vec{r}_1)\bar{u}_{s_1}(p_1)\phi_{\alpha_2}(\vec{r}_2) \\ &\quad - e^{-i\vec{p}_2\cdot\vec{r}_1}e^{-i(\vec{p}_1-\vec{q})\cdot\vec{r}_2}\bar{u}_{s_2}(p_2)\phi_{\alpha_1}(\vec{r}_1)\bar{u}_{s_1}(p_1)\Gamma^\mu_{\gamma N^*}\phi_{\alpha_2}(\vec{r}_2)\Big\}\,. \end{aligned} \tag{B.6}$$

Introducing center-of-mass (c.m.) and relative coordinates $\vec{R}_{12} = \frac{\vec{r}_1+\vec{r}_2}{2}$, $\vec{r}_{12} = \vec{r}_1 - \vec{r}_2$, the following approximations that are crucial in order to reach factorization of the cross section are applied,

$$\begin{aligned} g(\vec{R}_{12} + \frac{\vec{r}_{12}}{2}, \vec{R}_{12} - \frac{\vec{r}_{12}}{2}) &\approx g(\vec{r}_{12}) \\ \mathscr{F}_{\mathrm{FSI}}(\vec{R}_{12} + \frac{\vec{r}_{12}}{2}, \vec{R}_{12} - \frac{\vec{r}_{12}}{2}) &\approx \mathscr{F}_{\mathrm{FSI}}(\vec{R}_{12}) + O(\vec{r}_{12}) \\ \phi_{\alpha_{1,2}}(\vec{R}_{12} \pm \frac{\vec{r}_{12}}{2}) &\approx \phi_{\alpha_{1,2}}(\vec{R}_{12}) + O(\vec{r}_{12})\,. \end{aligned}$$

The last two approximations are a zero-order expansion in the relative coordinate $\vec{r}_{12}$. It assumes that the interaction selects two nucleons that are close compared to the distance scale of the nucleus and the single-particle wave functions [1, 2]. This limits this derivation to the study of short-range correlations (SRC). The hadron current of Eq. (B.6) becomes,

$$\begin{aligned} J^\mu = \int \mathrm{d}\vec{R}_{12} \int \mathrm{d}\vec{r}_{12} \mathscr{F}_{\mathrm{FSI}}(\vec{R}_{12}) g(\vec{r}_{12}) \Big\{ & \\ & e^{-i(\vec{p}_1+\vec{p}_2-\vec{q})\cdot\vec{R}_{12}} e^{-i(\vec{p}_1-\vec{p}_2-\vec{q})\cdot\frac{\vec{r}_{12}}{2}} \bar{u}_{s_1}(p_1)\Gamma^\mu_{\gamma N^*}\phi_{\alpha_1}(\vec{R}_{12})\bar{u}_{s_2}(p_2)\phi_{\alpha_2}(\vec{R}_{12}) \\ & + e^{-i(\vec{p}_1+\vec{p}_2-\vec{q})\cdot\vec{R}_{12}} e^{-i(\vec{p}_1-\vec{p}_2+\vec{q})\cdot\frac{\vec{r}_{12}}{2}} \bar{u}_{s_1}(p_1)\phi_{\alpha_1}(\vec{R}_{12})\bar{u}_{s_2}(p_2)\Gamma^\mu_{\gamma N^*}\phi_{\alpha_2}(\vec{R}_{12}) \\ & - e^{-i(\vec{p}_1+\vec{p}_2-\vec{q})\cdot\vec{R}_{12}} e^{i(\vec{p}_1-\vec{p}_2+\vec{q})\cdot\frac{\vec{r}_{12}}{2}} \bar{u}_{s_2}(p_2)\Gamma^\mu_{\gamma N^*}\phi_{\alpha_1}(\vec{R}_{12})\bar{u}_{s_1}(p_1)\phi_{\alpha_2}(\vec{R}_{12}) \\ & - e^{-i(\vec{p}_1+\vec{p}_2-\vec{q})\cdot\vec{r}_1} e^{i(\vec{p}_1-\vec{p}_2-\vec{q})\cdot\frac{\vec{r}_{12}}{2}} \bar{u}_{s_2}(p_2)\phi_{\alpha_1}(\vec{R}_{12})\bar{u}_{s_1}(p_1)\Gamma^\mu_{\gamma N^*}\phi_{\alpha_2}(\vec{R}_{12}) \Big\}\,. \end{aligned}$$

After introducing the c.m. and relative momentum of the initial nucleon pair, $\vec{P}_{12} = \vec{p}_1+\vec{p}_2-\vec{q}$ and $\vec{k}^{\pm}_{12} = \frac{\vec{p}_1-\vec{p}_2}{2} \pm \frac{\vec{q}}{2}$, the hadron current adopts the form,

$$\begin{aligned} J^\mu = \int \mathrm{d}\vec{R}_{12} \int \mathrm{d}\vec{r}_{12} \mathscr{F}_{\mathrm{FSI}}(\vec{R}_{12}) g(\vec{r}_{12}) e^{-i\vec{P}_{12}\cdot\vec{R}_{12}} \Big\{ & \\ & e^{-i\vec{k}^-_{12}\cdot\vec{r}_{12}} \bar{u}_{s_1}(p_1)\Gamma^\mu_{\gamma N^*}\phi_{\alpha_1}(\vec{R}_{12})\bar{u}_{s_2}(p_2)\phi_{\alpha_2}(\vec{R}_{12}) \\ & + e^{-i\vec{k}^+_{12}\cdot\vec{r}_{12}} \bar{u}_{s_1}(p_1)\phi_{\alpha_1}(\vec{R}_{12})\bar{u}_{s_2}(p_2)\Gamma^\mu_{\gamma N^*}\phi_{\alpha_2}(\vec{R}_{12}) \\ & - e^{i\vec{k}^+_{12}\cdot\vec{r}_{12}} \bar{u}_{s_2}(p_2)\Gamma^\mu_{\gamma N^*}\phi_{\alpha_1}(\vec{R}_{12})\bar{u}_{s_1}(p_1)\phi_{\alpha_2}(\vec{R}_{12}) \\ & - e^{i\vec{k}^-_{12}\cdot\vec{r}_{12}} \bar{u}_{s_2}(p_2)\phi_{\alpha_1}(\vec{R}_{12})\bar{u}_{s_1}(p_1)\Gamma^\mu_{\gamma N^*}\phi_{\alpha_2}(\vec{R}_{12}) \Big\}\,, \end{aligned}$$

with $g(\vec{k}^{\pm}_{12}) = \int \mathrm{d}\vec{r}_{12} e^{-i\vec{k}^{\pm}_{12}\cdot\vec{r}_{12}} g(\vec{r}_{12})$,

$$\begin{aligned} J^\mu = \int \mathrm{d}\vec{R}_{12} \mathscr{F}_{\mathrm{FSI}}(\vec{R}_{12}) e^{-i\vec{P}_{12}\cdot\vec{R}_{12}} \Big\{ & \\ & g(\vec{k}^-_{12}) \bar{u}_{s_1}(p_1)\Gamma^\mu_{\gamma N^*}\phi_{\alpha_1}(\vec{R}_{12})\bar{u}_{s_2}(p_2)\phi_{\alpha_2}(\vec{R}_{12}) \\ & + g(\vec{k}^+_{12}) \bar{u}_{s_1}(p_1)\phi_{\alpha_1}(\vec{R}_{12})\bar{u}_{s_2}(p_2)\Gamma^\mu_{\gamma N^*}\phi_{\alpha_2}(\vec{R}_{12}) \\ & - g(-\vec{k}^+_{12}) \bar{u}_{s_2}(p_2)\Gamma^\mu_{\gamma N^*}\phi_{\alpha_1}(\vec{R}_{12})\bar{u}_{s_1}(p_1)\phi_{\alpha_2}(\vec{R}_{12}) \\ & - g(-\vec{k}^-_{12}) \bar{u}_{s_2}(p_2)\phi_{\alpha_1}(\vec{R}_{12})\bar{u}_{s_1}(p_1)\Gamma^\mu_{\gamma N^*}\phi_{\alpha_2}(\vec{R}_{12}) \Big\}\,. \end{aligned}$$

In order to progress towards a factorized expression in c.m. ($\vec{P}_{12}$) and relative momentum ($\vec{k}_{12}$) the photon-nucleon coupling $\Gamma^{\mu}_{\gamma N^*}$ is decoupled from the c.m. coordinate $\vec{R}_{12}$. This can be achieved by inserting the identity,

$$\mathbb{1} = \sum_s \left[u_s(p)\bar{u}_s(p) - v_s(p)\bar{v}_s(p)\right]$$

between the coupling $\Gamma^{\mu}_{\gamma N^*}$ and the single-particle wave functions $\phi_{\alpha_1}, \phi_{\alpha_2}$. Neglecting projections on the antiparticles v the hadron current can be written as,

$$\begin{aligned} J^{\mu} = \sum_s \int \mathrm{d}\vec{R}_{12} \mathscr{F}_{\mathrm{FSI}}(\vec{R}_{12}) e^{-i\vec{P}_{12}\cdot\vec{R}_{12}} \Big\{ & \\ & g(\vec{k}^{-}_{12}) \left[\bar{u}_{s_1}(p_1)\Gamma^{\mu}_{\gamma N^*}u_s(p_1)\right] \bar{u}_s(p_1)\phi_{\alpha_1}(\vec{R}_{12})\bar{u}_{s_2}(p_2)\phi_{\alpha_2}(\vec{R}_{12}) \\ & + g(\vec{k}^{+}_{12})\bar{u}_{s_1}(p_1)\phi_{\alpha_1}(\vec{R}_{12}) \left[\bar{u}_{s_2}(p_2)\Gamma^{\mu}_{\gamma N^*}u_s(p_2)\right] \bar{u}_s(p_2)\phi_{\alpha_2}(\vec{R}_{12}) \\ & - g(-\vec{k}^{+}_{12}) \left[\bar{u}_{s_2}(p_2)\Gamma^{\mu}_{\gamma N^*}u_s(p_2)\right] \bar{u}_s(p_2)\phi_{\alpha_1}(\vec{R}_{12})\bar{u}_{s_1}(p_1)\phi_{\alpha_2}(\vec{R}_{12}) \\ & - g(-\vec{k}^{-}_{12})\bar{u}_{s_2}(p_2)\phi_{\alpha_1}(\vec{R}_{12}) \left[\bar{u}_{s_1}(p_1)\Gamma^{\mu}_{\gamma N^*}u_s(p_1)\right] \bar{u}_s(p_1)\phi_{\alpha_2}(\vec{R}_{12}) \Big\} . \end{aligned}$$

Let $\widetilde{J}^{\mu}_{s_1,s}(p) = \bar{u}_{s_1}(p)\Gamma^{\mu}_{\gamma N^*}u_s(p)$ and,

$$\begin{aligned} F^{D}_{(s,\alpha_1)(s_2,\alpha_2)}(\vec{P}_{12}) &= \int \mathrm{d}\vec{R}_{12} \mathscr{F}_{\mathrm{FSI}}(\vec{R}_{12}) e^{-i\vec{P}_{12}\cdot\vec{R}_{12}} \bar{u}_s(p_1)\phi_{\alpha_1}(\vec{R}_{12})\bar{u}_{s_2}(p_2)\phi_{\alpha_2}(\vec{R}_{12}) \\ F^{D}_{(s_1,\alpha_1)(s,\alpha_2)}(\vec{P}_{12}) &= \int \mathrm{d}\vec{R}_{12} \mathscr{F}_{\mathrm{FSI}}(\vec{R}_{12}) e^{-i\vec{P}_{12}\cdot\vec{R}_{12}} \bar{u}_{s_1}(p_1)\phi_{\alpha_1}(\vec{R}_{12})\bar{u}_s(p_2)\phi_{\alpha_2}(\vec{R}_{12}) . \end{aligned}$$

The Dirac spinors $u_s(p)$ depend on the momentum $\vec{p}$ of the particle. In writing F^D as a function of only the c.m. momentum $\vec{P}_{12}$ this momentum dependence (lower component) of the Dirac spinors is neglected.

$$\begin{aligned} J^{\mu} = \sum_s \Big(& \widetilde{J}^{\mu}_{s_1,s}(p_1) F^{D}_{(s,\alpha_1)(s_2,\alpha_2)}(\vec{P}_{12}) g(\vec{k}^{-}_{12}) + \widetilde{J}^{\mu}_{s_2,s}(p_2) F^{D}_{(s_1,\alpha_1)(s,\alpha_2)}(\vec{P}_{12}) g(\vec{k}^{+}_{12}) \\ & - \widetilde{J}^{\mu}_{s_2,s}(p_2) F^{D}_{(s,\alpha_1)(s_1,\alpha_2}(\vec{P}_{12}) g(-\vec{k}^{+}_{12}) - \widetilde{J}^{\mu}_{s_1,s}(p_1) F^{D}_{(s_2,\alpha_1)(s,\alpha_2)}(\vec{P}_{12}) g(-\vec{k}^{-}_{12}) \Big) . \end{aligned} \tag{B.7}$$

Of these four terms only the first one is kept (direct diagram), the three remaining terms are discarded. The direct diagram corresponds with diagram (a) in Fig. B.2. This is a valid approximation if the kinematics are tuned in specific way that allows us to differentiate the two nucleons in the final state and identify which nucleon absorbed the photon. The hadron current then becomes,

$$J^{\mu} \approx \sum_s \widetilde{J}^{\mu}_{s_1,s}(p_1) F^{D}_{(s,\alpha_1)(s_2,\alpha_2)}(\vec{P}_{12}) g(\vec{k}^{-}_{12}) . \tag{B.8}$$

$\widetilde{J}^{\mu}_{s_1,s}(p_1)$ can be identified as the "free" nuclear current $\langle p_1, s_1|\Gamma^{\mu}_{\gamma N^*}|p_1, s\rangle$. $\widetilde{J}^{\mu}_{s_1,s}(p_1)$ depends on both c.m. and relative momentum through $\vec{p}_1 = \frac{\vec{P}_{12}}{2} + \vec{k}^{-}_{12} + \vec{q}$, however the dependence on the c.m. momentum $\vec{P}_{12}$ can be safely ignored as in kinematics probing SRC the typical values of $|\vec{q}|$ and $|\vec{k}_{12}|$ are much larger than $|\vec{P}_{12}|$. $J^{\mu}_{s_1,s}(p_1) \approx J^{\mu}_{s_1,s}(\vec{k}^{-}_{12} + \vec{q}) = J^{\mu}_{s_1,s}(\vec{k}^{+}_{12})$. The sum over s in Eq. (B.8), coupling $J^{\mu}_{s_1,s}(\vec{k}^{+}_{12})$ and $F^{D}_{(s,\alpha_1)(s_2,\alpha_2)}(\vec{P}_{12})$ is now the only remaining

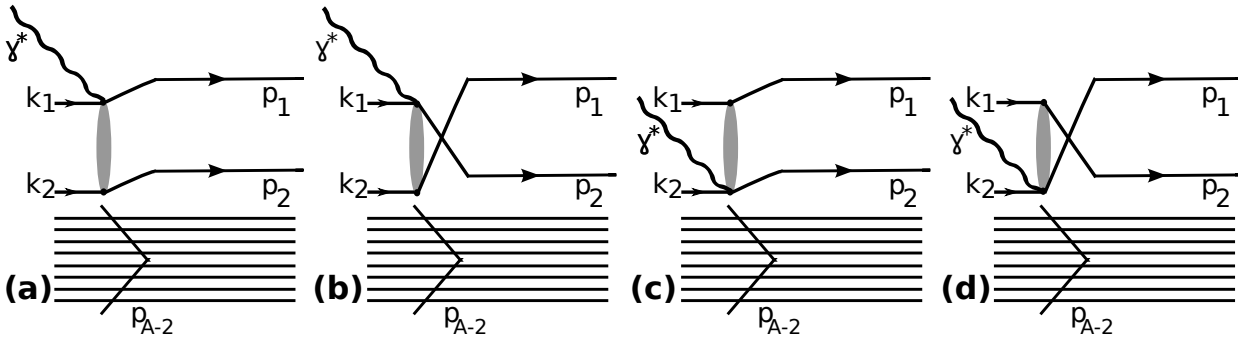

Figure B.2 – The four diagrams contributing to the hadron current of Eq. (B.7).

factor that couples the c.m. momentum to the relative momentum. A fully factorized expression can be obtained by requiring that $\Gamma^{\mu}_{\gamma N^*}$ is spin conserving,

$$\widetilde{J}^{\mu}_{r,s}(p) = \bar{u}_r(p)\Gamma^{\mu}_{\gamma N^*}u_s(p) = \widetilde{J}^{\mu}_{r,s}(p)\delta_{r,s}\,. \tag{B.9}$$

From the fact that electromagnetic interactions conserve parity and are time reversal invariant it can be shown that $\widetilde{J}^{\mu}_{r,s}(p)\delta_{r,s} = \widetilde{J}^{\mu\,*}_{-r,-s}(p)\delta_{r,s}$. In what follows the complex conjugation of the hadron current can be safely ignored when the modulus of the matrix element is considered. With Eq. (B.9) the hadron current of Eq. (B.8) can then be written as,

$$J^{\mu} \approx \sum_{s} \widetilde{J}^{\mu}_{s_1,s}(p_1)F^{D}_{(s,\alpha_1)(s_2,\alpha_2)}(\vec{P}_{12})g(\vec{k}^{-}_{12}) = \widetilde{J}^{\mu}(p_1)F^{D}_{(s_1,\alpha_1)(s_2,\alpha_2)}(\vec{P}_{12})g(\vec{k}^{-}_{12})\,.$$

Taking the modulus squared of the matrix element $\mathcal{M}_{fi}$ of Eq. (B.1) gives,

$$|\mathcal{M}_{fi}|^2 = \frac{e^4}{Q^4}\eta_{\mu\nu}\widetilde{W}^{\mu\nu}|F^{D}_{(s_1\alpha_1)(s_2\alpha_2)}(\vec{P}_{12})|^2|g(\vec{k}^{-}_{12})|^2\,.$$

There, $\eta_{\mu\nu}$ is the lepton tensor and $\widetilde{W}^{\mu\nu}$ is the "free" nuclear tensor $\widetilde{J}^{\nu *}\widetilde{J}^{\mu}$. The summation over the initial quantum numbers of the nucleon pair (α_1, α_2) and averaging over the final spins s_1, s_2 gives,

$$\begin{aligned}\overline{\sum_{fi}}|\mathcal{M}_{fi}|^2 &= \frac{e^4}{Q^4}\eta_{\mu\nu}\widetilde{W}^{\mu\nu}|g(\vec{k}^{-}_{12})|^2\frac{1}{4}\sum_{s_1s_2}\sum_{\alpha_1\alpha_2}|F^{D}_{(s_1\alpha_1)(s_2\alpha_2)}(\vec{P}_{12})|^2 \\ &= \sigma_{e,\gamma^*N}(\vec{k}^{-}_{12})\mathrm{F}^{D}(\vec{P}_{12})\,,\end{aligned}$$

with $\mathrm{F}^{D}(\vec{P}_{12})$ and $\sigma_{e,\gamma^*N}(\vec{k}^{-}_{12})$ defined as,

$$\begin{aligned}\mathrm{F}^{D}(\vec{P}_{12}) &= \frac{1}{4}\sum_{s_1s_2}\sum_{\alpha\beta}\left|F^{D}_{(s_1\alpha)(s_2\beta)}(\vec{P}_{12})\right|^2\,, \\ \sigma_{e,\gamma^*N}(\vec{k}^{-}_{12}) &= \frac{e^4}{Q^4}\eta_{\mu\nu}\widetilde{W}^{\mu\nu}|g(\vec{k}^{-}_{12})|^2\,.\end{aligned}$$

The factorized cross section is then given by, [1]

$$\mathrm{d}\sigma \propto \sigma_{e,\gamma^*N}(\vec{k}^{-}_{12})\mathrm{F}^{D}(\vec{P}_{12})\,. \tag{B.10}$$

[1]Note that strictly speaking the kinematical prefactors in the cross section do not factorize in c.m. and relative momentum. However, under conditions where F^D is "sharp" enough in $\vec{P}_{12}$-space this dependence can be safely ignored

$\sigma_{e,\gamma^* N}(\vec{k}_{12}^{-})$ depends on the relative momentum of the nucleon pair and encodes all the information concerning the complex photon-two nucleon coupling. The only factor depending on the nuclear structure (single-particle wave functions) is $\mathrm{F}^D(\vec{P}_{12})$. When different nuclei are considered $\mathrm{F}^D(\vec{P}_{12})$ is the only quantity subject to change, depending on the specific nucleus involved in the scattering reaction. This makes this expression very suitable to investigate the mass dependence of nuclear properties in a systematic and consistent way.

APPENDIX C

Publications

C.1 Publications

- Colle, Camille and Cosyn, Wim and Ryckebusch, Jan and Vanhalst, Maarten, *Factorization of exclusive electron-induced two-nucleon knockout*, Phys. Rev. C **89**, 024603 (2014)
- Colle, C. and Hen, O. and Cosyn, W. and Korover, I. and Piasetzky, E. and Ryckebusch, J. and Weinstein, L. B., *Extracting the mass dependence and quantum numbers of short-range correlated pairs from $A(e, e'p)$ and $A(e, e'pp)$ scattering*, Phys. Rev. C **92**, 024604 (2015)
- Colle, Camille and Cosyn, Wim and Ryckebusch, Jan, *Final-state interactions in two-nucleon knockout reactions*, Phys. Rev. C **93**, 034608 (2016)

C.2 Presentations

Talks

- *Mass dependence of proton-proton correlations*, C. Colle, W. Cosyn, S. Stevens, J. Ryckebusch, BriX workshop May 7-8, 2014, Gent.
- *Mass dependence of short-range correlations*, C. Colle, W. Cosyn, J. Ryckebusch, ECT* July 30, 2014, Trento.
- *Mass dependence of proton-proton correlations*, C. Colle, W. Cosyn, J. Ryckebusch, Frontiers and careers in photonuclear physics, August 7-9, 2014, MIT, Boston, MA.

- *Mass dependence of short-range correlations in nuclei*, C. Colle, W. Cosyn, J. Ryckebusch, M. Vanhalst, FENS inside-out, October 20, 2014, Ghent University, Gent.
- *Mass dependence of short-range correlations in nuclei*, C. Colle, W. Cosyn, J. Ryckebusch, S. Stevens, M. Vanhalst, BriX workshop May 27-28, 2015,Liége.
- *Mass dependence of short-range correlations in nuclei*, C. Colle, W. Cosyn, J. Ryckebusch, S. Stevens, ENPC August 30 to September 4, 2015, Groningen.
- *Probing nuclear short-range correlations in two-nucleon knockout reactions*, W. Cosyn, C. Colle, J. Ryckebusch, BriX meeting, November 20, 2015, Leuven.
- *Mass dependence of short-range correlations in nuclei*, C. Colle, W. Cosyn, J. Ryckebusch, S. Stevens, ESNT workshop "neutrino-nucleus scattering", April 18-22, 2015, Saclay.

Poster presentations

- *Mass dependence of short-range correlations*, C. Colle, W. Cosyn, J. Ryckebusch, M. Vanhalst, GRC Photonuclear reactions, August 10-15 2014, Holderness NH.

Samenvatting

Een volledige beschrijving van de kernstructuur is een van de hoofddoelen van theoretische kernfysica. De zoektocht naar de beschrijving van hoe nucleaire observabelen worden gegenereerd door de complexe nucleon-nucleon interactie is een zeer complex vraagstuk. Sinds het ontstaan van de kernfysica wordt er gezocht naar een antwoord hierop. Een erg succesvol model dat vele nucleaire eigenschappen kan verklaren is de gemiddeld-veld benadering [1, 2]. Daarbij bewegen de nucleonen in een gemiddeld-veld potentiaal die het uitgemiddeld effect beschrijft van de individuele nucleon-nucleon interacties. Het is zo dat de nucleon-nucleon kracht correlaties veroorzaakt in de kern. Deze correlaties kunnen niet beschreven worden in gemiddeld-veld benaderingen waar de nucleonen onafhankelijk van elkaar bewegen. De nucleoncorrelaties kunnen onderverdeeld worden in twee categorieën: lange-afstandscorrelaties (LRC) en korte-afstandscorrelaties (SRC). De LRC corresponderen met collectieve lage-energie excitaties van de kern. Boven de Fermi-impuls spelen de LRC geen belangrijke rol meer in de beschrijving van de dynamica in een kern. De harde repulsieve kern en het attractieve-tensor deel van de nucleon-nucleon kracht induceren SRC. De SRC genereren nucleon paren, gekenmerkt door een hoge relatieve impuls en een lage massamiddelpunt-impuls in vergelijking met de Fermi-impuls in de kern [3–6]. De effecten van SRC zijn dominant boven de Fermi-impuls. Zij veroorzaken hoge-impulscomponenten in de nucleonimpulsdistributie (NMD). Doordat LRC en SRC dominant zijn bij verschillende impulsgrootte-schalen kunnen ze gescheiden worden en de SRC isoleren. Dit laat toe om de korte-drachtdynamica in kernen in detail te bestuderen [7–9].

Als men SRC effecten wil meten moeten die onderzocht worden in nucleaire verstrooiingsexperimenten. De exclusieve elektrogeïnduceerde tweenucleonuitstoot reactie is een ideale keuze om SRC te onderzoeken. Daarbij interageert een harde probe (elektron) met een SRC nucleon paar met een hoge relatieve impuls. Dit nucleon paar wordt vervolgens uitgestoten uit de kern en de impuls en energie van beide nucleonen wordt gemeten. De kinematica kan zodanig afgesteld worden dat de reactie gedomineerd wordt door SRC paren. De meting van deze reactie is zeer uitdagend omdat zowel het verstrooide projectiel als de twee uitgaande nucleon gededecteerd moeten worden. In dit werk worden de theoretische berekeningen vergeleken met experimentele data verworven in “Jefferson Lab Hall B CEBAF Large Acceptance Spectrometer (CLAS) data mining initiative” [10] en “Jefferson Lab Hall A collaboration” [5, 11]. De studie van SRC is niet gelimiteerd tot de exclusive elektrogeïnduceerde tweenucleonuitstoot reactie alleen. In Ref. [12] wordt het relatief aantal

SRC paren bepaald door middel van inclusieve elektronverstrooiing op veschillende kernen. Ook zijn SRC onderzocht in exclusieve tweenucleonuitstoot reacties met een hadronische probe. In Brookhaven National Laboratory zijn SRC bestudeerd met een reactie waarbij een inkomend proton een proton-neutron paar uit een koolstof kern, ^{12}C , slaat [3, 13]. Het werd aangetoond dat de meerderheid van SRC paren bestaan uit proton-neutron paren.

Een reactiemodel voor de exclusieve elektrogeïnduceerde tweenucleonuitstootreactie wordt voorgesteld in deze thesis [5, 14–16]. Daarmee worden SRC bestudeerd in kernen. Het gebruik van een gefactorizeerde uitdrukking voor de werkzame doorsnede laat toe om de SRC eigenschappen te bepalen over het volledige nucleaire massagebied. Door middel van de gefactorizeerde werkzame doorsnede kunnen verhoudingen van werkzame doorsnedes voor verschillende kernen berekend worden die onafhankelijk zijn van de interactie tussen het elektron en het nucleon paar. Dit maakt de numerieke resultaten robuust. Finaletoestandsreacties (FSI) worden beschouwd in de berekening van de werkzame doorsnede. Uit de resultaten blijkt dat de FSI een belangrijke rol spelen in het verstrooiingsproces. De FSI zorgen voor een aanzienlijke verzwakking van de werkzame doorsnede [14]. De massa-afhankelijkheid van de tweenucleonuitstoot werkzame doorsnede is bepaald. De berekende massa-afhankelijkheid is zacht, de FSI zijn hier voor een groot stuk verantwoordelijk voor. Het wordt vastgesteld dat de invloed van ladinguitwisselingsreacties in de FSI vrij beperkt is en nauwelijks invloed heeft op de massa-afhankelijkheid van de werkzame doorsnede. FSI zijn een essentieel ingrediënt in de beschrijving van tweenucleonuitstootreactie. De berekende werkzame doorsnede verhoudingen komen overeen met de gemeten verhoudingen. De kerntransparantie is een maatstaf voor de kracht van de FSI. Met de gefactorizeerde uitdrukking voor de werkzame doorsnede wordt de kerntransparentie berekend doorheen het volledige nucleaire massagebied. De berekende kerntransparantie is onafhankelijk van de elektron-tweenucleon koppeling. Dit leidt tot meer robuuste resultaten. De grootte van de afzwakking van de werkzame doorsnede kan efficiënt geschat worden met de bepaalde massa-afhankelijkheid van de kerntransparantie.

Het theoretisch kader ontwikkeld in deze thesis laat ook toe om eigenschappen van de initiële SRC paren, aanwezig in de kern, te reconstrueren uit de gemeten exclusieve elektrogeïnduceerde tweenucleonuitstootreactie. Daarbij wordt de gemeten werkzame doorsnede gecorrigeerd voor FSI om de SRC in de initiële kern te karakteriseren. De synergie tussen theorie en experiment heeft geleid tot een dieper inzicht in de korte-afstand dynamica in kernen. De fractie van nucleonparen die onderhevig zijn aan SRC is bepaald. De massa-afhankelijkheid van deze fractie laat toe om de interne structuur van SRC paren af te leiden, waarbij de relatieve kwantumgetallen en de isospin structuur worden bepaald. De berekende massa-afhankelijkheid is veel zachter dan een naïeve voorspelling waarbij men aanneemt dat de SRC paren een vaste fractie zijn van het totaal aantal paren in een kern ($\propto A(A-1)$). De berekende SRC eigenschappen, gereconstrueerd uit gemeten werkzame doorsnedes, zijn in overeenstemming met de theoretische voorspellingen.

Vooruitzicht

In het tweenucleonuitstootreactiemodel, ontwikkeld in deze thesis, worden de initiële SRC paren geïdentificeerd door middel van de ZRA. In de ZRA wordt de limiet genomen waarbij

de relatieve afstand van het nucleonpaar naar nul nadert. De ZRA is een proxy voor de meer geavanceerde correlatiemethodes gebruikt in het LCA-model. Het kan worden beargumenteerd dat deze twee methodes een vergelijkbare SRC-selectieprocedure implementeren. De mogelijkheid om de ZRA te vervangen door de LCA om de initiële SRC paren te selecteren, en dit te combineren met het tweenucleonuitstootreactiemodel, kan worden overwogen in verder onderzoek.

Het reactiemodel kan worden uitgebreid door de foton-tweenucleonkoppeling expliciet te beschouwen in de berekening van de werkzame doorsnede. Dit laat toe om absolute werkzame doorsnedes te berekenen. In het huidig model worden enkel relatieve werkzame doorsnedes bepaald. Idealiter zou de model-afhankelijkheid, geïntroduceerd door de beschrijving van de foton-tweenucleonkoppeling, kunnen onderzocht worden.

Een verbeterde kennis van nucleaire SRC is onder meer van belang bij het beschrijven van het multi-nucleon signaal in neutrino-kern interacties [17–19]. Dit laat toe om de neutrino-oscillatie met hogere nauwkeurigheid te bepalen. In het ArgoNeuT experiment is neutrinogeïnduceerde tweenucleonuitstoot waargenomen [20]. De beschrijving van SRC is ook belangrijk voor andere neutrino experimenten zoals MicroBooNE, DUNE, MINERvA en NOvA.

Het wordt verwacht dat SRC een belangrijke rol spelen in assymetrische kernen met "exotische" proton-neutron verhoudingen. Het theoretisch kader ontwikkeld in deze thesis kan gebruikt worden om de verstrooiings experimenten aan deze exotische kernen te onderzoeken. Dit geeft toegang nieuwe middelen om SRC te bestuderen en een antwoord te geven op de vraag of de robuuste SRC eigenschappen gelden in onstabiele kernen. Verstrooiingsexperimenten met onstabiele kernen worden in het algemeen gedaan in geïnverteerde kinematica, waarbij de onstabiele kern versneld wordt en verstrooit aan een hadronisch deeltje. Dit hadron induceert dan de tweenucleonuitstoot in de onstabiele kern. Het kan worden verwacht dat (initiële) finaletoestandreacties hierbij een nog grotere rol spelen vergeleken met elektrogeïnduceerde tweenucleonuitstoot. Het attenuatie-effect zal toenemen en de massa-afhankelijkheid van de werkzame doorsnede heel zacht maken. Het model beschreven in deze thesis kan direct toegepast worden voor deze soort reacties.

Referenties

[1] M. G. Mayer, Phys. Rev. **74**, 235 (1948).
[2] O. Haxel, J. H. D. Jensen, and H. E. Suess, Phys. Rev. **75**, 1766 (1949).
[3] A. Tang, J. W. Watson, J. Aclander, et al., Phys. Rev. Lett. **90**, 042301 (2003).
[4] E. Piasetzky, M. Sargsian, L. Frankfurt, et al., Phys. Rev. Lett. **97**, 162504 (2006).
[5] R. Subedi, R Shneor, P. Monaghan, et al., Science **320**, 1476 (2008).
[6] O. Hen, M. Sargsian, L. B. Weinstein, et al., Science **346**, 614 (2014).
[7] O. Benhar, A. Fabrocini, S. Fantoni, and I. Sick, Nuclear Physics A **579**, 493 (1994).
[8] M. Alvioli, C. Ciofi degli Atti, L. P. Kaptari, et al., Phys. Rev. C **87**, 034603 (2013).
[9] R. B. Wiringa, R. Schiavilla, S. C. Pieper, and J. Carlson, Phys. Rev. C **89**, 024305 (2014).
[10] O. Hen, H. Hakobyan, R. Shneor, et al., Phys. Lett. B **722**, 63 (2013).
[11] R. Shneor, P. Monaghan, R. Subedi, et al., Phys. Rev. Lett. **99**, 072501 (2007).

[12] N. Fomin, J. Arrington, R. Asaturyan, et al., Phys. Rev. Lett. **108**, 092502 (2012).
[13] J. Aclander, J. Alster, D. Barton, et al., Physics Letters B **453**, 211 (1999).
[14] C. Colle, W. Cosyn, and J. Ryckebusch, Phys. Rev. C **93**, 034608 (2016).
[15] C. Colle, O. Hen, W. Cosyn, et al., Phys. Rev. C **92**, 024604 (2015).
[16] C. Colle, W. Cosyn, J. Ryckebusch, and M. Vanhalst, Phys. Rev. C **89**, 024603 (2014).
[17] T. Van Cuyck, N. Jachowicz, R. González-Jiménez, et al., Phys. Rev. C **94**, 024611 (2016).
[18] T. Katori and M. Martini, (2016).
[19] L Alvarez-Ruso, Y Hayato, and J Nieves, New Journal of Physics **16**, 075015 (2014).
[20] R. Acciarri, C. Adams, J. Asaadi, et al., Phys. Rev. D **90**, 012008 (2014).